

8-2024

Development and Structural Origin of Stretchable Semiconducting Polymers and Composites

Yunfei Wang
University of Southern Mississippi

Follow this and additional works at: <https://aquila.usm.edu/dissertations>

 Part of the [Polymer and Organic Materials Commons](#), and the [Semiconductor and Optical Materials Commons](#)

Recommended Citation

Wang, Yunfei, "Development and Structural Origin of Stretchable Semiconducting Polymers and Composites" (2024). *Dissertations*. 2282.
<https://aquila.usm.edu/dissertations/2282>

This Dissertation is brought to you for free and open access by The Aquila Digital Community. It has been accepted for inclusion in Dissertations by an authorized administrator of The Aquila Digital Community. For more information, please contact aquilastaff@usm.edu.

DEVELOPMENT AND STRUCTURAL ORIGIN OF STRETCHABLE
SEMICONDUCTING POLYMERS AND COMPOSITES

by

Yunfei Wang

A Dissertation
Submitted to the Graduate School,
the College of Arts and Sciences
and the School of Polymer Science and Engineering
at The University of Southern Mississippi
in Partial Fulfillment of the Requirements
for the Degree of Doctor of Philosophy

Approved by:

Dr. Xiaodan Gu, Committee Chair

Dr. Derek Patton

Dr. Sarah Morgan

Dr. Sergei Nazarenko

Dr. Yoan Simon

August 2024

COPYRIGHT BY

Yunfei Wang

2024

Published by the Graduate School



ABSTRACT

Stretchable semiconductors are pivotal in advancing wearable and implantable electronics, with those boasting both high stretchability and self-healing capabilities being especially significant for a myriad of wearable applications. In this dissertation, we developed an extremely soft, highly stretchable, and self-healing elastomer based on H-bonding crosslinked amide-functionalized polyisobutylene (PIB-amide). When blended with a high-performance conjugated diketopyrrolopyrrole (DPP-T) polymer, the composite exhibits unprecedented stretchability, exceptionally low elastic modulus, and an innate ability to self-heal at room temperature.

The morphology of conjugated polymer/elastomer semiconducting composites have significant impacts on electrical and mechanical properties. Further investigations focused on manipulating the phase separation size in CP/elastomer composites by precise placement of H-bonding functional groups within both the CPs and the elastomers. This study elucidates how these strategic modifications influence the composites' mechanical and electrical performance. By introducing amide functional groups to both a DPP-based semiconducting polymer (DPPTVT-A) and a polyisobutylene-based elastomer (PIB-A), we facilitated inter- and intra-phase H-bonding crosslinks. This approach enabled us to fabricate composites with varying crosslinking patterns—dual, uni, and non-H-bonding—thereby allowing a comparative analysis of their phase behaviors and electronic and mechanical properties.

Additionally, an analysis of the mechanical properties of 65 CP thin films challenged the prevailing belief that rigidity and stretchability are mutually exclusive. Our

study of rigid deformable CPs reveals their mechanical behavior, electrical properties, and deformation mechanisms.

This dissertation contributes a novel perspective to the development and molecular origin of semiconductive polymers and composites that are stretchable and highly healable, heralding novel applications in the burgeoning field of stretchable electronics.

ACKNOWLEDGMENTS

First and foremost, I extend my deepest gratitude to my Ph.D. advisor, Prof. Xiaodan Gu, for his invaluable guidance throughout my journey in this research field. Over the past five years, Prof. Gu has mentored me in every facet of Ph.D. training, from project selection and design, experiment to scientific writing and career plan. His passion, vision, and creativity have been a constant source of inspiration. I consider myself incredibly fortunate to be a member of the Gu group, where I have grown from a novice to a skilled researcher under his tutelage. I am particularly grateful for his understanding and support in allowing me to pursue a project that aligned more closely with my interests, a decision that was pivotal in my ability to persevere through my degree. Prof. Gu's introduction to the field of X-ray scattering has opened doors for me, including the opportunity to conduct experiments at the Brookhaven National Lab (BNL)'s synchrotron X-ray scattering source and the Advanced Light Source (ALS) at Lawrence Berkeley National Lab (LBNL) through an ALS fellowship. This experience has not only enriched my knowledge but also introduced me to lifelong friends, a treasure I hold dear. Prof. Gu's nomination for several awards has significantly supported my career development, and words cannot fully express my gratitude for the honor of being his graduate student.

I also extend my sincere appreciation to my host, Dr. Chenhui Zhu, at ALS, and Dr. Yi Liu at the Molecular Foundry, LBNL, for their generous support during my year in Berkeley.

My thanks go to Prof. Derek Patton, Prof. Sarah E. Morgan, Prof. Sergei Nazarenko, and Prof. Yoan Simon for their invaluable contributions as my dissertation committee members. Their provision of instrumental access, collaboration opportunities,

and insightful suggestions have been instrumental in my research. Dr. Morgan's guidance on independent proposal writing has been particularly enlightening, teaching me crucial skills for my future career.

I am grateful for the support of all faculty members, staff, my 2019 PSE classmates, and friends at Hattiesburg, who have made my time there memorable.

To the past and present members of the Gu Research Group, your friendship, assistance, and support have made my graduate journey smoother and more enjoyable. A special acknowledgment to my mentor, Song Zhang, for his guidance and teachings in experimental work and project design. My gratitude also extends to my labmates at the Molecular Foundry and ALS for helping me adjust to life in Berkeley. Special thanks to He Li from MF for his career advice and food recommendations, Ka Hung Chan from ALS for his assistance with Python coding, and Zhengxing Peng from ALS for her help with soft X-ray scattering experiments.

This work would not have been possible without the collaboration of brilliant researchers from over ten institutions worldwide. I am especially thankful for the long-term collaboration with Prof. Simon Rondeau-Gagné's group at the University of Windsor, Prof. Yu-Cheng Chiu's group at the National Taiwan University of Science and Technology, Prof. Wenjie Xia's group at Iowa State University, and the beamline scientists Dr. Guillaume Freychet and Dr. Patryk Wasik at Brookhaven National Lab.

I am thankful for the access to state-of-the-art facilities like National Synchrotron Light Source II (NSLS-II) at BNL, ALS and Molecular Foundry at LBNL, and the Spallation Neutron Source at Oak Ridge National Laboratory (ORNL), crucial for my research.

I must also take a moment to acknowledge my own journey and the resilience I've cultivated along the way. Persisting steadfastly, facing every challenge with a never-give-up attitude, and maintaining optimism in the midst of adversity have been crucial to achieving this Ph.D. degree. These experiences will forever be treasured as invaluable assets of my life.

I am deeply grateful for the financial support from the U.S. National Science Foundation under award number DMR-2047689 and the ALS doctoral fellowship in residence.

Lastly, my profound thanks go to my family—my grandparents Yongsheng Wang and Baoqin Zhang, and my parents Qunli Wang and Jingjie Wu. Your unwavering support and trust have been my motivation to strive for excellence.

DEDICATION

To my loving grandparents and parents,
Yongsheng Wang, Baoqin Zhang, Qunli Wang and Jingjie Wu

TABLE OF CONTENTS

ABSTRACT.....	ii
ACKNOWLEDGMENTS	iv
DEDICATION.....	vii
TABLE OF CONTENTS.....	viii
LIST OF TABLES.....	xii
LIST OF ILLUSTRATIONS.....	xiii
LIST OF SCHEMES.....	xv
LIST OF ABBREVIATIONS.....	xvi
CHAPTER 1 – BACKGROUND.....	1
1.1 Overview.....	1
1.2 Mechanical analysis of conjugated polymers and characterization techniques.....	2
1.2.1 Mechanical properties.....	3
1.2.2 Mechanical testing methods.....	5
1.2.3 Understanding electronical properties upon stretching.....	7
1.2.4 Deformation mechanisms under stretching	9
1.3 Material design for stretchable conjugated polymers	12
1.3.1 Polymer’s length and dispersity effect.....	13
1.3.2 Design of intrinsic stretchable conjugated polymers	16
1.3.3 Conjugated polymer composites.....	27

1.3.4 Rigid stretchable conjugated polymers	29
1.3.5 Others	30
1.4 Few representative applications demonstration	31
CHAPTER 2 – STRETCHABLE AND SELF-HEALABLE SEMICONDUCTIVE	
COMPOSITES BASED ON HYDROGEN BONDING-CROSSLINKED	
ELASTOMERIC MATRIX.....	
2.1 Introduction.....	35
2.2 Experimental.....	40
2.2.1 Materials	40
2.2.2 Nuclear magnetic resonance (NMR) spectroscopy.....	41
2.2.3 Size-exclusion chromatography (SEC).....	41
2.2.4 Fourier-transform infrared spectroscopy (FT-IR).....	42
2.2.5 Film processing.....	42
2.2.6 Pseudo-free-standing tensile test.....	42
2.2.7 OFET fabrication and characterization.....	42
2.2.8 Atomic Force Microscope (AFM) and AFM-IR	43
2.2.9 Wide angle X-ray scattering (WAXS).....	43
2.2.10 Deformed composite film processing	43
2.2.11 Polarized UV-vis.....	43
2.2.12 Self-healing ability evaluation using cutting film method.....	44

2.3 Results and discussion	44
2.4 Conclusion	55
CHAPTER 3 – LEVERAGING NON-COVALENT INTERACTIONS TO CONTROL MORPHOLOGY, ELECTRICAL AND MECHANICAL PROPERTIES OF STRETCHABLE SEMICONDUCTING COMPOSITES	57
3.1 Introduction.....	57
3.2 Experimental.....	62
3.2.1 Materials	62
3.2.2 Film processing.....	62
3.2.3 Atomic force microscopic (AFM) and infrared-spectroscopy combined AFM (AFM-IR).....	62
3.2.4 Grazing-incidence wide angle X-ray scattering (GIWAXS).....	63
3.2.5 UV-Vis absorption spectroscopy	63
3.2.6 Film-on-elastomer tensile test.....	63
3.2.7 Film-on-water tensile test	64
3.2.8 OFET fabrication and characterization.....	64
3.3 Results and Discussion	64
3.4 Conclusion	82
CHAPTER 4 – HIGHLY DEFORMABLE RIGID GLASSY CONJUGATED POLYMERIC THIN FILMS	84

4.1 Introduction.....	84
4.2 Experimental.....	87
4.2.1 Materials and processing.....	87
4.2.2 Tensile deformation of 60nm thin-film sample.....	88
4.2.3 Morphological characterization.....	88
4.2.4 OFET fabrication.....	89
4.2.5 Overview of CG-MD Simulations.....	89
4.3 Results and Discussion.....	92
4.4 Conclusion.....	110
FUTURE DIRECTIONS.....	112
APPENDIX A – Supporting Information.....	114
APPENDIX B – Supporting Information.....	134
APPENDIX C – Supporting Information.....	145
REFERENCES.....	186

LIST OF TABLES

Table 3.1 Summary of morphological, electrical and mechanical properties of non-, uni- and dual-H-bonding crosslinked composites, DPPTVT/PIB-Br, DPPTVT-A/PIB-Br, DPPTVT/PIB-A and DPPTVT-A/PIB-A.	67
Table 3.2 Crystallographic parameters of non-, uni- and dual-H-bonding crosslinked composites, DPPTVT/PIB-Br, DPPTVT-A/PIB-Br, DPPTVT/PIB-A and DPPTVT-A/PIB-A from GIWAXS.	73
Table 4.1 Summary of the OFETs performance of stretched P3BT and P3OT thin films.	98
Table 4.2 Crystallographic Information for P3BT and P3OT extracted from wide-angle hard X-ray scattering.....	104

LIST OF ILLUSTRATIONS

Figure 1.1 Overview of Mechanical Properties and Measurement Techniques for CPs.	5
Figure 1.2 Charge mobility measurement upon stretching.	9
Figure 1.3 Deformation mechanism study of PDPPTC2C8C10.	12
Figure 1.4 Molecular weight effect on stretchability of CPs.	15
Figure 1.5 Backbone engineering for design of intrinsic stretchable CPs.	20
Figure 1.6 Side chain engineering for design of intrinsic stretchable CPs.	23
Figure 1.7 CP-b-elastomer block copolymers for intrinsic stretchable CPs.	25
Figure 1.8 Semi-crystalline structure of CPs and Intrinsic low-crystallinity CPs.	27
Figure 1.9 Stretchable and self-healable conjugated polymer/elastomer composites.	29
Figure 1.10 E~COS relationship and stress–strain curve for CPs.	30
Figure 1.11 Stretchable electronic devices.	34
Figure 2.1 Mechanical, electrical, and morphology for DPP-T/PIB-Amide composite films with different blending ratios.	48
Figure 2.2 Charge mobility stability upon stretching and cyclic stretching.	50
Figure 2.3 Deformation mechanism of 20% DPP-T/PIB-Amide.	52
Figure 2.4 Self-healing ability of 20% DPP-T/PIB-Amide composite films.	55
Figure 3.1 AFM phase images of composites.	70
Figure 3.2 GIWAXS and UV-vis results of composites.	72
Figure 3.3 Charge mobility comparison of DPPTVT/PIB-Br (red), DPPTVT-A/PIB-Br (orange), DPPTVT/PIB-A (green) and DPPTVT-A/PIB-A (black) composites.	74
Figure 3.4 Mechanical properties of composites.	76
Figure 3.5 Charge mobility of stretched composites.	77

Figure 3.6 AFM phase images of stretched composites.	80
Figure 3.7 Herman’s orientation parameter f versus strain based on polarized UV–vis for DPPTVT/PIB-Br, DPPTVT-A/PIB-Br, DPPTVT/PIB-A and DPPTVT-A/PIB-A composite films at 0%, 20%, 50%, 100%, and 150% strain.....	80
Figure 3.8 Charge mobility comparison along parallel direction of stretched composites after stretching 1 and 10 cycles and staying for 24 and 48 h at strain of 50% and 150%. 82	
Figure 4.1 Mechanical properties of 65 samples were tested here.	94
Figure 4.2 Molecular structure and true stress-strain curves for P3BT and P3OT thin films.	96
Figure 4.3 Normalized transistor mobility of stretched P3BT and P3OT at different degree of strain.....	97
Figure 4.4 Experimental result for hard/tender WAXS experiment on P3BT and P3OT polymer thin films under various true strain.	103
Figure 4.5 Whole chain alignment study from polarized UV-vis spectroscopy.....	106
Figure 4.6 Amorphous component alignment study from CG-MD simulation.....	108
Figure 4.7 Molecular structure, true stress-strain curves, representative 2D scattering patterns and Herman’s orientation parameter f versus strain based on (100) peak from hard and tender WAXS and of F8BT.	110

LIST OF SCHEMES

Scheme 2.1 Schematic of stretchable and self-healable DPP-T/PIB-Amide composite. .	40
Scheme 2.2 Synthetic route of PIB-Amide.....	44
Scheme 3.1 Chemical structure of DPPTVT, DPPTVT-A, PIB-Br and PIB-A and schematic of non-, uni- and dual-H-bonding crosslinked composites, DPPTVT/PIB-Br, DPPTVT-A/PIB-Br, DPPTVT/PIB-A and DPPTVT-A/PIB-A.	66

LIST OF ABBREVIATIONS

<i>AFM-IR</i>	Atomic force microscopic combined with infrared-spectroscopy
<i>ALS</i>	Advanced Light Source
<i>BCF</i>	Tris(pentafluorophenyl)borane
<i>BNL</i>	Brookhaven National Lab
<i>BR</i>	Butyl rubber
<i>CB</i>	Chlorobenzene
<i>CBS</i>	Conjugated breaker spacers
<i>CD</i>	Constructive degradation
<i>CG-MD</i>	Coarse-grained molecular dynamics
<i>CONPHINE</i>	Conjugated polymer/elastomer phase Separation-induced elasticity
<i>COS</i>	Crack onset strain
<i>CP</i>	Conjugated polymers
<i>CP-E BCP</i>	<i>CP-block-elastomer diblock copolymers</i>
<i>D-A</i>	Donor-acceptor
<i>DBB</i>	Dibutylbenzene
<i>DCM</i>	Dichloromethane
<i>DPP</i>	Diketopyrrolopyrrole
<i>DPPTVT-A</i>	Amide functional DPPTVT
<i>E</i>	Elastic modulus
<i>EMG</i>	Electromyograms

<i>EO</i>	Oligo(ethylene oxide)
<i>EQE</i>	External quantum efficiency
<i>f</i>	Orientation parameter
<i>FOE</i>	Film-on-Elastomer
<i>FOW</i>	Film-on-water
<i>FT-IR</i>	Fourier-transform infrared spectroscopy
<i>FWHM</i>	Full width at half maximum
<i>GIWAXS</i>	Grazing-incidence wide-angle hard X-ray scattering
<i>GM</i>	Gastrocnemius medialis
<i>HDPE</i>	High-density polyethylene
<i>HT-GPC</i>	High-temperature gel permeation chromatography
<i>IDTBT</i>	Indacenodithiophene-co-benzothiadiazole
<i>LAMMPS</i>	Large-scale atomic/molecular massively parallel simulator
<i>LBNL</i>	Lawrence Berkeley National Lab
<i>MALLS</i>	Multiangle laser light scattering
<i>MW</i>	Molecular weight
<i>NMP</i>	N-methyl-2-pyrrolidone
<i>NMR</i>	Nuclear magnetic resonance
<i>NSLS-II</i>	National Synchrotron Light Source II
<i>OECT</i>	Organic electrochemical transistor

<i>OFET</i>	Organic field-effect transistor
<i>OLED</i>	Organic light-emitting diodes
<i>OM</i>	Optical microscopy
<i>ORNL</i>	Oak Ridge National Laboratory
<i>OTS</i>	Octyltrichlorosilane
<i>P3BT</i>	Poly(3-butylthiophene-2,5-diyl)
<i>P3HpT</i>	Poly(3-heptylthiophene)
<i>P3OT</i>	Poly(3-octylthiophene-2,5-diyl)
<i>PCE</i>	Power conversion efficiency
<i>PCL</i>	Polycaprolactone
<i>PDCA</i>	2,6-Pyridine dicarboxamide
<i>PDMS</i>	Polydimethylsiloxane
<i>PDPPT3</i>	Poly(2,5-bis(4-hexyldodecyl)-2,5-dihydro-3,6-di-2-thienyl-pyrrolo[3,4-c] pyrrole-1,4-dione-alt-thiophene)
<i>PE</i>	Polyethylene
<i>PEDOT:PSS/CNT</i>	(poly(3,4-ethylenedioxythiophene):poly(styrenesulfonate))/carbon nanotube
<i>PFO</i>	poly(9,9-dioctyl fluorene)
<i>PIB</i>	Polyisobutylene
<i>PNDI2T</i>	Poly(naphthalenediimide-bithiophene)

<i>POO</i>	Poly(octylene oxide)
<i>PP</i>	Polypropylene
<i>PS</i>	Polystyrene
<i>R</i>	Dichroic ratio
<i>r.p.m.</i>	Revolutions per minute
<i>SAXS</i>	Small-angle hard X-ray scattering
<i>SEBS</i>	Styrene-ethylene-butylene-styrene
<i>SEC</i>	Size-exclusion chromatography
<i>SIS</i>	Polystyrene-block-polyisoprene-block-polystyrene
<i>SPM</i>	Supramolecular polymeric material
<i>TADF</i>	Thermally activated delayed fluorescence
T_g	Glass transition temperature
<i>THF</i>	Tetrahydrofuran
<i>TPU</i>	Thermoplastic polyurethane
<i>UPy</i>	2-Ureido-4[1H]-pyrimidone
<i>VMD</i>	Visual molecular dynamics
<i>WAXS</i>	Wide-angle X-ray scattering

CHAPTER 1 – BACKGROUND

(Adapted from “Wang, Y.; Cao, Z.; Gu, X. Stretchable conjugated polymers and composites for wearable electronics. Submitted, 2024.”)

1.1 Overview

Our contemporary existence is unimaginable without the constant interaction with electronic devices and the Internet. This entire ecosystem originated from inorganic semiconductor devices, specifically transistors. The creation of the transistor in 1947 by William Shockley, John Bardeen, and Walter Brattain at Bell Laboratories represents a monumental leap in 20th-century technology. This innovation not only had a profound and extensive impact on technology, society, and the global economy but also laid the groundwork for the digital era. The advent of the Internet later in the 20th century revolutionized communication methods. Technologies such as email, messaging, social media, and video conferencing have fundamentally changed our ways of interaction, facilitating instantaneous global communication. Additionally, the Internet has reshaped global economies, paving the way for e-commerce, digital marketplaces, and new employment sectors. It is fair to say that the invention of the transistor revolutionized our society and heralded the digital age.

Building on the initial achievements of inorganic semiconductors, organic semiconductors introduce new possibilities in material design. In contrast to inorganic materials, which are held together by strong bonds (covalent, ionic, metallic) in solids, soft materials are generally disordered and bonded by weaker forces (van der Waals, hydrogen, electrostatic), leading to significantly different mechanical properties. Polymers, celebrated for their synthetic versatility, find use in a broad spectrum of applications due

to their diverse mechanical properties. These range from soft hydrogels and elastomers to strong commodity polymers used in packaging, and even to extremes like Kevlar and carbon fiber composites in the aerospace industry. This versatility in material design extends to conjugated polymer (CP) systems. To be used in wearable devices, stretchable CPs are in urgent needs. However, the rigid and planar conjugated backbone structure contributed to the exceptional electrical performance of CPs also make the CPs stiff and brittle, posing a significant challenge in the development of stretchable CPs.^{1,2}

Thus, this dissertation will focus on development and structural origin study of stretchable CPs. The discussion is divided into the following three chapters, followed by envisioned future directions.

Chapter 2: We designed a stretchable and self-healable semiconductive composite based on hydrogen bonding-crosslinked elastomeric matrix.

Chapter 3: We leveraged non-covalent interactions to control morphology, electrical and mechanical properties of stretchable semiconducting composites.

Chapter 4: We detailed studied the highly deformable rigid glassy conjugated polymeric thin films.

1.2 Mechanical analysis of conjugated polymers and characterization techniques

Stretchable conjugated polymers (CPs) represent a distinct category of polymer-based materials that retain high levels of stretchability alongside superior charge carrier mobility, even when the thin film is significantly deformed (e.g. 50% strain).³⁻⁶ Those materials are highly useful for wearable devices to ensure conformal contact with skin in the case of wearable electronics, and conformal contact with organs when implanted. Therefore, it is essential to assess their mechanical property and electrical capabilities of

any conjugated polymeric materials or composite, before, during, and after stretching. This evaluation is key for the advancement of new semiconductive materials and devices. Moreover, a deep comprehension of the deformation processes at play is critical, as it plays a significant role in understanding the overall device performance, and underlying design rule. This understanding also provides crucial insights that aid in the innovation of advanced stretchable CPs. In this context, we aim to highlight several fundamental properties of CPs, encompassing their mechanical properties, characterization methods, and deformation mechanisms.

1.2.1 Mechanical properties

Gaining a thorough understanding of mechanical properties is vital for the development of stretchable CPs.⁷⁻¹⁰ To grasp the mechanical behaviors of CPs effectively, it will be fundamental to start with a solid foundation in basic mechanical parameters. There are several reviews exist in this domain, such as an excellent review article by Lipomi group.⁹

Key characteristics of stretchable CPs include their elastic modulus (E), crack onset strain (COS), and elastic hysteresis. The elastic modulus, also referred to as Young's modulus, measures the stiffness of CPs. A higher E means the material is more resistant to being deformed when subjected to a load. On the other hand, COS gauges the material's ability to stretch, marking the point at which cracking begins. A higher COS indicates that the material can withstand more deformation before failing. Soft CPs are defined as having an elastic modulus of less than 700 MPa, while stretchable CPs are those with a COS greater than 20%. Recently, elastic CPs have gained interest due to their ability to undergo

deformation that is predominantly elastic, with minimal permanent plastic deformation, making them ideally suited for applications requiring repeated stretching.

The E and COS are determined from the engineering stress (σ) vs. engineering strain (ϵ) curve, showcasing how a material behaves mechanically upon stretching. When a force is applied to a material of initial dimensions (length L_0 , width w_0 , and thickness t_0), it experiences an elongation ΔL , defining engineering strain as $\epsilon = \Delta L/L_0$. σ is calculated using $\sigma = F/A_0$, where A_0 is the material's initial cross-sectional area, and F is the applied force on the sample's thin film. Typical behaviors of glassy and viscoelastic CPs on these curves are depicted in **Figure 1.1a**, showing glassy CPs going through elastic, yielding, strain-softening, and strain-hardening phases, whereas viscoelastic CPs display continuous elastic and plastic behavior without a distinct yield point or strain-softening. The E corresponds to the initial slope of the curve, and COS is identified at the point where the films begin to fracture. Elasticity in stretchable CPs is examined through stress-cyclic strain curves and hysteresis studies. A stress-cyclic strain curve without residual strain after releasing indicates perfect elasticity (**Figure 1.1b**). Hysteresis, shown in **Figure 1.1c**, measures the energy dissipated during stretching and releasing, calculated from the area differences between stretching and releasing curves (**Figure 1.1d**), with more hysteresis suggesting more plastic deformation. While fracture energy, adhesive strength, and cohesion are crucial for structural materials, an in-depth analysis of these aspects is beyond this chapter's scope.

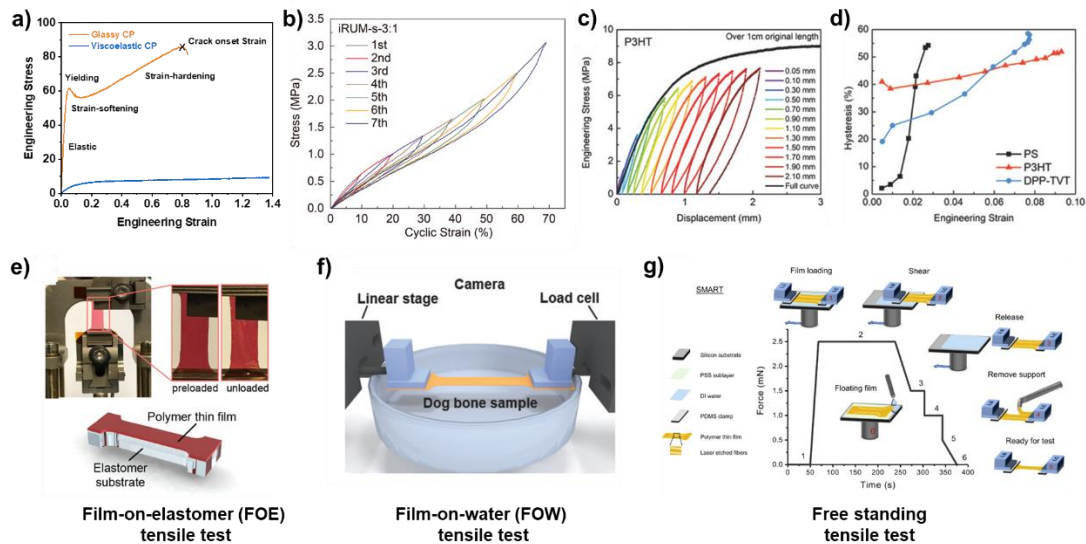


Figure 0.1 *Overview of Mechanical Properties and Measurement Techniques for CPs.*

(a) Typical stress-strain curve of glassy and viscoelastic CPs.²⁷ (b) Stress-strain (engineering) curves with a cyclic strain range of 10–70%.²⁸ (c) Hysteresis study and (d) calculation of P3HT.²⁰ Schematic of (e) film-on-elastomer,²⁹ (f) film-on-water and (g) free standing tensile test.²⁵

1.2.2 Mechanical testing methods

Traditional methods for mechanical characterization usually focus on bulk materials with millimeter thickness. Yet, thin films (tens to hundreds nm in thickness), often used in the functional layers of devices, can display unique mechanical properties as a result of confinement effects.¹¹ Assessing the mechanical characteristics of these thin films presents a challenge, particularly because of their delicate nature, which complicates their transfer and loading into a tensile testing apparatus. Therefore, there is a significant demand within the scientific community for innovative techniques specifically designed to evaluate the mechanical properties of thin films, as detailed below.

The Film-on-Elastomer (FOE) tensile test is a popular technique for measuring the mechanical properties of CP thin films.^{12–15} In this method, CP thin films are first spin-cast onto silicon wafers before being transferred to an elastomer substrate, typically

polydimethylsiloxane (PDMS) (**Figure 1.1e**). The thin films are then stretched together with the substrate, and optical microscopy (OM) is used to observe the formation of cracks. The strain level at which cracks first appear is recorded as the COS. The E is determined through a buckling-based metrology approach introduced by Stafford et al., which involves transferring CP thin films onto a pre-stretched substrate and then releasing the strain to produce wrinkled samples.¹⁵ The E of the thin film E_f is subsequently calculated using the following equation:

$$\frac{E_f}{(1 - \nu_f^2)} = \frac{3E_s}{(1 - \nu_s^2)} \left(\frac{\lambda}{2\pi h_f}\right)^3$$

where λ is buckling wavelength, h_f is the thickness of the CP films, E_s is the elastic modulus of the PDMS substrate, ν_f and ν_s are the Poisson ratios of the film and substrate. While the FOE method is a recognized approach for assessing the mechanical properties of CP thin films, deriving stress-strain curves and calculating the E using this method can be complex. Additionally, isolating the effects of the elastomer substrate proves difficult, and the FOE method is unsuitable for materials that are too soft or deformable to form wrinkles, specifically those with an elastic modulus lower than that of PDMS or a crack onset strain greater than PDMS.

An alternative approach, the Film-on-Water (FOW) tensile test, has been developed and popularized by the Kim group for thin metals and the Crosby group for thin polymers.¹⁶⁻¹⁹ This method involves stretching nanometer-thick films floated on water to directly obtain stress-strain curves of CP thin films (**Figure 1.1f**).¹⁶ The FOW tensile test has shown that the mechanical properties of polystyrene thin films are comparable to their bulk counterparts tested with standard tensile testing equipment, such as Instron machines,

underscoring the FOW method's accuracy.²⁰ However, this technique is primarily applicable to hydrophobic materials, which fortunately includes most CPs. Numerous samples have been successfully tested using this method, with findings reported in the literature by Gu group and the Lipomi group.^{21–24}

In an effort to compare outcomes from both FOE and FOW methods, Rodriguez et al. examined P3HT with varying molecular weights.¹¹ The study found consistent trends in the COS values across both methods, although differences in the E were noted. These discrepancies were linked to factors like voids in the films, thickness variations, and differing strain rates, even though other research, such as that by Gu, showed similar E values between the two methods.

To minimize the influence of water on the measurements, the free-standing tensile test was developed.²⁵ This technique involves directly stretching free-standing films after water support is removed (**Figure 1.1g**). Other methods for measuring the mechanical properties of nanometer-thick films include nanoindentation and dynamic mechanical analysis, offering a range of options for accurately characterizing thin film materials.²⁶

1.2.3 Understanding electrical properties upon stretching

Evaluating the retention of electrical properties after stretching is essential for the practical use of stretchable devices, making the assessment of charge mobility after deformation a critical step. To this end, both ex-situ and in-situ techniques have been devised to test charge transport behavior under strain.

The ex-situ approach, which is widely used, involves measuring the charge mobility of samples that have been stretched and then placed on a silicon substrate for analysis (**Figure 1.2a**). The process begins with CP thin films being spin-cast on

octyltrichlorosilane (OTS)-coated Si/SiO₂ wafers, followed by transfer to PDMS, stretching along with the PDMS to a predetermined strain, and then transferring back to Si/SiO₂ wafers. Gold electrodes are then applied to the CP thin films to serve as source and drain, with the doped Si substrate acting as the gate electrode and SiO₂ as the dielectric layer. Charge mobility is evaluated in directions both parallel and perpendicular to the stretch. Typically, charge mobility tends to stay the same or slightly increase in the parallel direction, while it decreases in the perpendicular direction due to morphological changes in the polymer chains within the film, such as crystallite domain rotation and alignment of amorphous chains. Charge mobility is also assessed after cyclic stretching to gauge the material's elasticity. While ex-situ measurement is straightforward and convenient, it may not accurately reflect electrical performance due to possible relaxation effects after stretching due to the fact that many CPs are viscoelastic.

In contrast, *in-situ* measurements are designed to avoid the effects of chain relaxation by incorporating a more complex fabrication process. In this method, stretchable organic field-effect transistors (OFETs) are used, featuring stretchable electrodes and dielectrics (**Figure 1.2b**). Devices are stretched, and charge mobility is measured directly to account for post-stretching performance. This process requires careful calculation to account for changes in device geometry as the electrodes deform. Charge mobility observed in fully stretchable OFETs is slightly lower compared to traditional rigid Si/SiO₂ setups, likely due to a reduced electric field from a thicker dielectric layer.³⁰

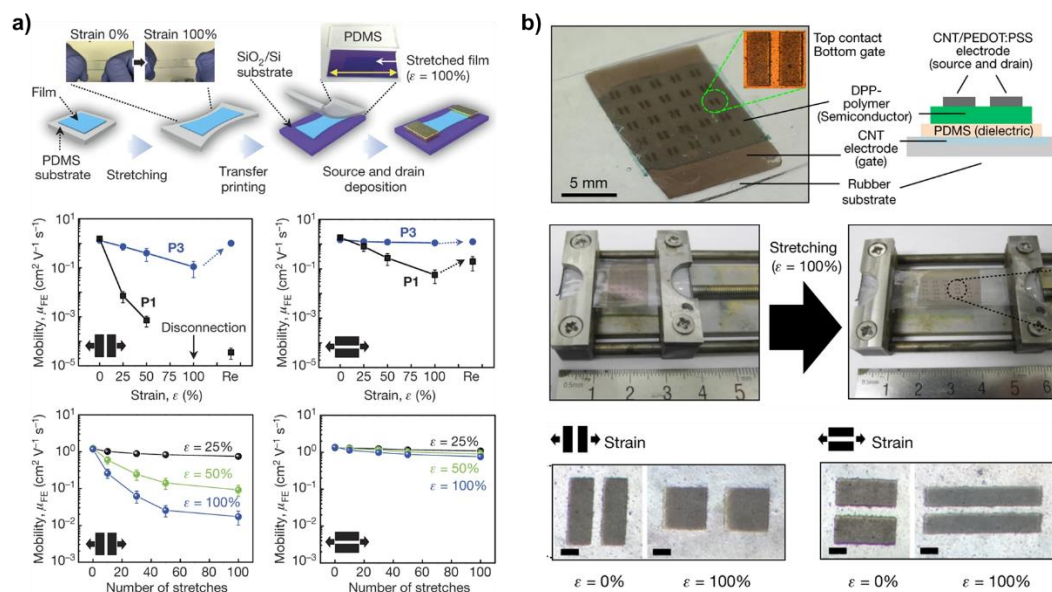


Figure 0.2 Charge mobility measurement upon stretching.

(a) *Ex situ* and (b) *in situ* charge mobility measurement upon stretching.³⁰

1.2.4 Deformation mechanisms under stretching

Grasping the deformation mechanisms of stretchable polymer films during stretching is crucial for understanding the fundamental principles behind the creation of stretchable organic semiconductors.³¹ Given the semi-crystalline nature of CPs, both their amorphous and crystalline sections play roles in accommodating significant plastic deformation, with the crystallite domains being particularly crucial for charge mobility.³² The amorphous chains linking these crystalline areas are equally important as they support charge transfer across domains. Therefore, delineating the deformation behaviors of both crystalline and amorphous regions is essential. Several techniques have been developed to dissect the deformation mechanisms in these different regions, and a holistic view of CP deformation mechanisms emerges from integrating findings across these methodologies. For instance, **Figure 1.3** illustrates how the deformation mechanism of a viscoelastic

diketopyrrolopyrrole (DPP)-based conjugated polymer with long branched alkyl side chains is elucidated using X-ray scattering and polarized UV-vis spectroscopy.³³

To investigate crystallite domain alignment, transmittance wide-angle hard X-ray scattering (WAXS) with high-energy X-rays (over 8 keV) is used, leveraging a synchrotron X-ray beam (**Figure 1.3c**). The sample orientation is perpendicular to the X-ray direction, allowing for the analysis of anisotropic changes in lamella packing, which reveal how crystallite domains rotate post-stretching. From 2D scattering images, 1D data along equatorial and meridian directions are extracted to quantify changes parallel and perpendicular to the stretch axis, respectively. Changes in the peak position and full width at half maximum (FWHM) of the (100) peak are examined to assess lamellar packing distance and crystallite deformation. Grazing-incidence WAXS (GIWAXS) offers an alternative, examining stretched films on Si wafers aligned both parallel and perpendicular to the X-ray beam to determine crystallite domain alignment.

Transmittance wide-angle tender X-ray scattering, utilizing lower-energy X-rays (2~6 keV), focuses on backbone orientation within crystalline domains, highlighting backbones' pivotal role in charge transport (**Figure 1.3d**).³³⁻³⁶ Since most CPs contain sulfur only in the backbones, running WAXS near the sulfur K-edge enhances the scattering signal from the sulfur, aiding in analyzing deformation related to the backbone.

Polarized UV-vis spectroscopy examines overall chain alignment (**Figure 1.3e**), where the dichroic ratio (R) and orientation parameter (f) are derived from the absorption spectrum, measured with a polarizer in the light path. Additionally, atomic force microscopy (AFM) is also employed to analyze changes in the surface morphology of thin films, particularly

effective in examining the phase transitions within CP/elastomer composites under stretching.^{37,38}

The variations in the f of DPP-based polymers at different levels of strain, as deduced from the aforementioned analyses, are compiled in **Figure 1.3f**. The findings indicate that the deformation mechanism of viscoelastic DPP conjugated polymers is predominantly based on the alignment of crystalline domains and the slippage of amorphous chains, as shown in **Figure 1.3g**. These investigative techniques have been similarly applied to explore rigid stretchable CPs.²⁷ In contrast to the softer, stretchable DPP polymers, the deformation of rigid stretchable CPs, like poly(3-butylthiophene-2,5-diyl) (P3BT), initially relies on the alignment of amorphous chains, with the process of crystallite fracturing and rotation becoming significant as deformation progresses.

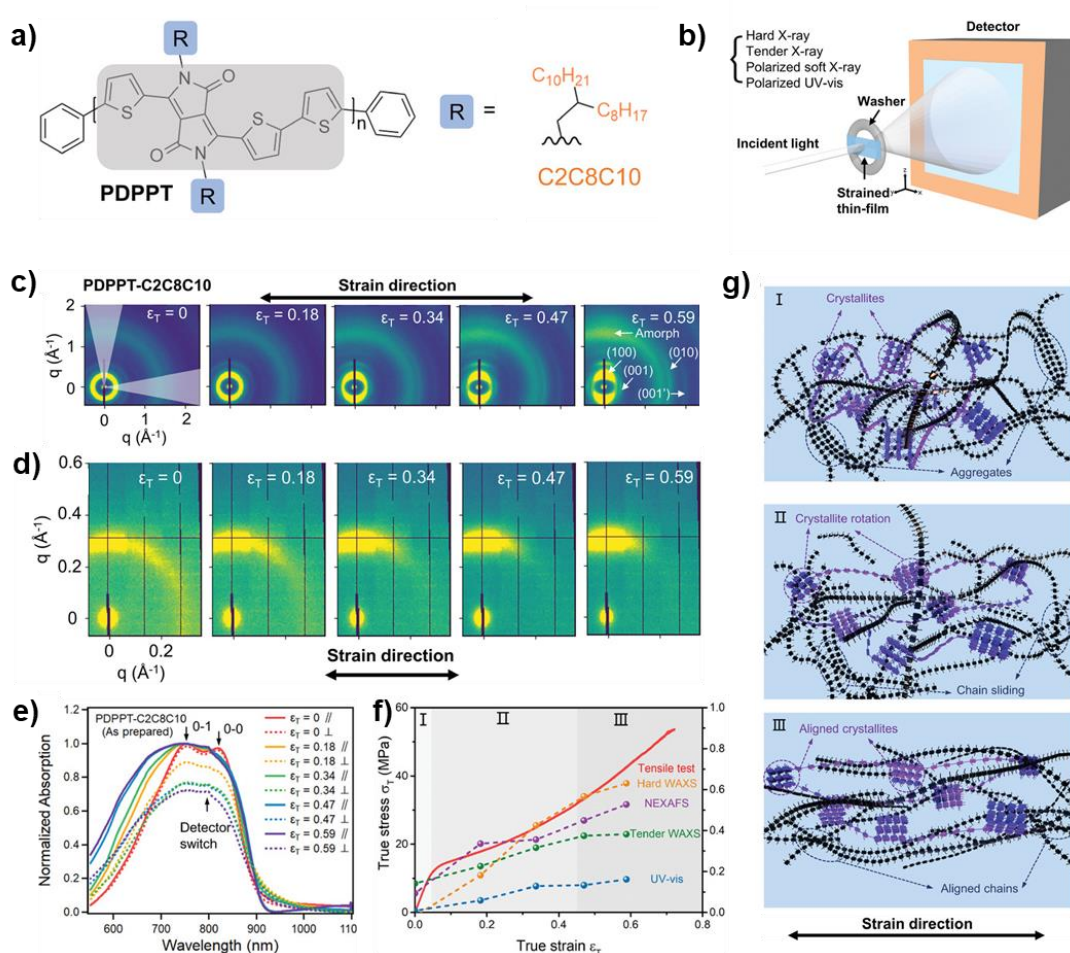


Figure 0.3 Deformation mechanism study of PDPPTC2C8C10.

(a) Chemical structure of PDPPTC2C8C10. (b) Schematic of multimodal morphological characterization tools on tensile strained free-standing thin films. Representative 2D scattering patterns and characteristic crystallographic peaks from (c) hard WAXS and (d) tender WAXS. (e) UV-vis absorption plot at different wavelengths. (f) Stress-strain response and summarized Herman's orientation parameter for PDPPT-C2C8C10 polymer under three stages of strain. I: Initial deformation; Stage II: Medium strain; Stage III: High degree of alignment. (g) Schematic snapshots of deformation mechanisms under three stages showing crystallite orientation, chain alignment, and chain sliding.³³

1.3 Material design for stretchable conjugated polymers

Stretchable CPs are distinguished by their ability to withstand high COS levels while preserving efficient charge carrier mobility after being stretched.^{4-6,39-43} The exceptional electrical performance of CPs is attributed to their conjugated backbone

structure.^{1,2} However, the natural stiffness and flatness of the CP backbone contribute to its rigidity, posing a significant challenge in the development of stretchable CPs. Recent strategies to overcome this obstacle include fine-tuning fundamental polymer chain's properties such as molecular weight (MW) and regioregularity, crafting intrinsically stretchable CPs, and forming semiconducting composites by integrating CPs with soft, elastic elastomers. While the focus has predominantly been on enhancing the stretchability of soft CPs, rigid CPs have also shown promising stretchability, offering an alternative avenue for the development of stretchable CP materials.

1.3.1 Polymer's length and dispersity effect

Unlike small molecules, synthetic CPs display distinct traits tied to their MWs and dispersity, which markedly impact their attributes. Furthermore, the regioregularity of CPs, particularly noted in polymers such as poly(3-alkylthiophene) (P3ATs) that consist of asymmetric thiophene monomers, influences their packing structure. This, in turn, results in unique mechanical and electrical properties.⁴⁴

1.3.1.1 Molecular weight effect

The molecular weight (MW) of synthetic polymers, which is determined by the polymerization process, varies significantly between batches and plays a pivotal role in defining the mechanical and electrical properties of a CP. Each polymer has a critical entanglement molecular weight (M_e), which is indicative of the point at which polymer chains begin to entangle. Above this M_e threshold, the polymer chains interlock more extensively, creating additional knots between the chains and enhancing the polymer's stretchability (**Figure 1.4**).^{11,32,45-47} On the other hand, when the MW is below M_e , the

polymer chains and crystalline domains tend to stay separated, making the CPs more prone to becoming brittle.

An example of this phenomenon can be seen in the traditional CP, P3HT, whose interaction between MW and mechanical properties has been thoroughly investigated (**Figure 1.4a-c**).¹¹ The M_e for P3HT is reported to be around 35 kDa. In a study by Daniel et al., P3HT thin films were prepared with MWs ranging from 15 kDa to 80 kDa to examine the influence of MW on mechanical properties.¹¹ For P3HT with an MW of 15 kDa (below M_e), the COS was 4.5%, with an E of 0.2 GPa. When the MW increased to 40 kDa (above M_e), the COS improved to 13%, while maintaining a similar E of ~0.26 GPa. Increasing the MW further to 63 and 80 kDa led to progressive improvements in COS (59% and 96%, respectively) while keeping the E constant at 0.26 GPa, indicating a significant increase in stretchability. Coarse-grained molecular dynamics simulations have shown that for low MW P3HT, fractures occur through chain pullout, whereas for high MW P3HT, entanglements focus stress, and chain scission becomes the predominant mode of fracture, resulting in higher COS. This pattern has been similarly observed across various donor-acceptor CPs.⁴⁷⁻⁵¹ Pei et al. explored the morphology, mechanical, and electrical properties of poly(2,5-bis(4-hexyldodecyl)-2,5-dihydro-3,6-di-2-thienyl-pyrrolo[3,4-c] pyrrole-1,4-dione-alt-thiophene) (PDPPT3) at different MWs, demonstrating the correlation between MW and performance metrics (**Figure 1.4d, e**).⁴⁹

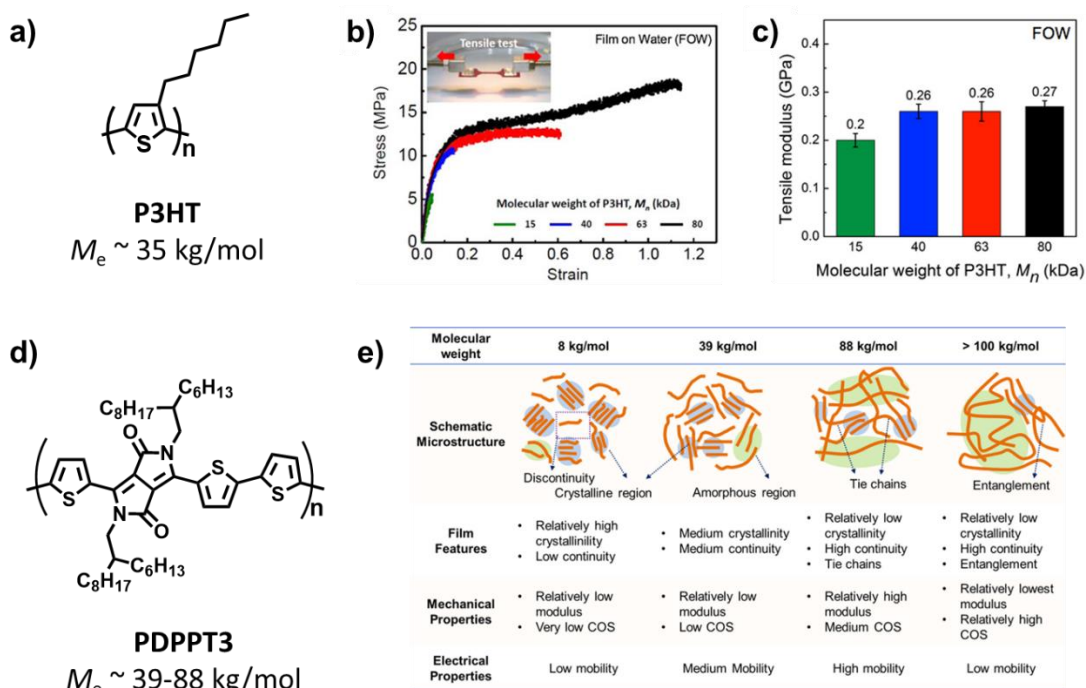


Figure 0.4 *Molecular weight effect on stretchability of CPs.*

(a) Chemical structure and critical MW of P3HT. (b) Stress-strain curve and (c) summarization of E of P3HT with different MWs of 15, 40, 63, 80 kDa. (d) Chemical structure and critical molecular weight of PDPPT3. (e) Schematic representation of the film microstructure of PDPPT3 with the increase of molecular weight and its relation to mechanical and electrical properties.^{11,49}

1.3.1.2 Regioregularity

Beyond MW, regioregularity is another fundamental characteristic of CPs that significantly affects their mechanical properties through its influence on molecular packing. Regioregularity pertains to the uniform arrangement of monomer units along a polymer chain, especially the consistent orientation of substituents or functional groups at the sites of chemical reactivity.

The synthesis of P3ATs with varying degrees of regioregularity is feasible due to the asymmetrical nature of thiophene rings and their alkyl side chains. This variance in regioregularity affects how polymer chains are packed, their crystallinity, and, consequently, the mechanical and electrical characteristics of the CPs. Generally, a higher

level of regioregularity is linked to better charge mobility, attributable to more orderly chain packing and increased crystallinity. Nonetheless, the enhanced chain packing and crystallinity associated with higher regioregularity can also render CPs more rigid and prone to brittleness. Thus, it is crucial to identify an optimal level of regioregularity that offers a good compromise between mechanical flexibility and electrical performance.^{44,52,53}

1.3.2 Design of intrinsic stretchable conjugated polymers

While adjusting basic parameters like MW can influence the mechanical properties of CPs, their intrinsic characteristics often limit the extent of these modifications. Hence, synthesizing inherently stretchable CPs has become increasingly important.^{3,5,30,41,54} The general strategies for designing stretchable CPs involve disrupting large and rigid crystalline structures, reducing the stiffness of CP chains, and introducing more amorphous regions to allow for better energy dissipation when stretched.^{55,56} To achieve these objectives, various approaches have been adopted, including modifying the side chains and backbones of CPs, integrating physical crosslinks between CPs, creating block copolymers with both conjugated and soft segments, and designing CPs with inherently low crystallinity.

1.3.2.1 Backbone engineering

The excellent electrical performance of CPs is due to their conjugated backbone structures. Yet, the inherent stiffness and planarity of these backbones contribute to brittleness and rigidity, which are not favorable traits for stretchable CPs. To enhance their stretchability, strategies such as developing more flexible backbones and disrupting the rigid conjugated structure are implemented. However, altering the conjugated structure might reduce charge mobility by interrupting the pathway for charge transport,

necessitating careful design to balance improved stretchability with preserved electrical functionality.

Employing smaller and fewer isolated thiophene rings in donor-acceptor (D-A) CPs has been shown to reduce both the persistence length and rigidity of the backbone, thereby increasing stretchability.^{10,57–60} Zhang et al. conducted a comprehensive examination of how the quantity and dimensions of isolated thiophene rings, including single thiophene (DPP-T), bithiophene (DPP-T2), terthiophene (DPP-T3), thienothiophene (DPP-TT), and dithienothiophene (DPP-TTT), affect the mechanical characteristics of DPP-based CPs (**Figure 1.5a**).⁵⁷ Their findings revealed that a reduction in both the number and size of these rings led to a decrease in crystallinity and glass transition temperature (T_g), which in turn increased elasticity and decreased brittleness (**Figure 1.5b,c**). However, variations in the presence of thiophene rings within the backbone affected the materials' properties differently, showing that more thiophene rings could lower the E while raising the COS, due to alterations in the molecular packing structure.⁶¹

Incorporating conjugated breaker spacers (CBS) serves as a strategy to disrupt the conjugated structure, thereby enhancing stretchability.⁴⁷ CBS refers to the introduction of non-conjugated groups into the CP backbone to interfere with the sp^2 -hybridized conjugated systems, initially aimed at enhancing solubility, reducing melting points, and facilitating processing.^{62–65} Subsequent findings revealed that CBS could also increase backbone flexibility and reduce crystallinity levels, significantly boosting stretchability.⁶⁶ Generally, CBS that are longer, bulkier, and more flexible lead to improved stretchability and a lower E.^{47,56,67–69} Alkyl chains, known for their simplicity and flexibility, are among the most commonly used CBS.^{56,67} For example, incorporating a hexyl group (C6) into

DPP-TVT raised the COS from 25% to 45%. Extending the CBS to a dodecyl group (C12) further enhanced the COS to 100% (**Figure 1.5d,e**).⁵⁶ In contrast, introducing a rigid dibutylbenzene (DBB) group into DPP-TVT only marginally increased the COS to around 40%. The proportion of CBS also impacts the mechanical properties; Savagatrup et al. explored the use of a propyl group as CBS in DPP-based D-A CPs across a range from 0 to 100%.⁶⁶ They observed that varying the CBS ratio altered the polymer morphology and, consequently, its mechanical properties, with the formulation containing 70% CBS exhibiting the highest COS and lowest E. However, incorporating higher amounts of alkyl-type CBS into the backbone significantly reduced charge mobility. As a result, additional strategies are required to optimize CBS for both enhancing stretchability and preserving charge mobility.

Introducing hydrogen bonding (H-bonding) crosslinks between CBS presents a promising solution to enhance stretchability while maintaining charge mobility.^{30,70,71} H-bonds, formed between hydrogen atoms and strongly electronegative atoms, are weaker and more reversible than covalent bonds, providing a unique energy dissipation pathway upon stretching.^{30,72–75} This property allows the H-bond to break first under strain, offering an additional mechanism to absorb and dissipate energy. Moreover, H-bonds contribute to improved intermolecular packing, which can bolster charge mobility.^{76,77} As a result, H-bonding has become a favored non-covalent bonding strategy in the development of stretchable CPs, with common H-bonding groups including amides, amines, ureas, urethanes, and 2,6-pyridine dicarboxamide (PDCA).^{26,30,71,77–79} For example, Oh et al. utilized PDCA as a CBS, incorporating it into the polymer backbone at ratios ranging from 0 to 20%, to facilitate H-bonding crosslinks (**Figure 1.5f**).³⁰ With 10 mol% PDCA, the

COS dramatically increased from 10% to 120%, while still achieving a high charge mobility of over $1 \text{ cm}^2/\text{V s}$ (**Figure 1.5g**). This improvement in mechanical stretchability was attributed to an increased amorphous fraction, reduced crystallinity, and slightly smaller crystallite sizes, with the added benefit of maintaining high charge mobility even after 100% strain. The density and strength of H-bonding are also critical factors influencing CPs' mechanical and electrical properties. Studies have shown that H-bond groups with a self-association constant above 0.7 tend to promote aggregation between polymer chains and increase crystallinity, leading to more rigid and brittle CPs.⁸⁰ Additionally, the length of the alkylene chains between amide groups on the backbone plays a significant role, where longer and more flexible chains enhance conformational freedom and reduce π - π stacking, resulting in more deformable and stretchable polymers.⁷¹ Recently, innovative types of CBS, such as peptides and biobased cellulose derivatives, have demonstrated effective performance in enhancing stretchability.^{81,82} Lastly, other backbone engineering strategies have also been explored, including the substitution of sulfur atoms with larger selenium atoms in thiophene rings and altering the backbone's central symmetry to further refine the stretchability and electrical performance of CPs.^{83,84}

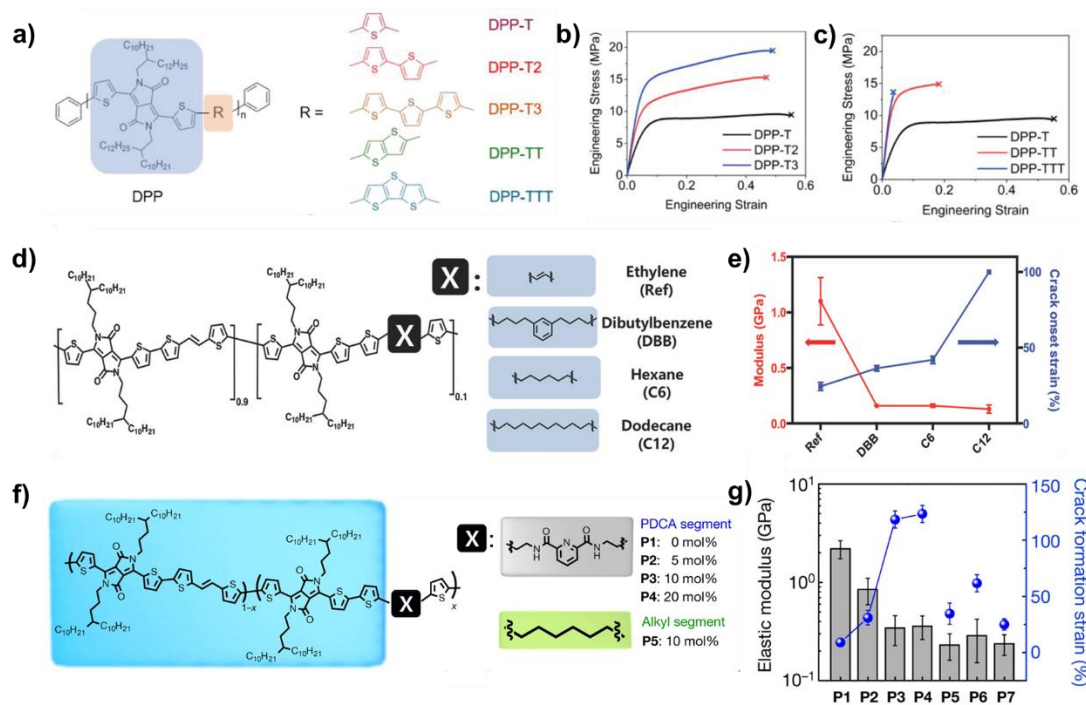


Figure 0.5 *Backbone engineering for design of intrinsic stretchable CPs.*

(a) Chemical structure of PDPP with different number of isolated ring and size of fused ring, PDPP-T, PDPP-T2, PDPP-T3, PDPP-TT and PDPP-TTT. Stress-strain curves of PDPP with (b) different number of isolated ring and (c) size of fused ring. (d) Chemical structure and (e) summarization of E and COS of PDPP CPs with different CBS, ethylene, DBB, C6 and C12. (f) Chemical structure and (g) summarization of E and COS of PDPP CPs with different ratio of H-bonding crosslinked CBS.^{30,56,57}

1.3.2.2 Side chain engineering

Besides focusing on the backbone structure, engineering the side chains of CPs is another effective strategy to modulate their mechanical properties and enhance stretchability.⁸⁵ Initially, side chains were incorporated into CPs to improve their solubility. Subsequent research has shown that varying the side chains can also alter molecular packing, thereby affecting both electrical and mechanical properties of CPs. In contrast to backbone modifications, altering side chains does not disrupt the conjugated structure or the charge transport pathway, allowing for the preservation of electrical properties while enhancing stretchability.

Adjustments to the size and length of side chains are commonly employed to influence mechanical properties. Strategies have included modifying the length of side chains, tweaking their branching structure and attachment points, incorporating asymmetric and bulky side chains, and utilizing other conjugated side chains to increase the stretchability of CPs.^{12,22,33,86–88}

Alkyl side chains are particularly favored for engineering stretchable electronics due to their impact on mechanical properties. The length and structure of these chains can significantly affect the polymers' behavior, where CPs with longer side chains are observed to have a lower E attributed to a decrease in T_g .^{12,33,87} This phenomenon was explored by Zhang et al., who examined the mechanical properties of DPP-based CPs with various side chain lengths (C2C6C8, C2C8C10, C2C10C12, and C2C12C14), demonstrating a reduction in E from 509 MPa to 104 MPa as the side chain length increased (**Figure 1.6a and Figure 1.6b**).³³ However, the COS did not display a clear correlation with side-chain length. Sugiyama et al. enhanced COS by incorporating a flexible linear oligo(ethylene oxide) (EO) side chain, noting improved performance over traditional linear alkyl side chains, with increased oxygen content correlating with higher COS.⁸⁹ Similarly, Wang applied siloxane as a crosslinker for DPP CPs with alkene side chains, achieving over 150% COS and maintaining charge mobility after extensive stretching, thanks to the flexible Si-O-Si bonds and covalent crosslinking (**Figure 1.6c**).⁷⁸ Further explorations into flexible side chains have included carbosilane, poly(butyl acrylate), and semifluorinated groups, opening new pathways for creating stretchable CPs.^{90,91}

Incorporating branching structures and adjusting the position of branching can expand the distance between crystalline planes, leading to less dense molecular packing,

which in turn lowers the E and raises the COS (**Figure 1.6d**).^{59,61} Lu et al. experimented with a branched side chain structure, C2C8C10, in PDPP CPs and compared its performance with that of a CP having a linear side chain, C16.⁶¹ The result was that the branched side chain variant exhibited a lower E (2.39 GPa compared to 4.44 GPa) and a higher COS (20% compared to 10%). Moreover, incorporating various asymmetric and bulky side chains also contributes to a looser packing arrangement, thereby enhancing the stretchability of CPs (**Figure 1.6e**).^{22,86,92,93}

Like the strategies employed in backbone engineering, the technique of H-bonding crosslinking has been applied to the side chains of CPs.^{26,94} Introducing a 10 mol% amide group into DPP-based CPs notably increased the COS from 30% to 75% (**Figure 1.6f,g**).²⁶ However, adding a higher concentration of amide groups (20 mol%) to the side chains resulted in a reduced COS to 50%, attributed to the enhanced crystallinity brought about by the hydrogen bonding crosslinks. Meanwhile, the E showed a continual decrease with the addition of more amide groups (**Figure 1.6h**), indicating the need for an optimal balance when integrating H-bonding groups into side chains.⁹⁵ This balancing act was underscored in further studies, where introducing a stronger H-bonding group, 2-ureido-4[1H]-pyrimidone (UPy), into the side chain was found to endow CPs with exceptional elasticity.⁹⁶

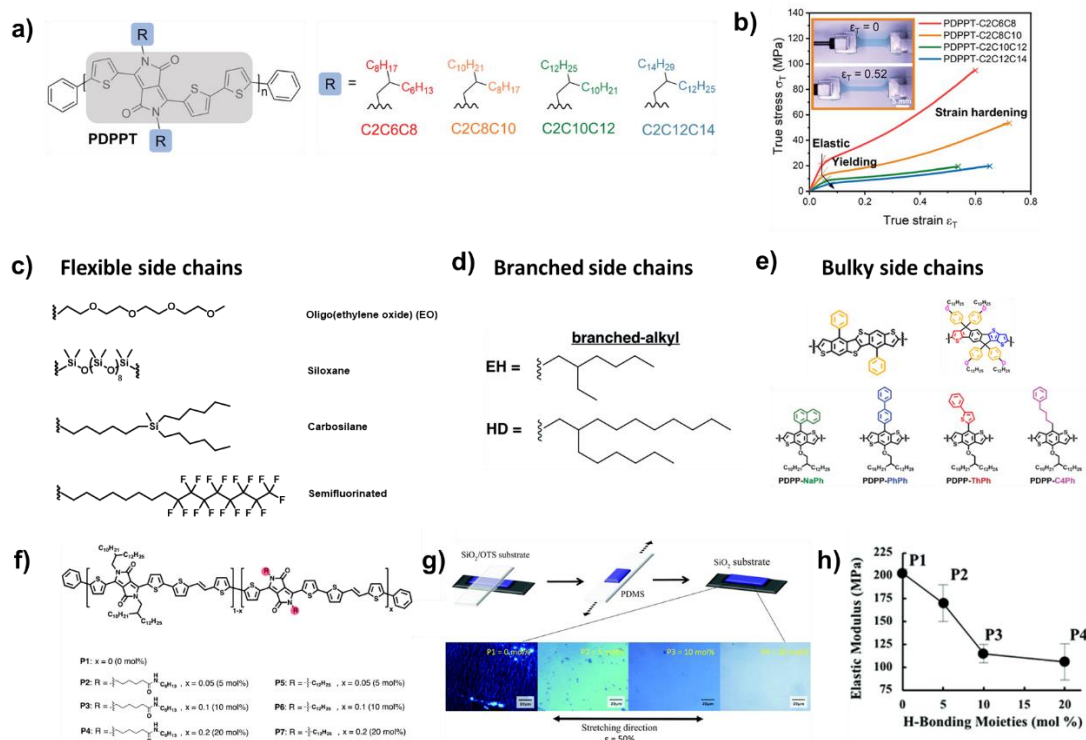


Figure 0.6 Side chain engineering for design of intrinsic stretchable CPs.

(a) Chemical structure and stress-strain curves of PDPPT with different length of side chains, C2C6C8, C2C8C10, C2C10C12 and C2C12C14. (b) Chemical structure of flexible side chains. (c) Chemical structure of branched side chains. (d) Chemical structure of bulky side chains. (e) Chemical structure of PDPPT with different ratios of side chains with H-bonding crosslinked amide groups.^{22,26,33,92}

1.3.2.3 Copolymerization between soft segments and conjugated polymers

Elastomers are materials known for their exceptional softness and stretchability. Leveraging these properties, CPs are combined with soft segments to create CP-*block*-elastomer diblock copolymers (CP-E BCP), merging the excellent electrical characteristics of CP blocks with the stretchability of elastomer blocks. Moreover, the inherent incompatibility between the two components allows CP-E BCPs to self-assemble into a variety of morphologies, each with unique mechanical and electrical properties.

Conjugated block copolymers incorporating traditional P3HT,^{97–99} p-type,^{100,101} and n-type D-A CPs^{102,103} have shown significantly enhanced stretchability compared to

their homopolymer counterparts. For instance, P3HT-*b*-polyethylene (P3HT-*b*-PE) BCPs have demonstrated remarkable stretchability, achieving a COS over 600% (**Figure 1.7a,b**),⁹⁸ while P3HT-*b*-polyisobutylene-*b*-P3HT (P3HT-*b*-PIB-*b*-P3HT) ABA block copolymers have shown a much lower elastic modulus, 1.14 MPa with a COS of 200%, due to the inclusion of soft PIB segments (**Figure 1.7c**).⁹⁷ DPP copolymerized with biodegradable polycaprolactone (PCL) resulted in a degradable DPP-*b*-PCL block copolymer that maintained charge mobility after being stretched to 100%.¹⁰⁴ An n-type CP, poly(naphthalenediimide-bithiophene) (PNDI2T), when copolymerized with PIB, retained almost constant charge mobility after 1000 stretching cycles at 60% strain (**Figure 1.7d**).¹⁰² The sequence of CP/elastomer BCPs has been studied for its impact on morphology and properties. Chiang et al. synthesized P3HT with poly(octylene oxide) (POO)-based CP/elastomer BCPs in AB, ABA, and BAB configurations. The ABA-type films exhibited a COS higher than 100%, significantly outperforming the AB and BAB films.¹⁰⁵

While some CP-*b*-elastomer copolymers may not exhibit stellar electrical properties on their own, they can act as an elastomer matrix to enhance compatibility between CPs and the matrix, thereby improving mechanical stretchability and electrical performance. For example, PBTTT-*b*-HTPB was synthesized with excellent mechanical properties, showcasing a COS of ~619% and elastic recovery (**Figure 1.7e**),¹⁰⁶ though its charge carrier mobility was relatively low. Blending this with TDPP-Se improved the blend's COS to 246% with a high mobility of 2.05 cm²/V s (**Figure 1.7f,g**).

Given the complexity of synthesizing block copolymers, supramolecular CP-elastomer block copolymers utilizing dynamic bonds instead of covalent bonds to connect CP and

elastomer blocks have been developed.¹⁰⁷ Wu et al. used dynamic metal-ligand coordination to construct a supramolecular block copolymer, PS-Zn-P3HT, enhancing the COS from 25% (P3HT) to 75%.

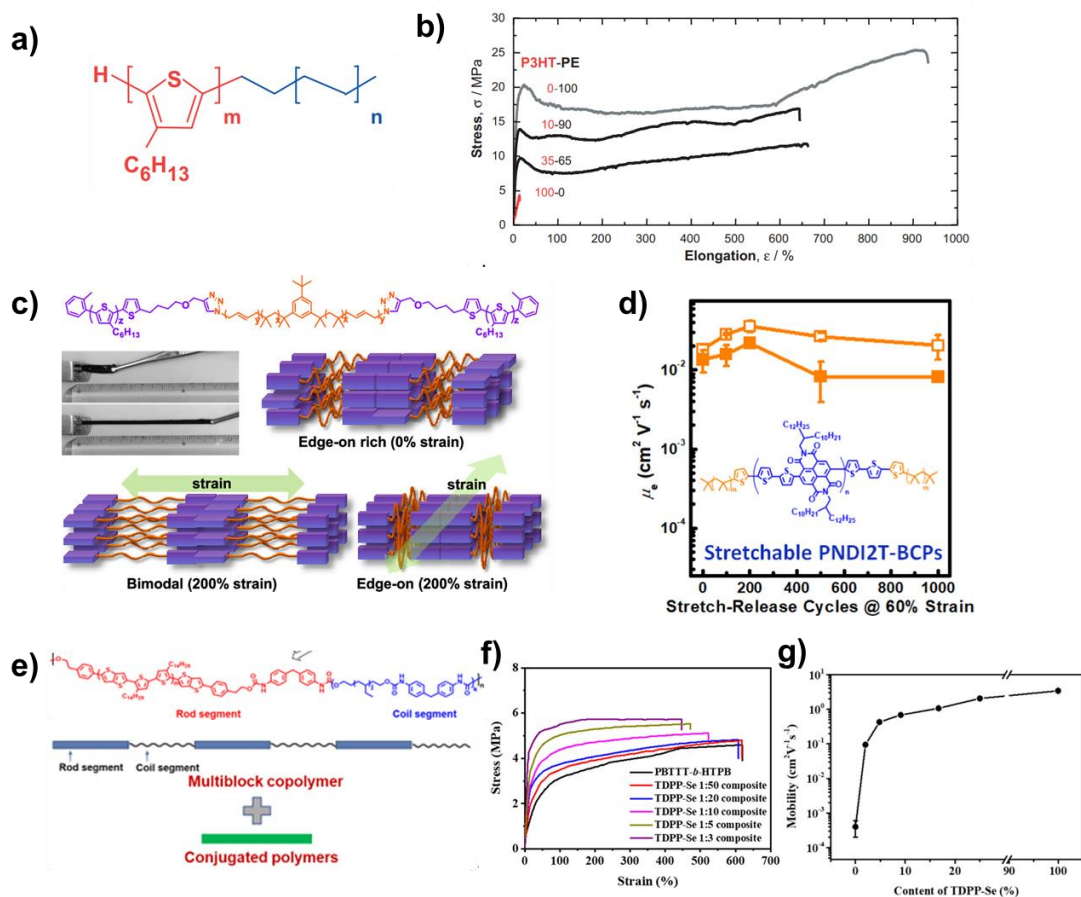


Figure 0.7 CP-b-elastomer block copolymers for intrinsic stretchable CPs.

(a) Chemical structure and (b) stress-strain curve of P3HT-b-PEs. (c) Chemical structure and photograph of the bulk P3HT-b-PIB-b-P3HT film before and after stretching and the illustration of the model for the deformation of microphase separated structure and crystalline orientation of the P3HT-b-PIB-b-P3HT thin film. (d) Chemical structure of PNDI2T-b-PIB block copolymers and correlation between μ_e and the stretch-release cycles for the polymer films. (e) Chemical structure of PBTTT-b-HTPB and schematic of multiblock copolymer/CPs composites. (f) Stress-strain curve of the composites and (g) mobility of composites with different ratios of TDPP-Se.

97,98,102,106

1.3.2.4 Intrinsic low-crystallinity conjugated polymers

Creating intrinsically low-crystallinity CPs has proven to be a successful strategy for enhancing stretchability.¹⁰⁸ CPs are typically semicrystalline, featuring both crystalline and amorphous regions (**Figure 1.8a**).³² The crystalline domains primarily facilitate charge transport, where charges move along both the intramolecular (along the backbone) and intermolecular (between π - π stacking) pathways. However, tight π - π stacking leads to strong crystallinity, which, while beneficial for charge transport, can render CPs more brittle due to the high degree of crystallinity. On the other hand, the amorphous domains consist mainly of disordered chains, offering pathways for energy dissipation that contribute to increased stretchability.

In response to this, Zheng et al. developed a new CP, indacenodithiophene-co-benzothiadiazole (IDTBT), characterized by notably low crystallinity. This was achieved by disrupting π - π stacking through the introduction of long side chains attached to a tetrahedral carbon within the conjugated polymer backbone (**Figure 1.8b**).⁵⁵ This structural modification allowed IDTBT to achieve remarkable stretchability, with a COS exceeding 100% (**Figure 1.8c**). Furthermore, their design preserved high backbone coplanarity and minimized energetic disorder, facilitating efficient intrachain charge transport. As a result, despite its low crystallinity, the CP maintained high charge mobility, reaching up to 1.8 $\text{cm}^2/\text{V s}$.

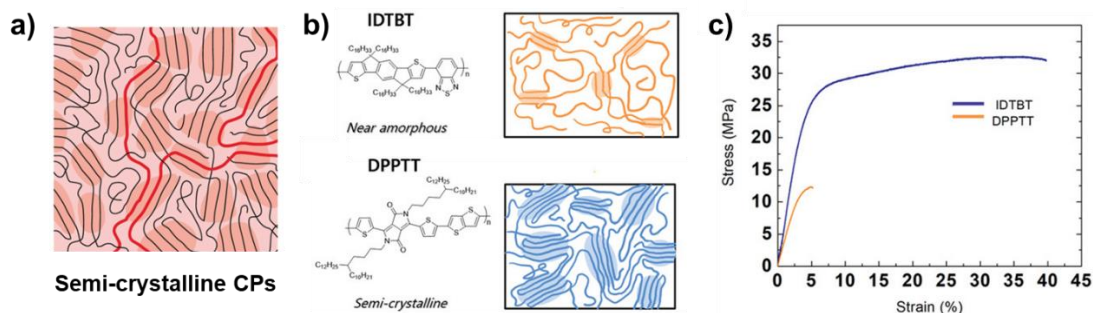


Figure 0.8 *Semi-crystalline structure of CPs and Intrinsic low-crystallinity CPs.*

(a) Common semicrystalline morphology of CPs. (b) Chemical structure and morphology of near-amorphous IDTBT and semi-crystalline DPPTT. (c) Stress-strain curve of near-amorphous IDTBT and semi-crystalline DPPTT.^{32,55}

1.3.3 Conjugated polymer composites

Physical blending of CPs with soft, stretchable elastomer matrices to create CP/elastomer composites offers a straightforward alternative to the complex synthesis of inherently stretchable CPs.^{109–125} This method involves mixing a small proportion of CPs into an elastomer matrix, where the CPs enhance electrical properties, and the elastomer matrix adds stretchability. Moreover, due to their incompatibility, CPs and elastomers tend to phase separate, leading to fiber-like aggregates that can further improve charge mobility.

Elastomers such as PDMS,^{111–114} styrene-ethylene-butylene-styrene (SEBS),^{110,115,120,123,126,127} polystyrene-block-polyisoprene-block-polystyrene (SIS),¹¹⁶ and polyurethane¹²⁸ are commonly used in these composites. For instance, Xu et al. incorporated DPPT-TT into an SEBS matrix, producing a composite that sustained high charge mobility of 1 cm²/V s at 100% strain, thanks to fiber-like aggregation from phase separation (**Figure 1.9a, b, c**).¹¹⁰ The Reichmanis group found that blending P3HT with PDMS significantly increased stretchability from 5% to over 100%, along with a rise in charge mobility.¹¹⁴

CP/elastomer composites can also incorporate additional functionalities by using elastomers with specific properties.^{37,117} Zhang et al. mixed DPPTVT with self-healable butyl rubber (BR), achieving a composite with excellent stretchability and self-healing capabilities (**Figure 1.9d, e**).¹¹⁷ Li et al. combined a redox-active CP with a bioadhesive polymer, resulting in strong adhesion to wet tissue surfaces, showing promise for bioadhesive organic electrochemical transistors (OECTs).²³ Composites made with degradable elastomer E-PCL also exhibited degradability.¹²⁵

Similar to the design of inherently stretchable CPs, introducing H-bonding crosslinks into CP/elastomer composites can enhance stretchability and self-healing properties. Wang et al. introduced amide groups into an elastomer (PIB-Amide) and blended it with DPPT-T, creating a highly stretchable (COS ~1500%) and self-healable composite that maintained high charge mobility under strain (**Figure 1.9f, g, h**), with the H-bonding also boosting self-healing efficiency (**Figure 1.9i**).³⁷ The placement of H-bonding crosslinks significantly affects the composites' morphology and, consequently, their mechanical and electrical characteristics. By systematically studying the effect of crosslink location, it was found that composites with dual H-bonding showed the lowest mobility initially, which improved after stretching, while those without H-bonding exhibited the highest mobility but lower stretchability.³⁸ The introduction of H-bonding crosslinks to either component improved stretchability and charge mobility.²⁸ Research has also shown that the MW of both CP and elastomer components affects stretchability and charge mobility.¹²⁹ Composites with CP MW above a critical threshold exhibited higher mobility, whereas those with lower CP MW showed increased COS without a clear impact on mobility.²¹

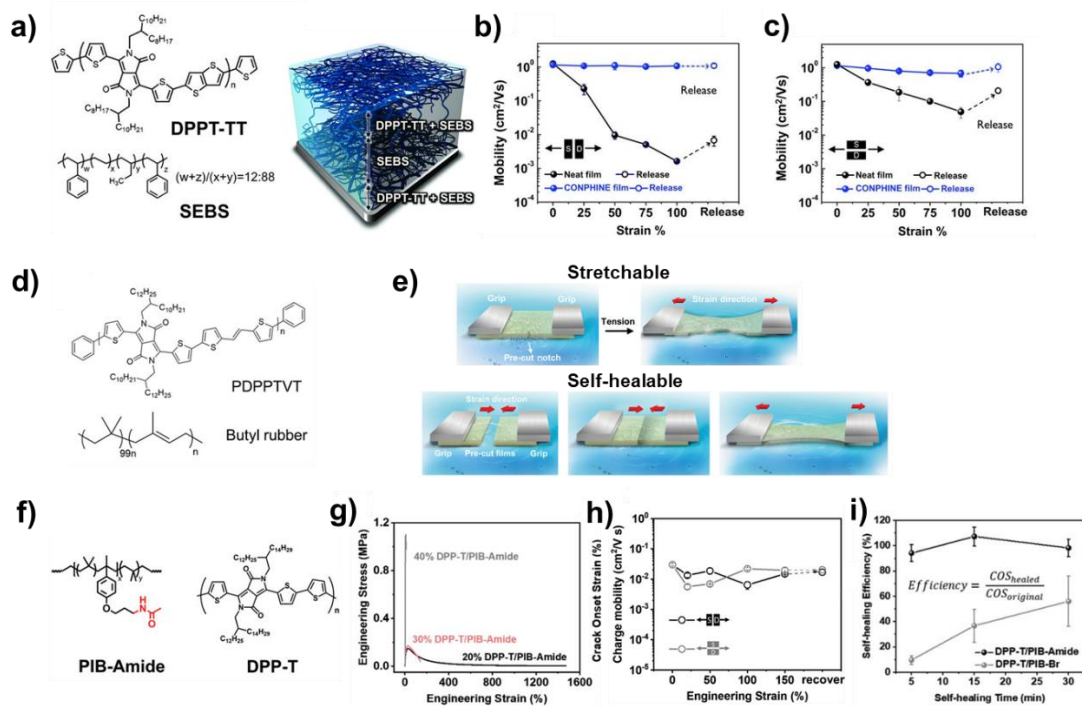


Figure 0.9 *Stretchable and self-healable conjugated polymer/elastomer composites.*

(a) Chemical structures of semiconducting polymer DPPT-TT and SEBS elastomer and 3D illustration of the morphology of the composite film. Mobilities from the composite film (blue) and the neat film (black) at different strains (b) parallel and (c) perpendicular to the charge transport direction. (d) Chemical structures for PDPPTVT and BR. (e) 3D schematic illustration and optical images of notched 2:3 PDPPTVT/BR composite film before and after tensile deformation on water surface and self-healing process. Two pre-cut films were floated on water upon compression. (f) Chemical structures of PIB-Amide and DPP-T. (g) stress-strain curve of PIB-Amide/DPP-T composites. (h) Charge mobility of the 20% DPP-T/PIB-Amide composite after stretching to different strains and (i) self-healing efficiency through the self-healing process.^{37,110,117}

1.3.4 Rigid stretchable conjugated polymers

The conventional approach to designing stretchable CPs has favored softer materials for their presumed superior deformability. Yet, recent research by Zheng et al. has challenged this paradigm, demonstrating that IDTBT, despite its high elastic modulus, can exhibit remarkable deformability.⁵⁵ Wang et al. extended this investigation by analyzing the E to COS relationship across 65 CPs using the FOW tensile test, revealing no straightforward correlation between a CP's rigidity and its ability to deform (**Figure**

1.10).²⁷ Notably, several rigid CPs ($E > 700$ MPa) exhibited unexpectedly high stretchability ($COS > 20\%$), suggesting a new avenue for the development of stretchable CPs.

Further analysis compared charge mobility post-stretching and the deformation mechanisms between rigid and soft stretchable CPs, finding that the rigidity of CPs did not directly affect changes in charge mobility. Beyond the initial strain region, the deformation mechanism appeared similar across both types of CPs, indicating that rigid stretchable CPs also hold promise for device applications. This insight suggests that incorporating rigid CPs into the design of stretchable materials could open up possibilities for applications that require both high modulus and stability, expanding the scope of stretchable electronics design.

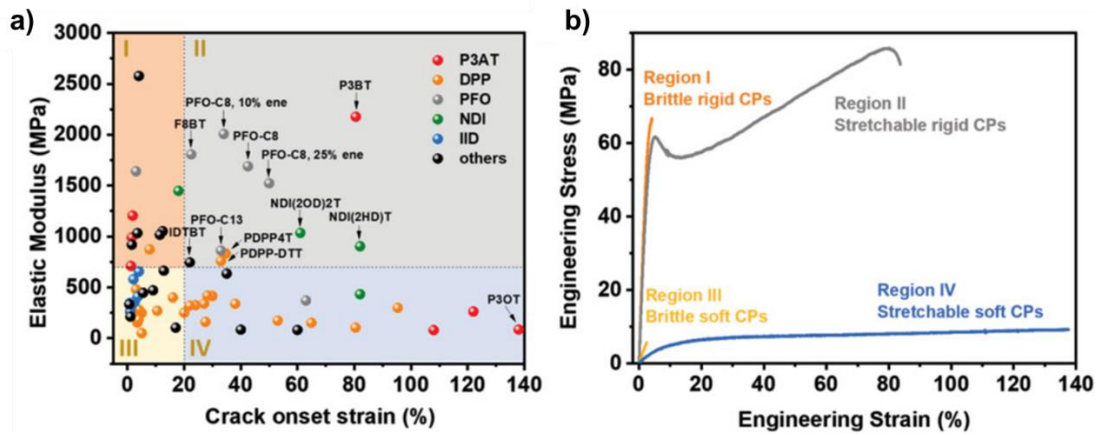


Figure 0.10 $E \sim COS$ relationship and stress-strain curve for CPs.

a) Summarized E and COS of a library of CPs. Region I: Rigid and brittle CPs with high E and low COS . Region II: Rigid and deformable CPs with high E and high COS . Region III: Soft and brittle CPs with low E and low COS . Region IV: Soft and deformable CPs with low E and high COS . b) Representative stress-strain curve for polymers from each region.²⁷

1.3.5 Others

Structural engineering involves adapting the material into a pre-strain configuration, such as wavy¹³⁰, buckled¹³¹, wrinkled¹³², serpentine¹³³, island¹³⁴, kirigami-

inspired¹³⁵, horseshoe¹³⁶ and mesh-like¹³⁷ structures, to absorb tensile strains during stretching.^{138–141} This approach allows energy to be dissipated upon releasing the pre-strained configurations. For instance, Bettinger and colleagues created the first stretchable organic transistor using a wavy structure.¹⁴² However, the fabrication techniques for these structures are often complex, expensive, and challenging to precisely control. Moreover, the use of stretchable metal interconnects and circuits necessitates large areas, leading to a significant drawback of reduced device density.

The method of processing CP thin films also influences their stretchability. Choudhary et al. evaluated the mechanical properties of poly(3-heptylthiophene) (P3HpT) using various techniques, including interfacial spreading, solution shearing, spray coating, with spin coating serving as a baseline for comparison.¹⁴³ They discovered that the processing methods affected the material's free volume and surface topography, leading to variations in mechanical properties. Specifically, P3HpT films produced by spray coating were the most brittle, attributed to defects and uneven thickness. Films created through shearing exhibited superior modulus, strength, and toughness due to reduced free volume. Meanwhile, films formed by interfacial spreading were found to be softer and more stretchable than those produced by spin coating.

1.4 Few representative applications demonstration

Stretchable CPs have facilitated the development of tissue- and skin-like stretchable devices, revolutionizing wearable electronics for human health monitoring and enhancing human-machine interaction.^{144–148} Devices such as transistors, organic solar cells, sensors, and light-emitting diodes have been predominantly fabricated using these materials.^{149–153} Both structural engineering and materials intrinsic stretchability contribute to

advancements in this field. Here, we highlight few representative examples centered on intrinsically stretchable electronics.

Organic field-effect transistors (OFETs) serve as foundational components in integrated electronics, comprising source, drain, and gate electrodes, along with a semiconducting and a dielectric layer.^{3,5,154} Achieving fully stretchable OFETs requires that all components be stretchable. For instance, the Bao group developed efficient all-stretchable OFETs using (poly(3,4-ethylenedioxythiophene):poly(styrenesulfonate)/carbon nanotube (PEDOT:PSS/CNT) as electrolytes and PDMS as the dielectric layer, with novel CPs as the active layer (**Figure 1.11a**).¹¹⁰ Xu et al. also created all-stretchable OFETs with DPPTT/SEBS composites as the active layer, maintaining charge mobility at 0.99 cm²/V s under 100% strain, demonstrating resilience to twisting and poking (**Figure 1.11b**).

Organic electrochemical transistors (OECTs) differ from OFETs in that their electrodes are not in direct contact with active layers, relying on ions for charge transport.^{155,156} This makes them ideal for use in aqueous environments and biosensing due to their low operation voltage and label-free detection capabilities. Li et al. developed a highly stretchable, fully bioadhesive OECT-based sensor using a double-network polymer semiconductor, showcasing stable performance even when stretched (**Figure 1.11c, d, e**).²³

For energy supply in wearable devices, all-stretchable organic solar cells (OSCs) have garnered significant interest.^{157–159} Despite the challenge of maintaining high power conversion efficiency (PCE) in stretchable formats, Wan et al. enhanced OSC stretchability and mechanical durability by incorporating thymine groups into PM7, achieving 80% of initial PCE even after 43% strain (**Figure 1.11f, g**).¹⁶⁰ The Lee group demonstrated an all-

stretchable OSC using thermoplastic polyurethane (TPU) as a substrate and a eutectic gallium–indium (EGaIn) alloy as the top electrode.¹⁶¹

Organic light-emitting diodes (OLEDs) represent a promising direction for next-generation displays, offering portability, foldability, and lightweight, skin-like displays.^{152,162} Liu et al. introduced a design strategy incorporating soft side chains into the backbone of materials for thermally activated delayed fluorescence (TADF), achieving substantial stretchability and maintaining external quantum efficiency (EQE), with devices capable of stretching to 60% while preserving luminescence characteristics (**Figure 1.11h, i-l**).¹⁶³

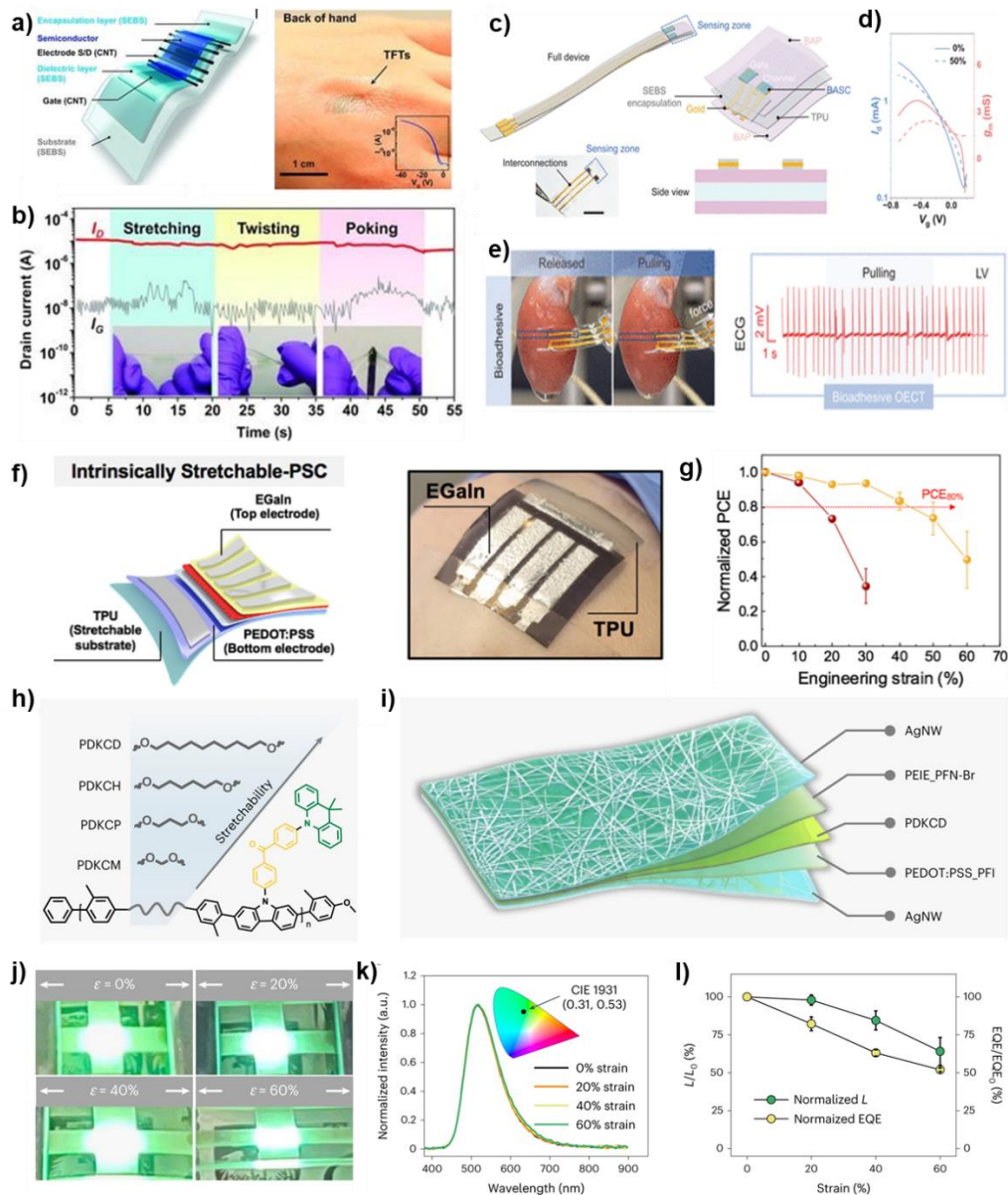


Figure 0.11 *Stretchable electronic devices.*

(a) Schematic of all-stretchable OFET. (b) Drain current (I_D) and gate current (I_G) of a fully stretchable TFT under sequential stretching, twisting, and poking with a sharp object. (c) Device structure of fully bioadhesive OECT sensor. (d) Transfer curves for a fully bioadhesive OECT under 0 and 50% strains. (e) Photographs that show a fully bioadhesive OECT attached to an isolated rat-heart surface maintaining stable contact during mechanical agitation and ECG signals recorded by the fully bioadhesive OECT on the left ventricle. (f) Device structure and image of all-stretchable OSC. (g) Normalized PCE of all-stretchable OSC during stretching. (h) Chemical structures of stretchable TADF polymers having different alkyl chains in the polymer backbone. (i) Schematic of the fully stretchable OLED. (j) Photographs of a representative OLED device stretched from 0% to 20%, 40% and 60% strains. (k) Normalized luminance intensity (L/L_0) and EQE (EQE/EQE_0) of the stretchable OLED at different strains.^{23,110,160,163}

CHAPTER 2 – STRETCHABLE AND SELF-HEALABLE
SEMICONDUCTIVE COMPOSITES BASED ON HYDROGEN
BONDING-CROSSLINKED ELASTOMERIC MATRIX

(Adapted from “Wang, Y.; Chen, K.; Prine, N.; Rondeau-Gagné, S.; Chiu, Y.; Gu, X. Stretchable and Self-Healable Semiconductive Composites Based on Hydrogen Bonding Cross-Linked Elastomeric Matrix. *Adv. Funct. Mater.* 2023, 2303031, 1–10.”)

2.1 Introduction

Developing stretchable and self-healable semiconductors is very important to meet the growing interest in designing wearable and implantable electronics.^{3,133,164–169} Conjugated polymers (CPs), due to wide range tunable chemical structures and high flexibility and deformability compared to their inorganic counterpart, are widely adopted in wearable devices, and used as the charge transport layer.^{170–173} Unfortunately, a rigid and coplanar backbone and high crystallinity are preferred to enable effective charge transport for CPs, commonly renders them as rigid and brittle.^{9,32,174} Therefore, designing CPs with balanced electrical performance and mechanical robustness is required. Besides, mechanical fracture and accidental scratching in long-term use in daily life make the materials less durable.³ In this regard, researchers developed a strong interest in making self-healing semiconductors or composite to mitigate above mentioned issues.^{166–169,175}

Most efforts have focused on modifying chemical structures via backbone/side-chain engineering to develop stretchable and self-healable CPs. To improve stretchability, attaching longer and branched alkyl side chains,^{33,87,89,90,92} inserting flexible conjugation breaker spacers^{9,30,56,62,64,66,80,109}, and copolymerizing soft segments with conjugated polymers^{57,98,99,103,176,177} are generally used. However, the increased stretchability often

resulted in sacrificed charge carrier mobility.¹⁷⁸ To introduce self-healing ability, dynamic covalent bonds (i.e., Diels-Alder reactions, imine bonds, disulfide exchanges, borate ester bonds) or noncovalent interactions (i.e., hydrogen bonds,^{30,72,95} metal-ligands interaction,¹⁷⁹ host-guest interactions¹⁸⁰) were often incorporated between the polymer chains. Despite considerable progress in developing self-healing polymeric materials,¹⁸¹ only a few have focused on electronically active materials and demonstrate their usage in thin-film field-effect transistors. Besides, it must be noted that the molecular design of novel CPs always needs elaborate synthesis. Due to the conjugated nature of CP's rigid backbone, the demonstration of intrinsically stretchable and room temperature self-healable CPs is still limited.

Alternatively, physical blending CPs with soft elastomers (i.e., polydimethylsiloxane (PDMS),¹¹¹⁻¹¹⁴ styrene-ethylene-butylene-styrene (SEBS),^{110,115,120,123} polystyrene-block-polyisoprene-block-polystyrene (SIS),¹¹⁶ rubber,^{117,121} etc.) is a straightforward and effective approach to create stretchable semiconductor.^{110,114,115,117,119-125} For example, Bao *et al.* blended SEBS with DPPT-TT fabricating DPPT-TT/SEBS semiconducting composite.¹¹⁰ Utilizing the conjugated polymer/elastomer phase separation-induced elasticity (CONPHINE) method, the high charge mobility of $\sim 1 \text{ cm}^2/\text{V s}$ was successfully retained even at 100% strain. Later on, the same group systematically studied the MW influence of both CPs and SEBS on the performance of composites. For CPs with high MW, the aggregation slightly decreased upon increasing MW of SEBS, while opposite trend for CPs with low MW.²¹ Furthermore, they also developed an elastic composite with the help of covalent crosslink between azide and C=C group in SEBS and C-C bond in CPs.²⁸ No residual strain showed up with increasing cyclic

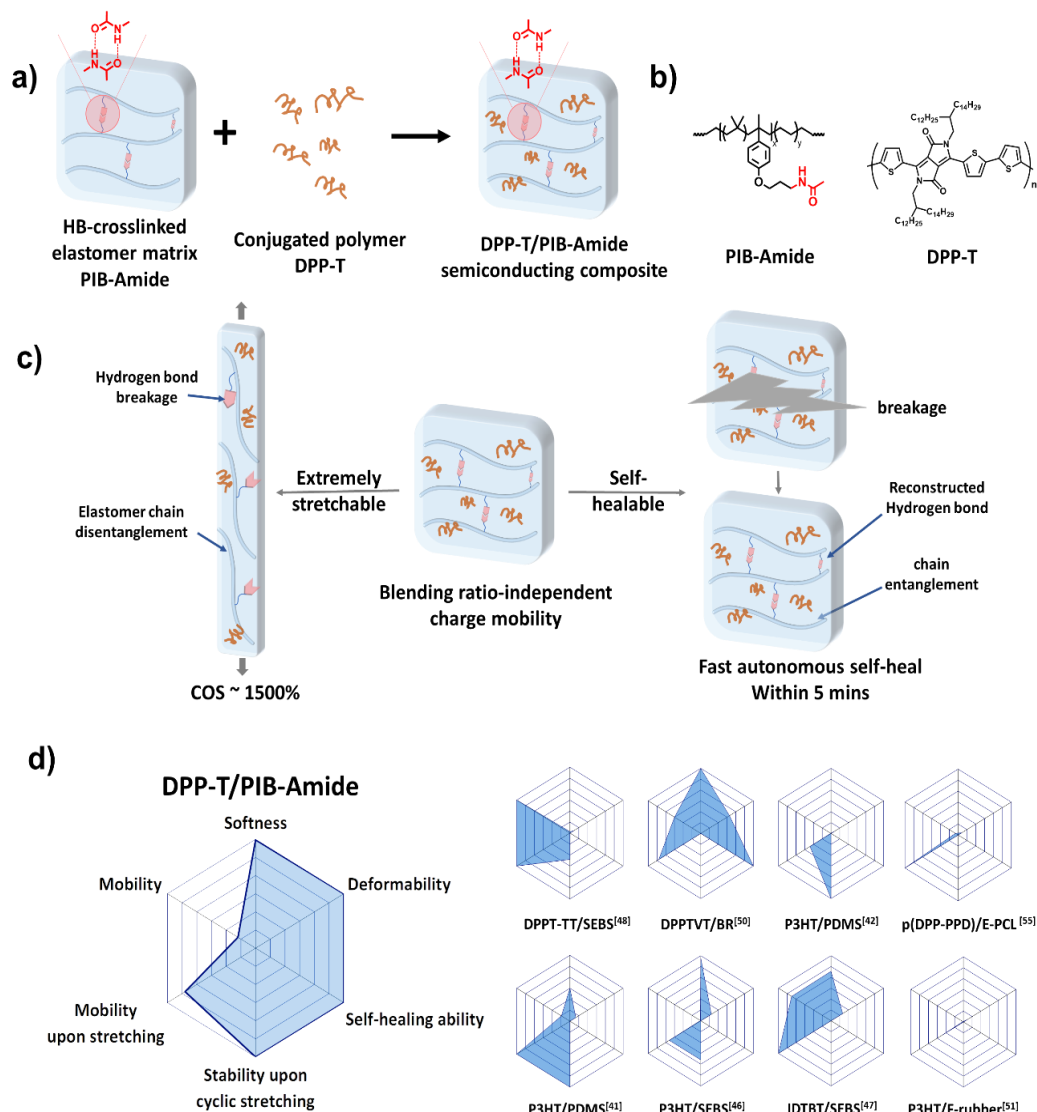
strains from 10-70%. Jeong *et al*, first used PDMS as elastomer matrix for the composite. The formation of P3HT bundle network in composite films enable high stretchability of composite (COS>50%).¹²³ However, the mobility significantly decreased upon stretching. Cho group embedded P3HT nanowires into PDMS matrix.¹¹² The obtaining composites showed stable stretchability at strain up to 100%. Reichmanis group detailed studied processing condition effect on the performance on the P3HT/PDMS composite.¹¹⁴ The one with 'predeposition processed' P3HT showed 44 times higher hole mobility than untreated one with high stretchability up to 100% strain. Apart from those previous demonstration of the deformable composite, the self-healable capability for semiconductor composites is rarely demonstrated. Recently, Zhang *et al*. selected butyl rubber, an elastomer with high elasticity and strong adhesion, as the matrix to blend with DPPTVT.¹¹⁷ Although stretchable and self-healing ability was successfully achieved, a mismatch happened between the composite with blending ratio for the highest electrical performance and best mechanical stretchability. Jeong *et al*. embedded Poly(3-butylthiophene-2,5-diyl) (P3BT) nanowires with dopant tris(pentafluorophenyl)borane (BCF) into thermoplastic elastomer matrix SIS fabricating SIS/P3BT/BCF composite. The obtained composites exhibited good thermoelectric performance, achieved self-healing under mild heat and pressure conditions and good stretchability.¹¹⁶ Oh, *et al*. fabricated metal-ligands crosslinked DPP-TVT-PDCA/PDMS-PDCA composites.¹⁸² With the dynamic metal-ligands interaction, the composites showed high stretchability (COS>1300%) and self-healing ability. But the healing rate was relatively low, which needs 1 day to heal fully. Therefore, developing composites with both high stretchability and strong self-healing ability is of great interest to expand the application space for stretchable electronics.

To achieve the above goal, one can resort to the design new high stretchable and self-healable elastomers with the needed properties for the semiconductive polymers. It's reported that polyisobutylene (PIB)-based networks have good flexibility and strong adhesion due to the softness and strong entanglement of the polymer chains.¹⁸³ Along this line, Higashihara incorporated PIB with P3HT synthesizing a block copolymer P3HT-*b*-PIB-*b*-P3HT. With the help of PIB segment, the obtained composite showed high stretchability with COS up to 200%.⁹⁷ Therefore, we expect PIB should own great potential to be used as elastomer matrix to achieve stretchability and self-healing ability.

Introducing hydrogen bond crosslink into elastomers was reported to improve the stretchability and self-healing ability effectively.^{77,184-193} The weaker dynamic bond is easy to break, providing an extra energy dissipation pathway to improve stretchability. After releasing stretching, the dynamic hydrogen bonds can reconnect again, enabling intrinsically self-healing ability.¹⁹³ For example, Yan *et al.* utilized the ureidopyrimidinone (UPy) group to successfully construct a hydrogen bonding crosslinked supramolecular polymeric material (SPMs).¹⁹⁴ With 20 mol% UPy group, an extremely stretchable material (COS= 17,000%) with excellent self-healing ability was obtained. Considering the excellent performance, hydrogen-bonding crosslinked elastomer should be a type of matrix with a high potential for stretchable and self-healable composites. However, far fewer advances have specifically addressed the availability of hydrogen bonding-crosslinked elastomers used in electronics and the influence of hydrogen bond on the performance of semiconducting composites.

Here, we designed a new hydrogen bonding crosslinked amide-functional PIB (PIB-Amide) to enable extremely soft, stretchable, and self-healable semiconductive

composites, With PIB-Amide as the elastomer matrix, the semiconducting composite DPP-T/PIB-Amide exhibits blend ratio-independent mobility, with the extreme softness ($E \sim 1.76$ MPa), high stretchability (COS $\sim 1500\%$), and strong self-healing ability at the room temperature (**Scheme 2.1**). In the meantime, the high charge carrier mobility of our composite can be mainly maintained under 100% cyclic strain for over 100 times. The properties were compared with reported semiconducting composites, which showed impressive improvement (**Scheme 2.1d**). Wide-angle x-ray scattering (WAXS), polarized UV-vis spectroscopy, and atomic force microscopic combined with infrared-spectroscopy (AFM-IR) were utilized to study the deformation mechanism. Through the in-depth morphology study, we conclude that the deformation happened mostly in the elastomer matrix while the network of the CPs fibril was connected throughout the stretching process, thus allows the composite to maintain stable charge carrier mobility at different strains. This work demonstrated that CP/elastomer composites with hydrogen bonding crosslinked elastomer as the matrix can dramatically increase the stretchability and self-healing ability, which enriches the stretchable semiconductors materials choice and provides a guideline for the future design of stretchable and healable semiconductive composites.



Scheme 0.1 Schematic of stretchable and self-healable DPP-T/PIB-Amide composite.

a) Fabrication of DPP-T/PIB-Amide composite. b) chemical structures of PIB-Amide and DPP-T. c) Schematic diagram showing the stretchable and self-healable DPP-T/PIB-Amide semiconducting composites. d) Comparison of the performance of the current system to previously reported semiconducting conjugated polymer/elastomer composites.

2.2 Experimental

2.2.1 Materials

Chemical reactants were used as received without further purification unless stated otherwise. Butyl rubber (EXXON™ Butyl 365S) was donated by ExxonMobil Corporation. Titanium(IV) chloride, hydrazine hydrate, (3-bromopropoxy)benzene,

magnesium sulfate, potassium phthalimide, triethylamine, poly (sodium 4-styrenesulfonate solution) (PSS, 30% in water) and acetyl chloride was purchased from Sigma Aldrich. DPP3T was purchased from Ossila. n-hexane, dichloromethane (DCM), methanol, hexane, N-Methyl-2-pyrrolidone (NMP), heptane, ethanol, sulfuric acid and tetrahydrofuran (THF) were ordered from Fisher Scientific. THF and DCM were distilled using Na and calcium hydride prior to use.

2.2.2 Nuclear magnetic resonance (NMR) spectroscopy

¹H NMR spectra were recorded using Varian MERCURY^{plus} 300 MHz (VNMR 6.1C) or a Bruker AVANCE III 600 MHz (TopSpin 3.1) spectrometer using CDCl₃ as the solvent. The residual proton signal of the deuterated solvent was used as a reference signal and multiplicities of the peaks are given as s = singlet, d = doublet, t = triplet, and m = multiplet. Broad signals that lack any fine structure (coupling patterns) are indicated as “br”. Coupling constants are given in Hz and only calculated for resolved 1st-order coupling patterns.

2.2.3 Size-exclusion chromatography (SEC)

SEC was conducted using a Waters Alliance 2695 separations module, an online multiangle laser light scattering (MALLS) detector fitted with a gallium arsenide laser (20 mW) operating at 658 nm (miniDAWN TREOS, Wyatt Technology Inc.), an interferometric refractometer (Optilab T-rEX, Wyatt Technology Inc) operating at 35 °C, and 685 nm, and two PLgel mixed E columns (Polymer Laboratories Inc.) in series (pore size 50-103 Å, 5 μm bead size). The mobile phase was freshly distilled THF delivered at a flow rate of 1.0 mL/min. Sample concentrations were 2.5 mg of polymer/mL of THF, and the injection volume was 100 μL. The detector signals were simultaneously recorded using

ASTRA software (Wyatt Technology, Inc.), and absolute molecular weights were determined by MALLS using a dn/dc value obtained from the interferometric refractometer response and assuming 100% mass recovery from the columns.

2.2.4 Fourier-transform infrared spectroscopy (FT-IR)

FT-IR was recorded using Bruker VERTEX 80 FTIR spectrometer.

2.2.5 Film processing

DPP3T and PIB-Amide with different blending ratio were dissolved in anhydrous chlorobenzene (CB) with concentrations of 30 mg/ml. The solutions were heated at 80 °C overnight and sonicated for 4.5 h at room temperature before processing. Thin films were spin-cast on Si wafer at 1000 revolutions per minute (r.p.m.) for 1 minute. Thin film thickness is around 60 nm. Thick films were drop-cast on pre-cut Si wafer with thickness of around 13 μm .

2.2.6 Pseudo-free-standing tensile test

Tensile test of BR, PIB-Br and PIB-Amide was performed using thin films. Tensile test of composites was performed using thick films. The films were prepared on PSS-coated Si wafer followed by floated on top of water and stretched at a strain rate 0.125 s^{-1} until break. The detailed instrument setup can be found in previous literature report.^{16,20}

2.2.7 OFET fabrication and characterization

To prepare the sample, 80 nm thin film were first spin-coated on OTS-treated Si/SiO₂ wafer followed by being transferred to PDMS. The thin film was uniaxially stretched on PDMS and transferred again to Si wafer. Gold electrode was finally deposited to obtain the top-contact bottom-gate OFET.

2.2.8 Atomic Force Microscope (AFM) and AFM-IR

AFM images were acquired on Bruker Dimension Icon in tapping mode. AFM-IR was performed using nanoIR3 AFM-IR from Anasys Instruments (Santa Barbara, CA) coupled to a MIRcat-QT quantum cascade, mid-infrared laser (frequency range of 917–1700 and 1900–2230 cm^{-1} and repetition rate of 1470 kHz). AFM-IR data were collected in tapping mode using a gold-coated AFM probe (spring constant [k]: 40 N m^{-1} and resonant frequency [fo]: 300 kHz). The pulsed, mid-IR laser was tuned to resonance bands unique to each component as determined by FTIR characterization (1708 cm^{-1} for DPP3T and 1688 cm^{-1} for PIB-Amide). Acquired images were flattened using Analysis Studio software.

2.2.9 Wide angle X-ray scattering (WAXS)

WAXS was performed on Xenocs Xeuss 2.0 beamline with an X-ray wavelength of 1.54 Å at a sample-to-detector distance of 150mm. GIWAXS was studied with an incidence angle of 0.2°. The scattering signal is collected by a Pilatus 1M detector and later processed using Igor 8 software combined with Nika package and WAXSTools.

2.2.10 Deformed composite film processing

Polymer films were stretched using pseudo-free-standing tensile test to a target strain and transferred to a washer.

2.2.11 Polarized UV-vis

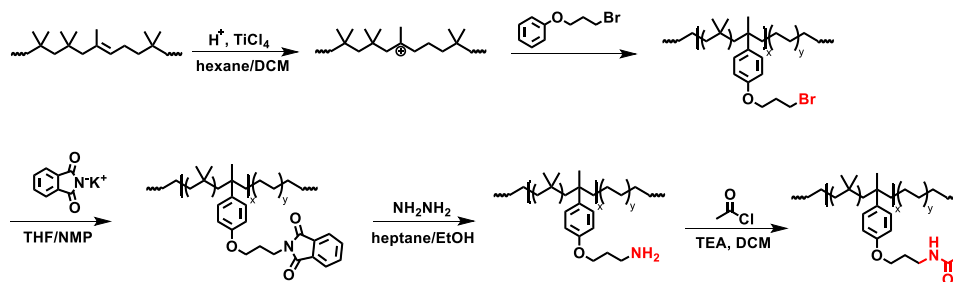
Composite films were prepared on OTS-treated Si/SiO₂ wafer and transferred to PDMS (10:1). The PDMS-polymer film were stretched to a target strain and performed UV-vis using a Cary 5000 UV-vis-NIR spectrophotometer.

2.2.12 Self-healing ability evaluation using cutting film method

The composite thick films were scratch using blade to generate a gap. The gap change was monitored using optical microscopy (Zeiss) and profilometer (Bruker).

2.3 Results and discussion

Scheme 2.1 showed the overall design strategy of the extremely soft, stretchable, and self-healable semiconductor composites DPP-T/PIB-Amide. In our design, we engineered the non-covalent interactions into the elastomeric matrix. We expect the hydrogen bonding crosslink in elastomer can effectively improve the composite's stretchability, self-healing ability and charge carrier mobility. PIB-Amide was designed as the hydrogen bonding crosslinked elastomer matrix to take advantages of properties of PIB and non-covalent hydrogen bonding crosslink (**Scheme 2.2**). PIB is a soft and deformable elastomer with strong adhesion. Hydrogen bonding is an effective method to improve stretchability and self-healing ability. Combining these two components, the obtained PIB-Amide enables extreme softness (~ 1 MPa), high stretchability (COS>1600%), and room temperature spontaneous self-healing ability. The detailed synthesis and characterization of PIB-Amide were described in detail in Supporting Information (**Figure A.1-7**). DPP-T was selected as the model CP because of the commercial availability and high charge mobility ($\mu \sim 0.2 \text{ cm}^2 \text{ V}^{-1} \text{ s}^{-1}$, **Figure A.8-9**).



Scheme 0.2 Synthetic route of PIB-Amide.

The blending ratio between CPs and elastomers was reported to significantly influence the electrical and mechanical properties of DPP-T/PIB-Amide composites.¹¹⁷ We first studied the effect of the blend ratios (weight ratio of DPP-T at 0, 20, 30 and 40% in the DPP-T/PIB-Amide composites) on their physical and electrical property. This blending ratio range is selected to ensure elastomer forms the matrix or continuous phase (weight ratio of CPs < 50%). A top-contact bottom-gate organic field-effect transistor (OFET) was fabricated to study the electrical properties of DPP-T/PIB-Amide composites (**Figure 2.1a and A.10-11**). A fixed V_{sd} value of -60 V was used for all the transfer curve measurement. Notably, to avoid overestimating the electrical properties, the reliability factor of mobility calculations have substantiated exceeding 90%.¹⁹⁵ As the result, an average charge carrier mobility around $0.09 \text{ cm}^2 \text{ V}^{-1} \text{ s}^{-1}$ was observed for all 10%-40% DPP-T/PIB-Amide composites, in which 20% DPP-T/PIB-Amide composite showed slightly higher average charge carrier mobility, $\sim 0.15 \text{ cm}^2 \text{ V}^{-1} \text{ s}^{-1}$. This stable charge mobility is attributed to fibril-like chain aggregation, which can exist in composites at different blending ratios, as will be discussed later. Pseudo-free standing tensile test was then performed to evaluate the mechanical properties of composites (**Figure 2.1b-c, A.12, Table A.2**).^{16,20} Sample composite film with 13 μm film thickness were prepared. 10% DPP-T/PIB-Amide composite absorbed water strongly, thus the data are not reported here. For the other three composites, 20% DPP-T/PIB-Amide showed a record highest COS of $\sim 1500\%$ while maintaining a low E of 1.65 MPa. As the ratio of DPP-T increased, the COS continuously decreased to $\sim 7.67\%$ (40% DPP-T/PIB-Amide) while E increased to 24.34 MPa, which was still much lower than pure DPP-T (483.62 MPa). Combining the aforementioned results, the blending ratio showed almost no effect on electrical properties but significant

influence on mechanical properties. 20% of DPP-T was determined to be the optimum blend ratio due to the highest stretchability and as well as high charge carrier mobility, which was selected for further studies.

Morphology study was then performed to fully elucidate the observed mechanical and electrical properties using infrared-spectroscopy combined atomic force microscopy (AFM-IR) and grazing-incidence wide-angle x-ray scattering (GIWAXS). To obtain AFM-IR images, FT-IR spectroscopy was first performed on both pure CPs and elastomers to find a non-overlapping absorption peak for both components (**Figure A.13**). Comparing the absorption spectra of CPs and PIB-Amide, 1666 cm^{-1} (-C=O stretching vibration in amide) and 1471 cm^{-1} (-CH_2 torsional vibration in backbone) were chosen for selectively excited DPP-T and PIB-Amide, respectively. AFM tapping modes were then applied to obtain phase images (**Figure 2.1d**). After applying IR mode, two components can be clearly distinguished and here they are labeled with two different colors (**Figure 2.1e**). The red and green region represent the DPP-T and PIB-Amide, respectively. Both nanoscopic fibril-like aggregation from CPs and macro phase separation between CPs and PIB-Amide were observed for composites with all blending ratios. However, with an increased ratio of DPP-T, the macro-phase separation became more extensive, while fibril-like aggregation remains constant and well dispersed in rubber matrix. We attributed this blending ratio-independent fibril-like aggregation to hydrogen bonding crosslink between PIB. The hydrogen bond limits the chain mobility of elastomer, making the CP chain interact more with each other to form both the fibril and the large aggregation. The aggregation of conjugated polymers was reported beneficial to electrical properties of composites.^{196,197} For example, Lee et al. added DMSO additive into PEDOT:PSS which inducing

aggregation of PSS phase.¹⁹⁷ The aggregation effectively enhanced cohesion and electrical conductivity. Ouyang et al. studied other additives and observed similar phenomenon.¹⁹⁶ The formation of aggregation and enhanced conductivity was also observed with additive DEG and PEG 400. In terms of charge mobility in OFET applications, previous literature reports fibril-like CP aggregations in CP/elastomer composites contribute mostly.¹⁹⁸ Therefore, this explains that for four different composites, they all showed similar charge mobility regardless of blending ratios. The morphology for bottom surface of the 20% DPP-T/PIB-Amide composite was also measured using AFM due to the significance for charge mobility, which showed similar result as top surface (**Figure A.14**). On the other hand, macro phase separation would lead to more rigid and brittle DPP phase due to their high modulus and low deformability. Therefore, with increasing mixing ratio of DPP-T in composites, the E increased while deformability decreased. GIWAXS was then performed to study the crystallite structure of DPP-T domain in DPP-T/PIB-Amide composites (**Figure A.15-16, Table A.3**). Similar value of lamella packing distance and FWHM were obtained, indicating that the blending ratio did not change the crystallite lattice packing, which also further provides insight to support the observed blending ratio-independent charge mobility.

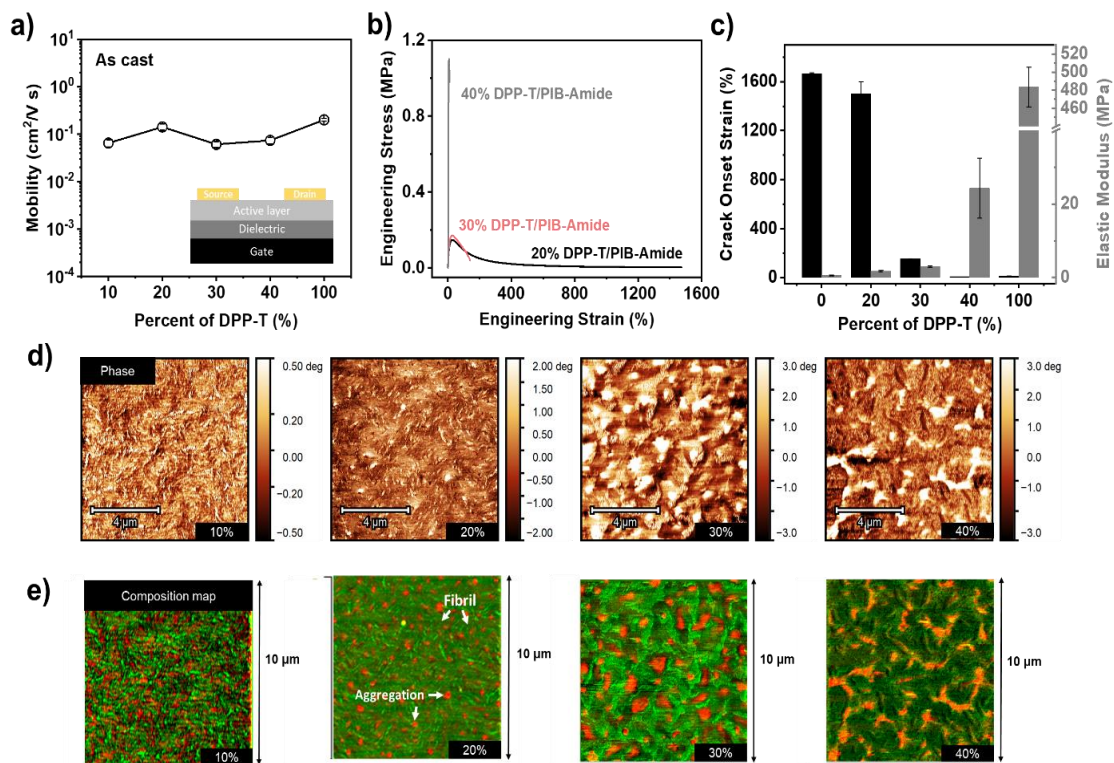


Figure 0.12 *Mechanical, electrical, and morphology for DPP-T/PIB-Amide composite films with different blending ratios.*

a) Charge carrier mobility of 10-40% DPP-T/PIB-Amide composites and DPP-T thin films from top-contact bottom-gate OFET devices. b) Representative stress-strain curve of 20-40% DPP-T/PIB-Amide composite films. c) Elastic modulus and crack onset strain of 0, 20-40%, and 100% DPP-T/PIB-Amide composite films. d) AFM phase images of 10-40% DPP-T/PIB-Amide composite films. e) AFM-IR overlay images highlighting the distributions of DPP-T and PIB-Amide in 10-40% DPP-T/PIB-Amide composite films (red color represents DPP-T domain selectively excited using 1664 cm^{-1} laser, and green color represents for PIB-Amide domain selectively excited using 1462 cm^{-1} laser).

The effect of hydrogen bonding on composites' electrical and mechanical properties was also studied using 20% DPP-T blended with various elastomer control samples (unmodified rubber, intermediate rubber product PIB-Br (**Scheme 2.2**) which does not have any hydrogen bonding functional group, and hydrogen bonding crosslinked PIB-Amide) (**Figure A.17, 18**). The synthesis of the PIB-Br can be found in supporting information as well.¹⁹⁹ The charge mobility of 20% DPP-T/BR, DPP-T/PIB-Br, and DPP-T/PIB-Amide were investigated. All composites performed similar charge mobilities

indicating that the hydrogen bond on elastomer didn't significantly influence the electrical properties (**Figure A.17a**). The effect of hydrogen bonds on mechanical properties was studied between 20% DPP-T/PIB-Br and DPP-T/PIB-Amide (**Figure A.17b, 18**). The 20% DPP-T/PIB-Br showed COS of 400%, which was much lower than 20% DPP-T/PIB-Amide (COS~1500%), demonstrating hydrogen bonding improved the stretchability of semiconducting composites due to the extra energy dissipation pathway provided by hydrogen bonds. Therefore, hydrogen bonding crosslink between elastomers can effectively improve the deformability of CP/elastomer semiconductor composites while maintaining device performance.

Maintaining electrical properties upon stretching and cyclic stretching plays a vital role in practical use. Next, the device's electrical property under cyclic mechanical stretch was investigated. The study focused on using 150% strain. The composite sample were deposited onto the crosslinked elastic PDMS substrate. Then the bilayer sample was cyclically stretched using a motorized tensile stage. The charge mobility remains constant upon stretching (**Figure 2.2a, A.19-22**). Furthermore, high charge mobility value of the semiconductive composite can maintain over 100 repeated stretching cycles to 100% strain at $0.01 \text{ cm}^2 \text{ V}^{-1} \text{ s}^{-1}$ (**Figure 2b, A.23-24**). These results indicate the 20% DPP-T/PIB-Amide composites show high stability upon stretching and cyclic stretching, which is related to the stable crystallite structure as discussed below.

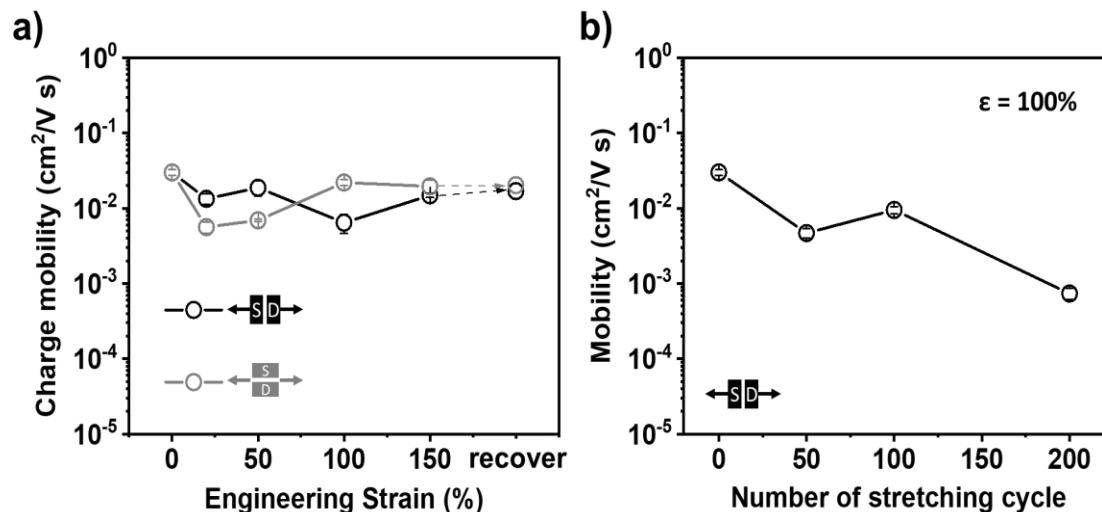


Figure 0.13 *Charge mobility stability upon stretching and cyclic stretching.*

a) Charge carrier mobility of 20% DPP-T/PIB-Amide composites film upon stretching and recovery in parallel and perpendicular direction to charge transfer direction at different strains without annealing. b) Mobilities of 20% DPP-T/PIB-Amide composites film as a function of 100% strain stretching cycles parallel to the charge transport direction.

The deformation mechanism of 20% DPP-T/PIB-Amide composites was performed to understand the stable charge mobility using multi-model characterization, including WAXS, polarized UV-vis absorption spectra, and AFM (**Figure 2.3**).³³ WAXS was first performed to investigate the crystallite domain alignment of DPP-T upon stretching. 2D scattering pattern and 1d line-cut profiles were shown in **Figure 2.3a and A.25-26a**. From 2D scattering patterns, the (100) peak attributed to the lamellae packing peak was isotropic at the first 150% strain, indicating no obvious crystallite alignment. At 200% strain, the (100) peak began to become slightly anisotropic, demonstrating the crystallite packing direction started to rotate, and align to the stretch direction. Orientation parameter f was calculated based on pole figure analysis of (100) peak to quantify the degree of crystallite alignment (**Figure A.26b**).³³ f showed a slight enhancement of 0.09 at the initial 150% strain and 0.16 at 200% (**Figure 2.3c**), indicating that the crystallite domain of DPP-T showed little alignment for the first 150% strain and moderate alignment

at 200%. Besides, the lamellar packing distance and FWHM was calculated from WAXS of unstretched 20% DPP-T/PIB-Amide thick film (**Table A.4**), which was similar to the thin film from GIWAXS indicating the thickness of film didn't significantly influence the morphology. Polarized UV-vis was next to study the whole DPP-T polymer chain alignment. The normalized absorption spectrum for 20% DPP-T/PIB-Amide composite films under strain was plotted in **Figure 2.3b**, where peaks at ~591 nm and ~499 nm were assigned to the 0→0 and 0→1 peaks, respectively. Orientation parameter f change based on polarized UV-vis was calculated from the dichroic ratio, R , which was given by $f = (R-1)/(R+1)$. Orientation parameter f also slightly increased to 0.08 for 100% strain, which was much lower than the reported pure DPP polymer value ($f = 0.36$ at 100% strain).³³ Thus, the whole chain of DPP-T also only aligned a little. Combining results from WAXS and polarized UV-vis, we concluded that the high modulus CP component in composites almost didn't contribute to the first 150% strain, which supported the stable charge mobility upon stretching.

The impressive deformability of the semiconductive composite should be related to the soft elastomer domain, which should account for large strain upon stretching. To certify the contribution of the PIB-Amide component on stretched composites, AFM was performed (**Figure 2.3d, A.27**). The white region, where there is higher phase shift in the tapping image, represents the softer elastomer phase, whereas the dark brown region represents high modulus DPP-T domains. At the strain of 150%, the white phase, PIB-Amide, and large DPP-T aggregation was stretched. In contrast, the fibril-aggregation remained constant, indicating that the deformation of elastomer and deformation of large

DPP-T aggregation contributed most of the first 150% strain, agreed well with the result from WAXS and polarized UV-vis.

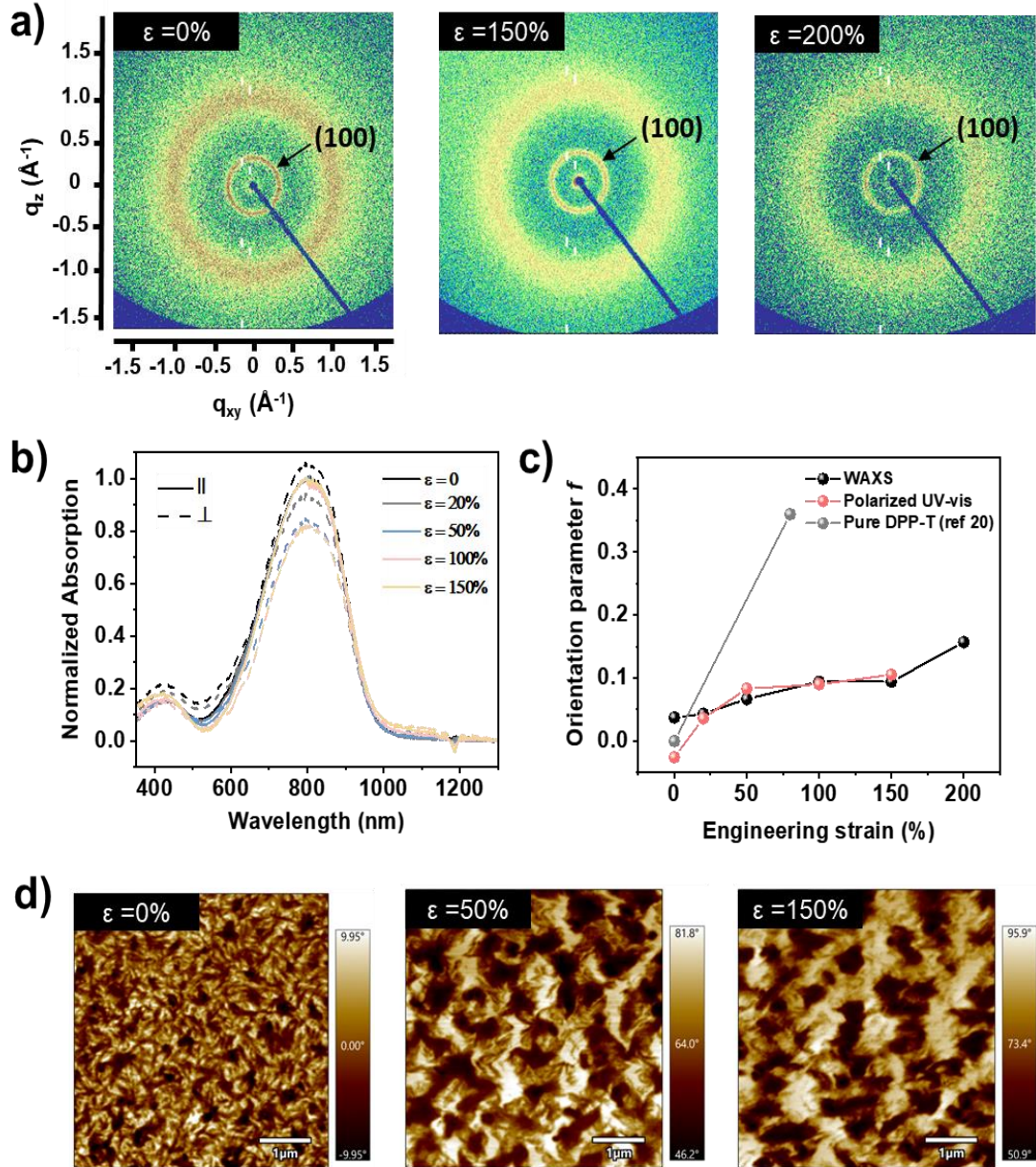


Figure 0.14 *Deformation mechanism of 20% DPP-T/PIB-Amide.*

a) 2D scattering patterns of stretched 20% DPP-T/PIB-Amide composite films at 0, 150 and 200% strain from WAXS. b) Polarized UV-vis absorption plot of 20% DPP-T/PIB-Amide composite films at 0, 20, 50, 100, and 150% strain. c) Herman's orientation parameter f versus strain based on WAXS and polarized UV-vis. d) AFM phase images of stretched 20% DPP-T/PIB-Amide composite films at 0, 50, and 150% strains.

Self-healing ability is an important property allowing for repair local defect under cyclic mechanic stress for wearable device in real life scenario. Due to the self-healing ability of PIB-Amide, we expected the DPP-T/PIB-Amide composites should also perform strong self-healing ability. The self-healing ability of 20% DPP-T/PIB-Amide composites was evaluated in two different methods, named ‘scratching film test’ and ‘cutting film healing test’ here respectively. The scratching film method was first performed. In detail, a thick composite film was drop-casted onto a flat silicon wafer and scratched using a razor blade to introduce a scratch into the film (**Figure 2.4a**). The scratched composites were placed in an air environment without any additional thermal or solvent vapor treatment. To evaluate the self-healing ability, the gap change was monitored using both optical microscopy (OM) and profilometer from 0 to 30 min after scratching (**Figure 2.4a**). The gap is quickly healed from OM images, where the scratch becomes lighter in color after 5 mins and almost disappeared after 30 mins. The thickness change of the gap was measured by profilometer to quantify the healing processing (**Figure 2.4b**). After scratching, a ~1.5 um crack was generated and became lighter and lighter within 30 min (~1 um for 8 min, 0.5 um for 15 min and 0.1 um for 30 min). Tensile test was then performed to calculate the self-healing efficiency, given by the ratio of COS after self-healing and COS of unscratched composite films.²⁰⁰In 5 mins, the self-healing efficiency of 20% DPP-T/PIB-Amide composite reached 94% and 100% after 15 mins (**Figure 2.4c**). Therefore, the 20% DPP-T/PIB-Amide composite showed excellent self-healing ability. To demonstrate the mechanism of self-heal of 20% DPP-T/PIB-Amide composite, the self-healing efficiency of a control sample using non-hydrogen bonding crosslink composite (20% DPP-T/PIB-Br) was also measured (**Figure 2.4c**). The self-healing efficiency of DPP-T/PIB-Br

composite film was 10% for 5 mins and increased to 56% at 30 mins indicating PIB itself has some healing ability due to the low glass transition temperature to promote local chain diffusion and chain entanglement. However, such capability is not on par with the composite using rubber matrix with hydrogen bonding crosslink, where the self-healing ability improved significantly. Therefore, the strong self-healing ability of 20% DPP-T/PIB-Amide composite is attributed to both the association effect of entanglement of PIB chains and hydrogen bonding crosslink. AFM was used to study morphology on the healed part. The healed film showed similar morphology but larger phase separation (**Figure 2.4d**).

The cutting film method is another method we used here to demonstrate the self-healing ability. Bulk composite films were first drop-cast on Si wafers. After immersing in liquid nitrogen, the bulk film was cut into two separate pieces. The separated pieces were pressed again for 25 seconds, followed by being stretched. The two parts successfully stuck and showed high stretchability indicating the self-healing of DPP-T/PIB-Amide composites were very fast and strong (**Figure 2.4e**).

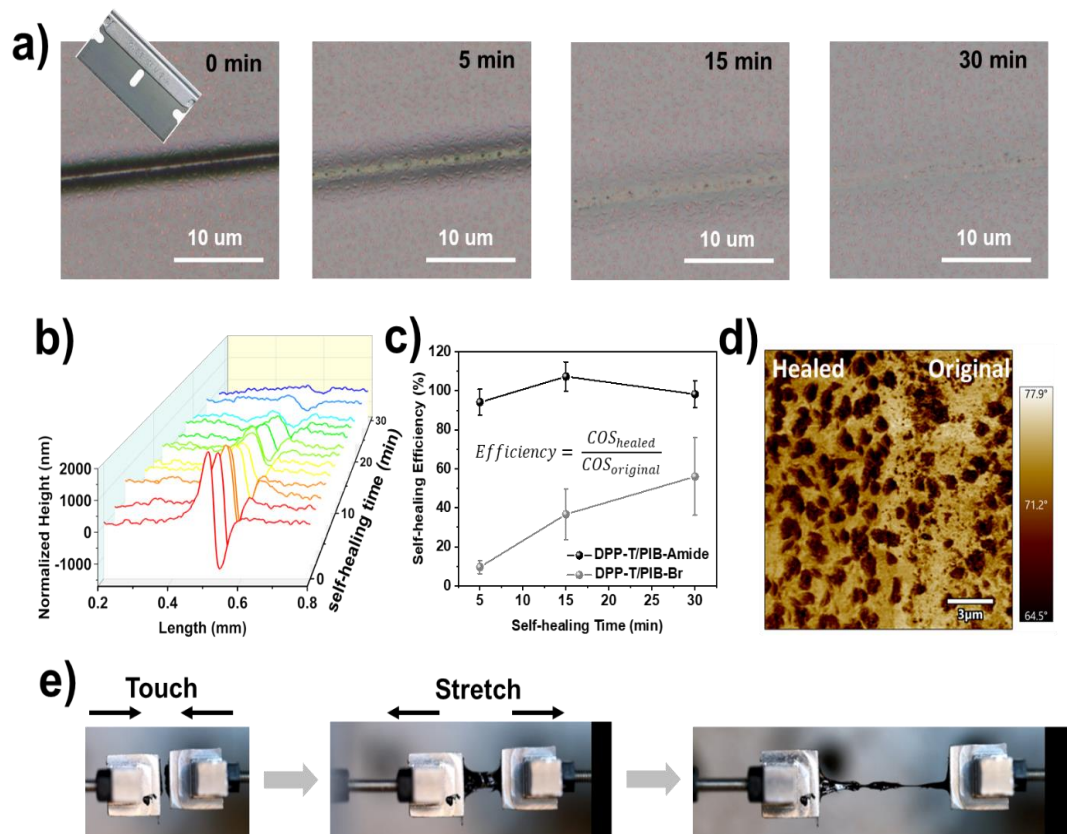


Figure 0.15 Self-healing ability of 20% DPP-T/PIB-Amide composite films.

a) Optical microscope (OM) images of scratched semiconducting film through a self-healing process. b) Thickness map of scratched composite films through the self-healing process. c) Self-healing efficiency through the self-healing process. d) AFM phase images of healed composite films. e) Photographs of the self-healing process of composites from 'cutting film' method.

2.4 Conclusion

In summary, we successfully synthesized hydrogen bonding crosslinked elastomer, PIB-Amide, to fabricate a CP/elastomer composite with record highest crack-onset strain of 1500%, the low elastic modulus of 1.6 MPa, blending ratio-independent charge mobility of $\sim 0.09 \text{ cm}^2 \text{ V}^{-1} \text{ s}^{-1}$ and stable electrical property upon cyclic stretching. Morphology study indicated the elastomer domain accommodated most of the strain upon stretching, allow the electronic active conjugated polymer fibril phase to remain intact, allow maintaining a high and stable charge carrier mobility. The strong self-healing ability originates from the association effect of chain entanglement of PIB and the dynamic nature of hydrogen bonds.

This work developed a new semiconducting composite with all-around high performance, which enriches the stretchable semiconducting polymer and provides a guideline for the future design of stretchable semiconductors.

CHAPTER 3 – LEVERAGING NON-COVALENT INTERACTIONS TO CONTROL MORPHOLOGY, ELECTRICAL AND MECHANICAL PROPERTIES OF STRETCHABLE SEMICONDUCTING COMPOSITES

(Adapted from “Wang, Y.; Chen, K.; Awada, A.; Prine, N.; Zhao, H.; Ocheje, M. U.; Cao, Z.; Liu, C.-T.; Zhang, S.; Rondeau-Gagné, S.; Chiu, Y.; Gu, X. Leveraging Non-Covalent Interactions to Control Morphology, Electrical and Mechanical Properties of Stretchable Semiconducting Composites. *Chem. Mater.* 2023, 35, 9713-9724.”)

3.1 Introduction

Stretchable semiconductors play a crucial role in the development of wearable and implantable devices such as healthcare monitoring, flexible electronics, and smart textiles.^{3,133,164–169} Conjugated polymers (CPs), known for their unique tunable organic structures through synthesis, hold significant potential as stretchable semiconductors compared to their inorganic counterparts.^{170–173} However, the inherent rigidity and coplanarity of CPs' backbone, combined with their high degree of crystallinity enhancing charge mobility, contradict the requirement for CPs to be soft and highly stretchable.^{9,32,174} To address this challenge, researchers have explored various strategies to enhance stretchability. These strategies include the incorporation of long alkyl side chains,^{33,87,89,90,92} the introduction of conjugated breaking spacers,^{9,30,56,62,64,66,80,109} and the insertion of elastomer blocks^{57,98,99,103,176,177}.

Fabricating CP/elastomer composites through physical blending has emerged as a simple but highly efficient as well as promising strategy for developing stretchable semiconductors.^{110,119–125} In this approach, CPs are incorporated into an elastomer matrix, capitalizing on the soft and stretchable nature of elastomers to impart high stretchability to

the composites. More importantly, some of these composites have shown the ability to maintain or even improve charge mobilities.^{37,114} Commonly used elastomers include polydimethylsiloxane (PDMS),^{111–114} styrene-ethylene-butylene-styrene (SEBS),^{110,115,120,123} polystyrene-block-polyisoprene-block-polystyrene (SIS),¹¹⁶ and rubbers.^{117,121} For example, Reichmanis group blended poly(3-hexylthiophene-2,5-diyl) (P3HT) into PDMS, resulting in a significant improvement in stretchability from 5% to more than 100%, accompanied by an increased charge mobility of 0.052 to 0.11 cm²/V s.¹¹⁴ Later on, Zheng et al. incorporated covalent crosslinks between azide and C=C group in SEBS and C–C bond in CPs, successfully developing an elastic composite, DPPTT/SEBS, which didn't show residual strain with increasing cyclic strain from 10% to 70%.²⁸ Recently, Li et al. blended a redox-active semiconducting polymer with a bioadhesive brush polymer, successfully achieving rapid and strong adhesion with wet tissue surfaces.²³ This material showcased high charge-carrier mobility of ~1 cm² V⁻¹ s⁻¹, high stretchability, and good biocompatibility, which showed great potential for *in vivo* bioadhesive organic electrochemical transistors (OECTs) measuring under-skin electromyograms (EMGs) from the gastrocnemius medialis (GM) muscle. In our previous work, we blended DPP-T with a hydrogen bonding crosslinked elastomer PIB-Amide, successfully achieving a crack onset strain (COS) of ~1300% while maintaining a charge mobility of 0.15 cm²/V s.³⁷

The morphology of CP/elastomer semiconducting composites was reported to have significant impacts on electrical and mechanical properties.^{198,201} Nanofibril aggregates have been identified as a crucial factor in enhancing the charge mobility of CP/insulator composites, primarily due to the connectivity between these nanofibril aggregates.^{115,198} For example, Angunawela *et al.* blended PDPP3T and polystyrene (PS) in various ratios.¹⁹⁸

With an increase in the PS ratio, the composites exhibited larger and more extended fibril networks, resulting in higher charge mobility. Similarly, Nikzad *et al.* blended P2TDPP2TFT4 with SEBS, resulting in improved polymer aggregation and orientation, leading to a five-fold increase in charge mobility from 0.3 to 1.5 cm²/V s.¹¹⁵ Consequently, current research on stretchable semiconducting composites has made significant efforts to promote fiber-like aggregates.^{110,202,203} In a very successful example, Xu *et al.* blended DPPT-TT into a SEBS matrix to utilize the nanoconfinement effect to induce the formation of fibril aggregates, and successfully maintained a high charge mobility of 1 cm²/V s at 100% strain.¹¹⁰ Additionally, the formation of bundle-like aggregations have proven beneficial for achieving mechanical stretchability.¹²³ Jeong *et al.* blended P3HT into PDMS resulting in the formation of a P3HT bundle network, which significantly improved the stretchability with a COS exceeding 50%.¹²³ However, the careful manifestation of the morphology for stretchable CP/elastomer composites is still lacking, and further understanding of its influence on both mechanical and electrical properties remains to be investigated.

Introducing hydrogen bonding (H-bonding) crosslinks into two incompatible polymers is an effective method to control the morphology of polymer composites.^{192,204,205} For example, polystyrene/polyethylene glycol (PS/PEG) composites perform a large phase separation due to their inherent incompatibility.²⁰⁶ After introducing complementary H-bonding into their chain ends, large phase separation depressed resulting in micro-phase separation. Similarly, when introducing ureidopyrimidinone (UPy) groups to a chain end of P3HT and PS to enable strong H-bonding interactions, large macroscale phase separations were successfully depressed.²⁰⁷ The same phenomenon was also observed for

poly(9,9-dioctyl fluorene) (PFO)/PEG and poly(3-hexylthiophene) (P3HT)/PFO composites. Therefore, hydrogen bonding crosslinks serve as an effective method for controlling the morphology of CP/elastomer composites. In addition, H-bonding crosslinks can also improve stretchability. The relatively weak H-bond can be broken upon stretching allowing for additional energy dissipation pathways to improve the stretchability of materials. Yan *et al.* introduced ureidopyrimidinone (UPy) groups to construct a hydrogen bonding crosslinked supramolecular polymeric material.¹⁹⁴ With 20 mol% UPy groups incorporated, the supramolecular polymeric material achieved extreme stretchability (COS= 17,000%). Oh *et al.* introduced 2,6-pyridine dicarboxamide (PDCA) into DPP-based CP to enable H-bonding crosslink between CP backbone. The COS was effectively improved from 5% to over 100%.³⁰ Chen *et al.* introduced amide groups into soft phase polyacrylate and copolymerized with rigid PS.²⁰⁸ With H-bonding crosslink, the materials performed microphase-separated system, which enhanced the toughness and self-healing ability. From these works and reporting, we hypothesize that introducing H-bonding crosslinks into both CPs and elastomers can effectively control the morphology of CP/elastomer composites and modulate the mechanical and electrical properties.

In this work, we introduced amide functional groups to DPPTVT polymers to obtain a DPPTVT-A and PIB elastomer matrix (amide-polyisobutylene, PIB-A) respectively, allowing for formation of intra- and inter-phase H-bonding crosslinks. By blending amide- or non-functional CPs and elastomers, four composites with different H-bonding crosslinking sites were fabricated: dual-H-bonding crosslinked DPPTVT-A/PIB-A, uni-HB crosslinked DPPTVT-A/PIB-Br and DPPTVT/PIB-A and non-HB crosslinked DPPTVT/PIB-Br composites. Their morphologies were studied combining atomic force

microscopy (AFM), atomic force microscopy with inferred spectroscopy (AFM-IR), grazing-incidence wide-angle X-ray scattering (GIWAXS) and UV-vis absorption spectroscopy. The mechanical properties were studied using film-on-water and film-on-elastomer tensile tester. The effect on electrical properties were studied by fabricating top-contact bottom-gate organic field-effect transistors (OFETs). The non-H-bonding crosslinked composite exhibited the most pronounced fibril aggregation and highly ordered crystallite packing, resulting in the highest charge mobility but the lowest stretchability. Introducing intra-phase hydrogen bonding crosslinks in CPs and elastomers led to larger and more large-scale aggregates due to stronger interactions, resulting in lower charge mobility but enhanced stretchability. Additionally, the charge mobility remained stable after stretching. Most interestingly, the dual-H-bonding crosslinked composite DPPTVT-A/PIB-A exhibited micro-phase separation due to a combination of inter- and intra-phase H-bonding interactions. However, the micro-phase separation morphology wasn't beneficial to electrical properties, resulting in the lowest charge carrier mobility. After stretching, the two phases reorganized into fibril-like aggregates, obtaining improved charge mobility. From polarized UV-vis spectroscopy study, the deformation was primarily contributed by the elastomer phase for all the composites. The H-bonding introduced at elastomer phase also improved the cyclic stretching stability and both locations will improve the self-healing ability. This work provides a method to control the morphology of stretchable CP/elastomer composites, enabling the complete understanding of morphology effects on mechanical and electrical properties, which will valuably guide the future design of stretchable semiconductors.

3.2 Experimental

3.2.1 Materials

DPPTVT, DPPTVT-A, PIB-Br and PIB-A were synthesized according to previous work.^{37,77,209} Poly (sodium 4-styrenesulfonate solution) (PSS, 30% in water) was purchased from Sigma Aldrich.

3.2.2 Film processing

Conjugated polymers (CPs), DPPTVT and DPPTVT-A, were blended with elastomer PIB-Br and PIB-A, respectively, with a CP/elastomer weight blending ratio of 1:4 in anhydrous chlorobenzene (CB) with concentrations of 10 mg/ml. The solutions were heated at 80 °C overnight before processing. Thin films were spin-cast on Si wafers at 1000 revolutions per minute (r.p.m.) for 1 minute. Thin film thickness was ~60 nm. Thick films were drop-cast on pre-cut Si wafers with thickness of ~40 μm .

Stretched thin films were first spin-cast on OTS-treated Si/SiO₂ wafers and transferred to PDMS substrates. The thin films were stretched together with PDMS substrate and transferred back onto Si wafers.

3.2.3 Atomic force microscopic (AFM) and infrared-spectroscopy combined AFM (AFM-IR)

AFM images were acquired on an Asylum Cypher S AFM microscope in the AC-air mode. Composite thin films on Si wafers were observed.

AFM-IR was performed using nanoIR3 AFM-IR from Anasys Instruments (Santa Barbara, CA) coupled to a MIRcat-QT quantum cascade, mid-infrared laser (frequency range of 917–1700 cm^{-1} and 1900–2230 cm^{-1} and repetition rate of 1470 kHz). AFM-IR data was collected in tapping mode using a gold-coated AFM probe (spring constant [k]: 40 N m^{-1}

and resonant frequency [f_0]: 300 kHz). The pulsed, mid-IR laser was tuned to resonance bands unique to each component as determined by FTIR characterization (1666 cm^{-1} for DPPTVT-A and 1462 cm^{-1} for PIB-A). Acquired images were flattened using Analysis Studio software.

3.2.4 Grazing-incidence wide angle X-ray scattering (GIWAXS)

GIWAXS measurements was conducted on beamline 7.3.3 at the Advanced Light Source in Berkeley Lawrence National Lab. Data was collected under a helium environment with an incident beam energy of 10 keV and an incidence angle of 0.14° . Composite thin film samples were performed on Si wafers. The scattering signal was collected by a Pilatus 2M detector and processed using Igor 8 software combined with Nika package and WAXSTools.

3.2.5 UV-Vis absorption spectroscopy

UV-Vis-NIR spectra were acquired by using a Cary 5000 UV-Vis-NIR spectrophotometer. Composite thin films were spin-cast on OTS-treated Si/SiO₂ wafers and transferred to PDMS substrate. Polarized UV-vis spectroscopy was recorded using polarized light with an angle of 0° and 90° to strain direction.

3.2.6 Film-on-elastomer tensile test

Composite thin films were first spin-cast on OTS-treated Si/SiO₂ wafers and transferred to PDMS substrates. The thin films were stretched together with PDMS substrate using a manual linear stage. The images were taken at the engineering strain of 0, 20, 50, 100, 150 and 200% using an optical microscopy (Zeiss Axio Imager).

3.2.7 Film-on-water tensile test

Tensile tests of composites were performed using thick films. The films were prepared on PSS-coated Si wafers followed by being floated on top of water and stretched at a strain rate 2 s^{-1} until fractured. The detailed instrument setup can be found in previous literature reports.^{16,20}

3.2.8 OFET fabrication and characterization

The device performance for stretched composites were measured under a strain-neutral state. To prepare the samples, 80 nm thin films were spin-coated on OTS-treated Si/SiO₂ wafers and transferred to PDMS substrates. The thin film was uniaxially stretched on PDMS and transferred fresh to Si wafers. Finally, gold electrodes were deposited to obtain top-contact bottom-gate OFETs. The error bars were associated with multiple devices with the same fabrication method.

3.3 Results and Discussion

The overall design strategy of semiconducting composites with or without H-bonding is shown in **Scheme 3.1**. We aim to control the morphology of stretchable CP/elastomer composites by introducing H-bonding crosslinks at different sites (no interaction or with intra- or inter-phase H-bonding crosslinks), and study the following effect on mechanical and electrical properties. Amide functional DPPTVT (DPPTVT-A) and amide functional PIB (PIB-A) were synthesized to endow the capability to form H-bonding crosslinking networks.^{37,209} Their non-amide counterparts DPPTVT and PIB-Br were used as non-H-bonding crosslinked control sample. By blending DPPTVT-A and DPPTVT with PIB-A and PIB-Br, four CP/elastomer composites with different H-bonding crosslinked sites were fabricated including dual-H-bonding crosslinked composite

DPPTVT-A/PIB-A with both inter- and intra-phase H-bonding crosslinks, uni-H-bonding crosslinked composites DPPTVT-A/PIB and DPPTVT/PIB-A with intra-CP or intra-elastomer H-bonding crosslink, and non-H-bonding crosslinked composite DPPTVT/PIB-Br. All the composites used a CP/elastomer 1:4 weight ratio, which was the optimized ratio in terms of mechanical and electrical properties reported in previous studies.³⁷ Fourier–transform infrared spectroscopy (FT-IR) spectroscopy was used to confirm the formation of H-bonding crosslinks, primarily by analyzing the wide -NH stretching peak in the range of 3700-3100 cm^{-1} (**Figure B.1a**).⁷⁷ However, the presence of an overlapping peak from the elastomer phase (**Figure B.1b**) and the shared utilization of amide groups for H-bonding crosslink formation in both components made it impossible to differentiate the location of these crosslinks. We expected the H-bonding crosslinking to effectively reduce phase separation between the semiconducting polymer and elastomer phase and have an influence on the electrical and mechanical properties (**Table 3.1**).

Table 0.1 Summary of morphological, electrical and mechanical properties of non-, uni- and dual-H-bonding crosslinked composites, DPPTVT/PIB-Br, DPPTVT-A/PIB-Br, DPPTVT/PIB-A and DPPTVT-A/PIB-A.

Sample	Morphology			Polarized UV-vis 0-0/0-1 peak intensity Ratio	Mechanical property COS	Electrical property		
	AFM	GIWAXS				Mobility (cm ² /V s)	Mobility upon stretching (cm ² /V s)	
		Lamellar Peak (Å ⁻¹)	Lamellar peak FWHM (Å ⁻¹)				ε = 50%	ε = 150%
DPPTVT/PIB-Br	Dominated fiber aggregates Large-scale aggregates	0.30	0.05	1.04	<100%	0.45 ± 0.05	0.46 ± 0.03	0.17 ± 0.01
DPPTVT-A/PIB-Br	Reduced fiber aggregates Larger large-scale aggregates	0.27	0.11	1.18	100-150%	0.16 ± 0.02	0.18 ± 0.02	0.16 ± 0.02
DPPTVT/PIB-A	Reduced fiber aggregates More large-scale aggregates	0.30	0.05	1.02	>200%	0.08 ± 0.01	0.05 ± 0.01	0.09 ± 0.01
DPPTVT-A/PIB-A	Micro-phase separation Large-scale aggregates	0.27	0.08	1.19	>200%	0.02 ± 0.01	0.04 ± 0.01	0.06 ± 0.01

The morphology of composites was first characterized by AFM, GIWAXS and UV-vis spectroscopy. AFM was employed to perform the surface morphology of the composites. The non-H-bonding crosslinked composite DPPTVT/PIB-Br, exhibited predominated large fibril aggregates, which was commonly observed in CP/elastomer composites in literature (**Figure 3.1a, B.2a**). Upon the introduction of H-bonding crosslinks into conjugated polymers, the number of fibril aggregates decreased, while the size of large-scale aggregates increased obviously (**Figure 3.1b, B.2b**). This observation can be attributed to stronger fibril aggregates induced by the additional H-bonding interaction between CP chains. Conversely, when H-bonding crosslinks were introduced within the elastomer phase, the size of large-scale aggregates from DPPTVT CPs remained constant, similar to the non-H-bonding crosslinked composite DPPTVT/PIB-Br, but their quantity increased (**Figure 3.1c, B.2c**). Thus, the constant size of aggregates results from the consistent interaction strength between CPs. However, the H-bonding crosslinks within the elastomer phase led to a preference of more large-scale aggregates formed from fibril aggregates. Consequently, in uni-H-bonding crosslinked composites, the H-bonding crosslinks within CPs dominated the size of the large-scale aggregates, while the H-bonding crosslinks within elastomer dominated the number of large-scale aggregates. Interestingly, a micro-phase separation morphology emerged in the dual-H-bonding crosslinked composite DPPTVT-A/PIB-A, accompanied by the presence of large-scale aggregates (**Figure 3.1d, e and B.2d-e**), originating from the inter-phase H-bonding crosslink between the elastomer and CP chains. To further confirm the micro-phase

separation morphology, atomic force microscopy with infrared-spectroscopy (AFM-IR) was employed to highlight the distribution of the DPPTVT/A-PIB-A composite (**Figure 3.1f**). We selectively excited the DPPTVT-A and PIB-A phase using 1666 cm^{-1} laser and 1462 cm^{-1} laser, respectively. Those two wavelengths were selected from the unique absorption spectrum shown in supporting **Figure B.3**. The red color represents the DPPTVT-A domain, while the green color represents PIB-A domain. A similar result was observed, showing micro-phase separation, further supporting the presence of micro-phase separation. The bottom surface morphology for the composites were also assessed using AFM due to its relevance to charge mobility. The composite films were initially spin-cast onto OTS-treated Si/SiO₂ wafer and subsequently transferred onto PDMS. AFM imaging of the bottom surface was conducted using PDMS as substrates. Remarkably, all the four composites exhibited similar morphology (**Figure B.4**). We attributed this similarity to the comparable surface energy of these composites when compared to Si wafer surface. It's worth noting that due to the thinness of the composite films, variations in morphology between the top and bottom surfaces have little impact on their electrical properties.

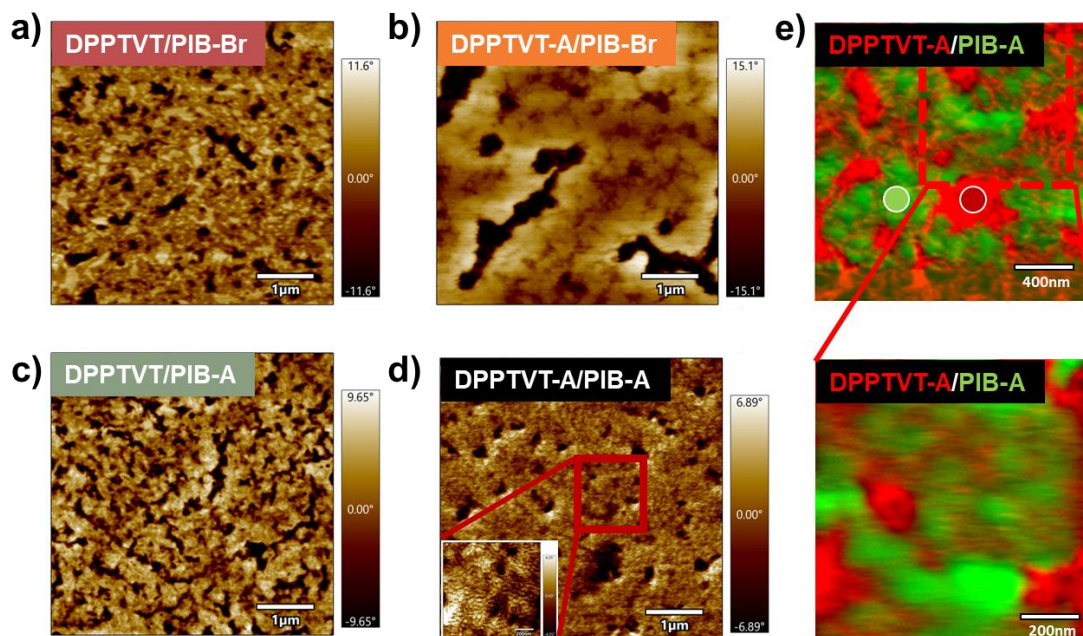


Figure 0.16 *AFM phase images of composites.*

AFM phase images of (a) DPPTVT/PIB-Br, (b) DPPTVT-A/PIB-Br, (c) DPPTVT/PIB-A and (d) DPPTVT-A/PIB-A composites. (e) AFM-IR overlay image highlighting the distributions of DPPTVT-A and PIB-A in DPPTVT-A/PIB-A composite films (red color represents DPPTVT-A domains selectively excited using 1666 cm^{-1} laser, and the green color represents PIB-A domains selectively excited using 1462 cm^{-1} laser).

GIWAXS and UV-vis were then employed to investigate the crystalline structure and aggregation behavior of the CP domain in the composites. The 2D scattering patterns and corresponding 1D scattering profiles from GIWAXS are shown in **Figure 3.2a-e**. The fitting peak position and FWHM (full width at half maximum) of the lamellar packing (100) and π - π stacking (010) are summarized in **Table 3.2**. It should be noted that some peaks couldn't be fitted due to the weak scattering signal resulting from the disordered nature of CPs in the composites. Lamellar packing peaks were observed for all composites, indicating the formation of a crystalline structure for the conjugated polymer phase for all composites. The non-H-bonding crosslinked composite DPPTVT/PIB-Br, exhibits the

most prominent higher-order lamellar packing peak (200), indicating the most ordered crystalline packing among the composites. In the uni-H-bonding crosslinked composites, DPPTVT-A/PIB-Br and DPPTVT/PIB-A, a weaker (200) peak was observed, suggesting a less ordered crystalline packing. In the dual-H-bonding crosslinked composite, DPPTVT-A/PIB-A, only a weak (100) peak was observed, with no clear (200) peak visible, indicating a nearly amorphous structure. This amorphous structure is likely a result of the inter-phase H-bonding crosslinks, which hinder the formation of crystalline structure in the DPPTVT-A/PIB-A composite. Additionally, composites with the same CP compounds exhibited similar lamellar packing distance, with values of 20.9 Å for DPPTVT/PIB-Br and DPPTVT/PIB-A composites, and 23.3 Å for DPPTVT-A/PIB-Br and DPPTVT-A/PIB-A composites, indicating the lamella packing distance is sidechain dependent for these conjugated polymers. The (010) peak of non-H-bonding crosslinked composite DPPTVT/PIB-Br appeared in the in-plane direction, suggesting a predominantly edge-on orientation. In contrast, no (010) peak was observed in the other three composites, further confirming the presence of a less ordered crystalline structure.

UV-vis absorption spectroscopy was utilized to investigate the aggregation behavior of CP chains in the composites (**Figure 3.2f**). The 0-0 peak and 0-1 peak were observed in all composites, indicating the presence of CP aggregations in all composites, which is consistent with the morphology observed in AFM. All the curves were normalized with 0-1 peak. The composites containing DPPTVT-A exhibited stronger 0-0 peaks compared to the composites containing DPPTVT, which can be attributed to the additional H-bonding crosslinks between CP phases.

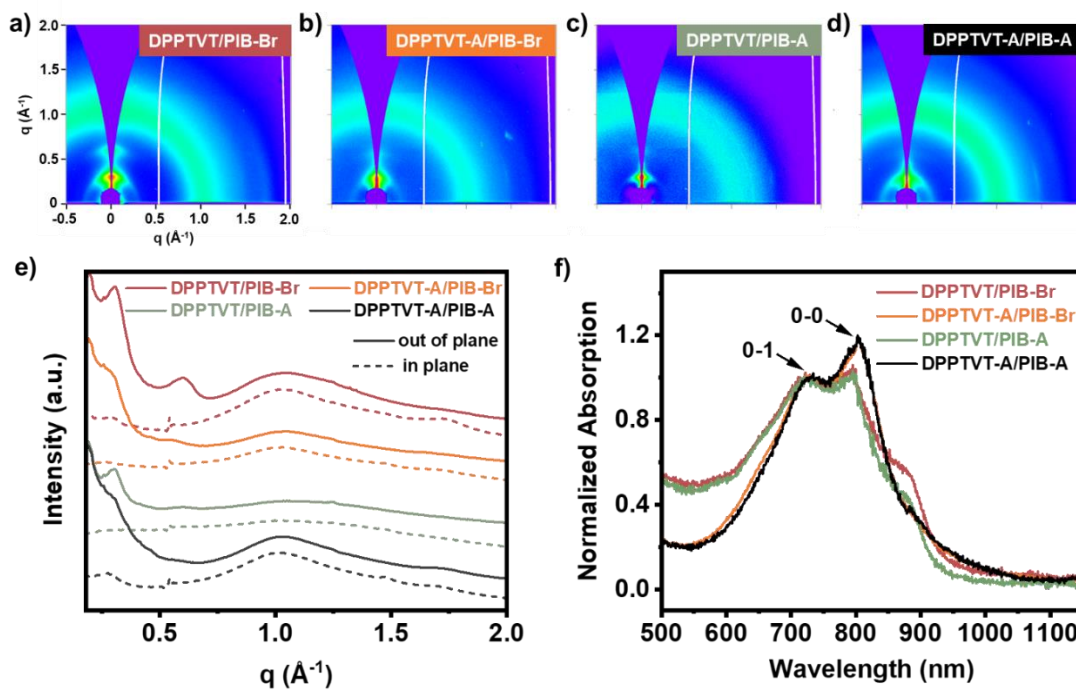


Figure 0.17 GIWAXS and UV-vis results of composites.

2D images for (a) DPPTVT/PIB-Br, (b) DPPTVT-A/PIB-Br, (c) DPPTVT/PIB-A and (d) DPPTVT-A/PIB-A composites from GIWAXS. (e) 1D line-cut profiles for DPPTVT/PIB-Br (red), DPPTVT-A/PIB-Br (orange), DPPTVT/PIB-A (green) and DPPTVT-A/PIB-A (black) composites in both out-of-plane direction (solid line) and in-plane direction (dotted line) from GIWAXS. (f) UV-vis absorption spectra of DPPTVT/PIB-Br (red), DPPTVT-A/PIB-Br (orange), DPPTVT/PIB-A (green) and DPPTVT-A/PIB-A (black) composites.

Table 0.2 Crystallographic parameters of non-, uni- and dual-H-bonding crosslinked composites, DPPTVT/PIB-Br, DPPTVT-A/PIB-Br, DPPTVT/PIB-A and DPPTVT-A/PIB-A from GIWAXS.

Materials	Out of plane			In plane		
	Lamellar peak (\AA^{-1})	Lamellar peak FWHM (\AA^{-1})	π - π stacking (\AA^{-1})	Lamellar peak (\AA^{-1})	Lamellar peak FWHM (\AA^{-1})	π - π stacking (\AA^{-1})
DPPTVT/PIB-Br	0.30	0.05	/	0.29	0.05	1.73
DPPTVT-A/PIB-Br	/	/	/	0.27	0.11	/
DPPTVT/PIB-A	0.30	0.05	/	/	/	/
DPPTVT-A/PIB-A	/	/	/	0.27	0.08	/

The effect of morphology on device performance was then investigated by fabricating top-contact bottom-gate OFETs as shown in **Figure 3.3, SB.5**. The non-H-bonding crosslinked composite, PIB-Br/DPPTVT, exhibited the highest charge mobility, $0.45 \text{ cm}^2/\text{V s}$. This excellent device performance was attributed to the predominated fibril aggregation and the highest ordered crystalline packing, as discussed previously. However, when H-bonding crosslinks were introduced into CPs, the mobility decreased to $0.16 \text{ cm}^2/\text{V s}$ due to the reduction of fibril aggregates and less order crystalline packing. Furthermore, when H-bonding crosslinks were introduced into the elastomer phase, the charge mobility further decreased to $0.08 \text{ cm}^2/\text{V s}$, primarily due to the further decreased amounts of fibril aggregates. Surprisingly, when both components were crosslinked with H-bonds, the DPPTVT-A/PIB-A composite exhibited the lowest mobility, $0.02 \text{ cm}^2/\text{V s}$, which can be attributed to the minimal fibril aggregates and nearly amorphous structure. The hysteresis of the composites was also analyzed from the transfer curves (**Figure B.5**).

The PIB-A/DPPTVT-A composite showed the remarkable hysteresis due to the doping of electrons by the amide groups in both components.

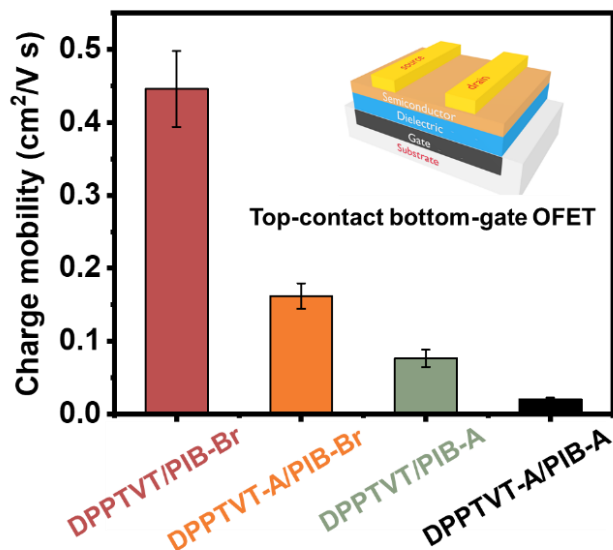


Figure 0.18 Charge mobility comparison of DPPTVT/PIB-Br (red), DPPTVT-A/PIB-Br (orange), DPPTVT/PIB-A (green) and DPPTVT-A/PIB-A (black) composites.

The mechanical properties of the composites were next studied using film-on-elastomer and film-on-water tensile tests. Considering H-bonding crosslinking influence on mechanical properties, the results originate from an association effect of morphology and H-bonding crosslink. Film-on-elastomer tensile tests were performed to evaluate the stretchability of the composite thin films. The spin-cast composite thin films were transferred onto PDMS and stretched to fixed strains. Optical microscopic (OM) images were used to monitor the formation of cracks (**Figure 3.4a, B.6**). Due to the limitation of PDMS, we only stretched them to the strain of 200%. At 200% strain, only DPPTVT/PIB-Br composite showed noticeable cracks. AFM images of stretched composites were also obtained in the following study, which revealed smaller cracks. The DPPTVT/PIB-Br

composite exhibited cracks starting at a strain of 100%, while the DPPTVT-A/PIB-Br composite showed cracks at a strain of 150%, indicating the COS of DPPTVT/PIB-Br composite was less than 100% and COS of DPPTVT-A/PIB-Br was between 100-150% (**Figure 3.6a**). In contrast, the other composites exhibited COS higher than 200%. These results indicate that introducing H-bonding crosslink to CP phases slightly improved stretchability, while introducing H-bonding crosslinks to elastomer phases significantly enhances the stretchability. Film-on-water tensile test was conducted to study the modulus of the composites (**Figure 3.4b, B.7**). Thick films with ~40 μm thickness were drop-cast on polystyrene sulfonate salt spin-cast Si wafers and transferred onto a water surface. The representative stress-strain curves were shown in **Figure 3.4b**, and the elastic modulus (E) extracted from the slope of elastic region were summarized in **Figure 3.4c**. The non-H-bonding crosslinked composite, DPPTVT/PIB-Br, showed the lowest elastic modulus. After introducing H-bonding crosslinks into the CP phase, the elastic modulus increased due to the physical crosslinks between CP chains. When introducing H-bonding crosslinks into the elastomer phase, the elastic modulus further increased. That's because the elastomer matrix dominates the mechanical properties of the composites. The H-bonding crosslinks between elastomers showed a more straightforward influence on the modulus improvement than that between CPs. Interestingly, when H-bonding crosslinks were introducing into both components, the E decreased slightly compared to elastomer crosslinked composite, DPPTVT/PIB-A, which can be attributed to some of the amide groups in elastomers interacting with the CP chains, reducing the crosslink density of elastomers and lowering the E of the overall composites. Besides, the lower crystallinity

observed from GIWAXS should also contribute to lowering the E. The COS determined from film-on-water tensile test was observed to be lower than that from film-on-elastomer tensile test, likely due to the presence of more aggregates formed during drop-casting, which act as defects in the films.

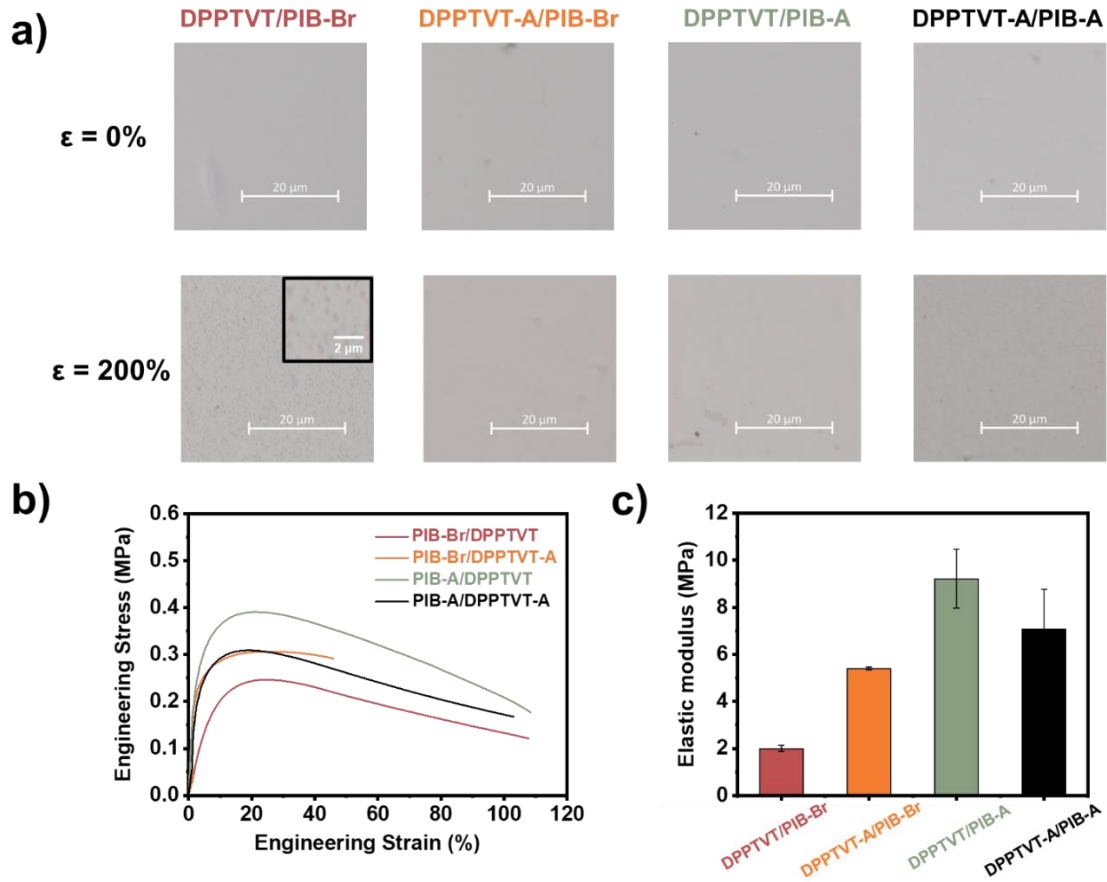


Figure 0.19 *Mechanical properties of composites.*

(a) Representative optical images of the stretched composites strained via the film-on-elastomer technique. (b) Representative stress–strain curve and (c) elastic modulus of DPPTVT/PIB-Br (red), DPPTVT-A/PIB-Br (orange), DPPTVT/PIB-A (green) and DPPTVT-A/PIB-A (black) composites.

The mobility of stretched composites was also studied to evaluate the stretchability of composite films (**Figure 3.5, B.8-11**). Sample preparation method was the same as previous reported literature.³⁷ Mobility measurements were conducted in both parallel and

perpendicular to the stretching direction. The mobility of the non-H-bonding crosslinked composite DPPTVT/PIB-Br started to decrease at a strain of 100% in both directions (Figure 3.5a). After introducing H-bonding crosslinks into either CP or elastomer phase, the charge mobility remained stable even after stretching to a strain of 150% (Figure 3.5b-c). For dual-H-bonding crosslinked DPPTVT-A/PIB-A, the mobility was first constant at an initial strain of 20% followed by a surprising increase at the strain of 50%, 100% and 150% (Figure 3.5d).

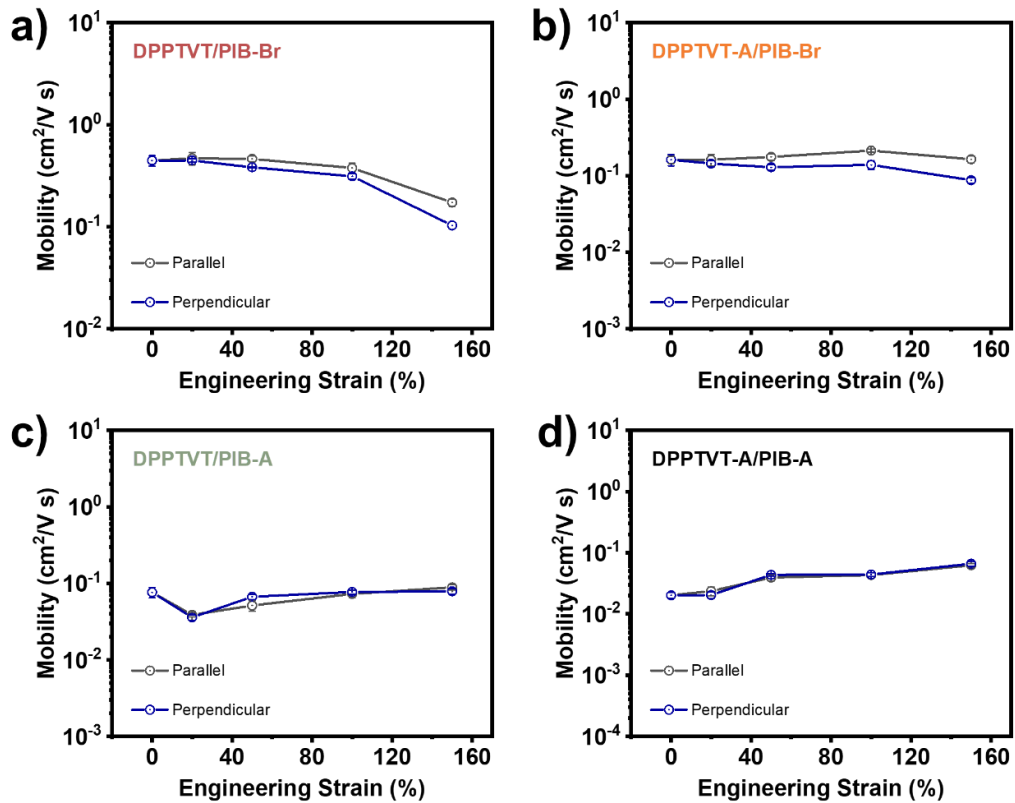


Figure 0.20 Charge mobility of stretched composites.

Charge mobility of stretched (a) DPPTVT/PIB-Br, (b) DPPTVT-A/PIB-Br, (c) DPPTVT/PIB-A and (d) DPPTVT-A/PIB-A composites in parallel and perpendicular direction to stretching direction at the engineering strain of 0, 20, 50, 100 and 150%, respectively.

To thoroughly comprehend the electrical property of the stretched composites, we conducted morphologies analyses of stretched composites using AFM and polarized UV-vis spectroscopy. AFM was employed to investigate changes in surface morphology change after stretching at different strains (**Figure 3.6, B.12**). For the non-H-bonding crosslinked composite DPPTVT/PIB-Br, the voids became larger at the strain of 50%, and cracks began to appear at the strain of 100%. This breakage explains the dropped charge mobility of DPPTVT/PIB-Br composite at strain of 100%. In contrast, the morphologies of both uni-H-bonding crosslinked composites, DPPTVT-A/PIB-Br and DPPTVT/PIB-A, remained stable after stretching to 100%, resulting in stable value charge mobility upon stretching. After stretching to 150%, intra-CP phase crosslinked composite DPPTVT-A/PIB-Br exhibited some cracks, leading to a decreased charge mobility. However, the intra-elastomer crosslinked composite DPPTVT/PIB-A maintained its morphology even after being stretched to 150%, obtaining a stable charge mobility. For the dual-H-bonding crosslinked composite DPPTVT-A/PIB-A, the morphology remained unchanged after stretching to 20%, resulting in constant mobility at strain of 20%. However, after stretching to the strain of 50%, the two phases reorganized and formed fibril aggregates, improving the charge mobility along both directions. These fibril aggregates remained stable after further stretching to 150%, resulting in maintained charge mobility. Polarized UV-vis spectroscopy was conducted to investigate the alignment of the whole CP chain for stretched DPPTVT/PIB-Br, DPPTVT-A/PIB-Br, DPPTVT/PIB-A and DPPTVT-A/PIB-A composites at various strains (**Figure 3.7, B.13**). The normalized absorption spectrum for the composite films under strain of 0, 20%, 50%, 100% and 150% was plotted in **Figure**

B.13. Peaks at $\approx 795, 806, 800$ and 804cm^{-1} correspond to the $0 \rightarrow 0$ peaks of DPPTVT/PIB-Br, DPPTVT-A/PIB-Br, DPPTVT/PIB-A and DPPTVT-A/PIB-A composites, respectively, while peaks at $\approx 795, 806, 800$ and 804cm^{-1} represent $0 \rightarrow 1$ peaks. Orientation parameter f was calculated from the dichroic ratio, R , using the formula $f = (R-1)/(R+1)$. For all the composites, f showed only a slight increase at strain of 150% (0.09, 0.01, 0.09, 0.02 for DPPTVT/PIB-Br, DPPTVT-A/PIB-Br, DPPTVT/PIB-A and DPPTVT-A/PIB-A composites, respectively). These values were significantly lower than the reported value for pure DPP polymer ($f = 0.36$ at 100% strain), indicating the whole chain of conjugated polymers didn't align extensively.³³ Combining these results with the AFM findings, it is evident that the deformation was primarily contributed by the elastomer phase in DPPTVT/PIB-Br, DPPTVT-A/PIB-Br, DPPTVT/PIB-A composites, which is consistent with our previous report.³⁷ In the case of DPPTVT-A/PIB-A composites, while the conjugated polymer phase reorganized into fibrils after strain of 50%, no distinct preferred orientation was observed.

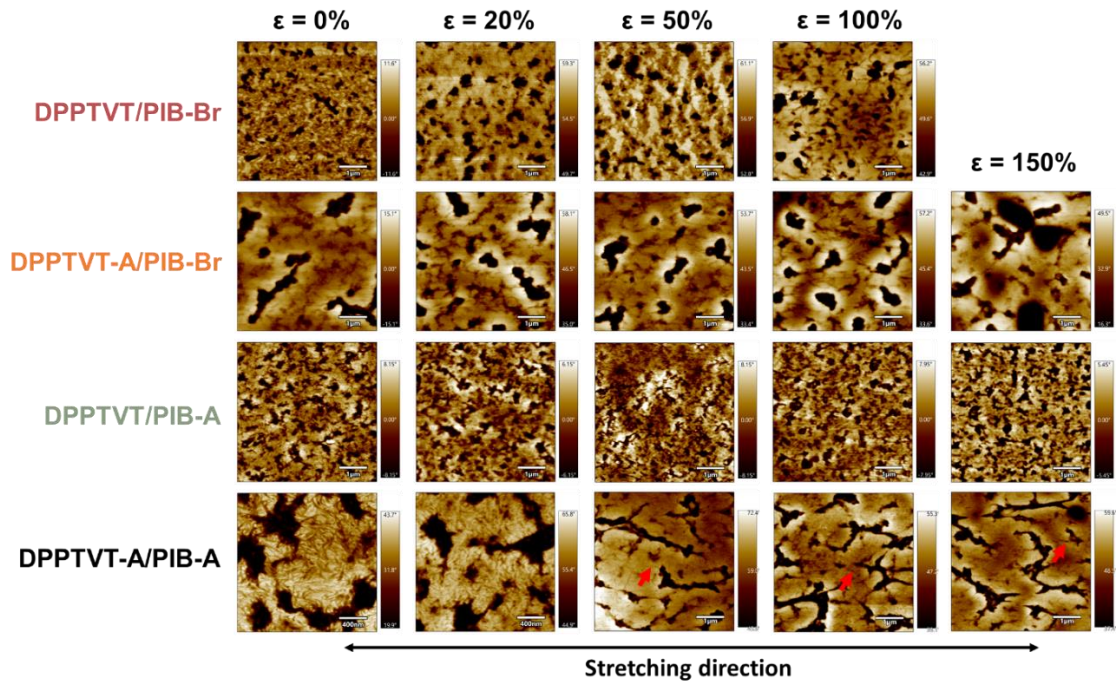


Figure 0.21 AFM phase images of stretched composites.

AFM phase images of stretched DPPTVT/PIB-Br (red), DPPTVT-A/PIB-Br (orange), DPPTVT/PIB-A (green) and DPPTVT-A/PIB-A (black) composites at strain of 0, 20, 50, 100 and 150%. The red arrows point out the fibril aggregates.

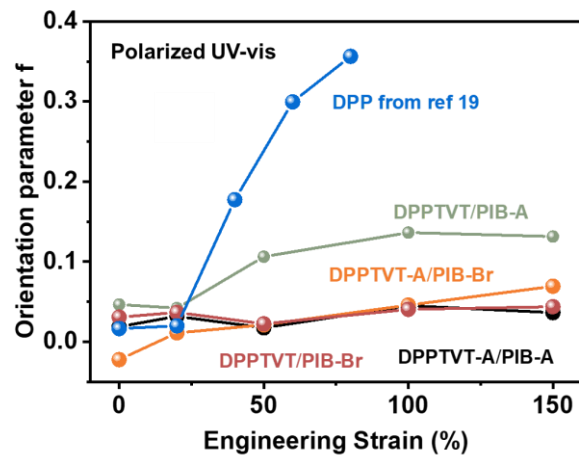


Figure 0.22 Herman's orientation parameter f versus strain based on polarized UV-vis for DPPTVT/PIB-Br, DPPTVT-A/PIB-Br, DPPTVT/PIB-A and DPPTVT-A/PIB-A composite films at 0%, 20%, 50%, 100%, and 150% strain.

The cyclic stretching stability and self-healing ability was evaluated by measuring electrical performance after subjecting the composites to 10 cycles of stretching at strain of 50% and 150%, with subsequent rests of 24 and 48 h (**Figure 3.8, B.14**). Upon subjecting the composites to 10 cycles of stretching at a 50% strain, the charge mobility decreased for DPPTVT/PIB-Br and DPPTVT-A/PIB-Br composites. Conversely, the charge mobility increased for DPPTVT/PIB-A and DPPTVT-A/PIB-A composites, indicating that the introduction of H-bonding crosslinks in the elastomer phase improves device stability during cyclic stretching at a 50% strain. However, after undergoing 10 cycles of stretching at a 150% strain, no consistent trend was observed among the composites. The charge mobility improved for DPPTVT/PIB-Br and DPPTVT/PIB-A composites, decreased for DPPTVT-A/PIB-Br composites, and remained constant for DPPTVT-A/PIB-A composites. This suggests that H-bonding crosslinks may not provide sufficient stability at very high strains (150%) for not chemically crosslinked network. Hysteresis changes after cyclic stretching were evaluated based on the transfer curves (**Figure B.15**). At a 50% strain, the hysteresis decreased after cyclic stretching for DPPTVT/PIB-Br and DPPTVT-A/PIB-Br, while there was almost no change for DPPTVT/PIB-A and DPPTVT-A/PIB-A composites. This further confirms the enhanced device stability when introducing H-bonding crosslinks in the elastomer phase. However, at a 150% strain, all hysteresis values remained unchanged after cyclic stretching, reinforcing that H-bonding crosslinks may not significantly improve stability at higher strains.

To assess the self-healing ability of the composites, charge mobilities of the cyclic stretched composites were measured after 24 and 48 hours. The charge mobility increased for DPPTVT-A/PIB-Br, DPPTVT/PIB-A, and DPPTVT-A/PIB-A composites after both 24 and 48 hours, whereas it remained almost constant for DPPTVT/PIB-Br. This indicates that the introduction of H-bonding crosslinks at either location enhances the self-healing ability, particularly when H-bonding is introduced into the elastomer phase, leading to charge mobility exceeding that of the original stretched state.

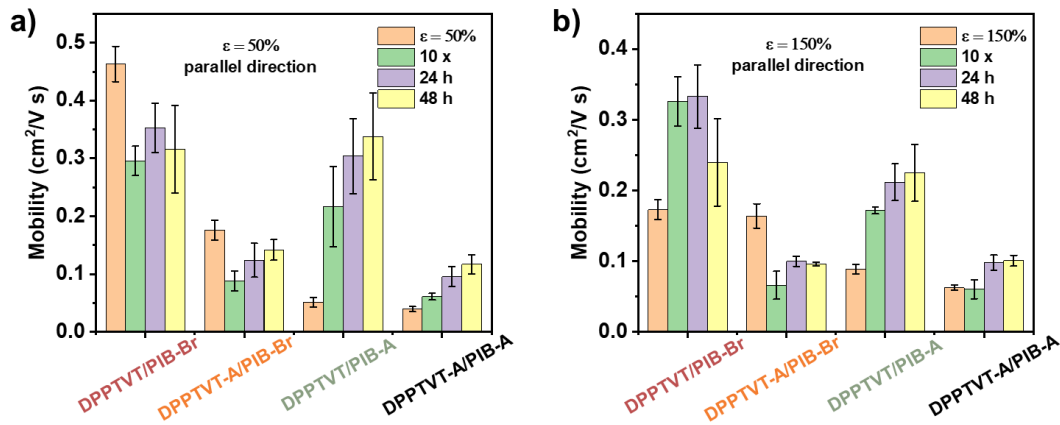


Figure 0.23 Charge mobility comparison along parallel direction of stretched composites after stretching 1 and 10 cycles and staying for 24 and 48 h at strain of 50% and 150%.

Charge mobility comparison along parallel direction of stretched DPPTVT/PIB-Br (red), DPPTVT-A/PIB-Br (orange), DPPTVT/PIB-A (green) and DPPTVT-A/PIB-A (black) composites after stretching 1 and 10 cycles and staying for 24 and 48 h at strain of (a) 50% and (b) 150%.

3.4 Conclusion

In summary, we created amide-functional CP and elastomer, DPPTVT-A and PIB-A, respectively, for formation of H-bonding crosslinks to control morphology of CP/elastomer composites and further influence on mechanical and electrical properties. By blending amide- and non-amide function CP and elastomers, we fabricated four different

CP/elastomer composites including non-H-bonding crosslinked composite, DPPTVT/PIB-Br, uni-H-bonding crosslinked composites, DPPTVT-A/PIB-Br and DPPTVT/PIB-A, and dual H-bonding crosslinked composite, DPPTVT-A/PIB-A. The non-H-bonding composites exhibited predominant fibril aggregates and the highest degree of ordered crystalline structures, resulting in the highest charge mobility. However, these composites exhibited the poorest stretchability, with the lowest COS and decreased mobility upon stretching. Introducing H-bonding crosslinks in CP or elastomer led to the larger and more large-scale aggregates, respectively, resulting in decreased charge mobility. However, the stretchability was improved, and the mobility was maintained after stretching. Most interestingly, the dual-H-bonding crosslinked composite, DPPTVT-A/PIB-A, displayed the lowest charge mobility, which could be attributed to the formation of micro-phase separation and large-scale aggregation without fibril formation. However, upon stretching, the H-bonds broke and the two-phase reorganized into fibril aggregates, leading to an improvement in charge mobility. Importantly, creating H-bonding crosslink into both domains of CP/elastomer composites was found not only improved stretchability, but also maintain the electrical performance when applying high tensile stress. Besides, the H-bonding introduced at elastomer phase also improved the cyclic stretching stability and both locations will improve the self-healing ability. These findings shed light on controlling the morphology of CP/elastomer composites and studying the effects of morphology on mechanical and electrical properties, which provides guidance in future design of stretchable semiconductors.

CHAPTER 4 – HIGHLY DEFORMABLE RIGID GLASSY CONJUGATED POLYMERIC THIN FILMS

(Adapted from “Wang, Y.; Zhang, S.; Freychet G.; Li, Z.; Chen, K.; Liu, C.-T.; Cao, Z.; Chiu, Y.; Xia, W.; Gu, X. Highly deformable rigid glassy conjugated polymeric thin films. *Adv. Funct. Mater.* 2023, 2306576, 1-11.)

4.1 Introduction

Over the past decades, there has been remarkable progress in the development of stretchable semiconductors, which find applications in wearable and implantable devices such as electronic skins, personalized healthcare monitors,^{133,148,210-212} wearable smart displays,^{146,162,213} and energy storage devices.¹³² These wearable devices hold immense potential in the field of health sensors, as they can be directly attached to the human skin, offering convenience and accuracy. For seamless integration with the skin, the materials utilized in these devices must be deformable to accommodate the strains resulting from body motion. Conjugated polymers (CPs) have emerged as preferred materials for wearable devices due to their tunable chemical structures and compliant mechanical properties compared to their inorganic counterparts.^{4-6,39,42,108,119,214,215} However, achieving high charge carrier mobility and high stretchability concurrently presents a challenge, as high charge carrier mobility often necessitates high crystallinity and chain rigidity, which tend to make the materials brittle.

In the pursuit of designing novel stretchable conjugated polymers (CPs), researchers have primarily focused on reducing the materials' elastic modulus, as it is widely believed that softer materials offer higher stretchability.¹⁰ For example, intrinsically

stretchable CPs were synthesized via incorporating conjugation-break spacers^{9,30,56,62,64,66,80,109} or soft moieties^{57,98,99,103,176,177} into the backbone and attaching longer or more flexible side chains.^{33,87,89,90,92} Another effective method involves blending conjugated polymers with soft and deformable elastomers such as PDMS, rubber, or SEBS, resulting in the fabrication of soft CP/elastomer composites.^{110,114,115,117,120–123} These strategies have demonstrated success in achieving stretchability in CPs and have provide solution for the development of innovative materials for various applications.

In a recent work, Zheng *et al.* made a remarkable discovery demonstrating that indacenodithiophene-cobenzothiadiazole (IDTBT), a high modulus (745 MPa) CPs, can be reasonably deformable (crack onset strain (COS) ~22%).⁵⁵ This interesting finding challenges the conventional notion that softness is a prerequisite for achieving deformability in stretchable semiconductive polymers. Similar phenomena have been observed in traditional non-conjugated polymers as well. For instance, polypropylene (PP) with a modulus (E) of 1360 MPa exhibits a COS of around 180% (true strain), while high-density polyethylene (HDPE) with E of 1050 MPa demonstrates a COS of approximately 200% (true strain).²¹⁶ These observations highlight the importance of stretchable rigid polymers for various applications that require robust mechanical properties (e.g. high toughness).²¹⁴ Consequently, it is crucial to consider rigid CPs as viable options for deformable materials, as they could become a pivotal component within the stretchable CP family. Despite their potential, the field of stretchable rigid CPs lacks in-depth studies and comprehensive understanding, warranting further research in this area.

The present study aimed to investigate the stretchability of rigid conjugated polymers (CPs) (e.g. $E > 700$ MPa) in order to explore their molecular origin of high deformability. Mechanical properties of 65 CPs based on different chemical building blocks measured by our group using the “film-on-water” (FOW) characterization technique were organized (chemical structure, molecular weight (MW), elastic modulus (E), and COS are summarized in **Table C.1**). Surprisingly, 11 CPs showed both high stretchability ($> 20\%$) and high elastic modulus (> 700 MPa), indicating that rigid IDTBT is not the sole example of stretchable rigid CPs. Again, this interesting finding challenges the notion that deformability is directly linked to softness. Subsequently, we conducted a thorough analysis of polymers with the same structure but different MWs and film thicknesses. We found both molecular weight and thickness influenced the mechanical properties by modulating the entanglement behavior of CPs.²¹⁷ This led us to deduce that the entanglement effect plays a dominant role in deformability. Furthermore, we systematically investigated the deformation mechanisms and electrical properties of glassy stretchable rigid CPs, focusing on a model polymer, poly(3-butylthiophene-2,5-diyl) (P3BT). This investigation involved multimodal characterization methods, including hard X-ray scattering to probe polymer crystallite, tender X-ray scattering to examine backbone alignment, polarized UV-vis absorption spectroscopy, and coarse-grained molecular dynamics (CG-MD) simulation for analyzing and understanding polymer chain conformation upon deformation. Notably, we observed different deformation mechanisms between glassy P3BT and a viscoelastic P3OT sample, primarily characterized by their initial strains. Only the amorphous domains deform at initial stretching ($< 20\%$) for rigid

stretchable CPs, whereas both amorphous and crystallite domains align for normal viscoelastic CPs. After stretching, the mobility increased for both P3BT and P3OT along the parallel direction to stretching. However, in perpendicular direction, the charge mobility decreased for P3OT at initial strain due to the alignment of crystallite domain whereas kept constant for P3BT. Such differences did not influence the changed mobility of CPs after stretching. Overall, this work provides new insights into the stretchability of rigid CPs, which can serve as valuable guidelines for the design of rigid stretchable organic semiconductors.

4.2 Experimental

4.2.1 Materials and processing

CPs were listed in **Table C.1**. The molecular weight (M_n) and PDI were measured by high-temperature gel permeation chromatography (HT-GPC) using trichlorobenzene as the eluent at 160 °C, polystyrene for calibration viscometer, and light scattering as the detectors. All polymers were dissolved in chlorobenzene with a concentration of 15 mg/ml upon stirring on the hot plate at 80 °C overnight. A commercially available water-soluble poly(sodium 4-styrenesulfonate) (PSS, Sigma-Aldrich) was dissolved in deionized water and coated on the bare silicon wafer with a thickness of 30 nm. Then the solution was spin-coated on the PSS-coated silicon substrate at 800 rpm/s to form a 60 nm thin film. Thermally annealed samples were prepared in the glove box through post-heating as-spun films on the hot plate at 100 and 200 °C for 1 h. The film thickness was measured by AFM using step height between film and substrate.

4.2.2 Tensile deformation of 60nm thin-film sample

The method was detailed in our previous works.¹⁶ The elastic modulus was calculated from the slope of elastic region in stress-strain curve. Crack onset strain (COS) is the strain the thin film began to break.

4.2.3 Morphological characterization

Both hard and tender X-ray scattering experiments were performed at NSLS-II Beamline 12-ID. The energy for hard X-ray was 16.1 keV, while the energy for tender X-ray was scanned from 2.45 keV to 2.5 keV with a spacing of 2 eV. The wide-angle X-ray scattering (WAXS) signal was captured by a Pilatus 300K-W detector, consisting of 0.172 mm square pixels in a 1475 × 195 array, mounted at a fixed distance of 0.275 m from the sample position. To cover the range of scattering angles desired, the vertically oriented elongated detector was moved horizontally on a fixed arc at three angles: 0°, 6.5°, and 13°. The images were later visualized in Xi-CAM software and stitched using custom code.²¹⁸ Two-dimensional (2D) Herman's orientation parameter f was then calculated based on the pole figures to quantify the degree of alignment, given by combining equations (1) and (2):

$$f = 2 \langle \cos^2 \theta \rangle - 1 \quad (1)$$

$$\langle \cos^2 \theta \rangle = \frac{\int_0^{\frac{\pi}{2}} I(\theta) \cos^2 \theta d\theta}{\int_0^{\frac{\pi}{2}} I(\theta) d\theta} \quad (2)$$

where θ is the azimuthal angle, $I(\theta)$ represent the scattering intensity at θ . The equatorial direction was defined as $\theta = 0$, where vertical direction was $\theta = -90^\circ$.

The small-angle X-ray scattering (SAXS) signal was obtained simultaneously with the WAXS data with a Pilatus 1M detector. The sulfur fluorescence yield was extracted

from the high-q intensity from 2D scattering images. The solid-state UV-vis spectra were recorded on Agilent Cary 5000 using polymer thin films using polarized light with an angle of 0° and 90° to strain direction.

4.2.4 OFET fabrication

The organic semiconducting thin films were first prepared on highly doped n-type Si(100) wafers with a 300 nm thick SiO₂ (capacitance per unit area $C_i = 10 \text{ nF cm}^{-2}$) modified with octadecyltrimethoxysilane (OTS) self-assembled monolayer. The polymer solutions (10 mg mL⁻¹) were prepared in chlorobenzene at 80 °C. The solution was dropped onto the OTS-modified Si substrate then spin-coated at 1000 rpm for 1 min. The organic semiconductor thin films were transferred onto PDMS substrates (15:1 base to cross-linker by mass ratio) where the films are stretched to desired strain level. After 5 minutes, the stretched thin films were transferred from PDMS substrates back onto silicon substrates with 300 nm SiO₂ layer. The source and drain electrodes were subsequently deposited as Au (50 nm) through a small-scale shadow mask with the channel length (L) and width (W) were 10 and 200 μm, respectively. All of the electrical characteristics of the stretched polymer thin films were measured with a Keithley 4200 semiconductor parameter analyzer at room temperature under a nitrogen atmosphere.

4.2.5 Overview of CG-MD Simulations

The present work employed a coarse-grained (CG) “bead-spring” model of glass-forming polymer, where the force field of model was expressed as the sum of the bonded and nonbonded interactions. The nonbonded interactions between all types of beads were modeled by the standard 12-6 Lennard-Jones (LJ) potential,

$$U_{LJ}(r) = \begin{cases} 4\varepsilon \left[\left(\frac{\sigma}{r}\right)^{12} - \left(\frac{\sigma}{r}\right)^6 \right], & r < r_c \\ 0, & r \geq r_c \end{cases} \quad (3)$$

where r is the distance between the centers of two beads, ε sets the energy scale of the system and σ refer to the effective diameter of the beads. The potential was truncated at the cutoff distance $r_c = 2.5 \sigma$ to include attractive nonbonded interaction. Note that the parameter ε (*i.e.*, the energy-well depth) controls the strength of the nonbonded interactions between the beads, where $\varepsilon = 1.0$ was chosen for the CG beads of backbones and $\varepsilon = 0.5$ for the CG beads of side-chains, which is consistent with previous studies.³³ In our simulations, all quantities and results were expressed in standard reduced LJ units by the properties of the polymer. Specifically, length, energy, time, pressure and temperature are, respectively, given in the units of σ , ε , τ , ε/σ^3 , and ε/k_B , where $\tau = \sqrt{m\sigma^2/\varepsilon}$ with m being the bead mass and k_B is Boltzmann's constant. The potential energy of bond stretching between neighboring beads was ensured by a stiff harmonic spring potential, $U_{\text{bond}}(r) = k_b(r - r_0)^2$, where $r_0 = 0.99 \sigma$ is the equilibrium bond length, and $k_b = 2500 \varepsilon/\sigma^2$ is the spring constant. Moreover, chain stiffness was controlled by using a three-body angular potential, $U_{\text{angle}}(\theta) = k_\theta(1 + \cos(\theta))$, where angular stiffness constant k_θ was set as 1.0ε to control the stiffness of backbone, $k_\theta = 0.5 \varepsilon$ for the angles between backbone beads and chain branching sites, and $k_\theta = 0.2 \varepsilon$ for the angles in the side-chains, respectively, consistent with the other investigated branched polymer studies.^{219–221} It should be noted that these forcefield parameters were implemented to qualitatively describe the approximate molecular structure informed from the experimentally studied CPs.

Large-scale Atomic/Molecular Massively Parallel Simulator (LAMMPS) simulation package was applied to perform all CG-MD simulations²²² and the visualization of simulation snapshots was performed through the Visual Molecular Dynamics (VMD).²²³ For the simulation of bulk system, all models with different side-chain length where each backbone chain was composed of 20 CG beads were randomly packed into the simulation cell. Periodic boundary conditions were applied in all directions, and a timestep of $\Delta t = 0.005 \tau$ was adopted to integrate the equations of motion for the better saving of computational cost. To equilibrate the system, the energy minimization was firstly performed using the iterative conjugate gradient algorithm; then, the equilibration of the bulk system was continued at the melt state a temperature $T = 2.0 \varepsilon/k_B$. The T was chosen to be sufficiently high so that the polymer melt can be properly equilibrated within the time window. Next, the system was performed under isothermal-isobaric (NPT) ensemble for 1×10^6 timestep where the pressure linearly ramped from the initial 10 to the final $5 \varepsilon/\sigma^3$, and further cooled down to the target temperature under zero pressure via NPT ensemble for 1.8×10^6 timestep before collecting the density to measure the T_g .

To carry out additional free-standing thin film simulations, we took the model with side-chain length of two as a representative polymer model to examine the influence of temperature on the mechanical behavior and chain alignment in thin film system. Specifically, periodic boundary conditions were applied in both x - and y -directions with dimensions of $20 \sigma \times 20 \sigma$, and non-periodic boundary conditions were applied in the z -dimension, allowing two free surfaces on top and bottom. The center of the film was aligned with the x - y plane at $z = 0 \sigma$. Then, a similar equilibrium process has been adopted

for MD simulations under the canonical ensemble (NVT). From the density profile of beads, the effective thickness can be estimated based on the z -coordinate where the number of beads deviates from 0. After the equilibration, the uniaxial tensile test was performed in the x -direction for the thin film polymer system under a constant strain rate of 5×10^{-4} , which lies in the range of values adopted in previous simulation studies.^{33,224} Three models were generated with independent initial configurations for each system to ensure adequate samplings and determine the averaged properties with standard deviation.

4.3 Results and Discussion

We initiated our study by examining the mechanical properties of a wide range of conjugated polymers (CPs) including the rigidity (determined by elastic modulus, E) and deformability (determined by crack onset strain, COS). To accomplish this, we employed a pseudo-free-standing (also known as film-on-water, FOW) tensile test, and the results of 65 CPs, measured by our research group, were organized (**Figure 4.1, C.1-6, Table C.1**).¹⁶ The CP thin films were all spin-cast on PSS-coated Si wafer followed by flowing on water. The elastic modulus E and COS were calculated based on the stress-strain curve of each CP, which are summarized in **Figure 4.1a**. Based on their softness and deformability, we categorized the CPs into four regions: Region I represents brittle rigid CPs, which is similar to ‘brittle plastics’ in polymer science. Region II represents stretchable rigid CPs, similar to ‘hard plastics’. Region III represents brittle soft CPs, similar to ‘tough plastics’. And Region IV represents stretchable soft CPs, similar to ‘elastomers’. The representative stress-strain curves for CPs from each region are shown in **Figure 4.1b**. It is evident that multiple CPs are distributed in each region, suggesting that there is no direct correlation

between the deformability and softness of CPs. Notably, Region II includes 11 rigid CPs that exhibit substantial deformability, thereby challenging the conventional notion that deformability is exclusively associated with softness. This discovery highlights that stretchability can be achieved by rigid CPs, breaking the stereotype that softness is a prerequisite condition for deformability.¹⁰

To understand why rigid CPs can exhibit high deformability, we conducted an analysis of CPs with similar structures but varying thicknesses and molecular weights (MWs). Notably, CPs with the same polymer but different MWs and thicknesses demonstrated distinct deformability. In a previous study by Galuska *et al.*, the mechanical properties of poly(naphthalenedimide) (PNDI)-based CPs with MW ranging from 10 kDa to 144 kDa were investigated, revealing the significant influence of MW on deformability, moving the point from Region III to Region IV (COS ranging from approximately 2% to over 400%).⁴⁷ We observed similar outcomes in our research. For example, DPPTC2C10C12 with a high MW of 60.6 kDa exhibited a COS approximately 16 times higher than that of the 19.0 kDa counterpart, also moving the point from Region III to Region IV (**Figure C.2, Table C.1**). Besides, Zhang *et al.* measured the mechanical property of P3HT with thickness of 20~95 nm.²⁰ The COS increased firstly with increasing thickness and then decreased for films thicker than 80 nm. The decreased COS in thin films was attributed to the reduced interchain entanglements in this film, whereas the decreased COS of thicker film was attributed to the presence of more defects which can initiate and propagate the cracks. Both MW and thickness have an effect on the entanglement of CP chains.²¹⁷ Based on these observations, we deduced that chain entanglement is a critical

factor governing the deformability of CPs, which is consistent with previous reports by the Lipomi group and the Lim Group.^{50,225} Rigid CPs with higher chain entanglement can still exhibit deformability.

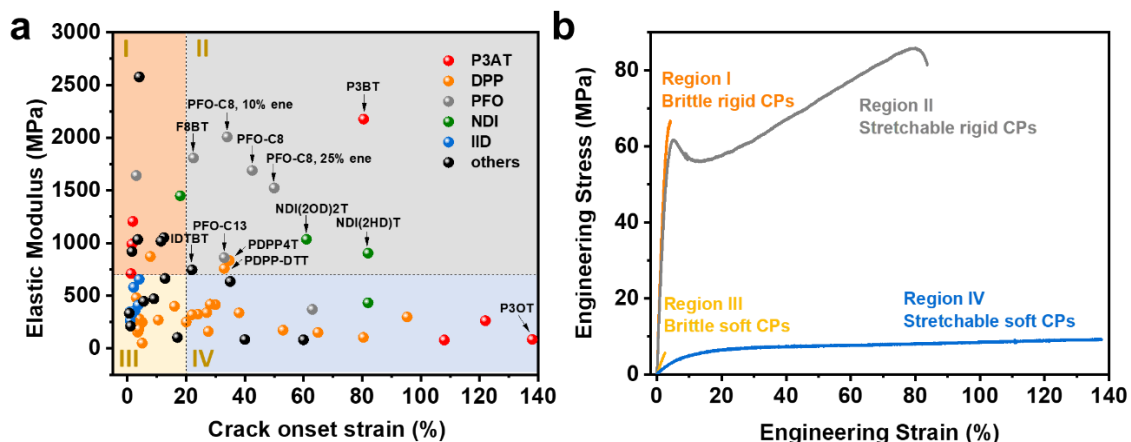


Figure 0.24 Mechanical properties of 65 samples were tested here.

(a) Summarized E and COS of a library of CPs surveyed in this work. Region I: Rigid and brittle CPs with high E and low COS.

Region II: Rigid and deformable CPs with high E and high COS. Region III: Soft and brittle CPs with low E and low COS.

Region IV: Soft and deformable CPs with low E and high COS. (b) Representative stress-strain curve for polymer from each region.

Representative material for Region I: PCPDTBT (MW: 17.8 kDa, thickness: 76 nm), Region II: P3BT (MW: 50-70 kDa, thickness: 46 nm), Region III: DPPTTC2C10C12 (MW: 29.0 kDa, thickness: 82 nm), Region IV: P3OT (MW: 70-90 kDa, thickness: 53 nm).

We proceeded to investigate the mechanical behavior, the influence of rigidity on electrical properties, and the deformation mechanism of deformable rigid CPs using a representative pair of model CPs: a glassy rigid P3BT and a viscoelastic soft P3OT (**Figure 4.2a**). These model CPs share a similar structure, molecular weight and thickness, differing only in their side-chain lengths. The rigidity of P3BT stems from its restricted chain mobility, attributed to its glassy state at room temperature ($T_g = 52\text{ }^\circ\text{C}$) (**Figure C.7, Table C.2**). In contrast, the lower elastic modulus (E) of P3OT is a consequence of its lower T_g ($-13\text{ }^\circ\text{C}$), achieved through the incorporation of longer alkyl side chains (**Figure C.7, Table C.2**).

The mechanical behavior of P3BT and P3OT was first studied. True stress-true strain ($\sigma_T - \varepsilon_T$) curve was used to describe the mechanical properties. True strain takes into account the instantaneous and local changes in the material's dimensions as it deforms.²²⁶ It provides a more accurate measure of strain when the material undergoes plastic deformation. True stress was calculated using the equation $\sigma_T = \sigma(1 + \varepsilon)$, where σ is the engineering stress, ε is the engineering strain. True strain was calculated using the equation, $\varepsilon_T = \ln(1 + \varepsilon)$. The true stress-true strain ($\sigma_T - \varepsilon_T$) curves for both CPs were shown in **Figure 4.2b**. P3BT showed a significantly higher E of 2216 MPa compared to P3OT (86 MPa) due to the limited chain mobility in its glassy state.²²⁷ Despite the approximately 30-fold difference in E, both CPs displayed high crack onset strains (COS) of approximately $\varepsilon_T \sim 60-80\%$. However, distinct mechanical behaviors were observed between P3BT and P3OT. Four regions were observed for P3BT from the $\sigma_T - \varepsilon_T$ curve, including a linear elastic region ($\varepsilon_T = 0 - 3\%$), a well-defined mechanical yielding ($\varepsilon_T = 5\%$), a strain-softening ($\varepsilon_T = 5 - 9\%$) and strain hardening region ($\varepsilon_T > 9\%$), which were similar to the previous report.²²⁸ In contrast, P3OT lacked a clear yielding point and strain-softening region. Traditional semicrystalline polymers with high degree of crystallinity, such as polyethylene (PE), typically exhibit yielding and strain-softening mechanisms associated with crystallographic deformations and necking.^{216,229} However, P3BT did not show necking behavior. The yielding and strain-softening observed in P3BT originated from amorphous chain deformations, as supported by the subsequent morphology study, distinguishing it from PE. Strain-hardening is typical for CPs. Previous finding from our group demonstrated that the slope of the strain-hardening region decreases with increasing

side-chain length, which is consistent with the behavior observed in P3BT and P3OT.³³

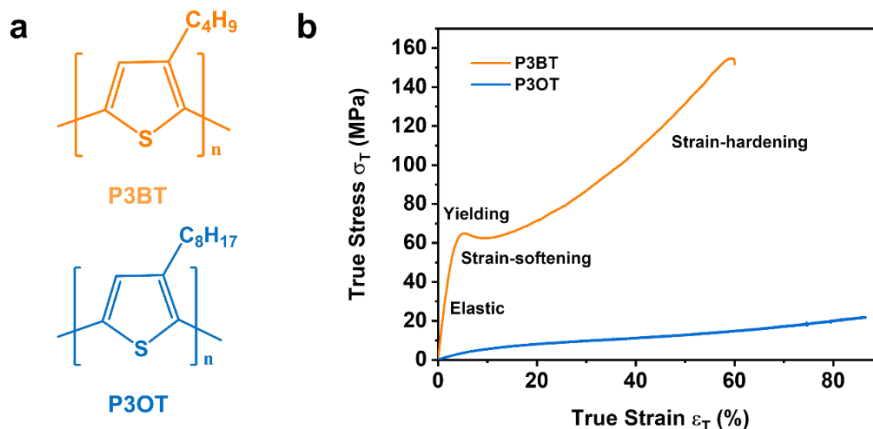


Figure 0.25 Molecular structure and true stress-strain curves for P3BT and P3OT thin films.

(a) Molecular structure and (b) true stress-strain curves for P3BT and P3OT thin films. Note the distinct mechanical response from glassy P3BT and viscoelastic P3OT systems.

The effect of glassiness on the electrical properties of strain-aligned CPs is then studied by fabricating top-contact bottom-gate OFET. To highlight the local alignment and charge transport anisotropy, we utilized a small channel length of 10 μm , a method previously employed to measure the anisotropy of charge mobility for P3AT CPs.²³⁰ Results are summarized in **Figure 4.3, Table 4.1 and C.3-4**. Transfer curves are shown in **Figure C.8-11**. We measured the charge mobility along both the parallel and perpendicular directions to the stretching, aiming to study the anisotropy in charge carrier mobility under deformation. Along the direction parallel to the strain, the charge mobility for both P3BT and P3OT remained relatively constant within the elastic region, as only the amorphous components were aligned. Subsequently, a significant increase in charge mobility was observed due to the alignment of the crystallite domains. Conversely, along the perpendicular direction, the charge mobility decreased for P3OT, similar to the previously

reported behavior for P3HT,²³¹ but remained nearly constant for P3BT. This discrepancy can be attributed to the frozen nature of the chains in P3BT, which hinders their alignment. Moreover, the charge transport along the polymer main chain exhibited significantly better performance compared to the π - π intermolecular transport. The intricate mechanism behind chain alignment will be further investigated in subsequent section. The changes in charge transport did not exhibit significant differences between rigid and soft stretchable CPs, highlighting the substantial potential of rigid stretchable CPs for future applications. The threshold voltage was found to be overall similar for both P3BT and P3OT. However, the on/off ratio of P3BT was observed to be lower compared to P3OT. This difference can be attributed to the higher homo energy level of P3BT, which makes it more sensitive to the doping effect caused by oxygen/water.^{232–234}

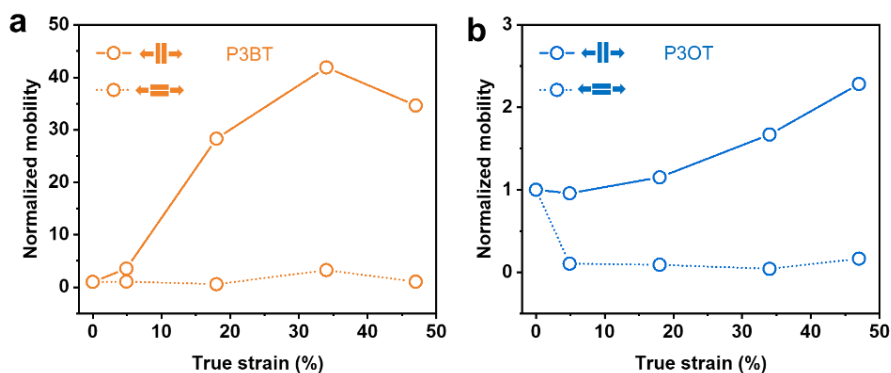


Figure 0.26 Normalized transistor mobility of stretched P3BT and P3OT at different degree of strain.

Normalized transistor mobility of stretched a) P3BT and b) P3OT at different degree of strain. The value of the charge carrier mobility is listed in Table 1, obtained from a organic thin film transistor setup.

Table 0.3 Summary of the OFETs performance of stretched P3BT and P3OT thin films.

ε_T (%) ^a	P3BT			P3OT		
	μ_{ave}^b ($\text{cm}^2 \text{V}^{-1} \text{S}^{-1}$) 1)	I_{on}/I_{off}	V_{th}	μ_{ave} ($\text{cm}^2 \text{V}^{-1} \text{S}^{-1}$)	I_{on}/I_{off}	V_{th}
0	9.5×10^{-6}	1.6×10^1	7.9	3.5×10^{-3}	6.8×10^3	-10.6
5	3.4×10^{-5}	1.3×10^2	-24.5	3.4×10^{-3}	2.6×10^3	-14.7
5 ⊥	1.8×10^{-5}	3.1×10^2	-14.9	6.7×10^{-4}	4.1×10^2	-7.8
18	2.7×10^{-4}	6.8×10^2	-15.8	4.0×10^{-3}	6.2×10^3	-12.2
18 ⊥	7.9×10^{-6}	3.8×10^1	-25.1	4.5×10^{-4}	3.8×10^2	-4.9
34	4.0×10^{-4}	1.2×10^2	-12.5	5.9×10^{-3}	6.2×10^3	-11.3
34 ⊥	7.4×10^{-5}	3.2×10^2	-17.4	3.3×10^{-4}	5.8×10^2	2.7
47	3.3×10^{-4}	1.3×10^2	-10.0	8.0×10^{-3}	5.5×10^3	-10.0
47 ⊥	1.3×10^{-5}	1.7×10^1	3.8	3.2×10^{-4}	1.6×10^2	-3.4

^aThe applied strains and channel directions parallel (||) and perpendicular (⊥) to the applied strains. ^bThe calculated electron mobility of the devices averaged from 5 devices within three batches.

The deformation mechanism difference between glassy P3BT and viscoelastic P3OT was then investigated using a comprehensive set of characterization methods to fully understand the device performance. The detailed procedure for sample preparation can be found in the Supporting Information. In summary, thin films of stretched CPs with a

thickness of approximately 60 nm were subjected to stretching using a pseudo-free-standing tensile tester. Subsequently, these strained free-standing films were transferred onto a washer's frame to facilitate further characterization (**Figure C.12a**).

Wide-angle hard X-ray scattering (WAXS) was conducted to investigate the alignment of crystallite domains.²³⁵ The measurements were performed in transmission geometry, with the X-ray beam perpendicular to the sample plane. The samples were mounted in a manner that aligned the stretching direction horizontally with the polarization direction of the beam (**Figure C.12b**). As a result, the equatorial and meridian directions corresponded to the parallel and perpendicular directions to the stretching axis, respectively. Detailed information about the characterization methods can be found in the Supporting Information. The 2D scattering patterns of the samples under different strain conditions are shown in **Figure 4.4a-b**, accompanied by the corresponding 1D scattering profiles and pole figures shown in **Figure C.13-14**. The results were processed using Python code according to a previous literature report.²¹⁸ Key parameters including peak position (q), full width at half maximum (FWHM), and coherence length (τ) extracted from the WAXS measurements were summarized in **Table 4.2**. Three representative peaks can be observed on the 2D patterns as illustrated on **Figure 4.4a**: the lamellae packing peak (100), the π - π stacking peak (010) and an amorphous halo. P3BT showed a smaller lamellar packing distance (13.4 Å) compared to P3OT (20.9 Å) due to its shorter side chain. Upon stretching, the peak position of the (100) peak for both polymers showed only a slight change, indicating an unchanged packing distance. For P3BT, the (100) peak started to exhibit anisotropy at $\varepsilon_T = 34\%$, signifying the initiation of crystallite orientation/rotation.

Concurrently, the coherence length along the equatorial direction experienced a significant decrease from $\varepsilon_T = 34\%$, indicating the deformation of crystallite domain parallel to the strain direction. In contrast, for P3OT, the (100) peak began to exhibit anisotropy at an earlier strain of $\varepsilon_T = 18\%$, while the coherence length started to decrease from $\varepsilon_T = 47\%$, suggesting the initiation of crystallite rotation at the smaller strain but large deformation occurring at $\varepsilon_T = 47\%$.

Two-dimensional (2D) Herman's orientation parameter f for the (100) peak was then calculated based on the pole figures (**Figure C.14**) to quantify the degree of alignment, following the method described in a previous report (**Figure C.4b**).³³ The values of f for P3BT and P3OT started to increase at $\varepsilon_T = 34\%$ and $\varepsilon_T = 18\%$, respectively, which aligned well with the observations from the 2D images shown in. At $\varepsilon_T = 0.47$, f increased by 0.23 for P3BT but 0.34 for P3OT. The larger increase in f for P3OT indicates a higher degree of alignment of the crystalline domain, attributed to the greater chain flexibility of viscoelastic polymer. Small-angle hard X-ray scattering (SAXS) was also performed to investigate the crystallite distance (**Figure C.15**). However, no peak was observed, probably due to a low degree of crystallinity. As a result, the spacing between crystals falls outside the q range probed by the measurement, similar to previous observations for DPP-based donor-acceptor polymers.³³ The alignment of the π - π stacking peak and the amorphous halo is discussed in **Figure C.16**. Based on the findings from hard X-ray scattering, we can conclude that there is no crystallite domain alignment for P3BT at initial strain, whereas crystalline rotation contributes to the strain at first and crystallite deformation join after $\varepsilon_T = 47\%$ for P3OT. Additionally, we performed *in-situ* hard

WAXS to stretch CP films under the same beamline (**Figure C.17-20**). The peak position almost kept constant upon stretching, indicating the film relaxation did not influence the study of the deformation mechanism (**Figure C.18e, f**). However, FWHM didn't change at strain of 50% either, which was different from the *ex situ* experiment. We attributed this difference to the variation in the thickness of the materials, which was thin-film for *ex situ* experiment and bulk for *in situ* experiment. The crystallite structure under thin-film state was easier to break due to less entanglement.

Tender WAXS was conducted using an X-ray energy near the sulfur K-edge (~2.47 keV) to specifically detect the backbone orientation in the crystalline regions of the CPs.³³⁻³⁶ The backbones of CPs are crucial for charge transport due to the conjugated structure. Given the inherent difference in rigidity between backbone and sidechain of CPs, we hypothesize that there may be distinct alignment behaviors between backbone and the entire polymer chains. As the energy was scanned across the sulfur K-edge (2.46 keV - 2.5 keV), scattering patterns were recorded. The background intensity variation at different energies, shown in **Figure C.21**, originates from the fluorescence of sulfur atoms. The fluorescence signal exhibits a plateau below 2.47 keV and a sharp increase for both polymers at 2.476 keV. The maximum of the fluorescence signal was reached at 2.478 keV, which is usually close to the energy where the sulfur atoms contribute optimally to the scattering signal. Characteristic 2D scattering patterns and corresponding 1D plots along equatorial and meridian directions under an X-ray energy of 2.478 keV are shown in **Figure 4.4c and C.22-26**. Due to the restricted high q range accessible with tender X-ray, only the (100) peak could be easily measured in this work. The fluorescence of sulfur was

too strong as the background at the sulfur K-edge (~2478 eV), which hindered the lamellar peak. Consistent with the findings from hard X-ray scattering, P3BT exhibited higher q values and a shorter packing distance compared to P3OT, attributable to its shorter side chains. Similar to the hard X-ray analysis, Herman's orientation parameter f at five energies from 2.470 to 2.478 keV was obtained from pole figures (**Figure C.25-26**) of both polymers, as summarized in **Figure 4.4d and C.27**. The f value obtained at 2.470 keV, away from the edge, closely matched the value extracted from the hard X-ray scattering experiments, as no resonant effect was present. From 2.470 to 2.474 keV, the f value gradually decreased. At 2.478 keV, the backbone orientation signal predominated. For P3BT, f remained almost unchanged upon stretching, suggesting the absence of backbone orientation in the crystallites. Conversely, for P3OT, a slight increase in f indicated less pronounced chain slippage behavior, consistent with our previous findings for low- T_g DPP-based CPs.³³ Consequently, while noticeable backbone alignment in the crystalline regions was observed in viscoelastic CPs, it was limited in glassy CPs. For both P3BT and P3OT, f s from tender X-ray scattering are much lower than those from hard X-ray scattering, indicating the backbone orientation is smaller than whole chain orientation due to the limited mobility of conjugated structures.

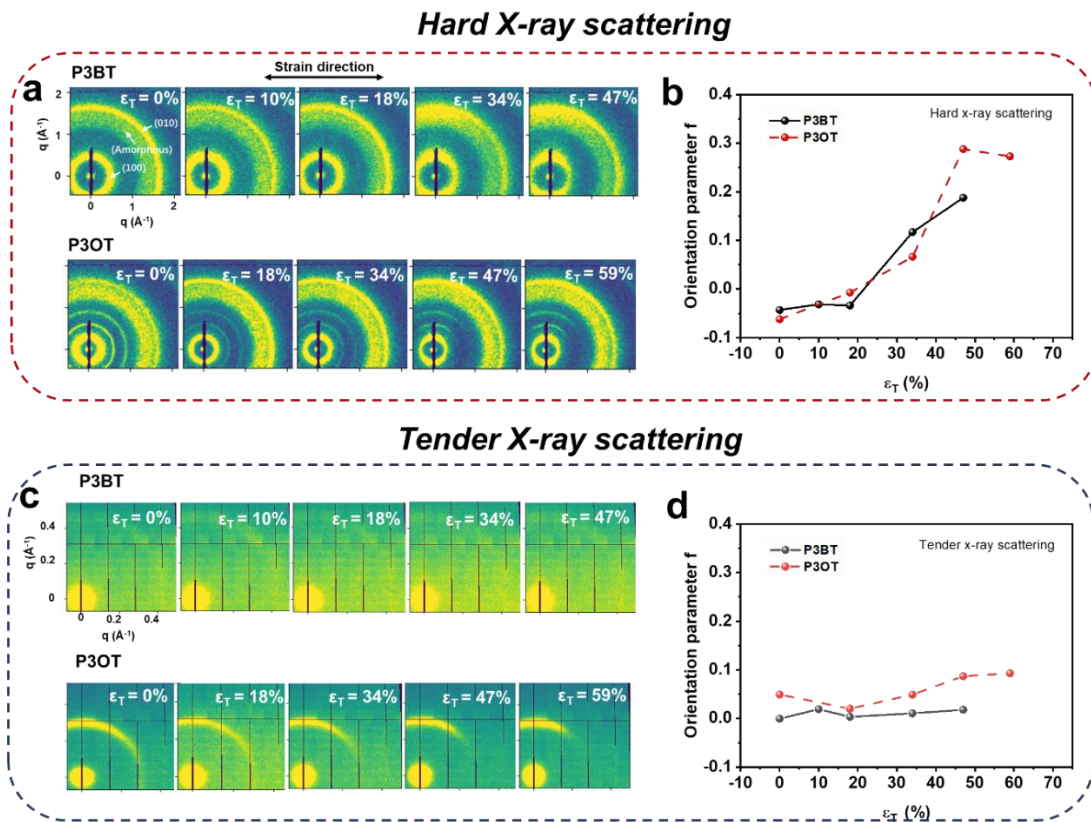


Figure 0.27 Experimental result for hard/tender WAXS experiment on P3BT and P3OT polymer thin films under various true strain.

Representative 2D scattering patterns and characteristic crystallographic peaks of P3BT and P3OT from (a) hard and (c) tender WAXS. Herman's orientation parameter f versus strain based on (100) peak of P3BT and P3OT from (b) hard and (d) tender WAXS.

Table 0.4 *Crystallographic Information for P3BT and P3OT extracted from wide-angle hard X-ray scattering.*

	ϵ_T	Equatorial direction				Meridian direction			
		(100)			(010)	(100)			(010)
		<i>(100)</i> <i>peak</i> <i>q</i> (\AA^{-1})	FWHM (\AA^{-1})	τ (\AA)	<i>(010)</i> <i>peak q</i> (\AA^{-1})	<i>(100)</i> <i>peak</i> <i>q</i> (\AA^{-1})	FWHM (\AA^{-1})	τ (\AA)	<i>(010)</i> <i>peak q</i> (\AA^{-1})
P 3 B T	0	0.47	0.10	7.7	1.65	0.47	0.10	7.98	1.64
	10%	0.47	0.10	7.3	1.65	0.47	0.10	7.93	1.65
	18%	0.47	0.11	7.1	1.64	0.47	0.11	7.27	1.62
	34%	0.49	0.25	3.2	1.67	0.47	0.10	7.48	1.63
	47%	0.48	0.23	3.5	1.66	0.47	0.12	6.49	1.65
P 3 O T	0	0.30	0.04	17.1	1.66	0.30	0.04	17.3	1.65
	18%	0.30	0.04	17.4	1.63	0.30	0.04	17.3	1.64
	34%	0.30	0.04	17.2	1.64	0.30	0.04	17.3	1.64
	47%	0.30	0.07	10.8	1.65	0.30	0.04	17.3	1.64
	59%	0.30	0.06	12.6	1.65	0.30	0.04	17.3	1.63

*The coherence length τ is calculated by the Scherrer equation: $\tau = (K \cdot \lambda) / (\beta \cdot \cos\theta)$, where $K = 0.9$, $\lambda = 0.77 \text{ \AA}$ for X-ray energy of 16.1 keV, β is the FWHM, θ is the Bragg angle.

Polarized UV-vis was used to study the overall polymer backbone alignment combining crystallite region and amorphous chain. This technique enables the examination

of the combined alignment of the crystalline regions and amorphous chains when the transition dipole moment (π - π^*) is parallel to the long axis of the polymer backbone.²³⁶ The normalized absorption spectrum of strained P3BT and P3OT thin films under strain were plotted in **Figure 4.5a, b**, respectively. The 0 \rightarrow 0 and 0 \rightarrow 1 transition occurred at ~591 nm and ~499 nm, respectively. 0-0 absorption peak was favorable along the strain direction, attributed to polymer long axis alignment.²³¹ To quantify the anisotropy, the dichroic ratio, R , was calculated using the following equation:

$$R = \frac{A_{\parallel}}{A_{\perp}} \quad (1)$$

where A_{\parallel} and A_{\perp} is the 0-0 peak absorbance of the film with polarized light parallel and perpendicular to the strain direction, respectively. Then, Herman's orientation parameter f can be determined:

$$f = \frac{R-1}{R+1} \quad (2)$$

Surprisingly, the Herman's orientation parameter, f , exhibited similar behavior for both P3BT and P3OT, suggesting that the glass transition temperature (T_g) did not significantly affect the alignment of the entire polymer chain during stretching (**Figure 4.5c**). Notably, f showed a gradual increase throughout the stretching process, albeit with a limited extent. This trend aligns with our previous findings in DPP-based polymers,³³ indicating that polymer chain alignment occurs throughout the deformation process but with relatively low anisotropy. In the case of P3BT, where crystallite alignment was initially limited, the alignment of the amorphous chains played a significant role in the initial deformation ($\epsilon_T < 0.18$). On the other hand, P3OT exhibited a distinction between crystallite and overall chain alignment, suggesting that both crystalline and amorphous regions contributed to the

deformation process. Therefore, the limitation in alignment was primarily observed in the crystallite domain for glassy CPs. Additionally, we also investigated polarized UV-vis spectroscopy for samples supported by PDMS, and the results are presented in **Figure C.28**. For more details, please refer to the Supporting Information.

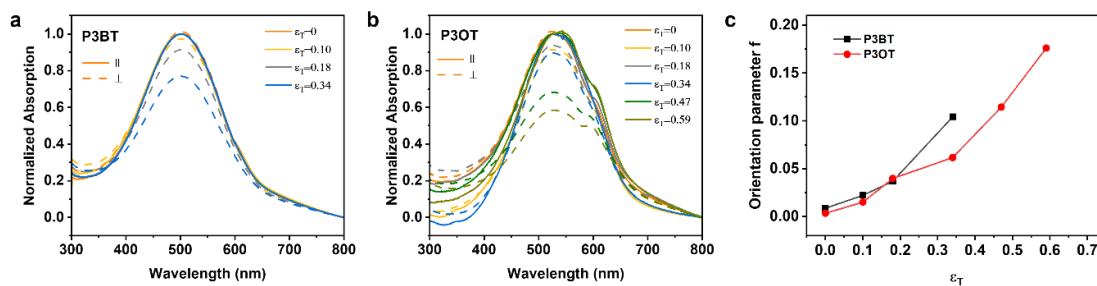


Figure 0.28 *Whole chain alignment study from polarized UV-vis spectroscopy.*

UV-vis absorption plot at different wavelengths for (a) P3BT and (b) P3OT under various strains. (c) Herman's orientation parameter f under strain.

In addition to the experimental investigations, we utilized coarse-grained molecular dynamics (CG-MD) simulation to gain further insights into the impact of measurement temperature on the mechanical behaviors and chain alignment upon thin-film deformation (**Figure 4.6, C.29-32**). Our CG model utilized a "bead-spring" representation of the polymer, incorporating a branched chain structure to capture the essential structural characteristics of CPs. Specifically, the CG model consisted of a linear backbone chain (represented by pink beads), with each backbone bead connected to an alkyl side chain (represented by blue beads) to simulate the alkyl groups (**Figure 4.6a**). **Figure 4.6b** showed a snapshot of free-standing thin film simulations using the CG model. The effect of side-chain length on thermomechanical behavior was first simulated, which was discussed in detail in Supporting Information. The result agreed reasonably well with experimental data. The orientation of polymer chains was evaluated by calculating the

orientation parameter f of the thin film system^{33,237}:

$$f = \langle \frac{3}{2} \cos^2 \theta - \frac{1}{2} \rangle \quad (3)$$

where θ is the angle formed by the bond vector connecting two consecutive backbone CG beads relative to the deformation direction, and the bracket denotes the ensemble average over all bond vectors (**Figure 4.6c**). Furthermore, we calculated the end-to-end distance of the polymer backbone to gain a deeper understanding of the chain orientation. **Figure 4.6d** showed clear evidence that, as the tensile strain increased, the polymer chains exhibited a greater tendency to align along the deformation axis, resulting in a higher orientation parameter, accompanied by the increase in the end-to-end distance of the polymer chains. To explore the local orientation distribution, we further generalized equation (3) to evaluate the local orientation parameter based on individual bond vector in the thin film system. The probability distributions of local orientation parameter upon deformation for different T were presented in **Figure C.31a**. In all cases, a Gaussian-like distribution was observed, with the peak gradually decreasing and shifting towards higher values, indicating a propensity for backbone orientation in the direction of strain. A similar trend was observed for the end-to-end distance distribution, as shown in **Figure C.31c**. It is worth noting that both f value and end-to-end distance at each strain were nearly independent of temperature (**Figure C.30, 31b, d**), which was also consistent with the above experimental observation that the T_g of CPs did not show direct influence on the chain alignment under strain. This observation aligns with the experimental finding, indicating that the T_g of CPs does not directly influence chain alignment under strain.

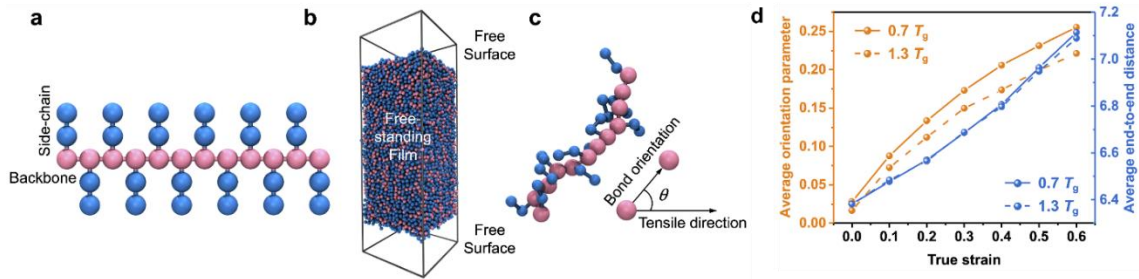


Figure 0.29 *Amorphous component alignment study from CG-MD simulation.*

(a) Schematic illustration of CG polymer model with branched side-chain. (b) Snapshot of the CG free-standing thin film. (c) Schematic of a single polymer chain with a defined angle between the bond orientation and tensile direction. (d) Average orientation parameter (left-y axis) and end-to-end distance (right-y axis) vs. strain for two representative T .

By combining the findings from both experiments and simulations, we can elucidate the deformation mechanisms of glassy P3BT and viscoelastic P3OT. In the case of glassy P3BT, during the initial stage of deformation ($\epsilon_T < 0.18$), only the orientation of the amorphous chains contributed to the overall deformation process. Subsequently, the crystalline domains experienced breaking, rotation, and alignment, as evidenced by the decreased coherent length and increased orientation parameter (f) values for the lamellar stacking peak, π - π stacking peak, and amorphous halo. The amorphous domain within P3BT serves as tie chains (bridging chains) between crystallite domains. It's reported that high content of tie chains in amorphous domain plays a crucial role in facilitating the charge transport due to the difficulty of charge transport between ordered regions.²³⁸ Therefore, with amorphous domains alignment within $\epsilon_T < 0.18$, the charge mobility increased. Upon further stretching, the crystallite domain begins to align resulting in higher charge mobility. In contrast, for the viscoelastic polymer P3OT, both the alignment of lamellar structures and the amorphous chains played significant roles throughout the entire deformation strains. The alignment of crystals is known to facilitate charge transport along the direction

parallel to the stretching direction, whereas crystal deformation can sometimes have a negative impact on charge mobility.²³¹ In the case of P3OT, both crystal alignment and crystal deformation occur. Interestingly, the charge mobility continues to increase in parallel direction but decreases in perpendicular direction indicating crystal alignment somehow overcompensate for the crystal disruption in P3OT. In a previous study, Salleo Group found that short-range intermolecular aggregation is sufficient for charge transport.³² Based on this understanding, we deduce that the deformed crystals are still large enough to support charge transport. This behavior is consistent with what has been observed in viscoelastic DPP-based polymers previously studied.³³

To verify the universality of our observations, we selected F8BT as another deformable glassy CP with a high T_g of 111.6 °C (**Figure 4.7a**). The stress-strain behavior of F8BT is shown in **Figure 4.7b**, with a critical strain (COS) of approximately 20% and a similar high elastic modulus of 1807 MPa compared to P3BT. Same morphology characterization methods were used for F8BT. However, unlike P3BT, F8BT did not show the 0-0 aggregation peak at 540 nm in UV-vis spectra as reported.²³⁹ Therefore, we focused on evaluating the chain alignment mechanism of F8BT using wide-angle hard/tender X-ray scattering. The results were shown in **Figure 4.7c, C.33-39, Table C.5**. We found the thin film broke without any crystallite alignment and deformation for F8BT, resembling the initial deformation region observed in P3BT. The earlier breakage in F8BT may be attributed to the difficulty in aligning the crystalline region, primarily influenced by intra/inter-crystallite interaction strength and a reduction in the number of entanglements/tie-chains. It is important to note that if there is a sufficient amorphous

domain allowing for the rotation of crystallite domains, rigid CPs can exhibit stretchability. However, if the amorphous domain is insufficient, the CPs tend to be brittle.

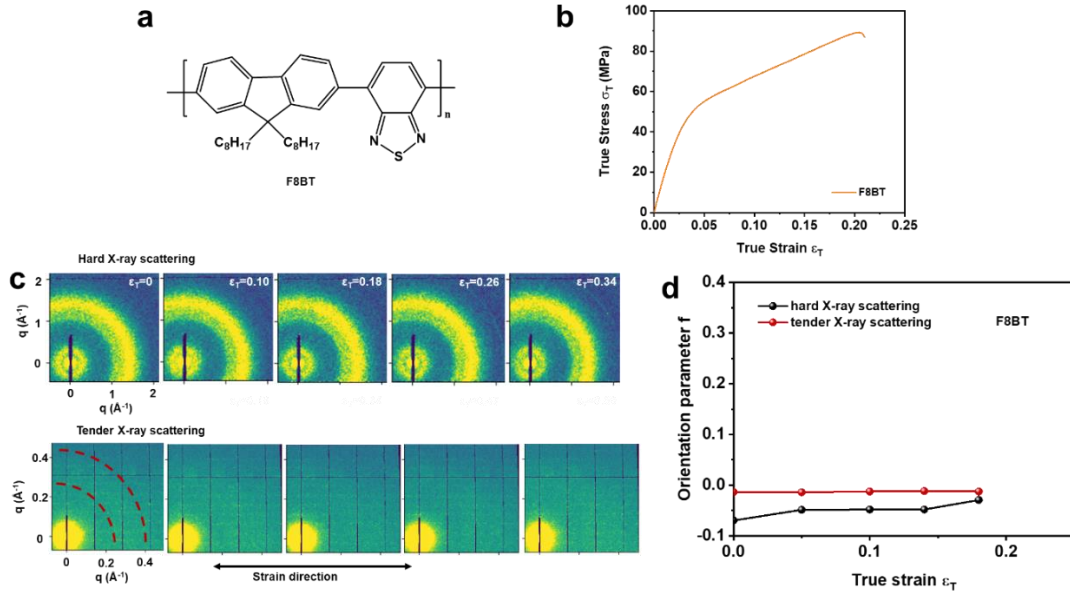


Figure 0.30 *Molecular structure, true stress-strain curves, representative 2D scattering patterns and Herman's orientation parameter f versus strain based on (100) peak from hard and tender WAXS and of F8BT.*

(a) Molecular structure for high- T_g F8BT. (b) True stress-strain curves for F8BT. (c) Representative 2D scattering patterns and characteristic crystallographic peaks of F8BT from hard and tender WAXS. (d) Herman's orientation parameter f versus strain based on (100) peak of F8BT from hard and tender WAXS.

4.4 Conclusion

Our study focused on the mechanical performance of 65 different CPs with the aim of assessing their suitability for stretchable electronics applications. Contrary to common assumptions, we discovered that the rigidity of a CP does not necessarily determine its deformability. In fact, our results suggest that even rigid, glassy CPs exhibit promising characteristics for stretchable electronics. To gain deeper insights into the mechanical behavior, electrical properties, and chain alignment mechanisms of these unique glassy CPs, we conducted a comprehensive analysis focused on a model CP called P3BT, as well

as its viscoelastic counterpart, P3OT. Our investigation revealed an intriguing feature in P3BT, namely an additional yielding and strain-softening region compared to P3OT. Remarkably, this difference did not significantly impact the charge mobility of the stretched CPs. By employing a combination of wide-angle hard/tender X-ray scattering, polarized UV-vis, and CG-MD simulation techniques, we scrutinized the chain alignment mechanism of these CPs. The results uncovered a key disparity between P3BT and P3OT, primarily in their initial strain behavior. In the case of P3BT, the deformation was predominantly facilitated by the slipping of amorphous domains, attributed to its frozen chain nature at room temperature, for the first 18% strain. In contrast, both amorphous chain and crystallite rotation played a role in the deformation of P3OT. Overall, our study provides a comprehensive understanding of the stretchability of glassy CPs and challenges the conventional notion that only flexible CPs are suitable for wearable electronics. These findings underscore the great potential of even rigid CPs in the realm of wearable electronics and offer valuable insights for the design and development of future stretchable electronic devices.

FUTURE DIRECTIONS

In summary, this dissertation has pioneered the development of stretchable and self-healable semiconducting polymers and composites, and has provided an in-depth examination of their deformation mechanisms. These foundational studies represent a significant step toward unlocking the potential of stretchable and self-healable semiconducting materials. However, the journey of discovery and innovation in this field is just beginning, with several avenues open for further exploration:

Elastic Semiconducting Composites Design: Despite the advancements made, the design of elastic semiconducting composites that can sustain repeated use due to their intrinsic elasticity remains a vital area for further research. This necessitates the exploration of covalently crosslinked semiconducting composites that retain both high stretchability and self-healing capabilities.

Morphology Dynamics During Processing: The transition of morphology from solution-state to solid-state during spin-coating processes warrants further investigation. The inherently weak and dynamic nature of hydrogen bonds, coupled with the high-speed conditions of spin-coating, poses challenges to the stability and morphological formation of the composites. A deeper understanding of thin film morphology dynamics during spin-coating and the influence of polymer solution and spin-coating parameters is essential for optimizing these materials for practical applications.

Thermal Annealing Effects: Thermal annealing serves as a critical processing technique that can potentially enhance the alignment of conjugated polymer (CP) chains and subsequently improve electrical properties. Investigating the effects of thermal

annealing on both the newly developed composites and rigid stretchable CPs is imperative for enhancing their performance and expanding their application scope.

These future directions underscore the ongoing need for innovative design strategies, advanced processing techniques, and comprehensive characterization to fully harness the capabilities of stretchable and self-healable semiconducting materials. As we continue to explore these pathways, the potential for groundbreaking applications in wearable and implantable electronics grows ever more promising.

APPENDIX A – Supporting Information

Synthesis and properties of amide-polyisobutylene (PIB-Amide). PIB-amide was synthesized via three steps including acid-catalyzed constructive degradation (CD) reaction of BR to introduce bromine group (PIB-Br), Gabriel reaction to transfer bromine to amine groups (PIB-amine) and esterification reaction to obtain amide functional PIB (PIB-amide) (Scheme A.1). PIB-Amide was the hydrogen bonding crosslinked elastomer. The precursor, PIB-Br, was the comparative reference.

Synthesis of PIB-Br. PIB-Br was first synthesized via constructive degradation reaction of butyl rubber according to previous report.²⁴⁰ Butyl rubber (5 g, 0.026 mmol) was dissolved in *n*-hexane (75 ml). After fully dissolving, DCM (50 ml) and (3-bromopropoxy)benzene (5.12 g, 23.8 mmol) were added. The mixture was stirred and cooled down to -50 °C. Then the catalyst TiCl₄ (4.33 g, 22.8 mmol) and sulfuric acid (0.23 g, 2.35 mmol) were injected. The reaction mixture was then stirred at -50 °C for 2.5 h. Methanol (10 ml) was injected to quench the catalyst. The crude product was collected by precipitation in excess methanol, followed by being purified using re-dissolving/precipitating in hexane/methanol for three times. The residue was then dissolved in hexane (100 ml) and extracted with two portions of water (50 ml). The organic phase was dried with anhydrous MgSO₄ and evaporated to give transparent elastomer. The ¹H NMR spectrum of PIB-Br was shown in Figure S1 and the number of Br group was calculated to be ~17 comparing the ratio of the integrated intensity of the peak at 2.4 ppm attributed to the methylene protons adjacent to the side chain to that of the peak at 1.1 ppm assigned to the methyl protons adjacent to PIB in the ¹H NMR spectrum. The molecular weight and molecular weight distribution (*D*) were determined by SEC-MALLS using

THF as an eluent. The SEC elution trace of PIB-Br reveals uni-modal and narrowly distributed molecular weight with $M_n = 56.1$ kDa and $D = 1.70$ (**Figure A.3**).

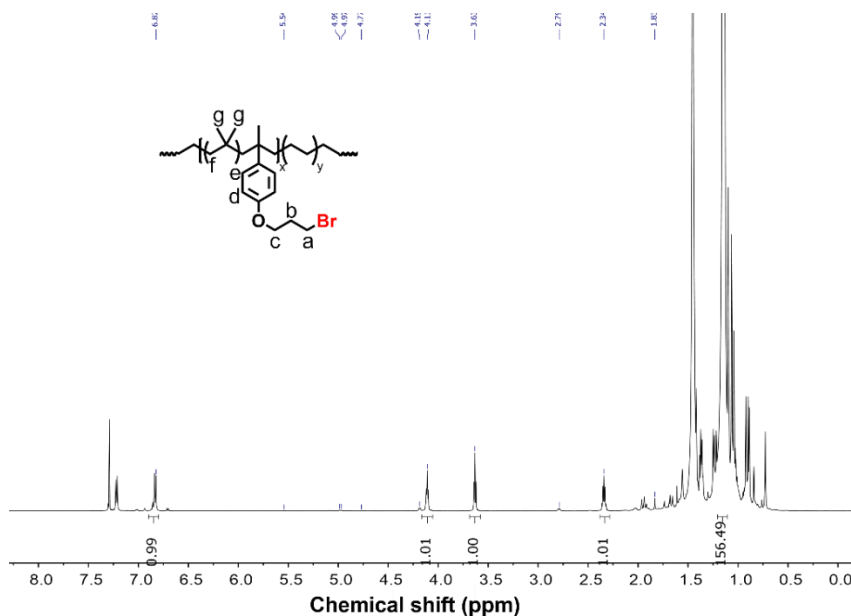


Figure A.1 ^1H NMR spectrum of PIB-Br in CDCl_3 .

Synthesis of PIB-Amine. PIB-Br (5.00 g, 0.09 mmol) was dissolved in THF (150 ml). After fully dissolve, NMP (75 ml), potassium phthalimide (17.55 g, 94.7 mmol), was added to the solution. The reaction mixture was then stirred at 85 °C for 4 h and cooled to room temperature. The crude product was collected by precipitation in excess methanol, and re-dissolved in hexane. The product was washed with DI-water (50 ml) for 6 times. The organic layer was dried with anhydrous MgSO_4 and evaporated to PIB-PI.

PIB-PI (2.42 g, 0.044 mmol) was then dissolved in heptane (100 ml) followed by adding ethanol (50 ml) and hydrazine hydrate (6.054 mg, 0.19 mmol). The reaction mixture was stirred at 105 °C for 5 h and cooled to room temperature. The crude product was precipitate in exceeded methanol and washed with water for 6 times. The organic layer was dried with anhydrous MgSO_4 and evaporated to PIB-Amine.

Synthesis of PIB-Amide. PIB-NH₂ (300 mg, 0.093 mmol) and triethylamine (14.12 mg, 0.014 mmol) was dissolved in anhydrous DCM (15 ml). Acetyl chloride (100 mg, 1.395 mmol) dissolved in anhydrous DCM (5 ml) was dropwise to the solution at 0 °C. The reaction mixture was stirred under 0 °C for another 1h and stirred at room temperature for 24 h. The crude product was precipitate in exceeded methanol and washed with water for 6 times. The organic layer was dried with anhydrous MgSO₄ and evaporated to PIB-Amide.

The successful synthesis of PIB-Amide was certified using ¹H NMR and SEC-MALLS (Figure A.2-3). From ¹H NMR spectra, the peak a always shifted during both Gabriel reaction and esterification reaction (the original peak a dismissed while new peaks showed up after reaction) confirming all end groups were successfully conversed. The elution peak from SEC-MALLS didn't move for PIB-Br and PIB-Amide indicating the molecular weight kept constant during end-group functionality processing.

The formation of hydrogen bonding was confirmed using FT-IR (Figure A.4). The relative intensity of -NH stretching peak (3051-3673 cm⁻¹) of PIB-Amide was much higher than PIB-Br indicating the successful formation of hydrogen bonding.

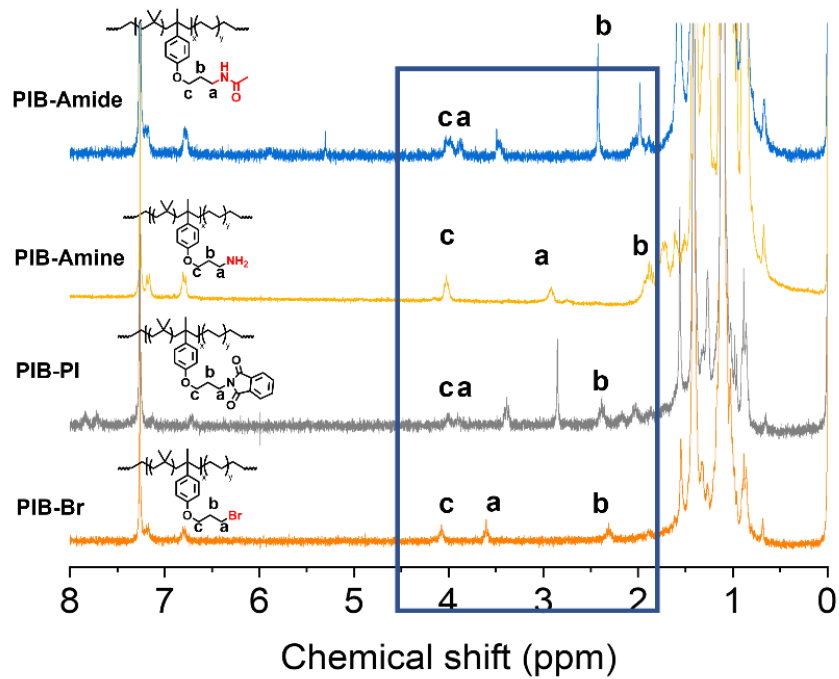


Figure A.2 ^1H NMR spectra of PIB-Br, PIB-PI, PIB-Amine and PIB-Amide in CDCl_3 .

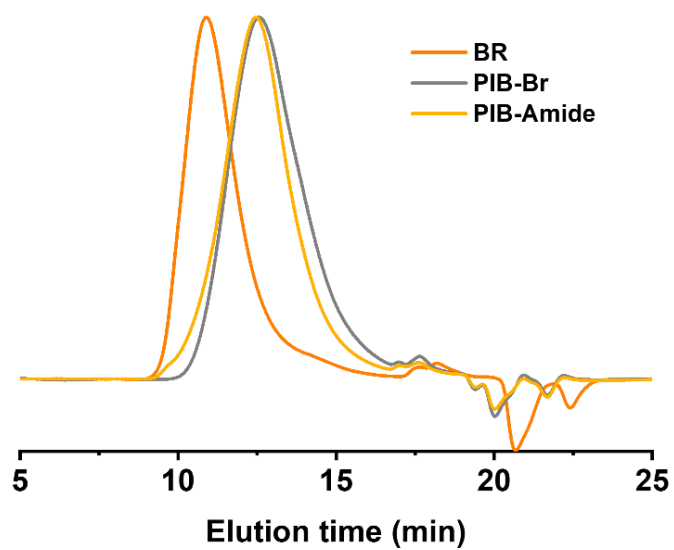


Figure A.3 SEC elution trace of BR, PIB-Br and PIB-Amide.

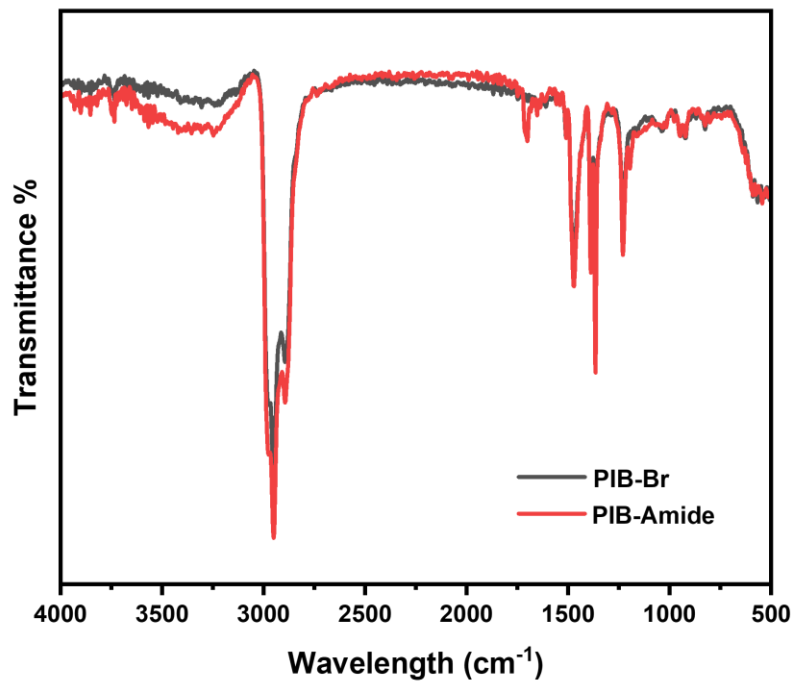


Figure A.4 FT-IR absorption spectrum of PIB-Br and PIB-Amide.

Thermomechanical properties of BR, PIB-Br and PIB-Amide. T_g of BR, PIB-Br and PIB-Amide was measured using DSC, which is -67.8 , -64.1 and -63.1 °C for BR, PIB-Br and PIB-Amide, respectively, indicating decreased MW and hydrogen bonding crosslink didn't influence T_g a lot. (Figure A.5).

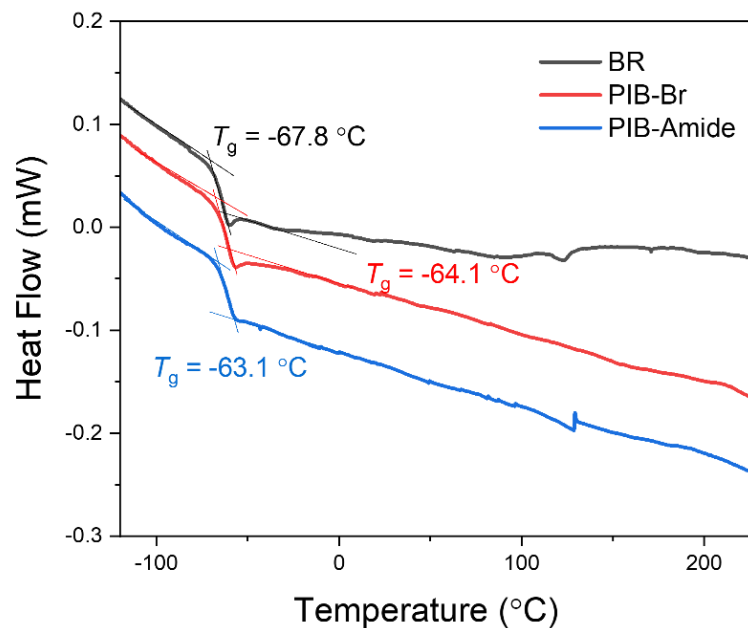


Figure A.5 DSC curve of BR, PIB-Br and PIB-Amide.

Mechanical properties of elastomers were evaluated using pseudo-free standing tensile tester (Figure A.6-7, Table A.1).^{16,20} 80 nm-thickness films of BR, PIB-Br and PIB-Amide were spin-coat on Si wafer followed by being transferred to the surface of water. Due to lower MW after CD reaction, PIB-Br showed lower E and COS (1.26 vs 0.45 MPa, 227% vs 66%) than original BR. After introducing amide group, the COS for PIB-Amide reached ~1660% with only slightly increased E (0.57 MPa) (Figure A.6c). The result indicated hydrogen bonding crosslink can effectively improve deformability of elastomer due to more energy dissipation without much influence on the softness.

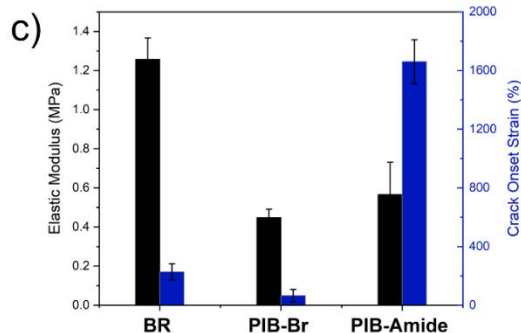
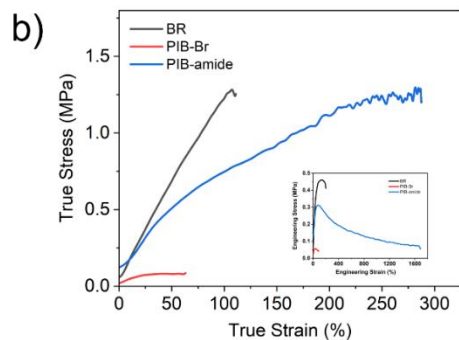
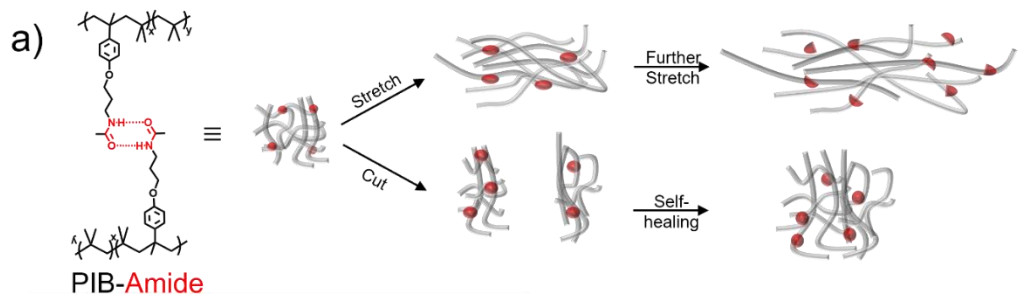


Figure A.6 a) Chemical structure of PIB-Amide and illustration showing the proposed mechanical and self-healing mechanism of the stretchable PIB-Amide. b) True stress–strain curves of BR, PIB-Br, PIB-Amide, with the plot of the engineering stress–strain curve of BR, PIB-Br, PIB-Amide insert. c) Elastic modulus and crack onset strain for BR, PIB-Br, PIB-Amide. d) Optical images of self-healing behavior for PIB-Br, PIB-Amide.

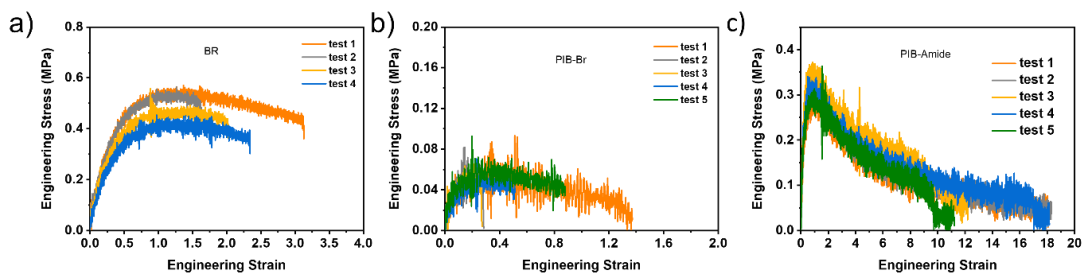


Figure A.7 Repeated tensile test result of BR, PIB-Br and PIB-Amide.

Self-healing ability of PIB-Amide

Self-healing ability of PIB-Amide was investigated visibly. A piece of elastomer was cut to two separated parts. Once being touched with each other, the PIB-Amide totally self-healed. (Figure 1d, video S1).

In summary, hydrogen bonding cross-linked made PIB-Amide elastomer extremely soft, stretchable and self-healable, which should be a great candidate for matrix of stretchable CP/elastomer semiconducting composites. The physical parameters were summarized in Table A.1.

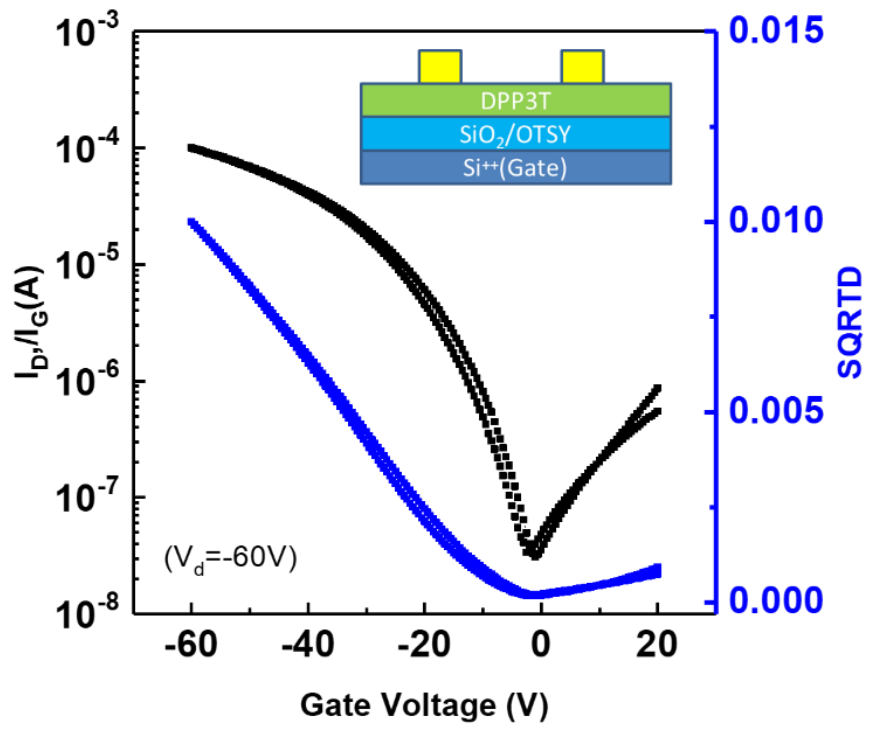


Figure A.8 Transfer curve of DPP-T.

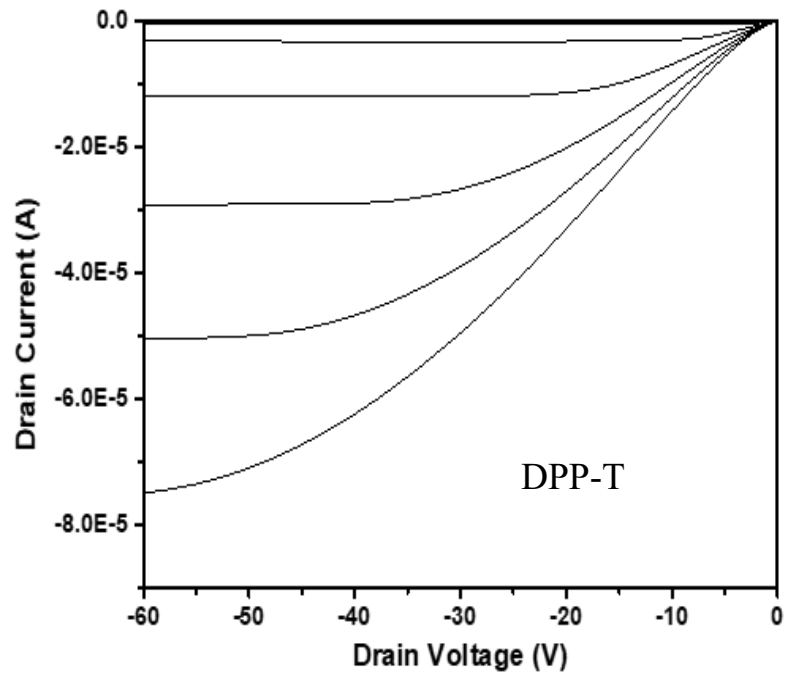


Figure A.9 Output curve of pristine DPP-T.

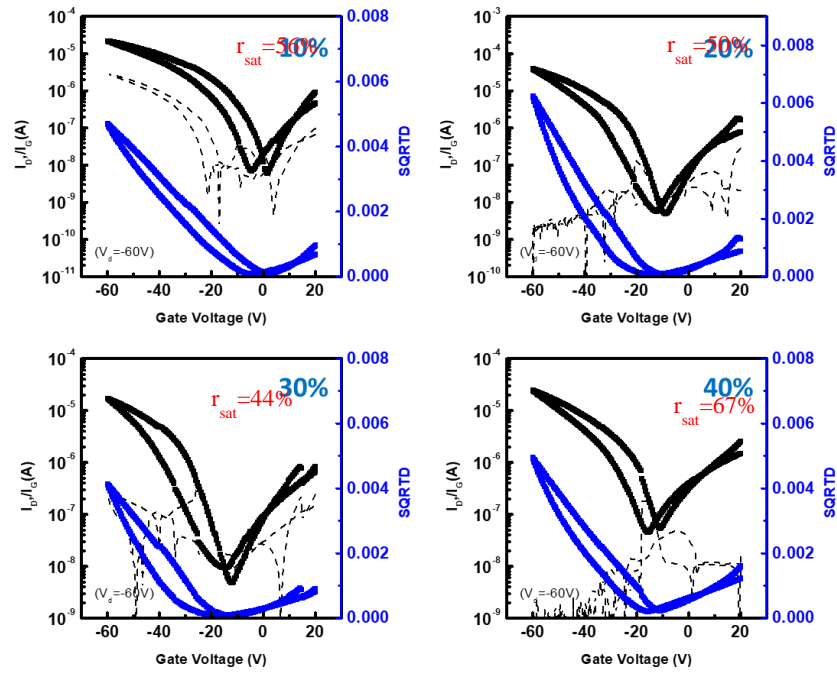


Figure A.10 Transfer curve of 10-40% DPP-T/PIB-Amide.

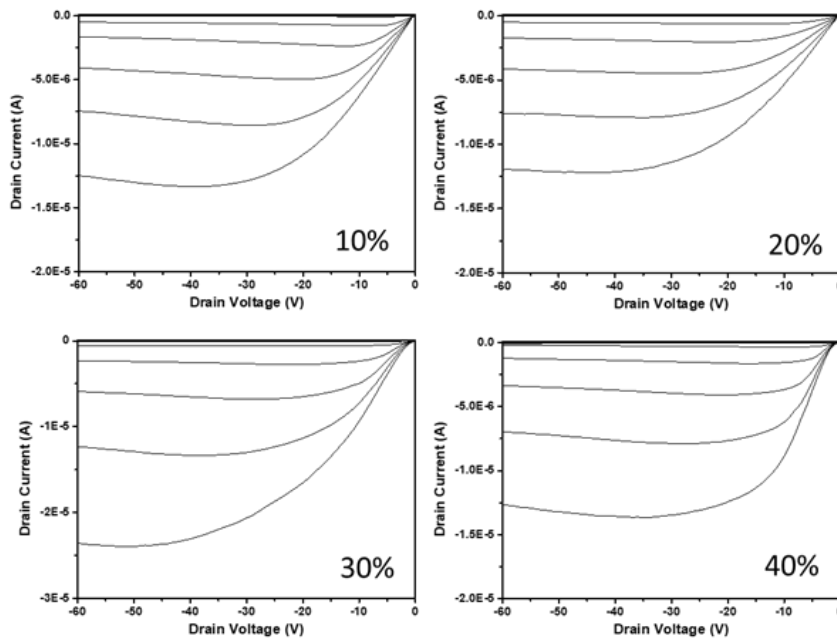


Figure A.11 Output curve of 10-40% DPP-T/PIB-Amide.

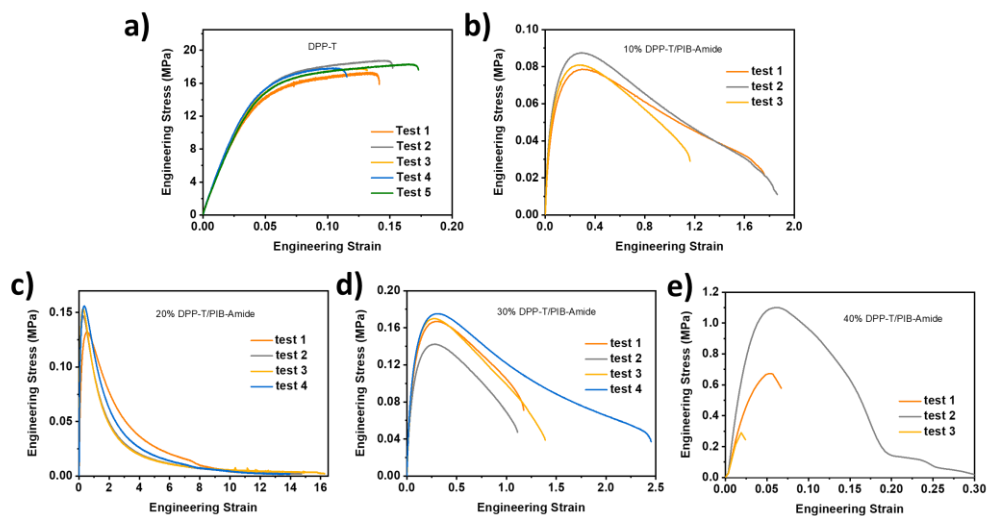


Figure A.12 Repeated tensile test result of DPP-T and 10-40% DPP-T/PIB-Amide.

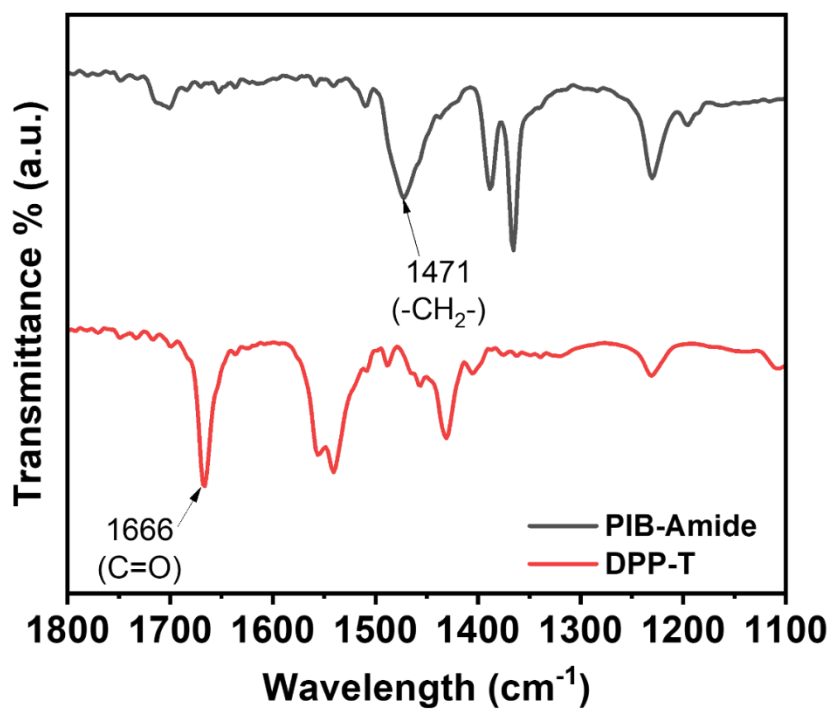


Figure A.13 FT-IR spectra of DPP-T and PIB-Amide.

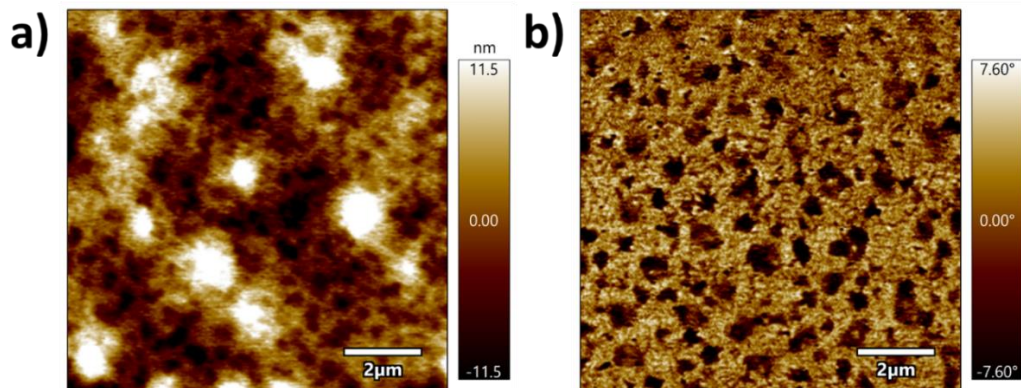


Figure A.14 AFM a) height and b) phase image of bottom surface of 20% DPP-T/PIB-Amide composite.

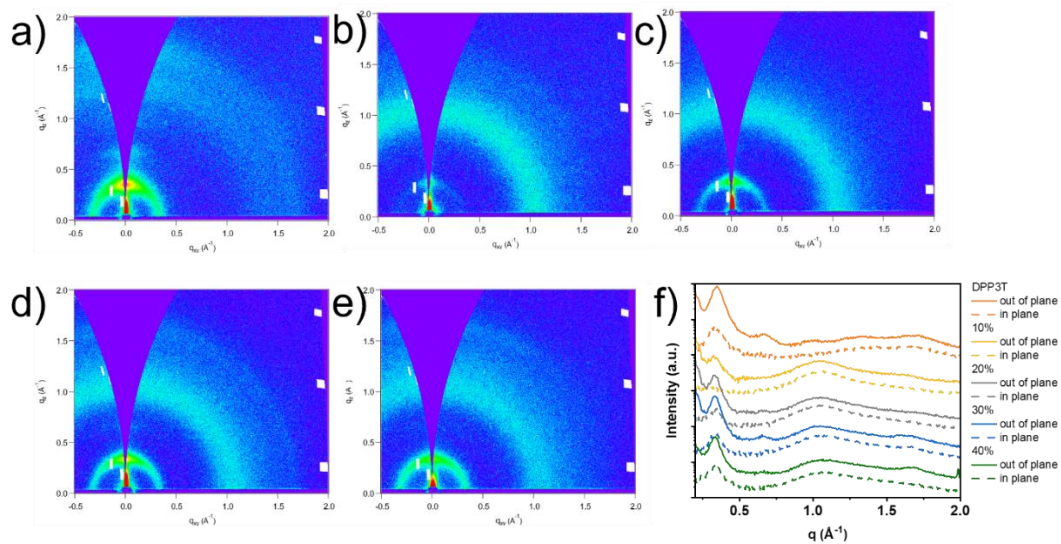


Figure A.15 2D images and 1D line-cut profiles for DPP-T and 10-40% DPP-T/PIB-Amide composites in both in-plane direction (dotted line) and out-of-plane direction (solid line) from GIWAXS.

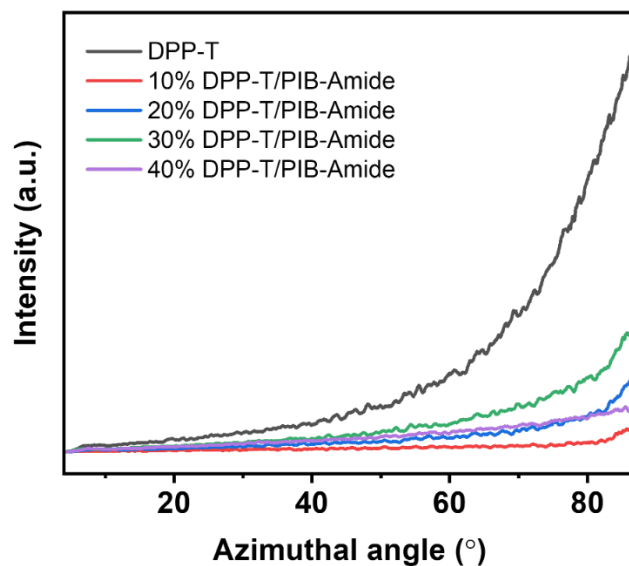


Figure A.16 Pole figure analysis for DPP-T and 10-40% DPP-T/PIB-Amide composites from GIWAXS.

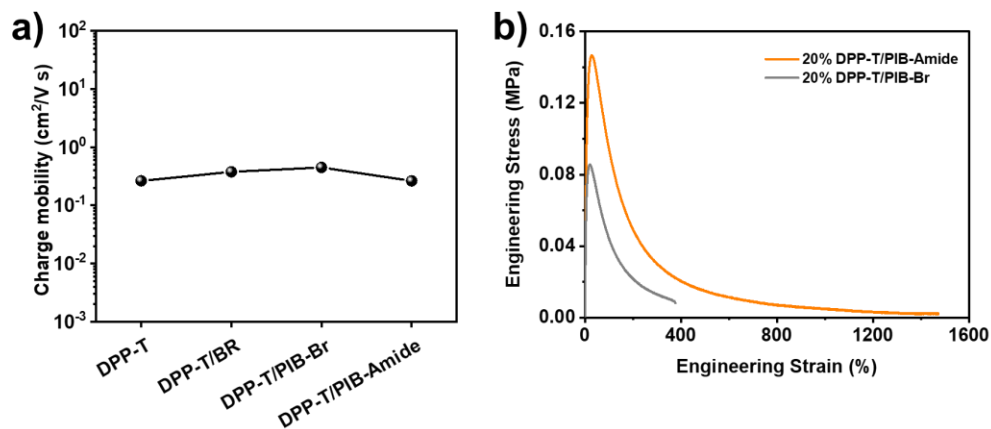


Figure A.17 (a) Charge mobility DPP-T, 20% DPP-T/BR, 20% DPP-T/PIB-Br and 20% DPP-T/Amide composite films. (b) Representative stress-strain curve of 20% DPP-T/PIB-Br and 20% DPP-T/Amide composite films.

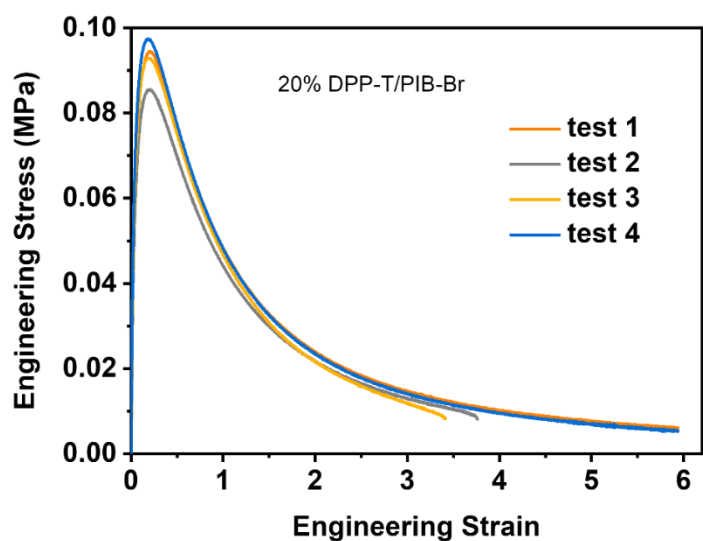


Figure A.18 Repeated tensile test results of 20% DPP-T/PIB-Br.

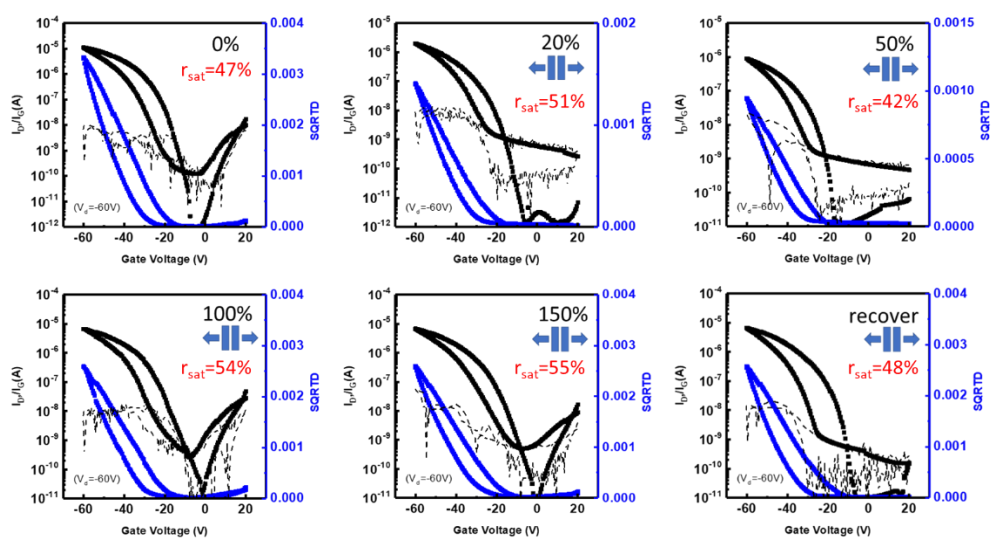


Figure A.19 Transfer curve of stretched 20% DPP-T/PIB-Amide in parallel direction to charge transfer direction. Drain voltage is -60V.

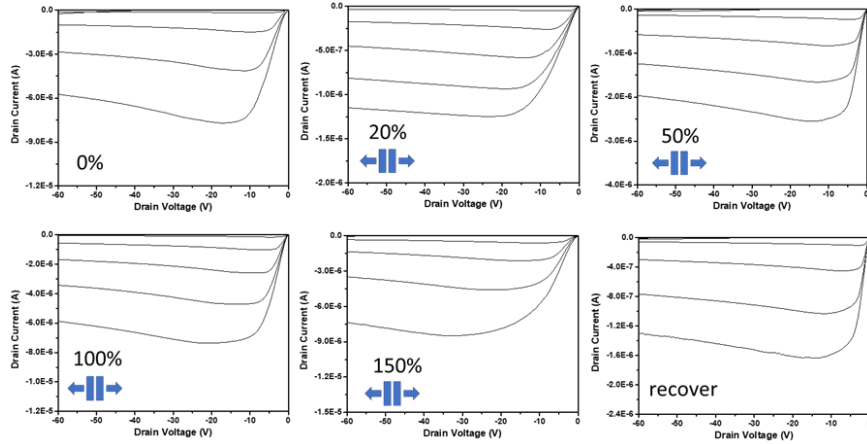


Figure A.20 Output curve of stretched 20% DPP-T/PIB-Amide in parallel direction to charge transfer direction. Drain voltage is -60V.

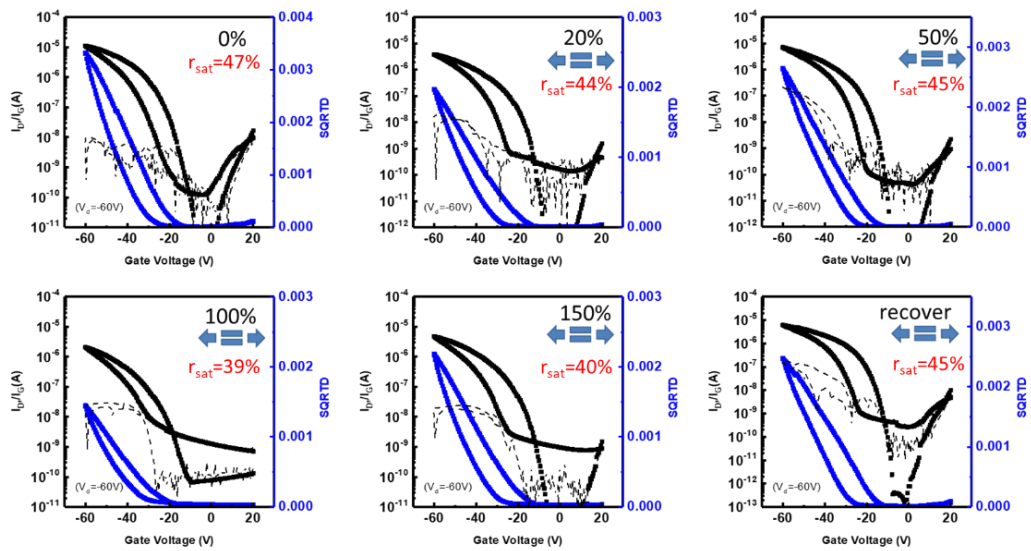


Figure A.21 Transfer curve of stretched 20% DPP-T/PIB-Amide in perpendicular direction to charge transfer direction. Drain voltage is -60V.

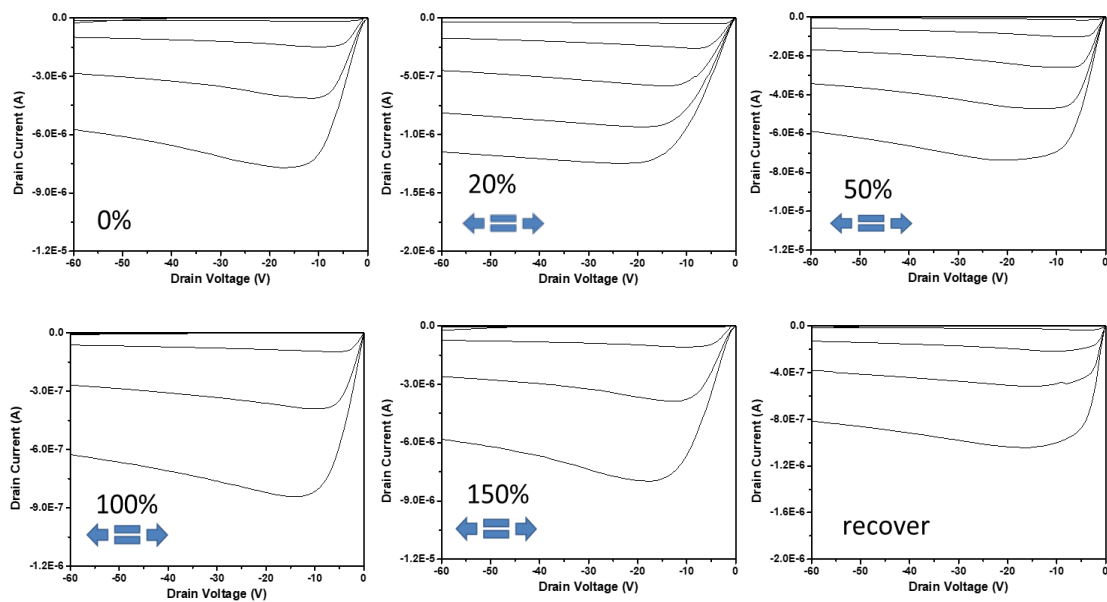


Figure A.22 Output curve of stretched 20% DPP-T/PIB-Amide in perpendicular direction to charge transfer direction. Drain voltage is -60V.

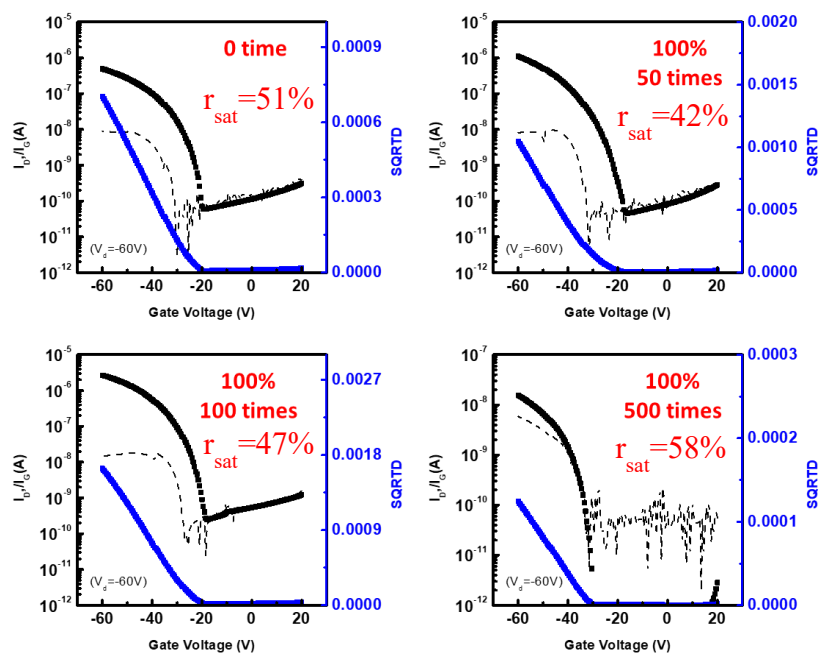


Figure A.23 Transfer curve of cyclic stretched 20% DPP-T/PIB-Amide

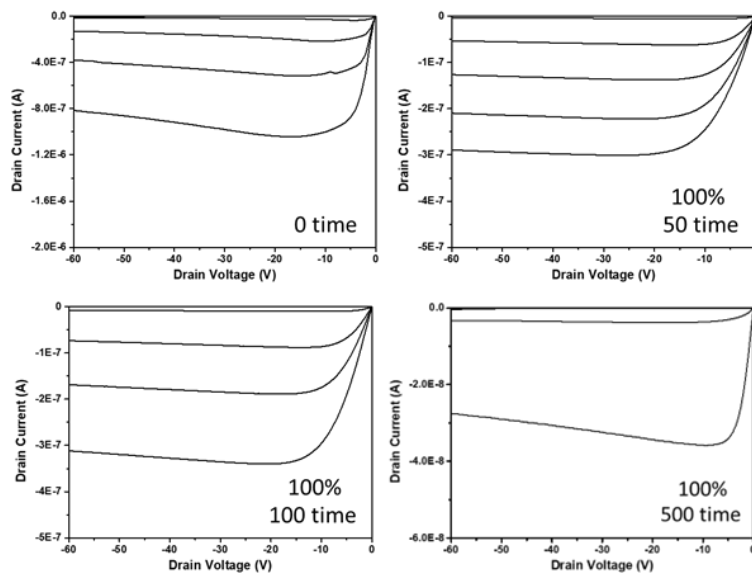


Figure A.24 Output curve of cyclic stretched 20% DPP-T/PIB-Amide.

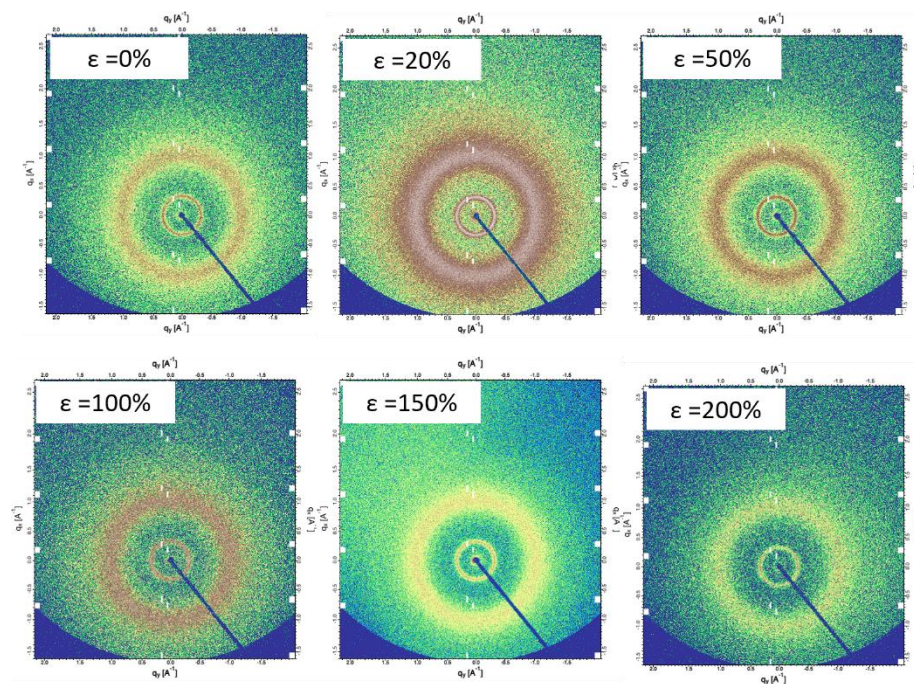


Figure A.25 Representative 2D scattering of 20% DPP-T/PIB-Amide films under strain of 0, 20%, 50%, 100%, 150%, 200% from WAXS.

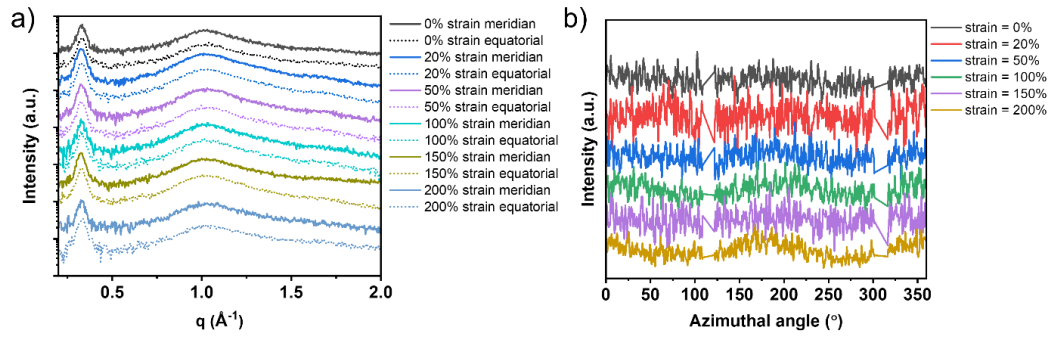


Figure A.26 1D integration and Pole figure analysis for 20% DPP-T/PIB-Amide films under strain of 0, 20%, 50%, 100%, 150%, 200% from WAXS.

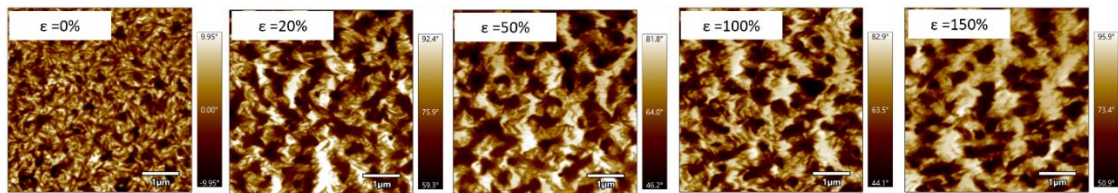


Figure A.27 AFM images for 20% DPP-T/PIB-Amide films under strain of 0, 20%, 50%, 100%, and 150%.

Table A.1 Summary of mechanical performance of BR, PIB-Br and PIB-Amide.

Material	Elastic modulus (MPa)	Crack onset strain (%)
BR	1.26 ± 0.11	227.5 ± 55.1
PIB-Br	0.45 ± 0.04	66.2 ± 41.7
PIB-Amide	0.57 ± 0.16	1660.0 ± 150.0

Table A.2 Summary of mechanical performance of DPP-T and 10-40% DPP-T/PIB-Amide composites.

Material	Elastic modulus (MPa)	Crack onset strain (%)
DPP-T	483.6 ± 21.9	13.2 ± 0.4
20% DPP-T/PIB-Amide	1.99 ± 0.29	1500.0 ± 100.0
30% DPP-T/PIB-Amide	2.98 ± 0.20	153.0 ± 54.1
40% DPP-T/PIB-Amide	24.34 ± 8.20	7.67 ± 5.6

Table A.3 Crystallographic parameters for DPP-T and 10-40% DPP-T/PIB-Amide composites from GIWAXS.

Materials	Out of plane		In plane	
	Lamellar spacing [Å]	Lamellar peak FWHM [Å ⁻¹]	Lamellar spacing [Å]	Lamellar peak FWHM [Å ⁻¹]
DPP-T	17.95	0.07	18.48	0.10
10% DPP-T/PIB-Amide	19.04	0.07	-	-
20% DPP-T/PIB-Amide	19.04	0.06	18.48	0.06
30% DPP-T/PIB-Amide	19.04	0.06	18.48	0.08
40% DPP-T/PIB-Amide	19.04	0.06	19.03	0.08

Table A.4 Crystallographic parameters for 20% DPP-T/PIB-Amide composites from WAXS.

Material	Lamellar spacing [Å]	Lamellar peak FWHM [Å ⁻¹]
20% DPP-T/PIB-Amide	19.03	0.05

APPENDIX B – Supporting Information

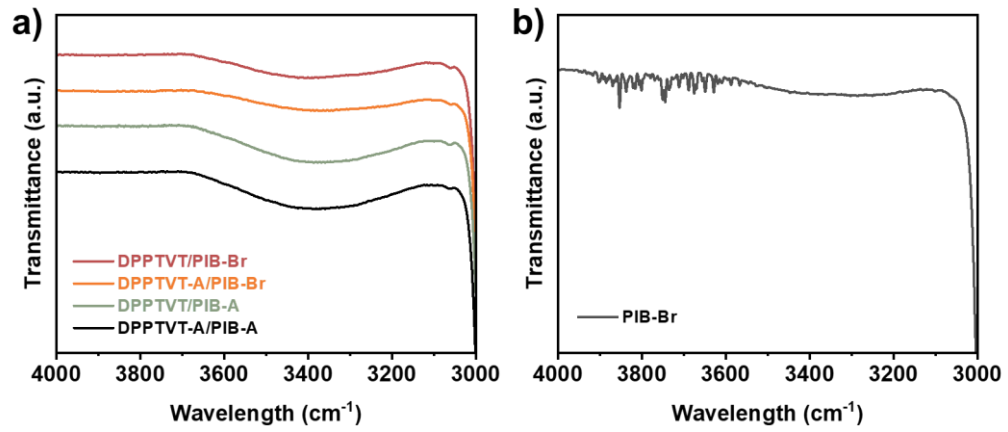


Figure B.1 FT-IR spectra of (a) DPPTVT/PIB-Br, DPPTVT-A/PIB-Br, DPPTVT/PIB-A, DPPTVT-A/PIB-A composites and (b) PIB-Br.

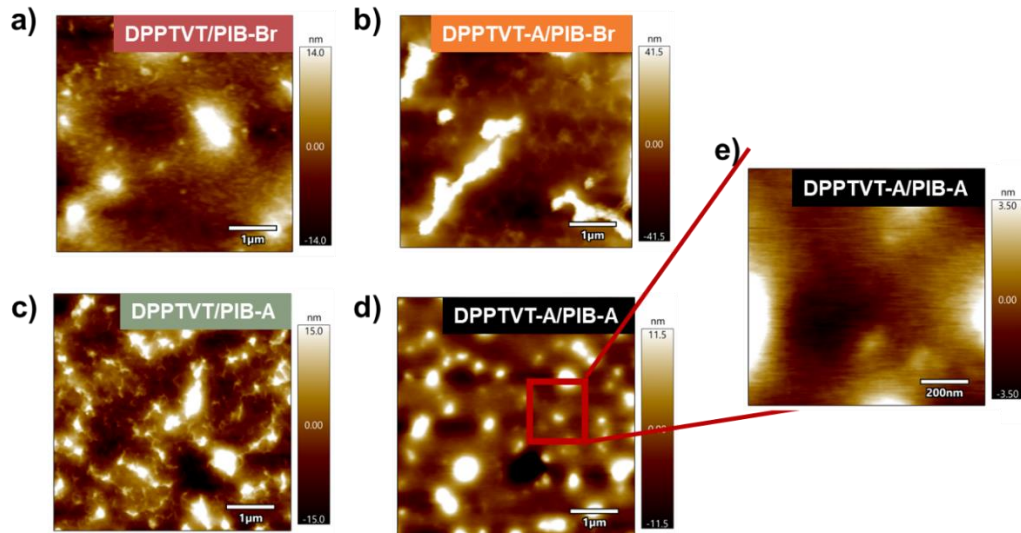


Figure B.2 AFM height images of (a) DPPTVT/PIB-Br, (b) DPPTVT-A/PIB-Br, (c) DPPTVT/PIB-A and (d) DPPTVT-A/PIB-A composites.

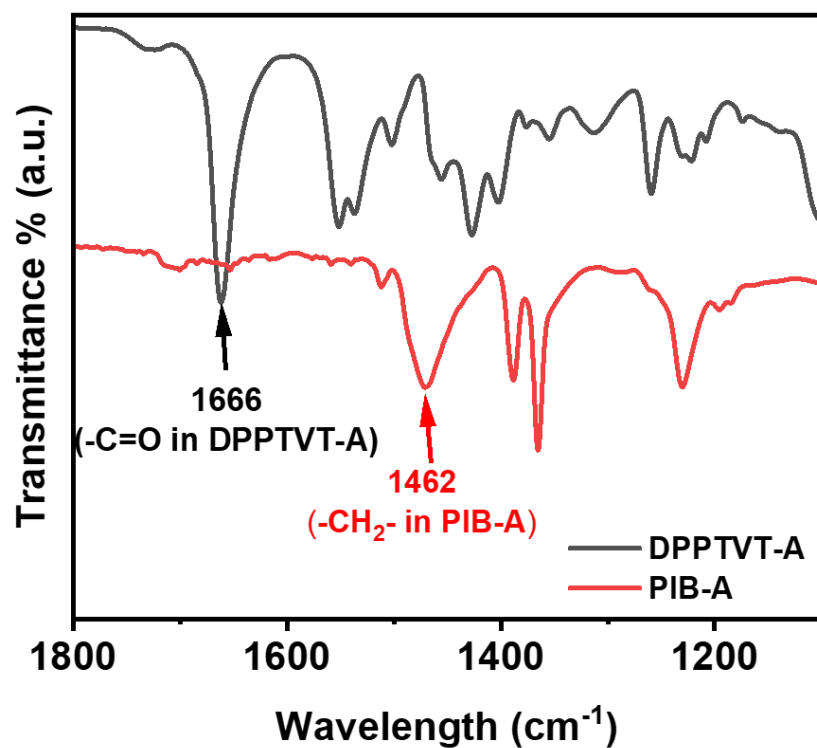


Figure B.3 FT-IR spectra of DPPTVT-A and PIB-A.

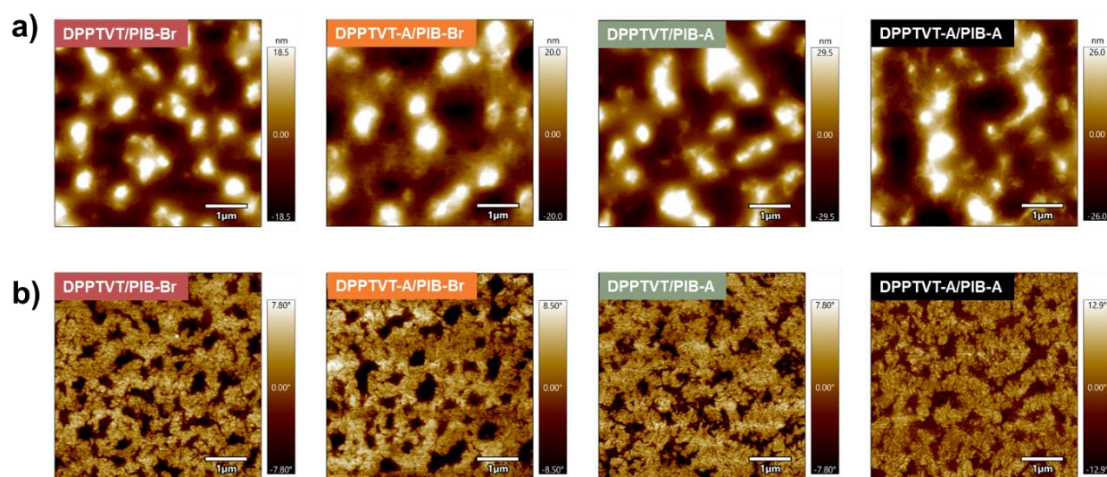


Figure B.4 AFM a) height and b) phase image of bottom surface of DPPTVT/PIB-Br, DPPTVT-A/PIB-Br, DPPTVT/PIB-A and DPPTVT-A/PIB-A composites.

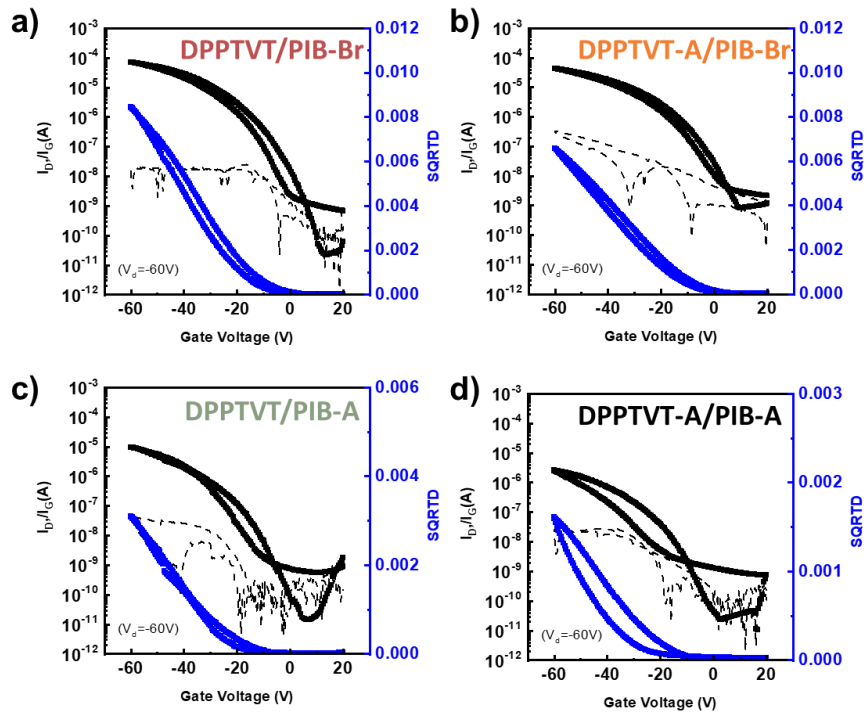


Figure B.5 Transfer curves of DPPTVT/PIB-Br, DPPTVT-A/PIB-Br, DPPTVT/PIB-A and DPPTVT-A/PIB-A composites. Drain voltage was -60V.

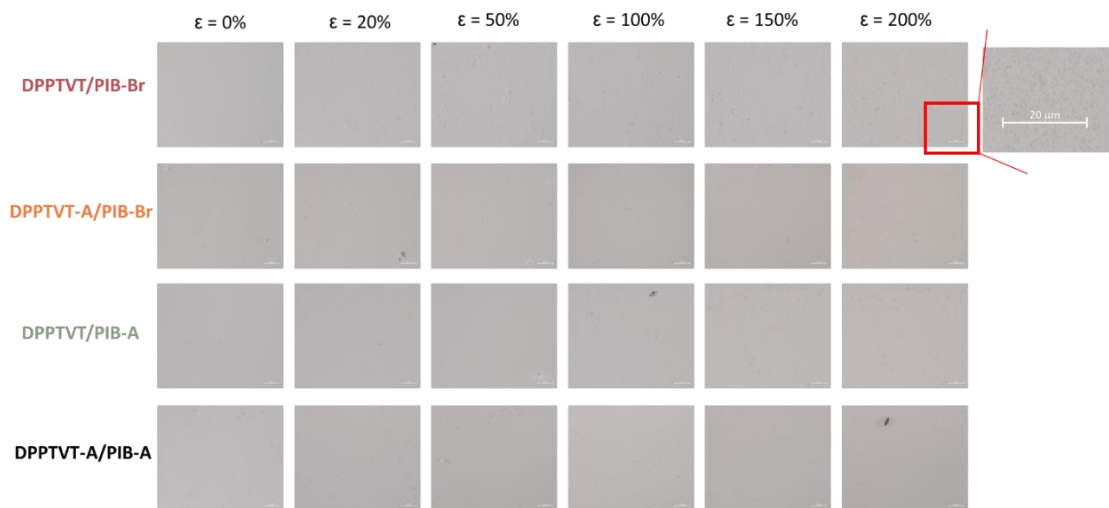


Figure B.6 Representative optical images of stretched composites strained via the film-on-elastomer technique.

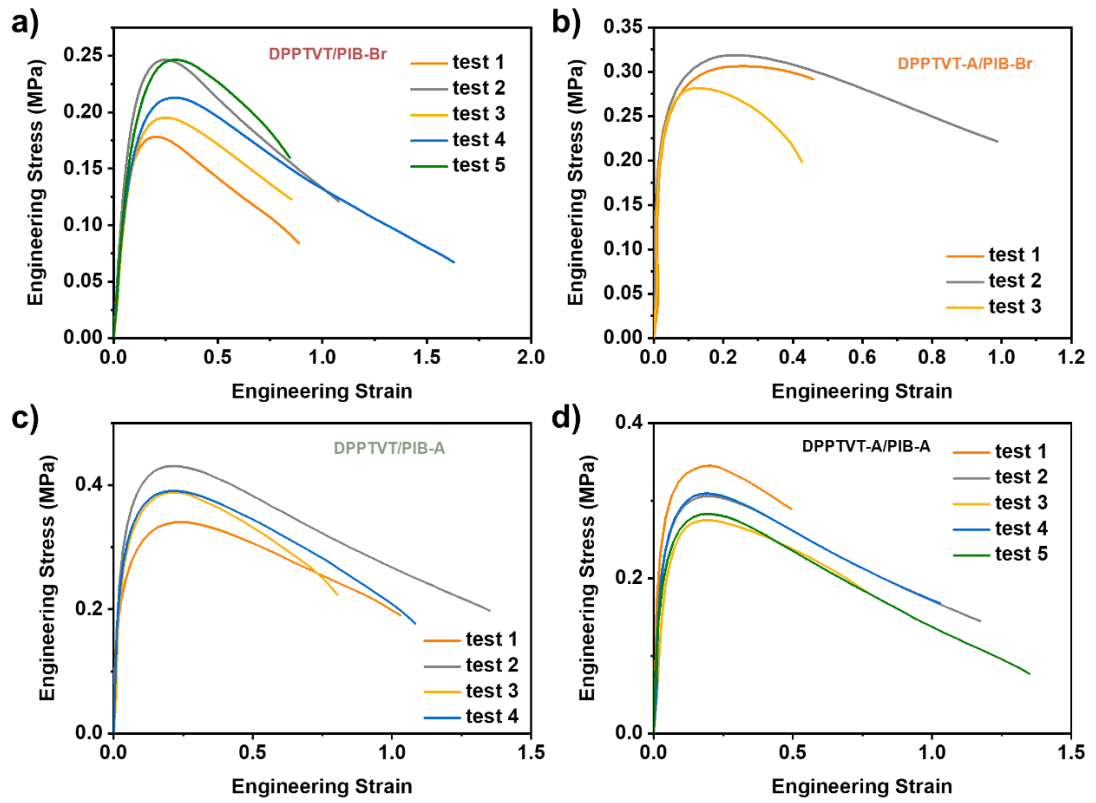


Figure B.7 Repeated tensile test results of composites from film-on-water tensile test.

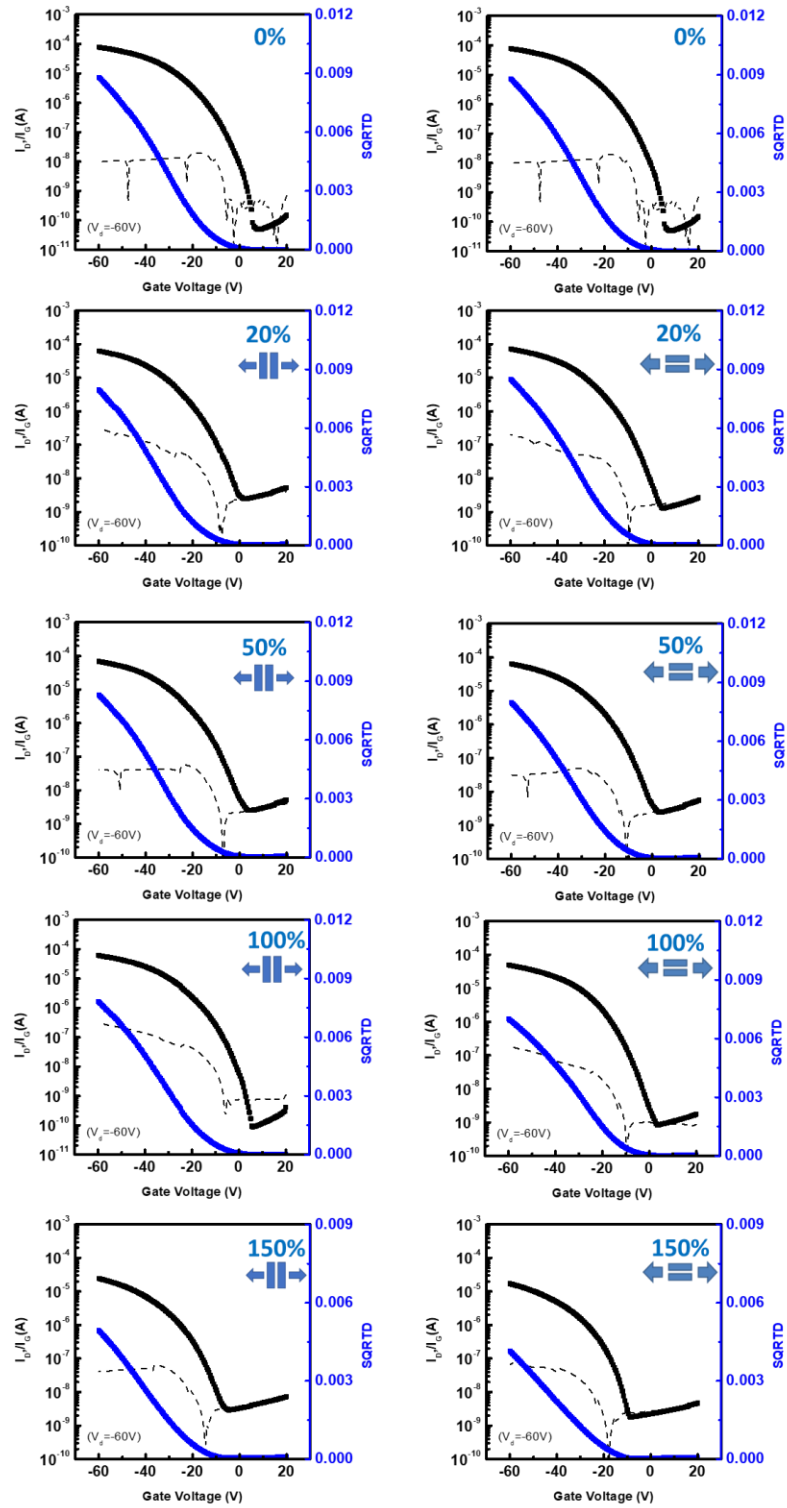


Figure B.8 Transfer curves of stretched non-H-bonding crosslinked DPPTVT/PIB-Br composites. Drain voltage was -60V.

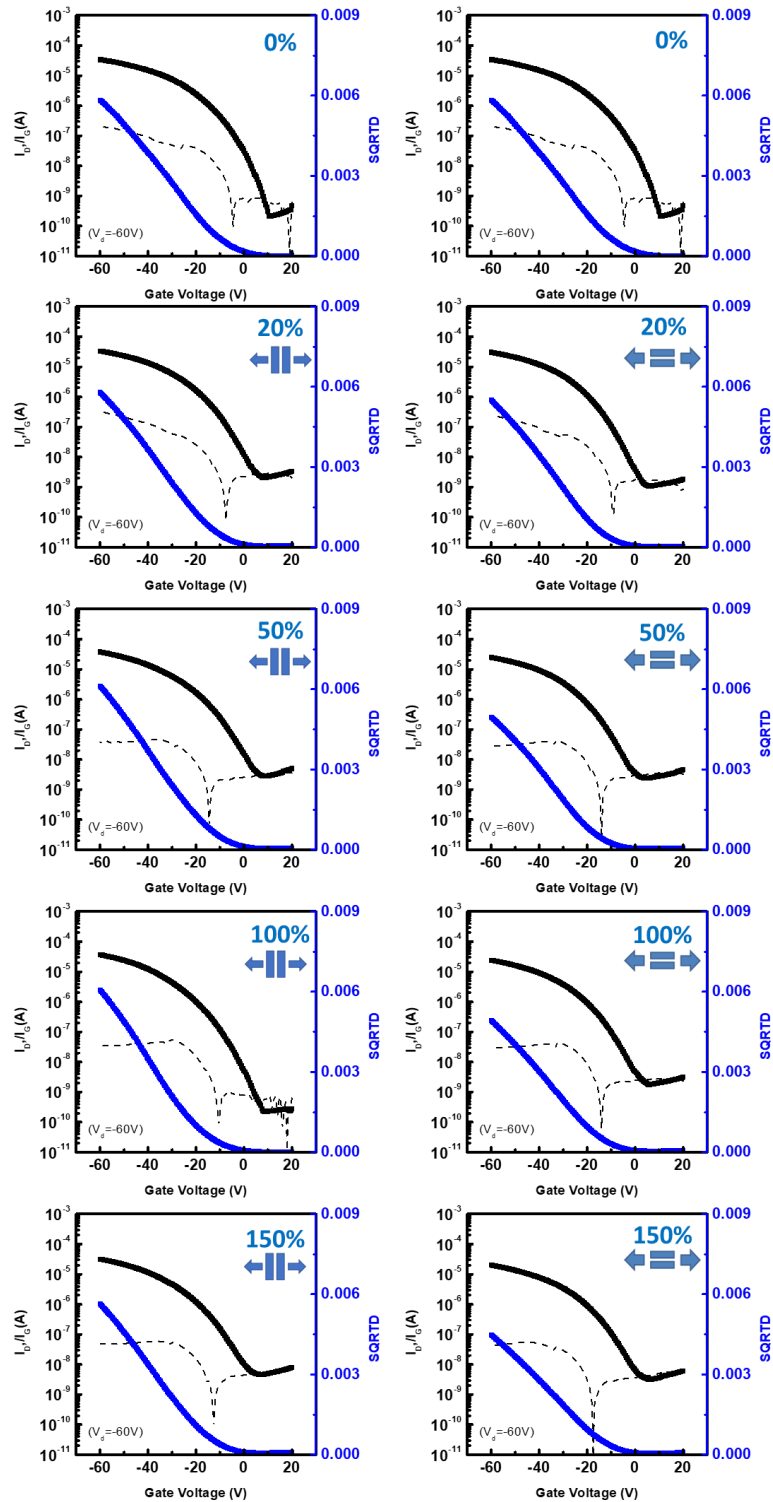


Figure B.9 Transfer curve of stretched uni-H-bonding crosslinked composites from CP, DPPTVT-A/PIB-Br. Drain voltage was -60V.

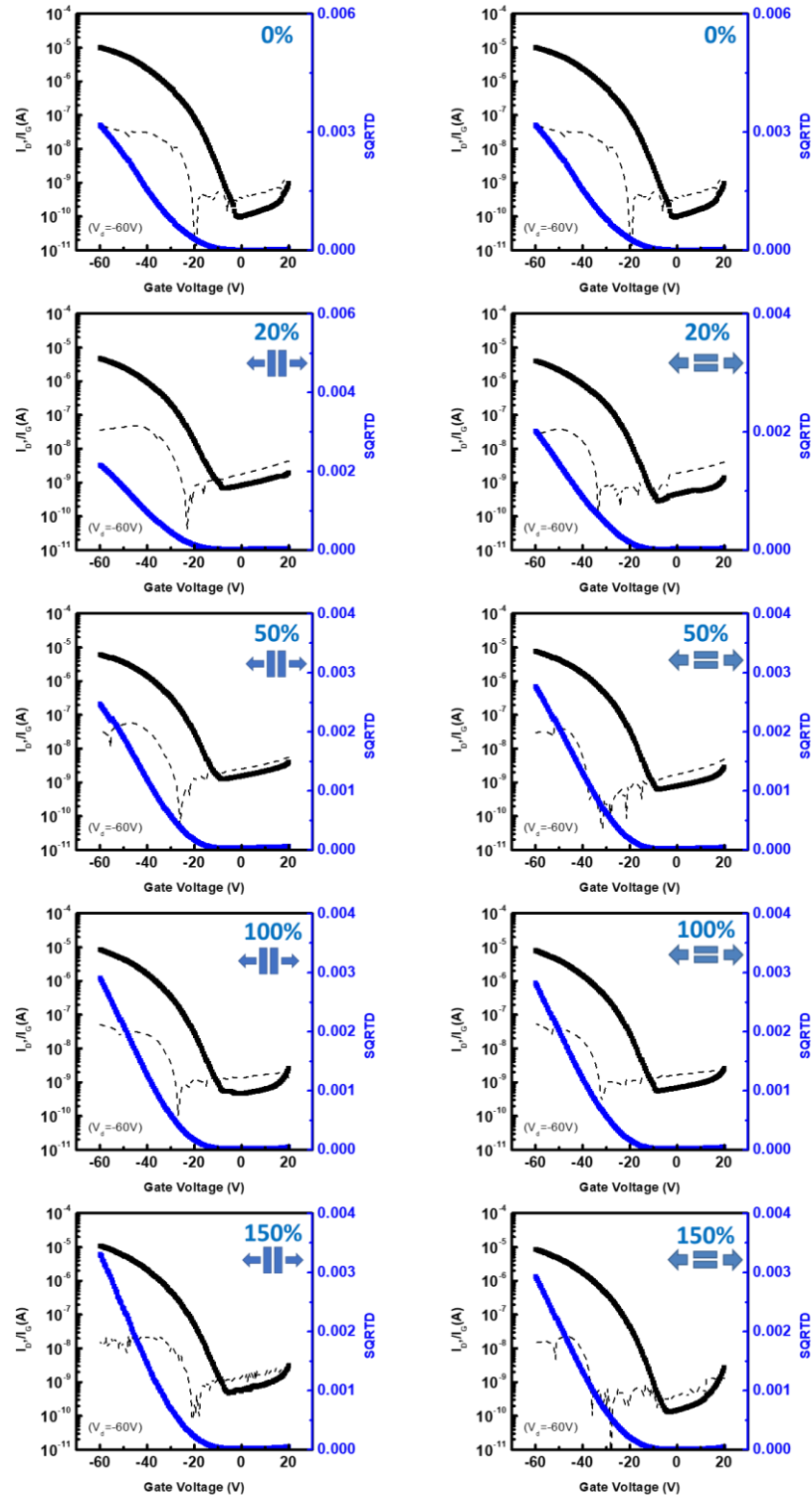


Figure B.10 Transfer curves of stretched uni-H-bonding crosslinked composites from elastomer, DPPTVT/PIB-A. Drain voltage was -60V.

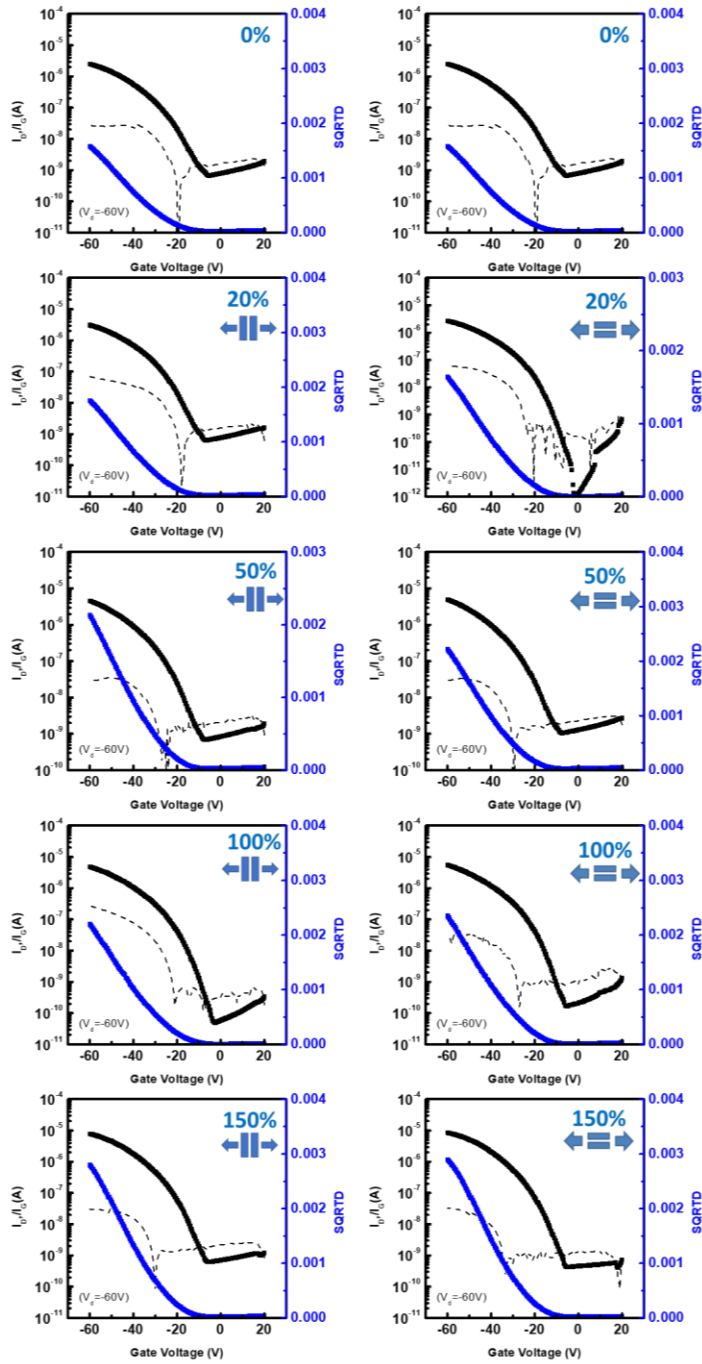


Figure B.11 Transfer curves of stretched dual-H-bonding crosslinked composites DPPTVT-A/PIB-A. Drain voltage was -60V.

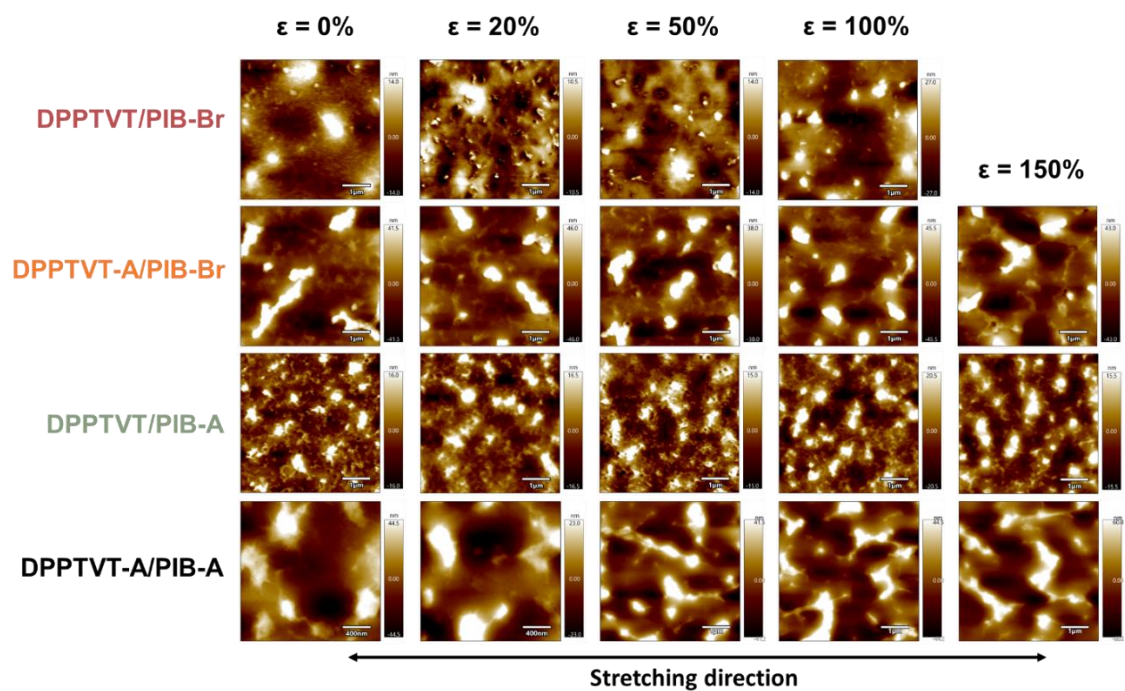


Figure B.12 AFM height images of stretched DPPTVT/PIB-Br (red), DPPTVT-A/PIB-Br (orange), DPPTVT/PIB-A (green) and DPPTVT-A/PIB-A (black) composites at strain of 0, 20, 50, 100 and 150%.

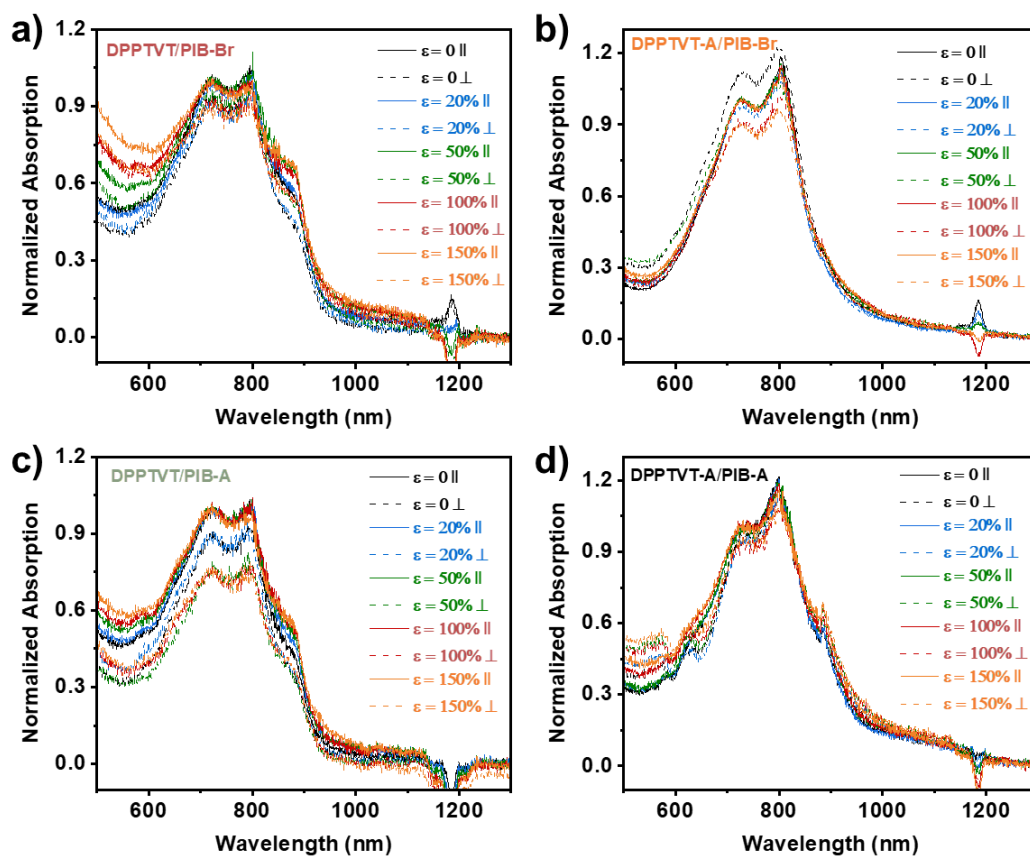


Figure B.13 UV-vis absorption spectroscopy result for strained DPPTVT/PIB-Br, DPPTVT-A/PIB-Br, DPPTVT/PIB-A and DPPTVT-A/PIB-A composites thin film.

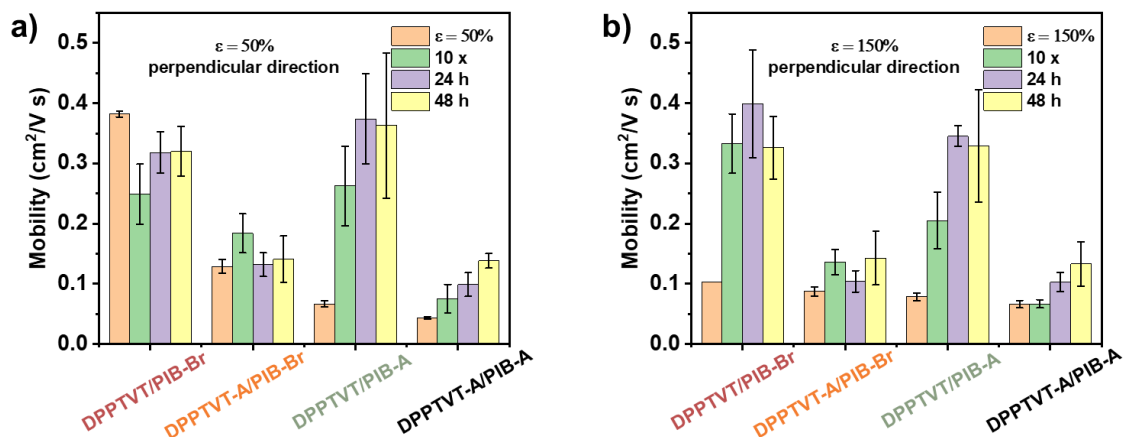


Figure B.14 Charge mobility comparison along perpendicular direction of DPPTVT/PIB-Br (red), DPPTVT-A/PIB-Br (orange), DPPTVT/PIB-A (green) and DPPTVT-A/PIB-A (black) composites after stretching 1 and 10 cycles and staying for 24 and 48 h at strain of (a) 50% and (b) 150%.

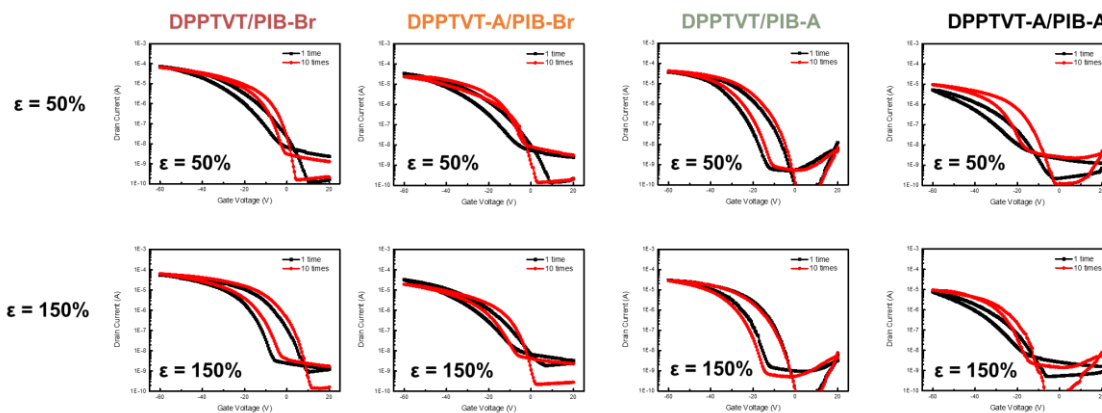


Figure B.15 Transfer curves of stretched DPPTVT/PIB-Br, DPPTVT-A/PIB-Br, DPPTVT/PIB-A and DPPTVT-A/PIB-A at strain of 50% and 150% for 1 and 10 cycles. Drain voltage was -60V.

APPENDIX C – Supporting Information

***In-Situ* Wide-Angle Hard X-Ray Scattering**

While all the data presented above result from ex-situ experiments, where the scattering experiments were performed days after the sample preparation, stress relaxation of aligned films could affect the final state of alignment. *In situ* hard X-ray WAXS measurements of P3BT and P3OT bulk samples (> 2 μm thick) were also performed. A low fracture strain of $\varepsilon_T = 0.12$ for P3BT and $\varepsilon_T = 0.65$ for P3OT was reached, which could result from a high defect density for drop-casted samples that initiated early fracture. The corresponding 2D scattering patterns, 1D intensity profiles and pole figures were shown in **Figure C.5-7**. The f value of all three peaks didn't change for P3BT, which agreed well with the result from *ex situ* experiments (**Figure C.8a**). For P3OT, f began to increase at $\varepsilon_T = 0.13$, while the f value for both (010) peak and amorphous halo did not change (**Figure C.8b**).

Polarized UV-vis optical absorption spectroscopy for samples supported by PDMS

Previous literature reported higher increasing f on PDMS substrates (~ 0.7 at engineering strain = 140%).²³¹ To directly compare our work with previous work, we then repeated chain alignment characterization using polarized UV-vis for samples supported by PDMS. f did increase more for PDMS-supported thin film than free-standing one (**Figure C.13**). We expected the difference between the two methods to lie in the PDMS substrate which can preserve all the chain slippage during deformation due to delocalized stress and consequently uniform strain.

CG-MD simulation of effect of side-chain length on thermo-mechanical properties

As discussed from experimental findings, side-chain groups affected the T_g of CPs considerably. Thus, glassy P3BT exhibits a higher elastic modulus than viscoelastic P3OT at the temperature between the T_g of the two materials. We began by characterizing the sidechain length-dependent bulk T_g of the CG model to verify the experimental results and gain more insights. Specifically, a generic “bead-spring” CG model of polymer with a branched chain structure was employed to preserve the essential structural features of CPs. The CG model has a linear backbone chain (pink beads) and each bead in the backbone is attached by a side-chain (blue beads) to represent alkyl groups (**Figure C.29a**). **Figure C.29a, b** displayed a representative CG chain configuration having the side-chain length n varying from 1 to 4 and a simulation box consisting of polymer chains, respectively. The CG model description was discussed in detail in our experimental section. As shown in **Figure C.29c**, the typical T_g was determined by linearly fitting the density vs. temperature data in the low- and high- T regimes, respectively, where the intersection value of two distinct slopes marks the T_g . **Figure C.29d** indicated that the growth of side-chain length leads to a noticeable reduction in T_g of the bulk polymer system, as the experiments found it that P3OT with more alkyl groups on side-chain exhibits lower T_g comparing to P3BT.

Taking the model with side-chain length of two as a representative polymer system, we proceed to carry out free-standing thin film simulations with free surfaces to investigate T effect on the mechanical properties and chain deformation at the fundamental molecular level (snapshot of thin film system was shown in **Figure 4.5b**). We compared the mechanical response of systems to uniaxial tensile loading over a T range from 0.7 to 1.3 T_g (**Figure C.30a**). **Figure C.30b** showed two representative stress-

strain curves obtained from these simulations, from which a clear difference in their mechanical response can be observed. At a strain less than 3%, we observed that the stress increases linearly with strain for both systems, where the elastic modulus E was determined by linearly fitting the stress-strain data. As the strain increased beyond the linear elastic regime, the polymer system at $T = 0.7 T_g$ exhibited a yielding behavior, followed by a strain-softening and strain-hardening; while the strain-softening was not obvious for system at $T = 1.3 T_g$. Moreover, the strain-hardening phenomenon at low T was more noticeable with a higher slope (*i.e.*, strain-hardening modulus) and the fluctuation amplitude of stress becomes larger in the strain-hardening regime. We also performed additional simulations at multiple T , indicating that the elastic modulus did show an obvious reduction with increasing T (**Figure C.30c**). These findings obtained from CG-MD were consistent with the experimental results, demonstrating that the T can strongly impact the mechanical behavior of polymer thin film, and verifying the fact that glassy P3BT exhibits enhanced mechanical performance compared to viscoelastic P3OT at the T between the T_g of the two polymers.

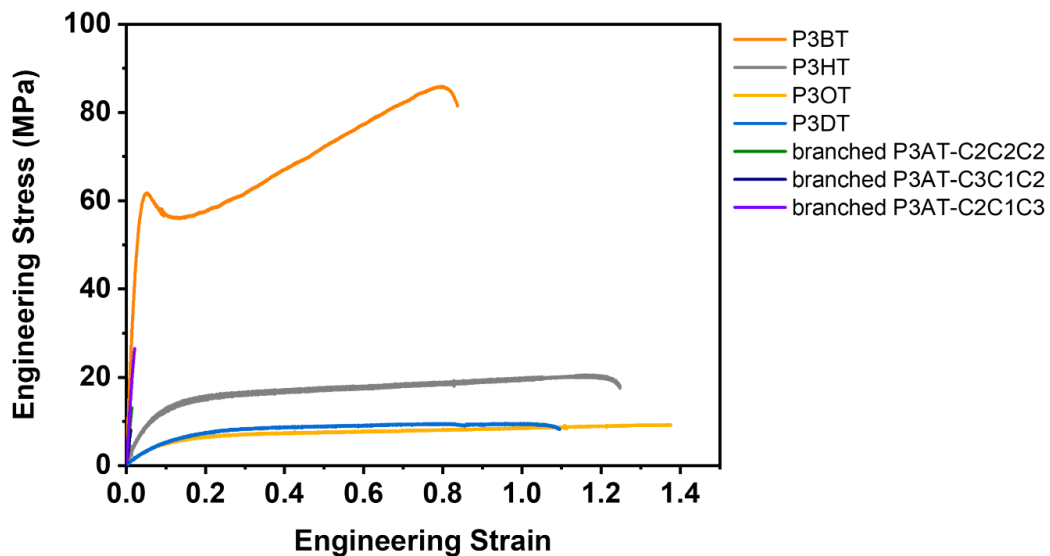


Figure C.1 Engineering stress-strain curve of P3ATs.

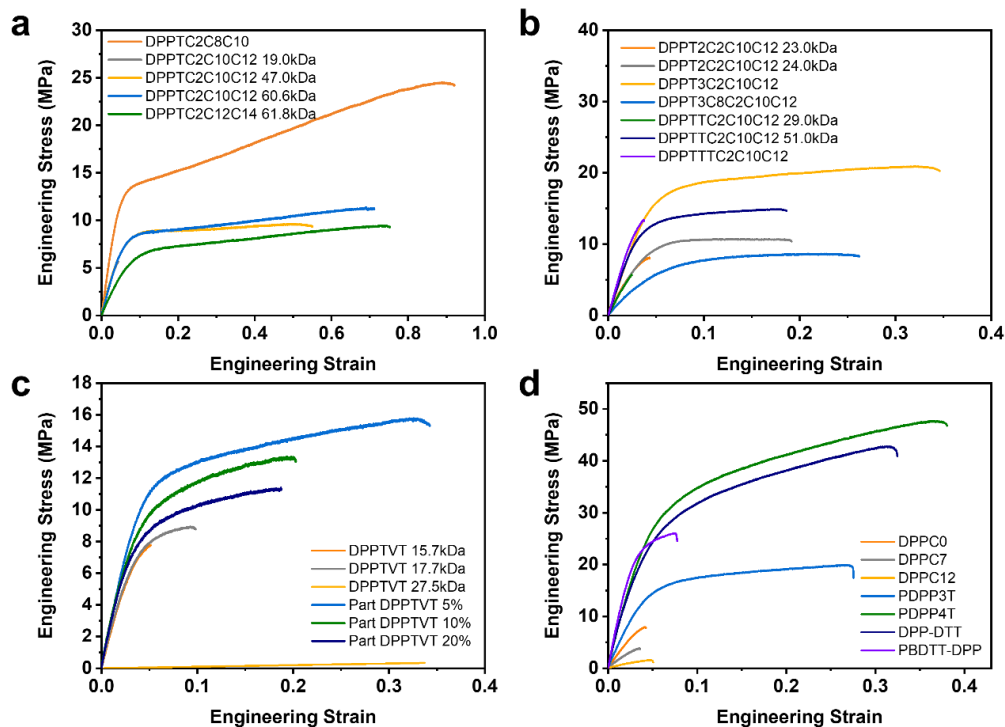


Figure C.2 Engineering stress-strain curve of DPP-based CPs.

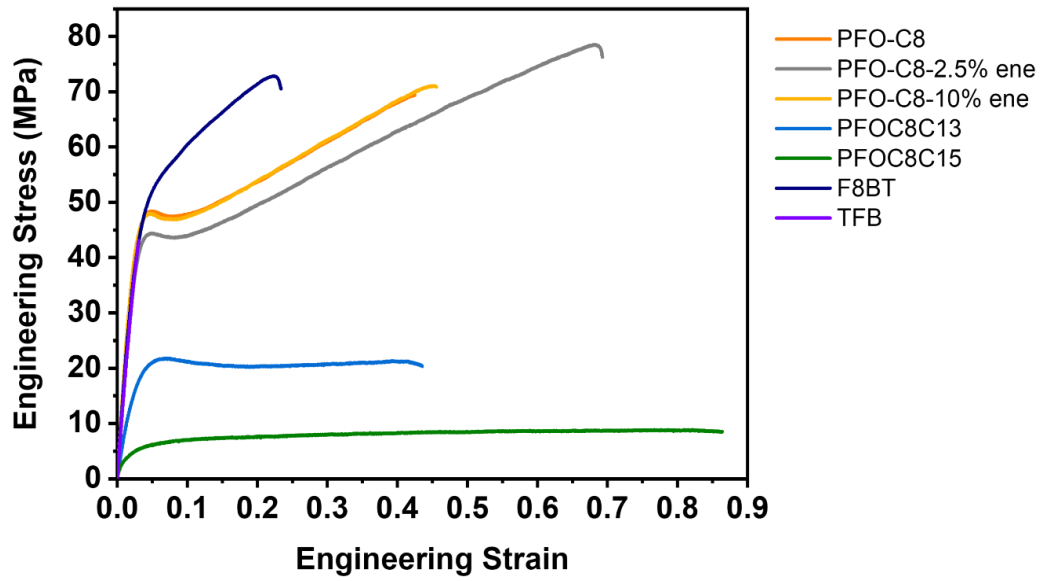


Figure C.3 Engineering stress-strain curve of PFO-based CPs.

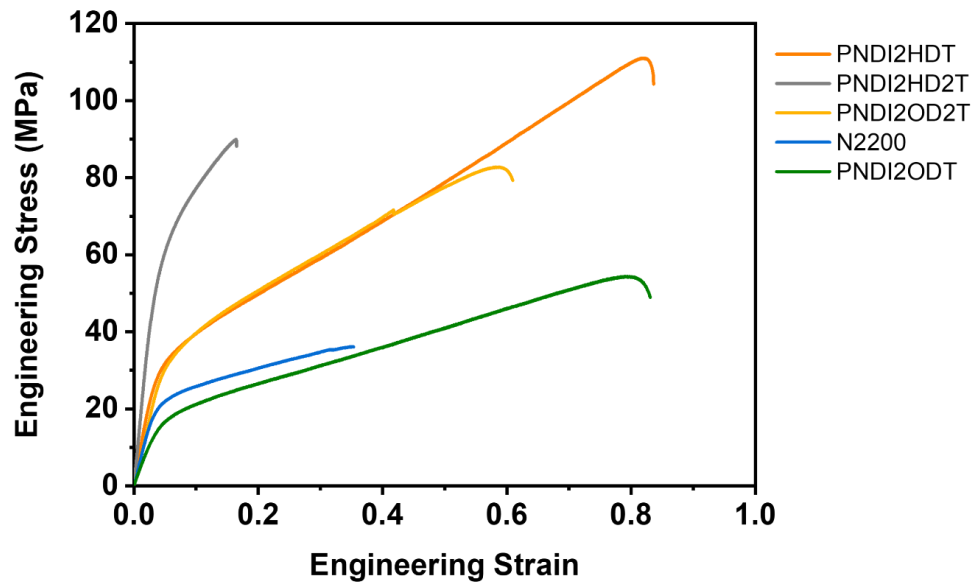


Figure C.4 Engineering stress-strain curve of NDI-based CPs.

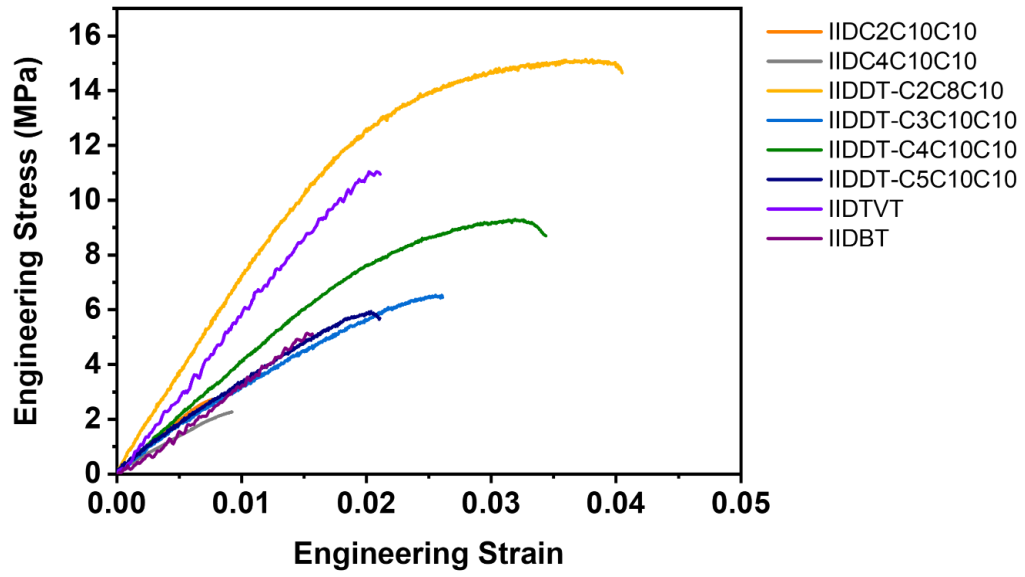


Figure C.5 Engineering stress-strain curve of IID-based CPs.

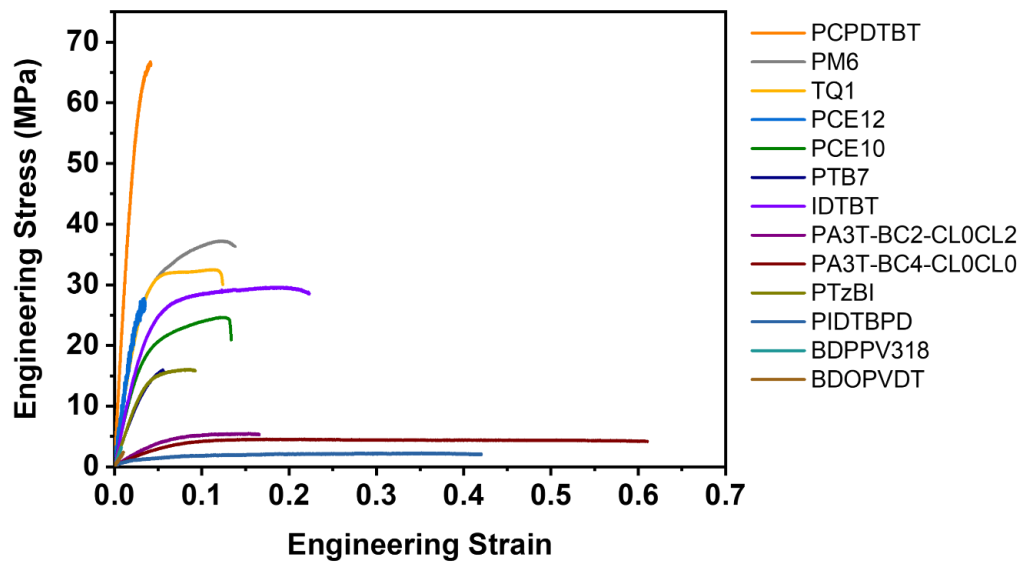


Figure C.6 Engineering stress-strain curve of other CPs.

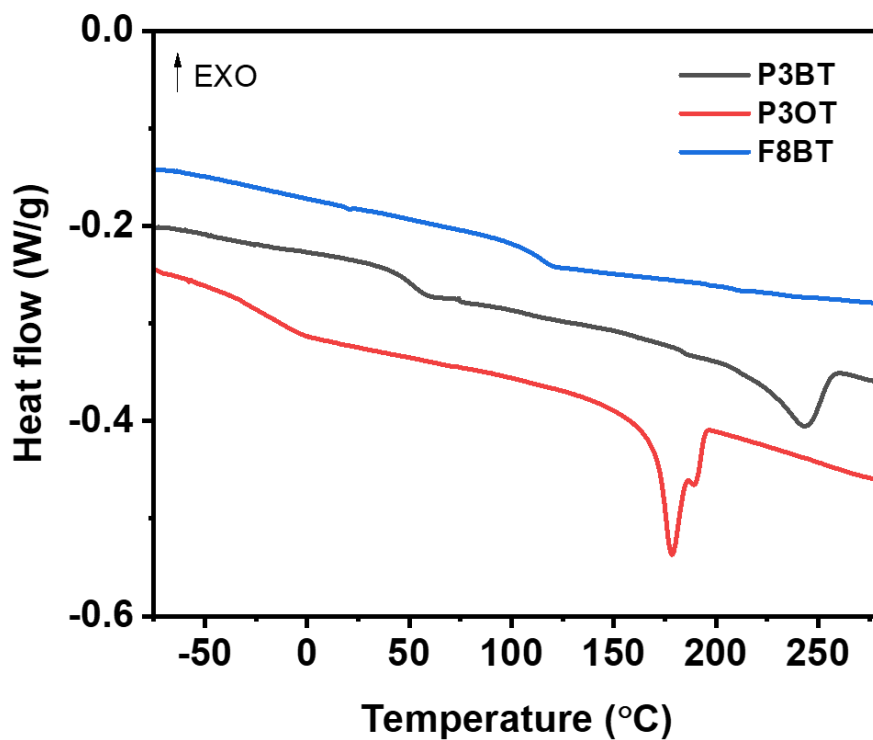


Figure C.7 DSC curve of P3BT, P3OT and F8BT.

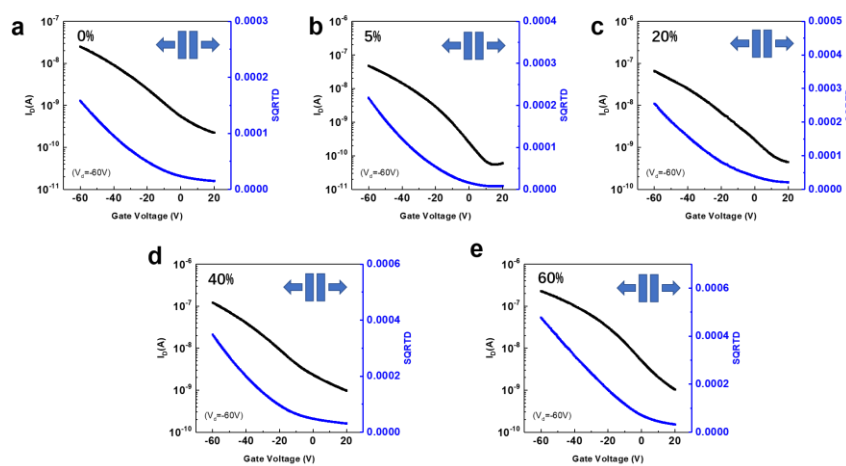


Figure C.8 FET transfer curves for stretched P3BT parallel to strain direction.

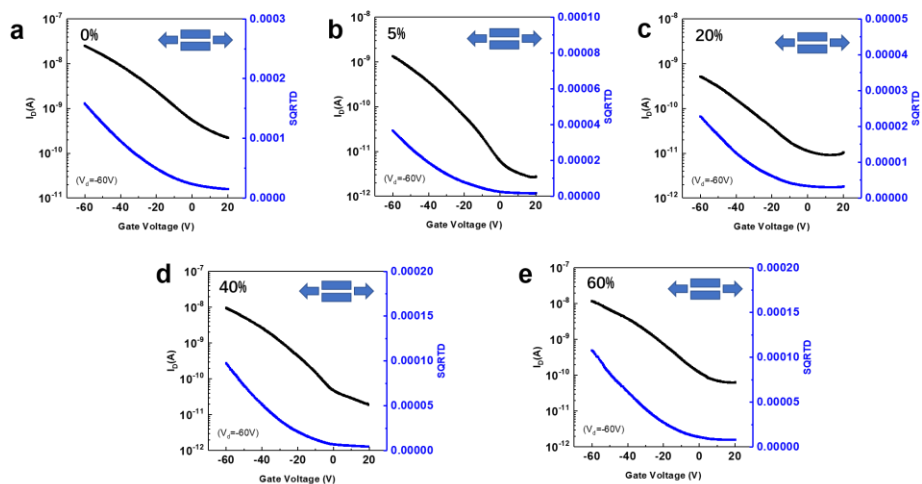


Figure C.9 FET transfer curves for stretched P3BT perpendicular to strain direction.

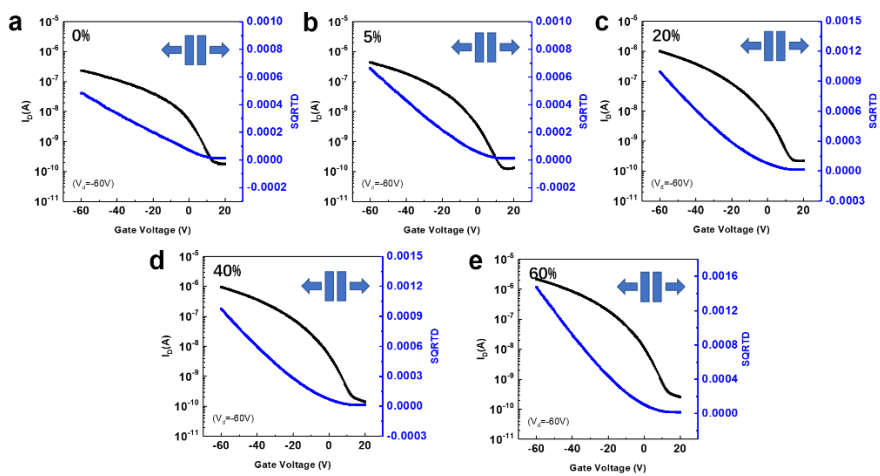


Figure C.10 FET transfer curves for stretched P3OT parallel to strain direction.

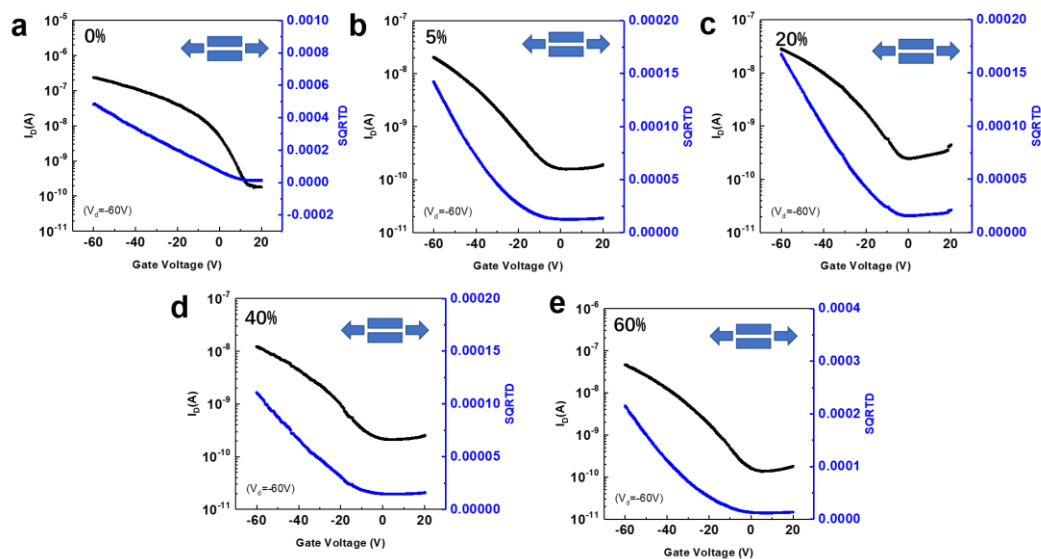


Figure C.11 *FET transfer curves for stretched P3OT perpendicular to strain direction.*

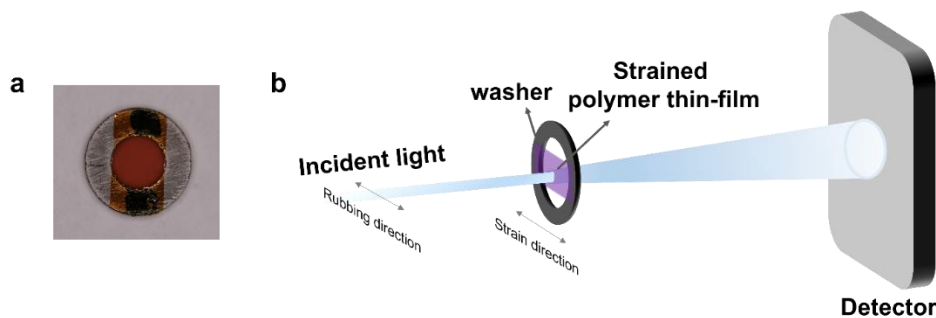


Figure C.12 (a) *Representative optical images of strained P3BT polymer thin films on top of hollow washers.* (b) *Schematic of transmission x-ray scattering on tensile strained free-standing thin films. The rubbing direction of the polarized X-ray beam is also shown.*

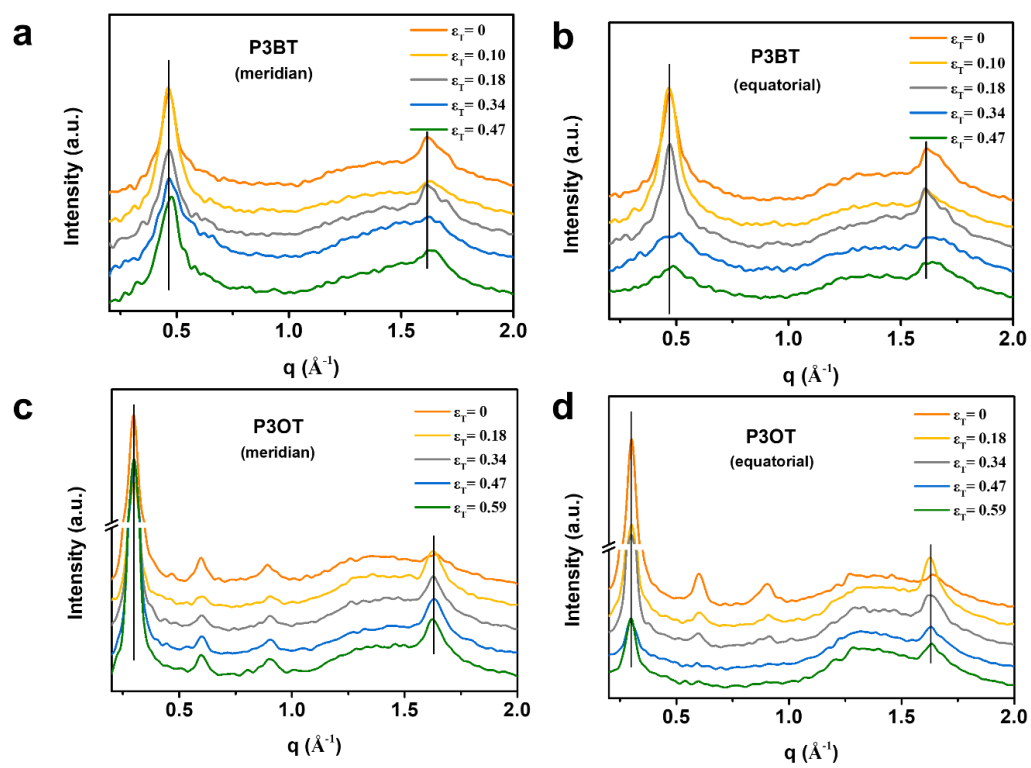


Figure C.13 1D integration for P3BT and P3OT thin films under various degrees of strain from wide-angle hard X-ray scattering.

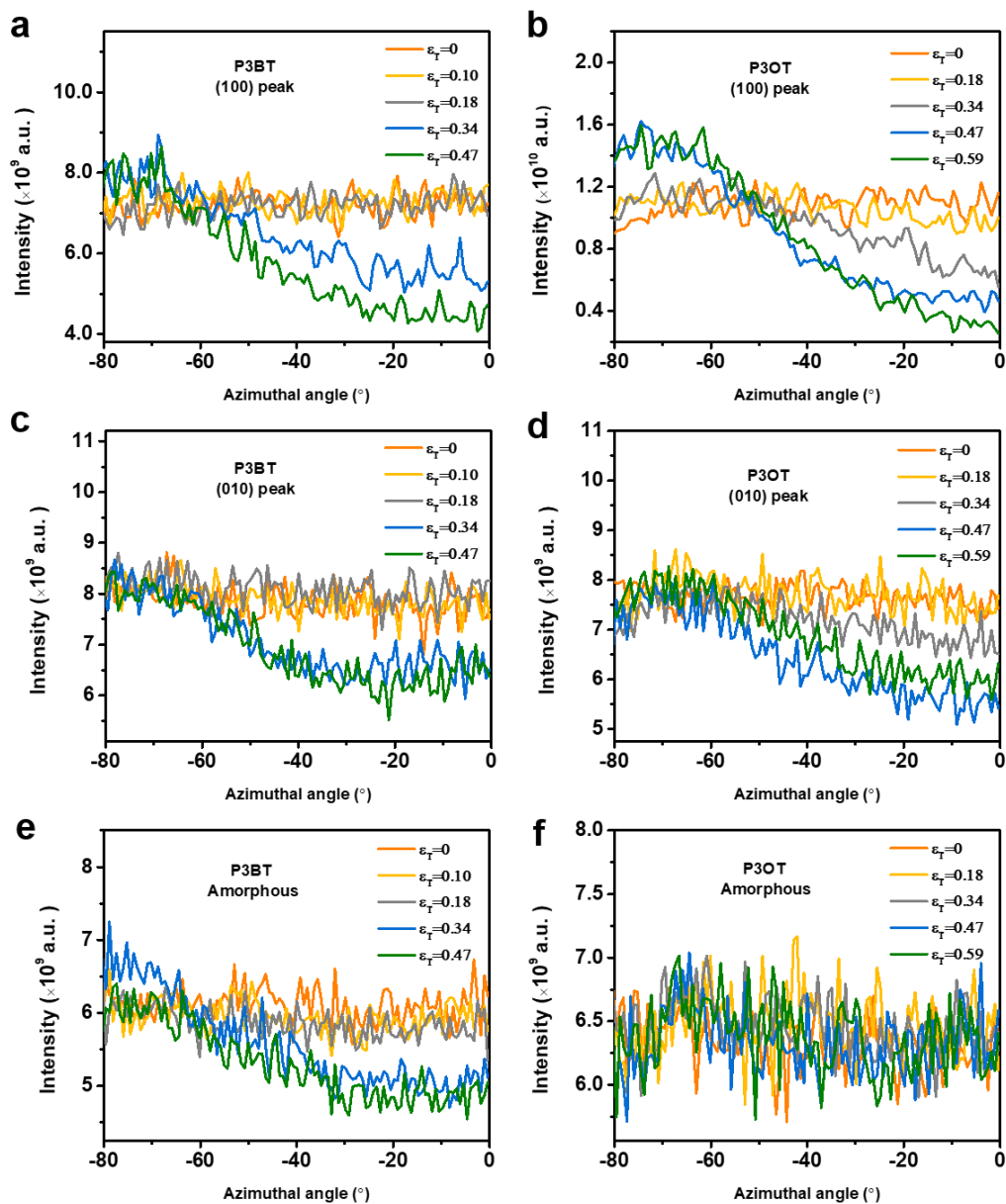


Figure C.14 Pole figure analysis for strained (a, c, e) P3BT and (b, d, f) P3OT polymer based on wide-angle hard X-ray scattering result. (a, b) (100) peak, (c, d) (010) peak, (e, f) Amorphous peak.

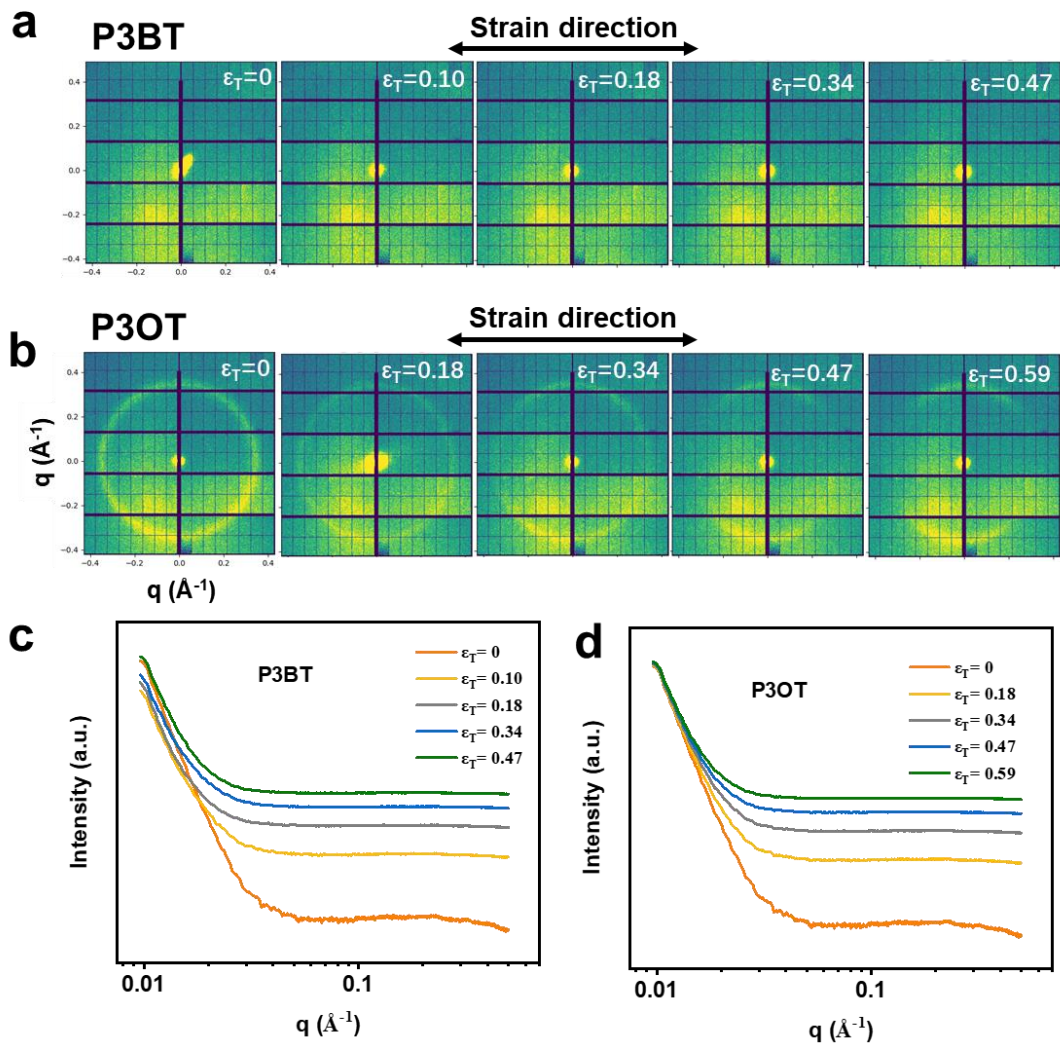


Figure C.15 Small-angle hard X-ray scattering 2D patterns and 1d line-cut of strained P3BT and P3OT thin films. (a, b) 2D scattering patterns for thin-films under various degrees of strain, (c, d) 1D radial averaged intensity versus q plot.

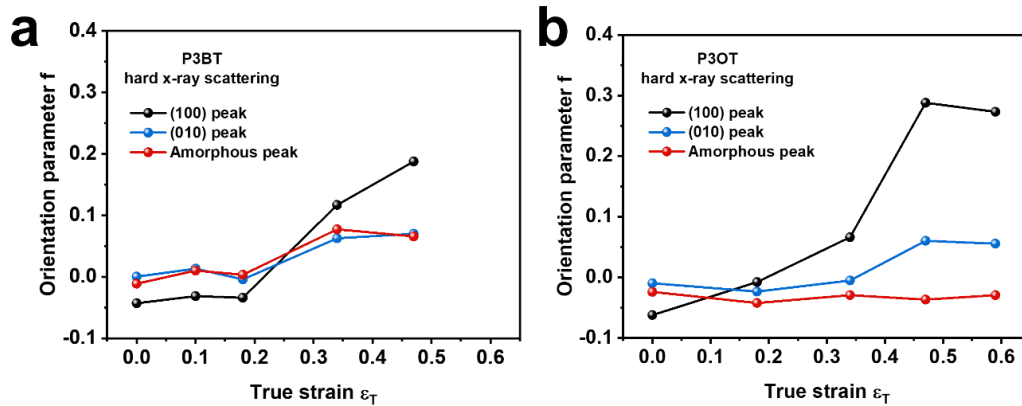


Figure C.16 Herman's orientation parameter f versus strain based on (100) peak of P3BT and P3OT from (b) hard and (d) tender WAXS. f from (010) peak slightly increased at $\epsilon_T = 0.47$. No clear alignment from the amorphous halo was observed.

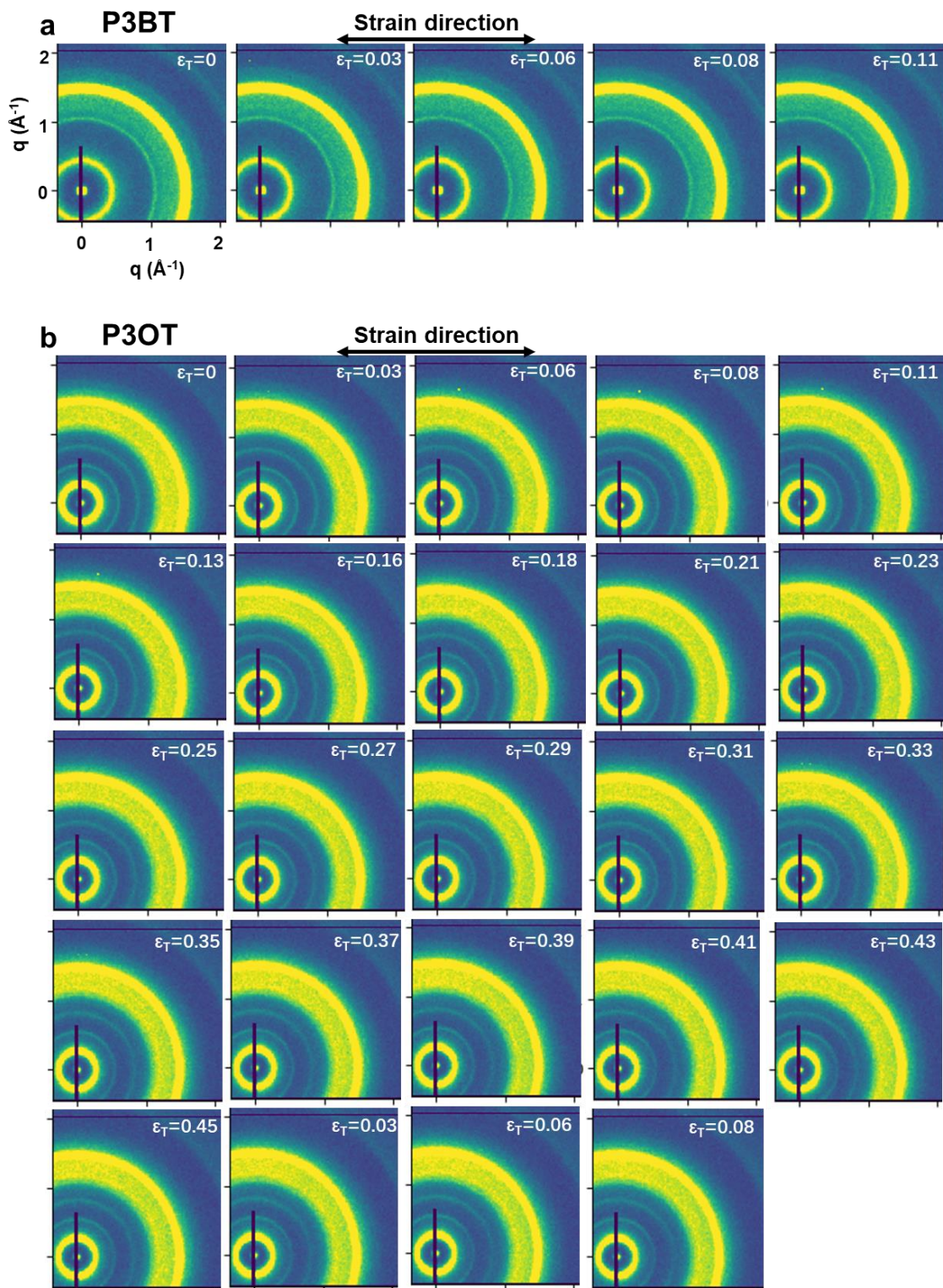


Figure C.17 *In Situ* wide-angle hard X-ray scattering 2D patterns of strained (a) P3BT and (b) P3OT thin films.

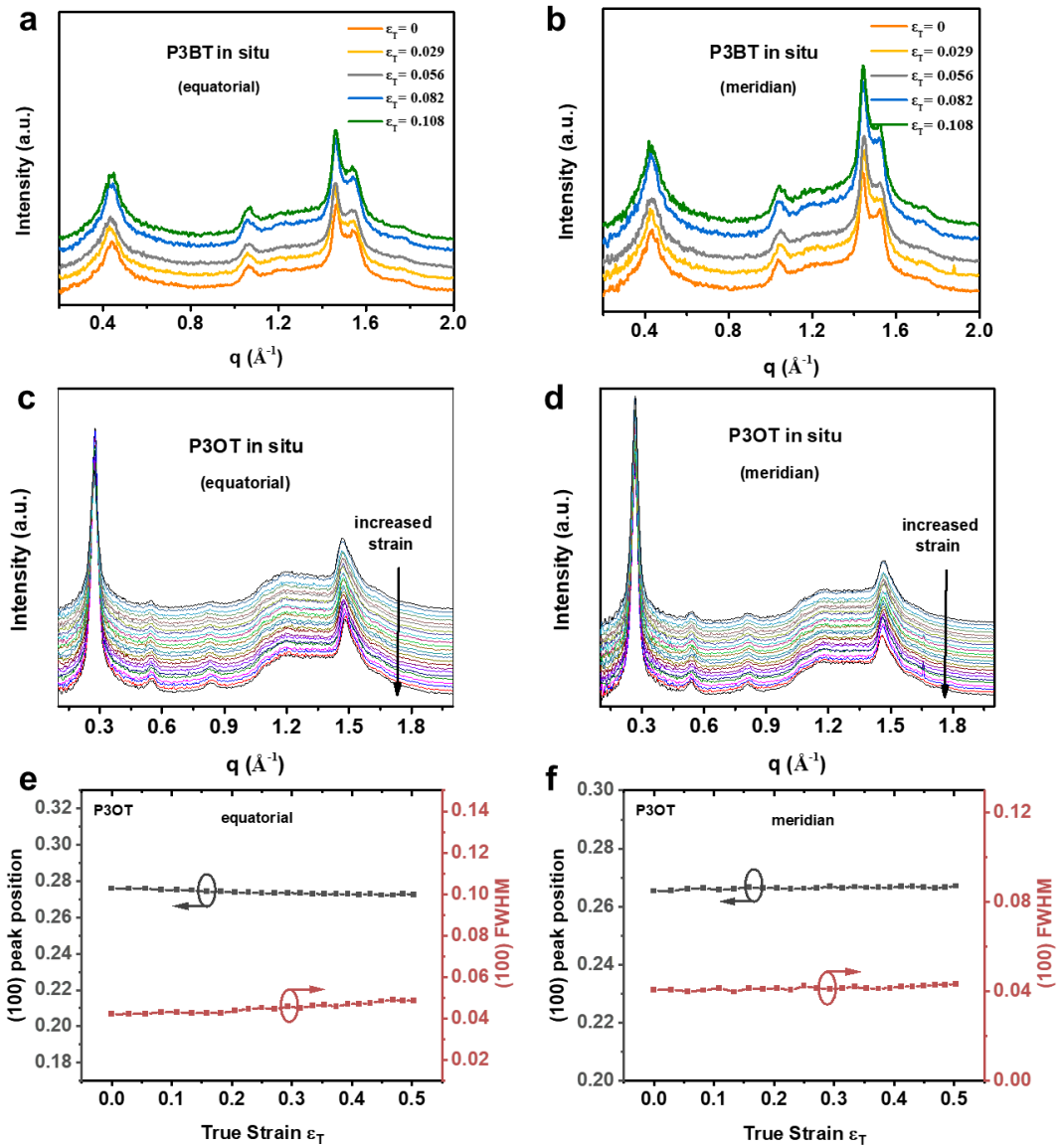


Figure C.18 *ID* integration for (a, b) P3BT and (c, d) P3OT thin-films under various degrees of strain from in situ Wide-angle hard X-ray scattering. (e) (100) peak position and (f) FWHM of P3OT under various degrees of strain.

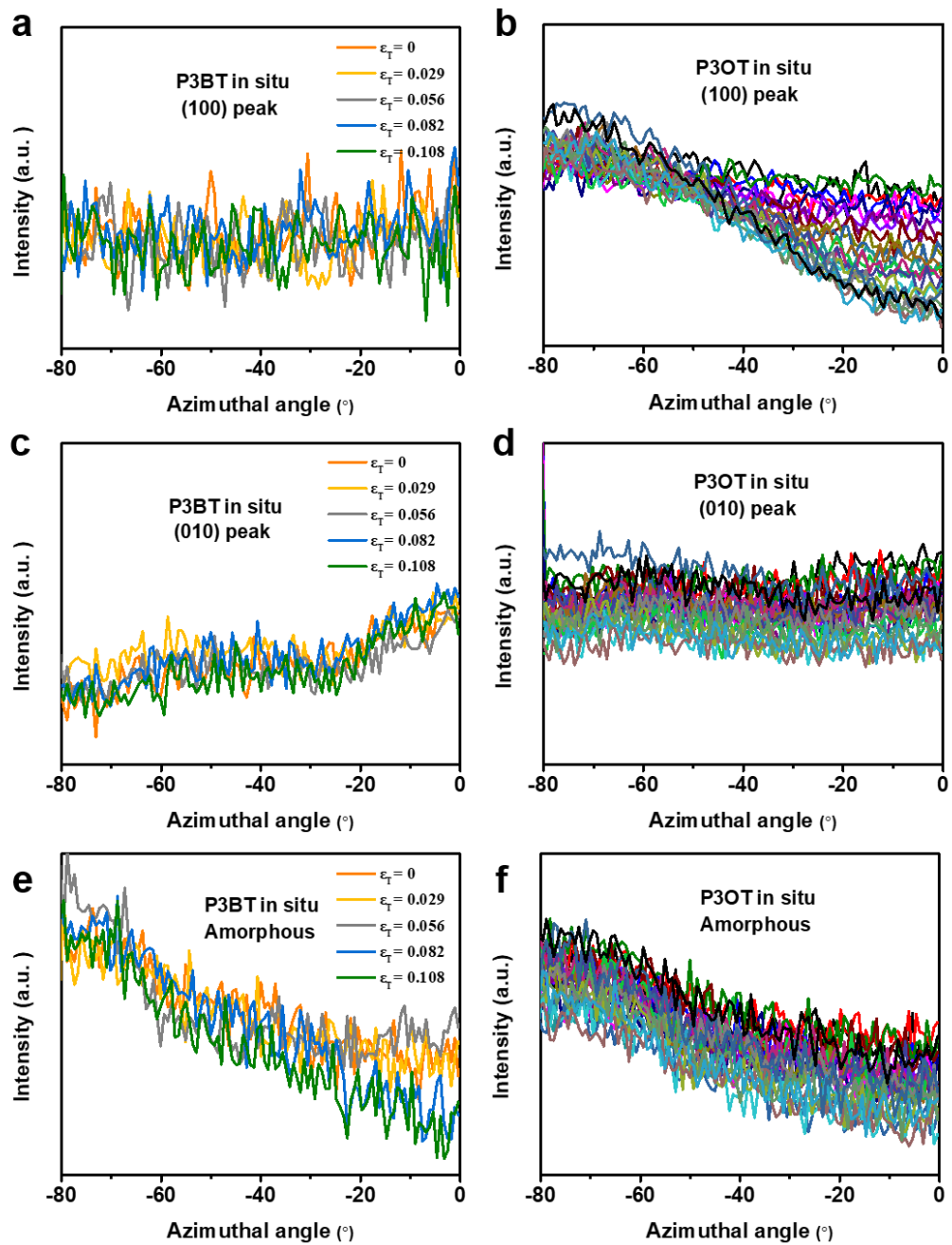


Figure C.19 Pole figure analysis for strained (a, c, e) P3BT and (b, d, f) P3OT polymer based on in situ wide-angle hard X-ray scattering result. (a, b) (100) peak, (c, d) (010) peak, (e, f) Amorphous peak.

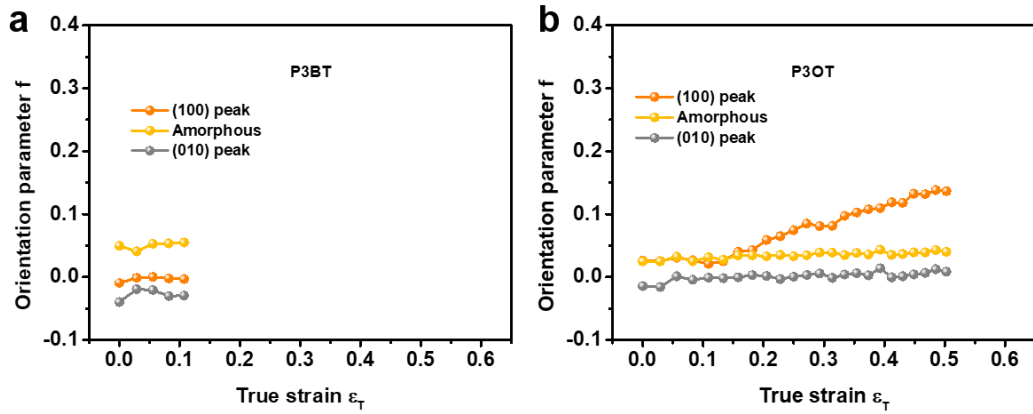


Figure C.20 Herman's orientation parameter f versus strain based on (100) peak, (010) peak, and amorphous halo of (a) P3BT and (b) P3OT from in situ hard WAXS experiment.

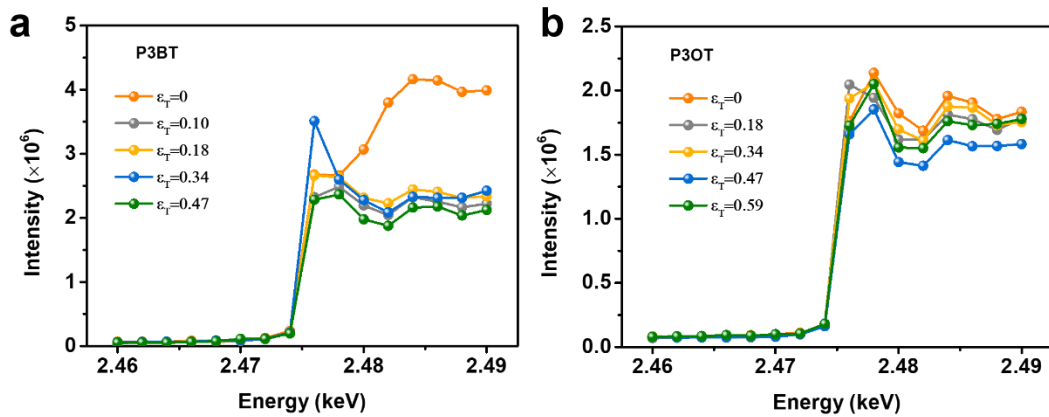


Figure C.21 The plot of background scattering intensity of (a) P3BT and (b) P3OT at various incident X-ray energies, indicating the fluorescence yield of sulfur atom at different energies, which corresponds to the sulfur absorption. The absorption starts from 2470 eV and the maximum absorption is shown at 2478 eV.

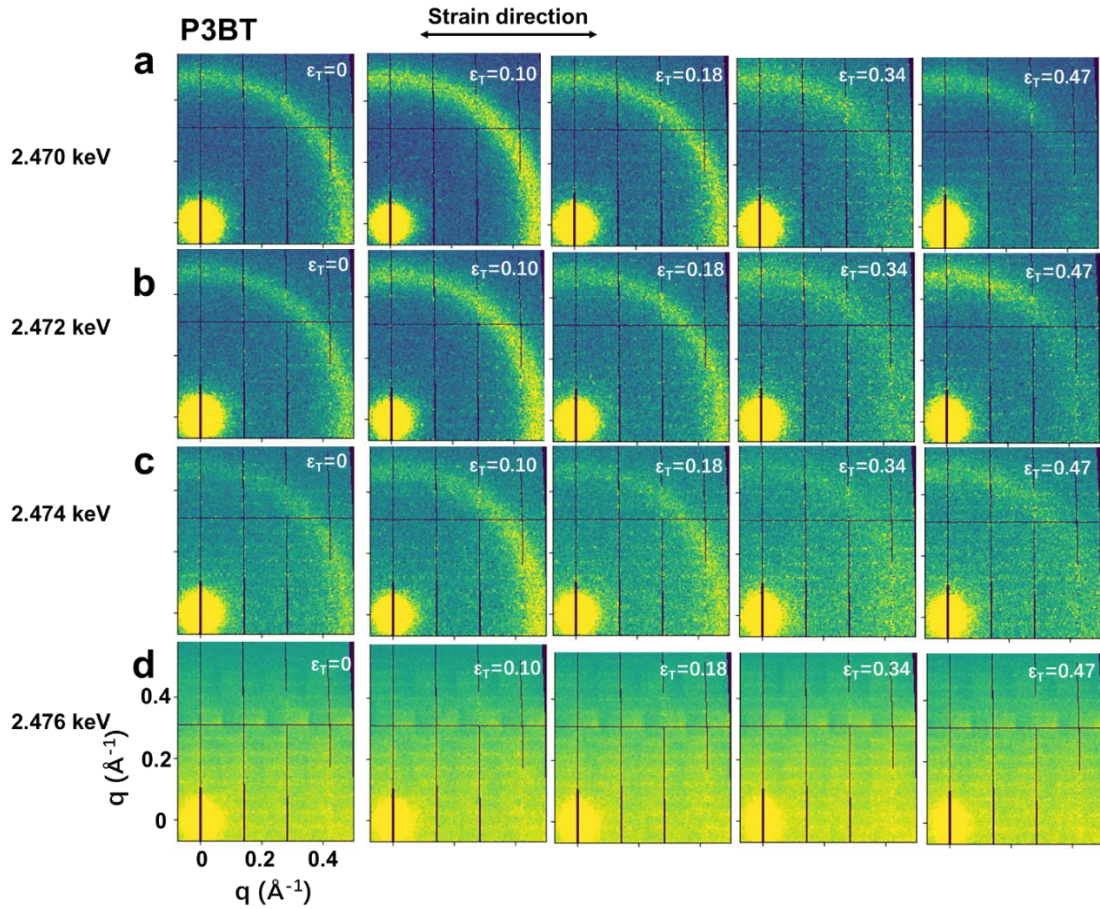


Figure C.22 Wide-angle tender X-ray scattering 2D patterns of strained P3BT thin films at different energies.

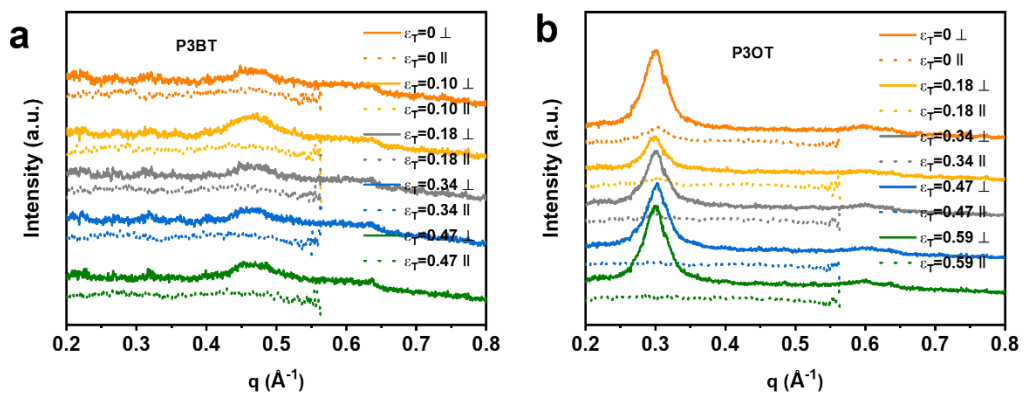


Figure C.23 1D integration for P3BT and P3OT thin-films under various degrees of strain from wide-angle tender X-ray scattering at different energies.

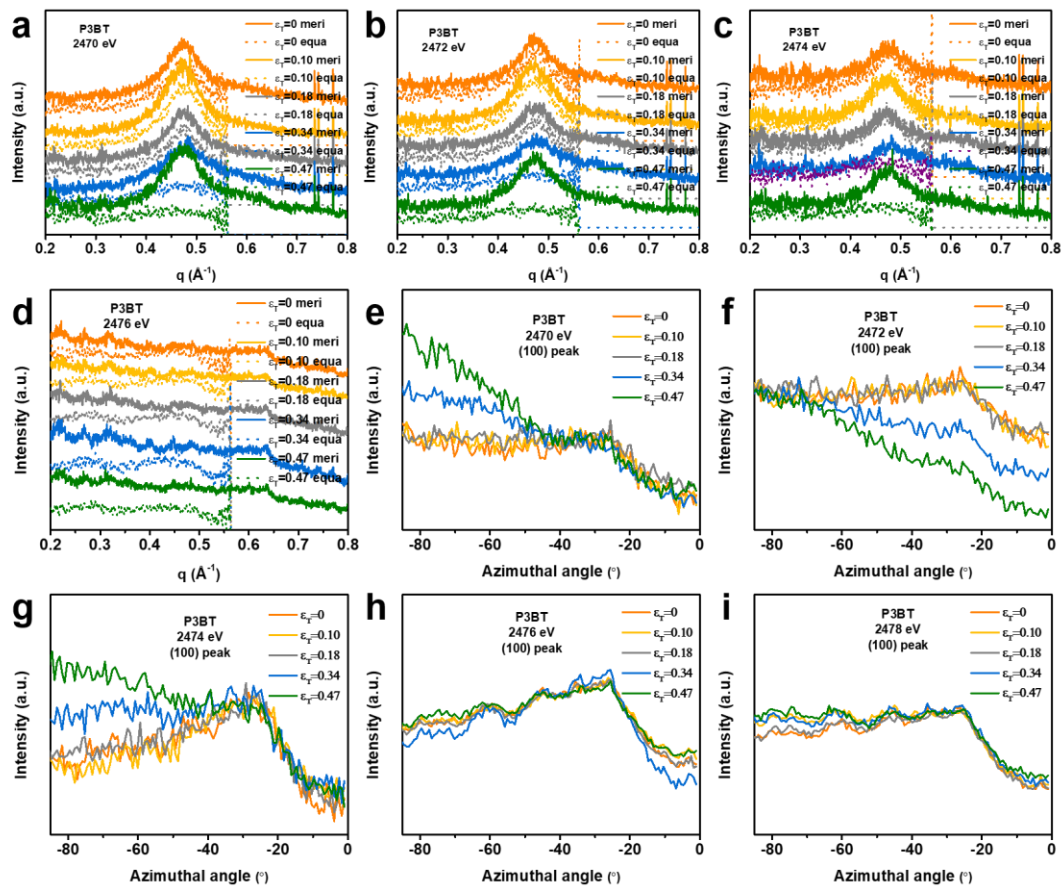


Figure C.25 1D line-cut (a-d) and (100) pole figure analysis (e-i) for strained P3BT thin films from tender X-ray scattering at different energies (a, e) 2.47 keV, (b, f) 2.472 keV, (c, g) 2.474 keV, (d, h) 2.476 keV, (i) 2.478 keV.

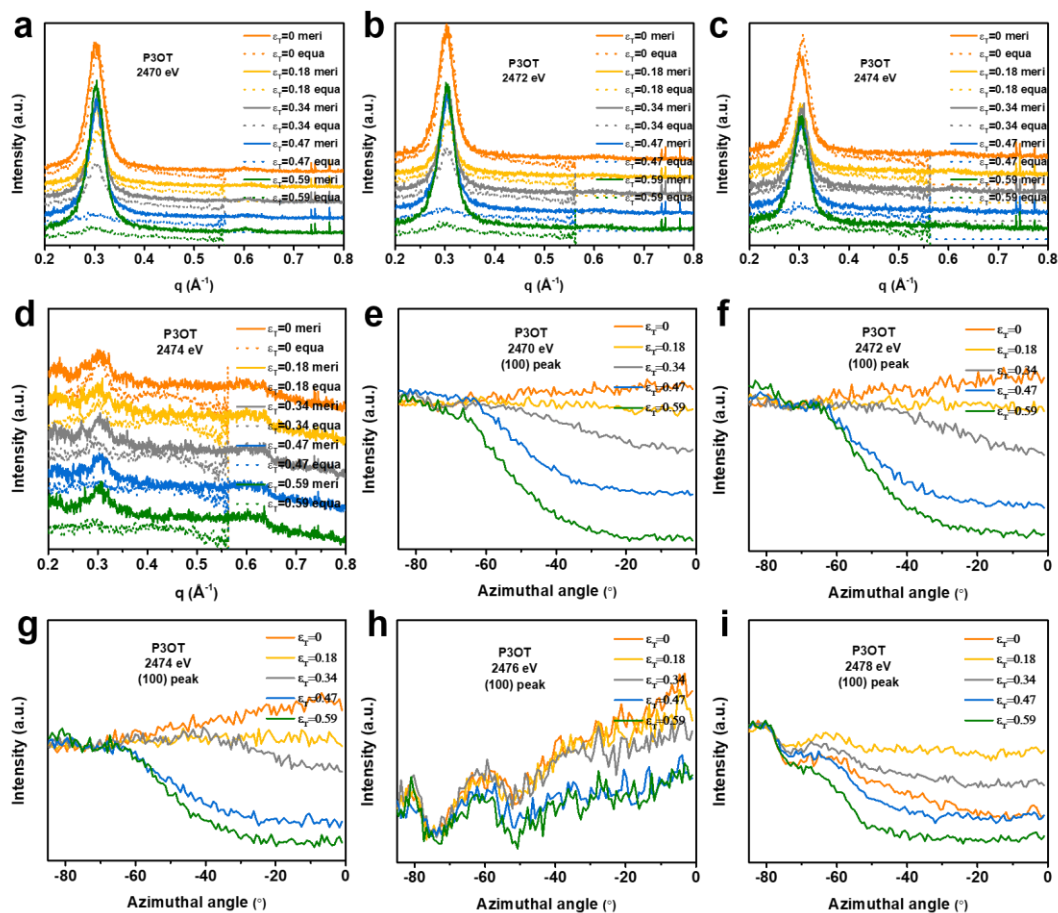


Figure C.26 1D line-cut (a-d) and (100) pole figure analysis (e-i) for strained P3OT thin films from tender X-ray scattering at different energies (a, e) 2.47 keV, (b, f) 2.472 keV, (c, g) 2.474 keV, (d, h) 2.476 keV, (i) 2.478 keV.

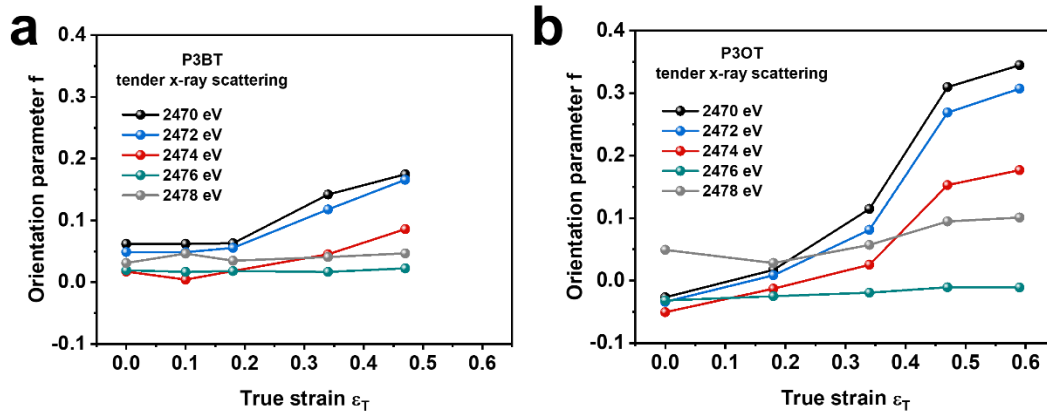


Figure C.27 Herman's orientation parameter f versus strain of (a) P3BT and (b) P3OT from tender X-ray scattering at different energies.

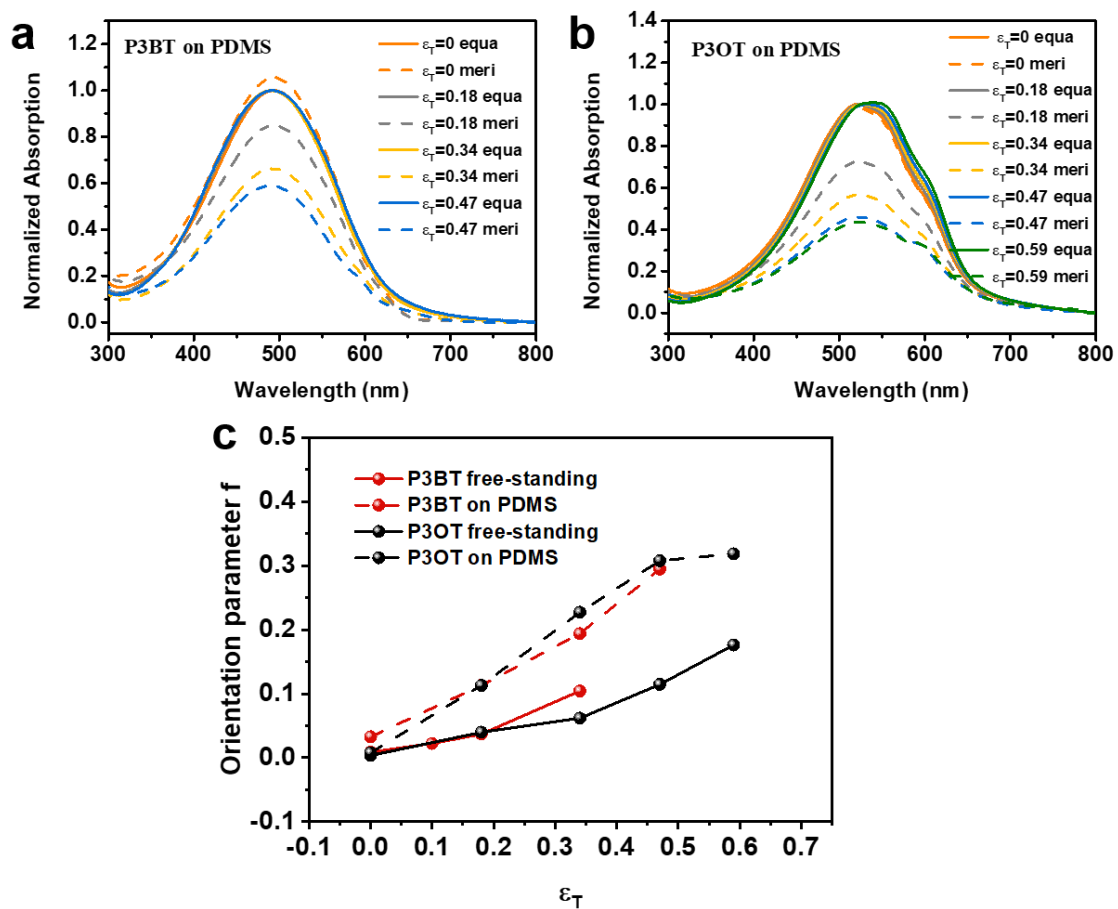


Figure C.28 UV-vis absorption spectroscopy result and orientation parameter for strained P3BT and P3OT thin films supported on the PDMS substrate.

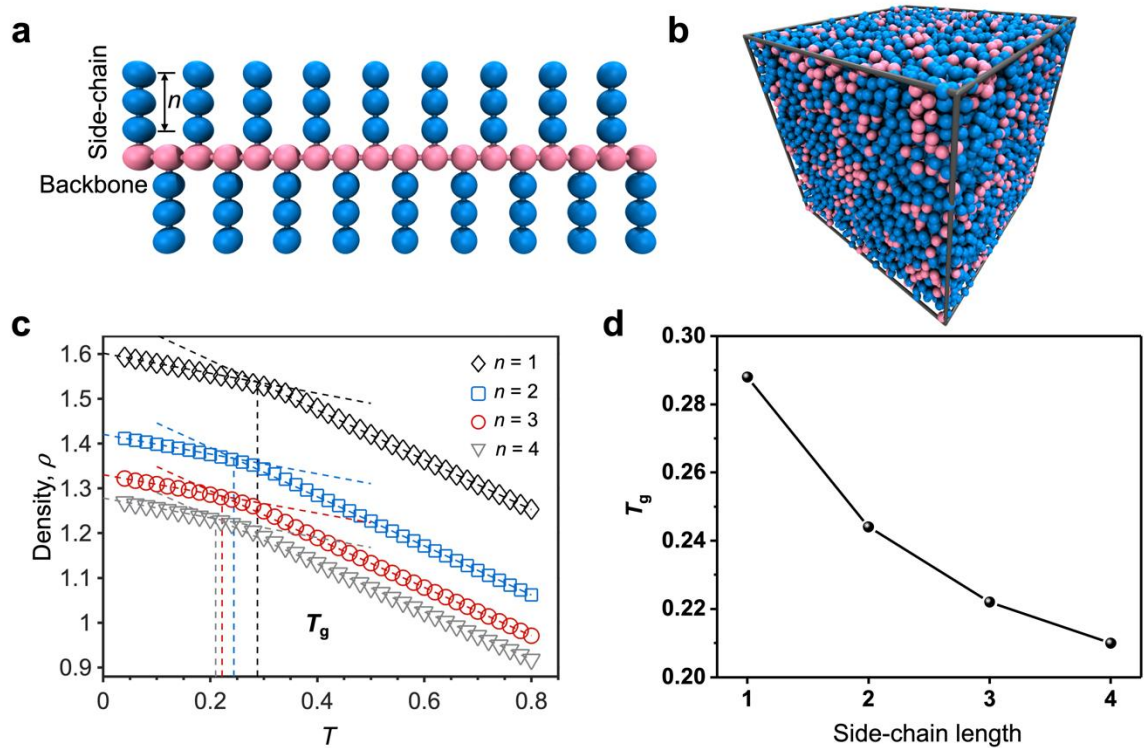


Figure C.29 (a) Schematic illustration of CG polymer model with different side-chain length varying from 1 to 4. (b) Snapshot of the bulk simulation box consisting of polymer chains. (c) Density vs. temperature for calculation of T_g of the CG bulk system with various side-chain length. The intersection of two distinct slopes was determined as value of the predicted T_g . (d) Simulated T_g vs. side-chain length n .

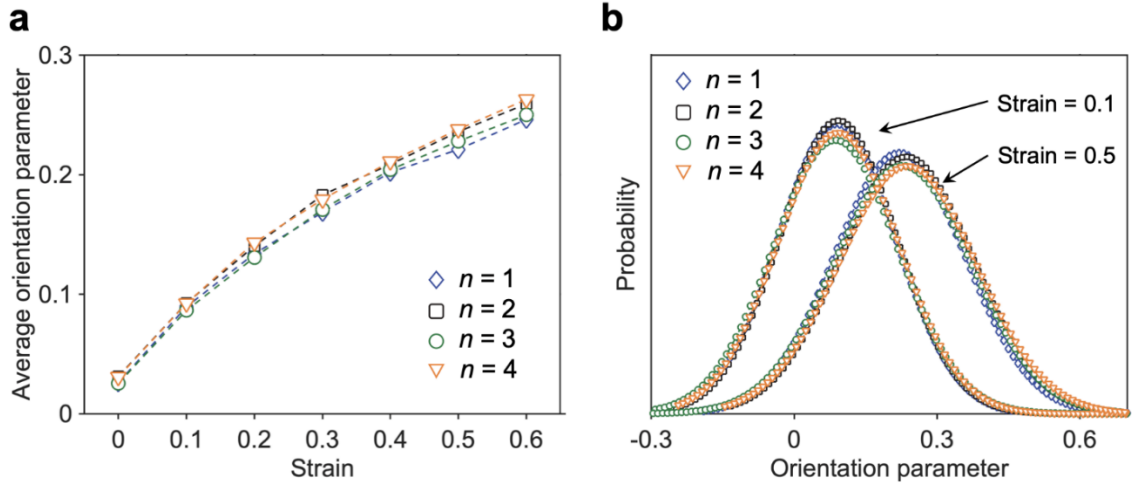


Figure C.30 (a) Averaged orientation parameter S within the films vs. strain for various side-chain length n at a certain T . (b) Probability distribution of local orientation parameter of the CG thin film model for various side-chain length n under two representative strain upon deformation.

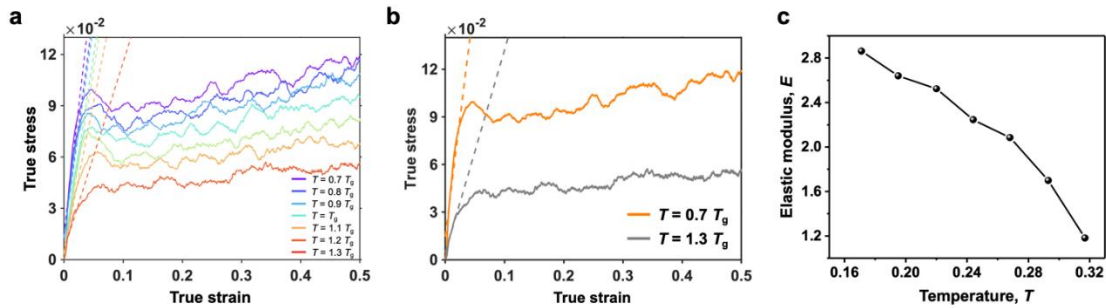


Figure C.31 (a) Representative tensile stress-strain response of polymer thin film system for different T , where the elastic modulus E was determined by linearly fitting the stress-strain data within 3% strain as marked by the dashed lines. (b) Representative tensile stress-strain response of polymer thin film system for two representative T . (c) Elastic modulus vs. T for polymer thin film system. CG-MD simulation results were expressed using the reduced LJ units.

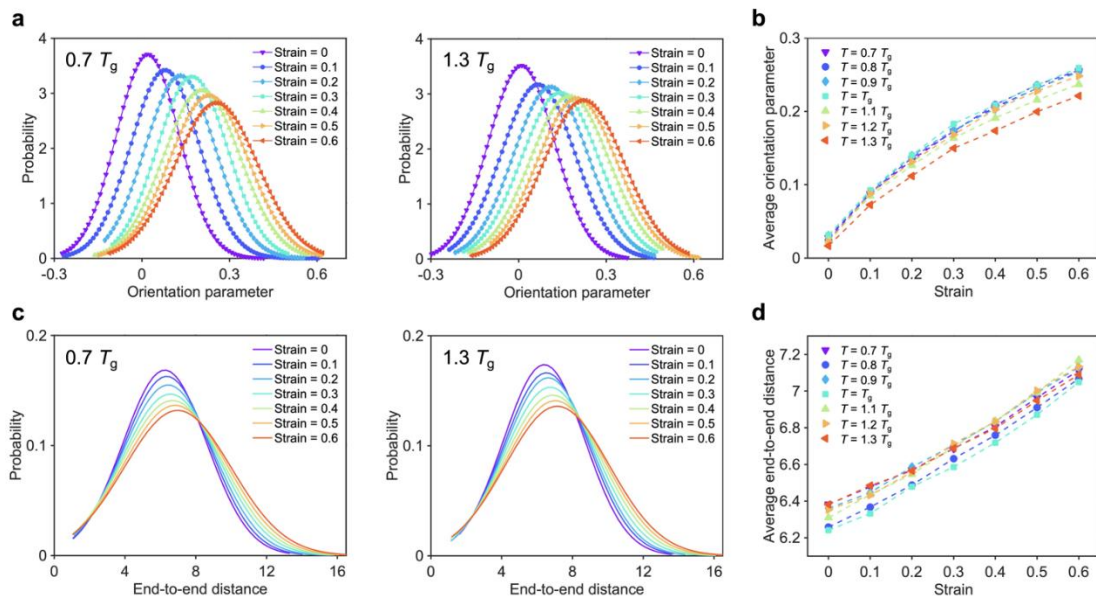


Figure C.32 (a) Probability distribution of local orientation parameter of the CG thin film model under various strain upon deformation for two representative T . (b) Averaged orientation parameter f within the films vs. strain at different T . (c) Probability distribution of end-to-end distance under various strain upon deformation for two representative T . (d) Averaged end-to-end distance within the films vs. strain at different T .

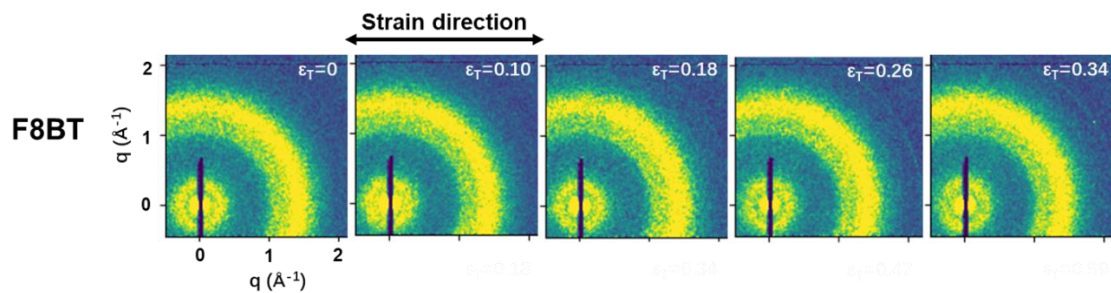


Figure C.33 Wide-angle hard X-ray scattering 2D patterns of strained F8BT.

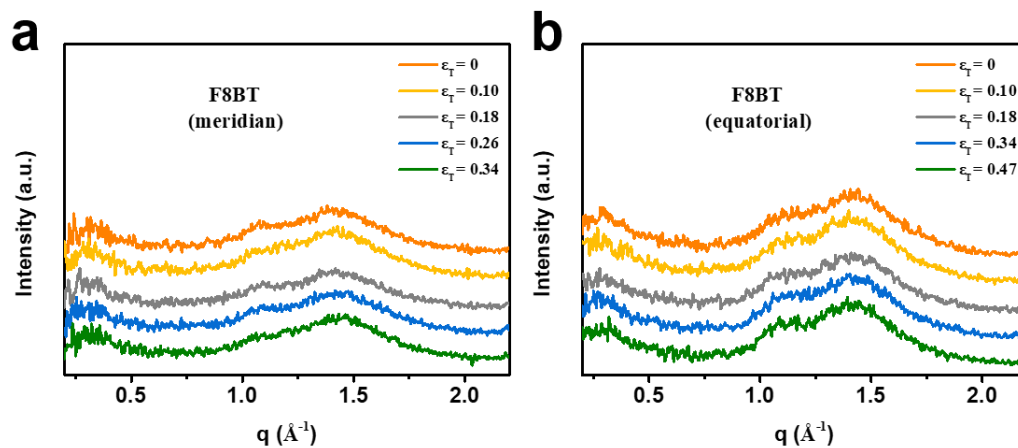


Figure C.34 Wide-angle hard X-ray scattering 1D line-cut of strained F8BT.

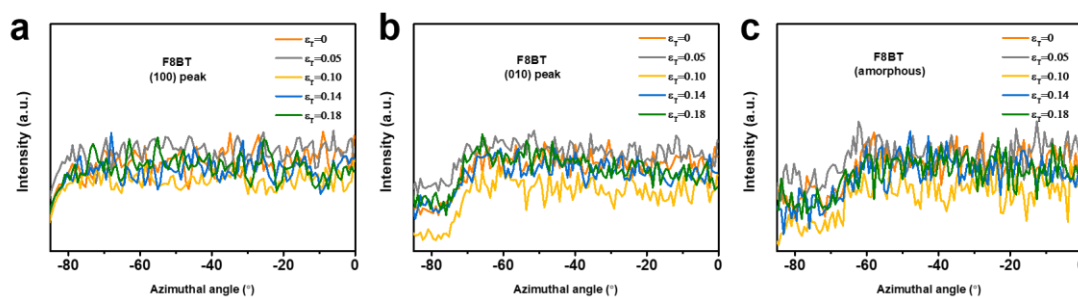


Figure C.35 Pole figure analysis for strained F8BT polymer based on wide-angle hard X-ray scattering result. (a) (100) peak, (b) (010) peak, (c) Amorphous peak.

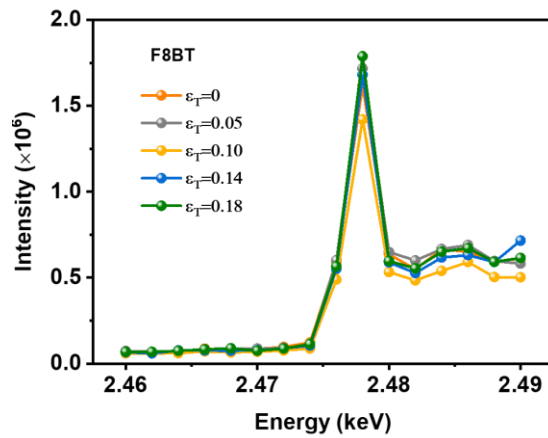


Figure C.36 Wide-angle tender X-ray scattering experiment for F8BT under various strain. The plot of background scattering intensity of F8BT at various incident X-ray energies

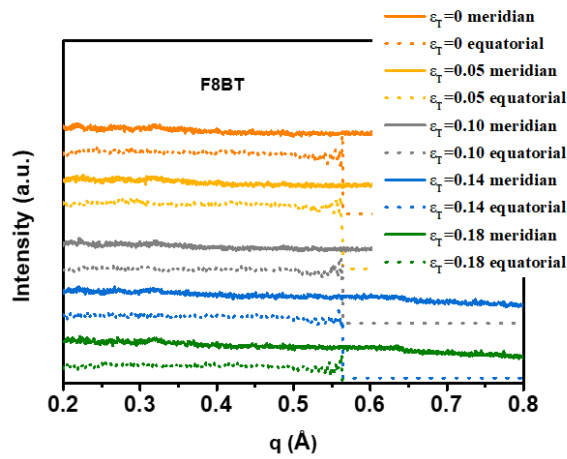


Figure C.37 Wide-angle tender X-ray scattering 1D line-cut of strained F8BT.

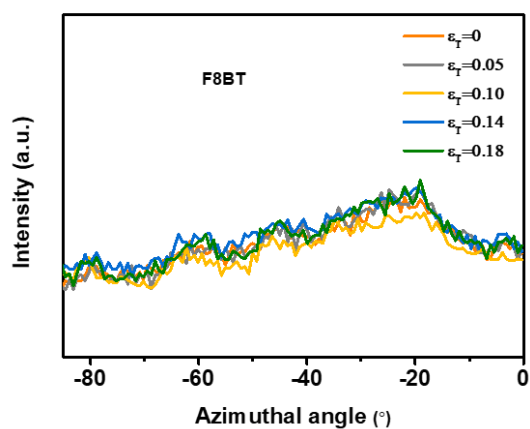


Figure C.38 Wide-angle tender X-ray scattering pole figure analysis of strained F8BT.

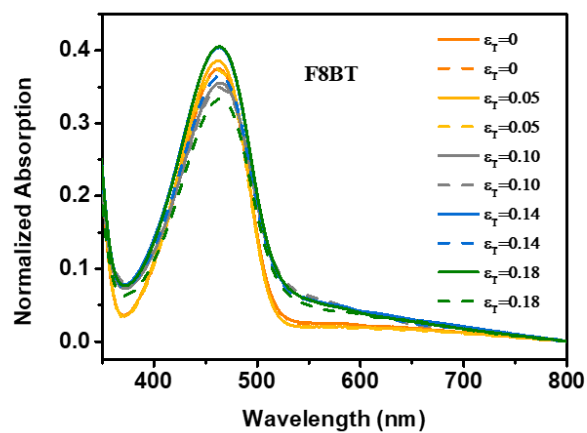


Figure C.39 UV-vis absorption spectroscopy result for stretched F8BT thin films.

Table C.1 Summarized molecular weight (MW), elastic modulus (E) and crack onset strain (COS) of CPs.

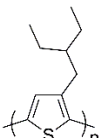
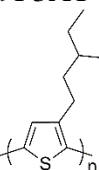
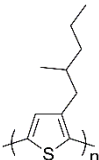
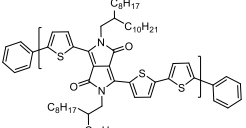
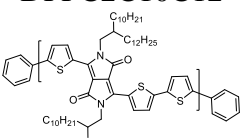
Type	Polymer	brand	MW (kDa)	COS	E (MPa)
P3AT	P3BT 	Rieke	50-70	0.805	2177
	P3HT 	Sigma-Aldrich	50-70	1.22	262
	P3OT 	Rieke	70-90	1.38	85
	P3DT 	Rieke	50-70	1.08	79
	branched P3AT-C2C2C2 	-	14.1	0.015	990
	branched P3AT-C3C1C2 	-	17.3	0.012	709
	branched P3AT-C2C1C3 	-	20.5	0.018	1205
DPP	DPPC2C8C10 	-	76.6	0.953	298.6
	DPPC2C10C12 	-	19.0	0.039	184

Table C.1 (continued). Summarized molecular weight (MW), elastic modulus (E) and crack onset strain (COS) of CPs.

<p>DPPC2C10C12</p>	-	47.0	0.53	173
<p>DPPC2C10C12</p>	-	60.6	0.649	150.8
<p>DPPTC2C12C14</p>	-	61.8	0.804	104.2
<p>DPPT2C2C10C12</p>	-	23.0	0.04	280
<p>DPPT2C2C10C12</p>	-	24.0	0.2	250
<p>DPPT3C2C10C12</p>	-	34.0	0.3	415
<p>DPPT3C8C2C10C12</p>	-	26.7	0.275	161.14
<p>DPPTTC2C10C12</p>	-	29.0	0.02	255

Table C.1 (continued). Summarized molecular weight (MW), elastic modulus (E) and crack onset strain (COS) of CPs.

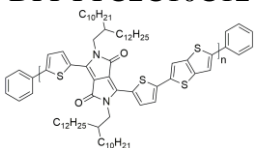
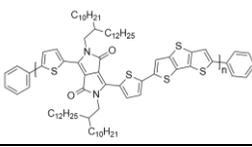
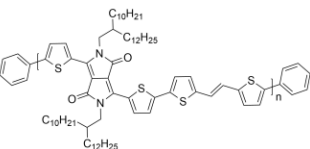
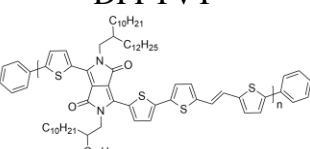
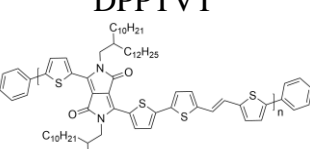
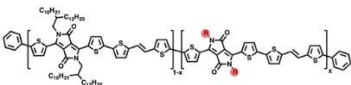
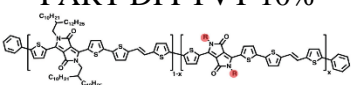
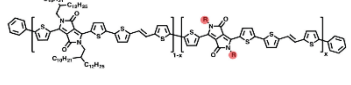
<p>DPPTTC2C10C12</p> 	-	51.0	0.16	400
<p>DPPTTC2C10C12</p> 	-	26.0	0.03	480
<p>DPPTVT</p> 	-	15.7	0.05	248
<p>DPPTVT</p> 	-	17.7	0.105	270
<p>DPPTVT</p> 	-	27.5	0.38	338
<p>PART DPPTVT 5%</p>  <p>P5: $R = \frac{1}{2} C_{12}H_{25}$, $x = 0.05$ (5 mol%)</p>	-	52.0	0.27	340
<p>PART DPPTVT 10%</p>  <p>P6: $R = \frac{1}{2} C_{12}H_{25}$, $x = 0.1$ (10 mol%)</p>	-	52.0	0.24	325
<p>PART DPPTVT 20%</p>  <p>P7: $R = \frac{1}{2} C_{12}H_{25}$, $x = 0.2$ (20 mol%)</p>	-	18.0	0.22	320

Table C.1 (continued). Summarized molecular weight (*MW*), elastic modulus (*E*) and crack onset strain (*COS*) of CPs.

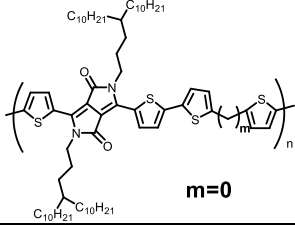
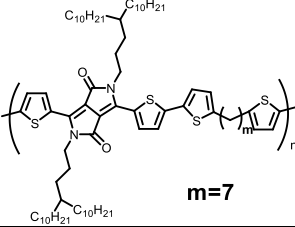
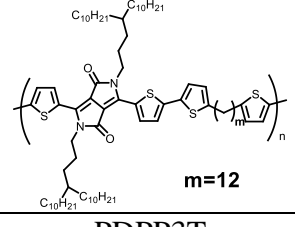
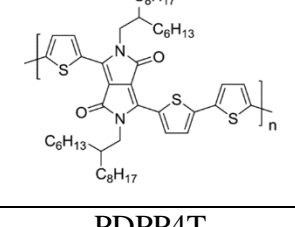
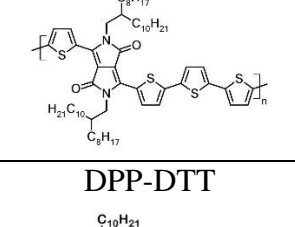
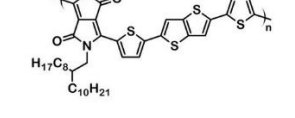
<p style="text-align: center;">DPPC0</p>  <p style="text-align: center;">m=0</p>	-	-	0.035	263
<p style="text-align: center;">DPPC7</p>  <p style="text-align: center;">m=7</p>	-	-	0.035	153
<p style="text-align: center;">DPPC12</p>  <p style="text-align: center;">m=12</p>	-	-	0.05	50
<p style="text-align: center;">PDPP3T</p>  <p style="text-align: center;">m=3</p>	Ossila	24.0	0.282	419.16
<p style="text-align: center;">PDPP4T</p>  <p style="text-align: center;">m=4</p>	Ossila	65.0	0.347	834
<p style="text-align: center;">DPP-DTT</p>  <p style="text-align: center;">m=4</p>	Ossila	54.0	0.33	758.2

Table C.1 (continued). Summarized molecular weight (MW), elastic modulus (E) and crack onset strain (COS) of CPs.

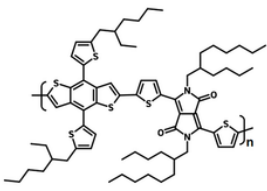
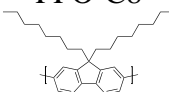
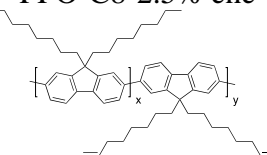
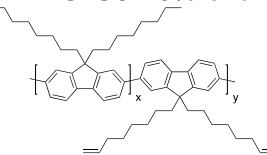
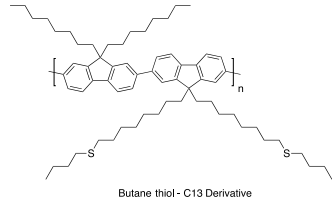
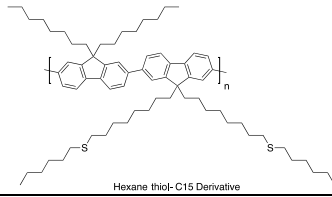
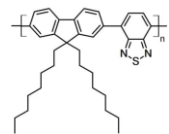
	<p>PBDTT-DPP</p> 	Ossila	120.2	0.078	872
	<p>PFO-C8</p> 	-	20.0	0.425	1689
	<p>PFO-C8-2.5% ene</p> 	-	22.9	0.5	1523
	<p>PFO-C8-10% ene</p> 	-	36.0	0.34	2007
	<p>PFOC8C13</p>  <p>Butane thiol - C13 Derivative</p>	-	9.3	0.33	861
PFO	<p>PFOC8C15</p>  <p>Hexane thiol- C15 Derivative</p>	-	9	0.63	370
	<p>F8BT</p> 	Ossila	26.79	0.225	1807

Table C.1 (continued). Summarized molecular weight (*MW*), elastic modulus (*E*) and crack onset strain (*COS*) of CPs.

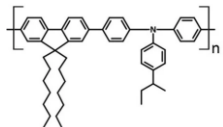
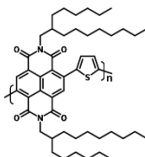
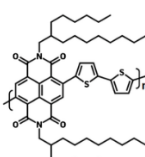
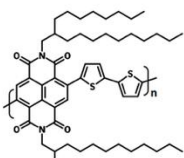
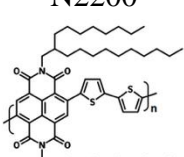
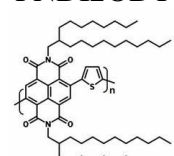
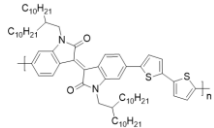
	<p>TFB</p> 	Ossila	10.25	0.03	1640
	<p>PNDI2HDT</p> 	Ossila	108	0.82	903.52
	<p>PNDI2HD2T</p> 	Ossila	89.3	0.18	1448
	<p>PNDI2OD2T</p> 	Ossila	66.8	0.61	1035
	<p>N2200</p> 	-	-	0.35	635
NDI	<p>PNDI2ODT</p> 	Ossila	91.7	0.82	433
	<p>IIDC2C10C10</p> 	Ossila	-	0.008	347

Table C.1 (continued). Summarized molecular weight (MW), elastic modulus (E) and crack onset strain (COS) of CPs.

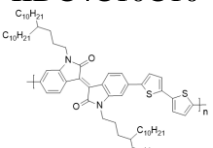
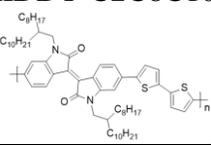
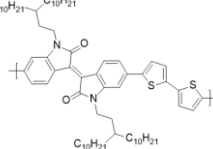
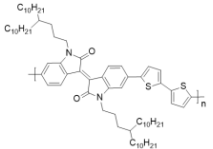
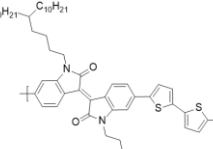
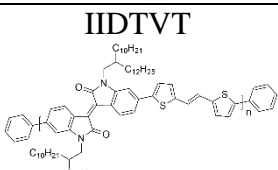
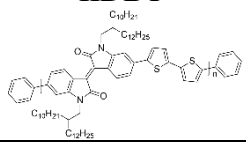
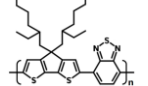
	<p>IIDC4C10C10</p> 	Ossila	-	0.009	263
	<p>IIDDT-C2C8C10</p> 	-	-	0.04	655.57
	<p>IIDDT-C3C10C10</p> 	-	-	0.026	360.72
IID	<p>IIDDT-C4C10C10</p> 	-	-	0.036	410
	<p>IIDDT-C5C10C10</p> 	-	-	0.02	349.44
	<p>IIDTVT</p> 	-	18.7	0.021	580
	<p>IIDBT</p> 	-	23.0	0.016	330
	<p>PCPDTBT</p> 	Ossila	17.77	0.04	2577

Table C.1 (continued). Summarized molecular weight (*MW*), elastic modulus (*E*) and crack onset strain (*COS*) of CPs.

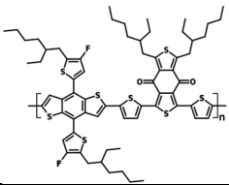
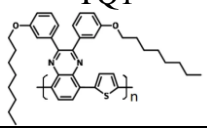
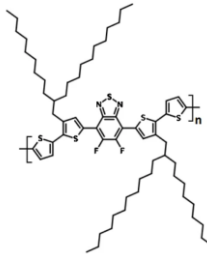
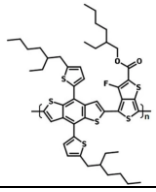
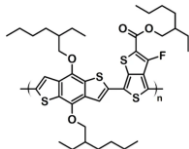
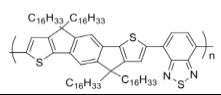
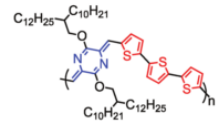
	<p>PM6</p> 	Ossila	42.67	0.124	1052
	<p>TQ1</p> 	Ossila	25.73	0.114	1017
	<p>PCE12</p> 	Ossila	62.32	0.035	1033
Others	<p>PCE10</p> 	Ossila	24.21	0.128	663
	<p>PTB7</p> 	Ossila	22.1	0.055	446
	<p>IDTBT</p> 	-	-	0.22	745
	<p>PA3T-BC2-CL0CL2</p>  <p>PA3T-BC2-C10C12</p>	-	103	0.17	103

Table C.1 (continued). Summarized molecular weight (*MW*), elastic modulus (*E*) and crack onset strain (*COS*) of CPs.

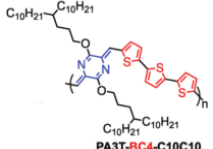
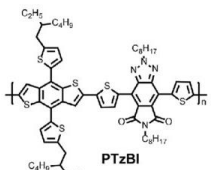
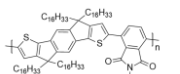
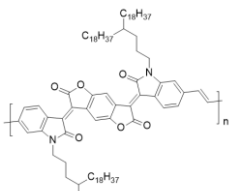
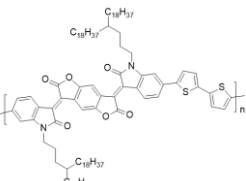
	<p style="text-align: center;">PA3T-BC4-CL0CL0</p>  <p style="text-align: center;">PA3T-BC4-C10C10</p>	-	81	0.6	81
	<p style="text-align: center;">PTzBI</p>  <p style="text-align: center;">PTzBI</p>	-	-	0.09	471
	<p style="text-align: center;">PIDTBDP</p> 	-	18	0.4	84
	<p style="text-align: center;">BDPPV318</p> 	-	27.4	0.006	333.35
	<p style="text-align: center;">BDOPVDT</p> 	-	35.4	0.01	211.44

Table C.2 Polymer characteristics for P3BT, P3OT and F8BT

Polymer	M_n (kDa) ¹	Dispersity ¹	Elastic modulus (MPa)	T_g (°C) ²
P3BT	12.3	2.81	2216 ± 30	52
P3OT	23.8	2.00	86 ± 2	-13
F8BT	26.8	2.73	1807 ± 82	111.6

¹The number-averaged molecular weight (M_n) and dispersity were obtained through high-temperature gel permeation chromatography.

² T_g were obtained using differential scanning calorimetry (DSC).

Table C.3 Summary of OFET device performance for P3BT under deformation.

	Strain (ϵ_T)	W/L	μ_{max} (cm ² V ⁻¹ s ⁻¹)	μ_{ave} (cm ² V ⁻¹ s ⁻¹)	on/off	Vt_sat (V)
Parallel	0	10	2.52E-05	9.50E-06 ± 0.0000017	1.58E+01	7.94
	0.05	10	6.10E-05	3.37E-05 ± 0.000024	1.33E+02	-24.46
	0.18	10	3.63E-04	2.69E-04 ± 0.00038	6.76E+02	-15.75
	0.34	10	8.12E-04	3.98E-04 ± 0.00024	1.16E+02	-12.52
	0.47	10	8.26E-04	3.29E-04 ± 0.00025	1.30E+02	-10.01
	Perpendicular	0	10	2.52E-05	9.50E-06 ± 0.0000017	1.58E+01
0.05		10	1.75E-05	1.02E-05 ± 0.0000072	3.11E+02	-14.92
0.18		10	7.93E-06	5.41E-06 ± 0.0000018	3.80E+01	-25.09
0.34		10	7.41E-05	3.10E-05 ± 0.00003	3.18E+02	-17.39
0.47		10	1.26E-05	9.86E-06 ± 0.000001	1.70E+01	3.80

Table C.4 Summary of OFET device performance for P3OT under deformation.

	Strain (ϵ_T)	W/L	μ_{\max} ($\text{cm}^2 \text{V}^{-1} \text{s}^{-1}$)	μ_{ave} ($\text{cm}^2 \text{V}^{-1} \text{s}^{-1}$)	on/off	V_{t_sat} (V)
Parallel	0	10	8.82E-03	$3.40\text{E-}03 \pm 0.0029$	2.70E+01	16.10
	0.05	10	7.59E-04	$3.52\text{E-}04 \pm 0.0002$	2.80E+01	17.62
	0.18	10	6.66E-04	$3.06\text{E-}04 \pm 0.00028$	1.01E+02	-14.05
	0.34	10	2.08E-04	$1.38\text{E-}04 \pm 0.000059$	2.39E+01	-1.12
	0.47	10	1.47E-03	$5.58\text{E-}04 \pm 0.00023$	7.68E+01	-11.60
	Perpendicular	0	10	3.99E-03	$3.51\text{E-}03 \pm 0.00045$	6.81E+03
0.05		10	4.15E-03	$3.36\text{E-}03 \pm 0.001$	2.60E+03	-14.73
0.18		10	4.58E-03	$4.04\text{E-}03 \pm 0.00054$	6.21E+03	-12.20
0.34		10	1.07E-02	$5.86\text{E-}03 \pm 0.0008$	6.22E+03	-11.26
0.47		10	1.14E-02	$8.01\text{E-}03 \pm 0.00085$	5.47E+03	-9.99

Table C.5 *Crystallographic information for F8BT extracted from wide-angle hard X-ray scattering.*

	ε_T	Equatorial direction				Meridian direction			
		(100)			(010)	(100)			(010)
		q (\AA^{-1})	β (\AA^{-1})	τ (\AA) ¹	q (\AA^{-1})	q (\AA^{-1})	β (\AA^{-1})	τ (\AA) ¹	q (\AA^{-1})
F 8 B T	0	0.32	0.11	6.8	1.42	0.33	0.17	4.2	1.42
	0.05	0.29	0.06	13.1	1.41	0.32	0.17	4.3	1.42
	0.10	0.31	0.11	6.3	1.42	0.31	0.14	5.1	1.42
	0.14	0.29	0.13	5.3	1.42	0.32	0.16	4.6	1.42
	0.18	0.31	0.14	5.0	1.41	0.32	0.20	3.7	1.44

¹⁾The coherence length τ is calculated by the Scherrer equation: $\tau = (K \cdot \lambda) / (\beta \cdot \cos\theta)$, where $K = 0.9$, $\lambda = 0.77 \text{ \AA}$ for X-ray energy of

16.1 keV, β is the FWHM, θ is the Bragg angle.

REFERENCES

- (1) Salleo, A. Charge Transport in Polymeric Transistors. *Mater. Today* **2007**, *10* (3), 38–45. [https://doi.org/10.1016/S1369-7021\(07\)70018-4](https://doi.org/10.1016/S1369-7021(07)70018-4).
- (2) Brédas, J. L.; Beljonne, D.; Coropceanu, V.; Cornil, J. Charge-Transfer and Energy-Transfer Processes in π -Conjugated Oligomers and Polymers: A Molecular Picture. *Chem. Rev.* **2004**, *104* (11), 4971–5003. <https://doi.org/10.1021/cr040084k>.
- (3) Laysandra, L.; Njotoprajitno, A.; Prakoso, S. P.; Chiu, Y. C. From Stretchable and Healable to Self-Healing Semiconducting Polymers: Design and Their TFT Devices. *Mater. Adv.* **2022**, *3* (19), 7154–7184. <https://doi.org/10.1039/d2ma00581f>.
- (4) Kim, D. C.; Shim, H. J.; Lee, W.; Koo, J. H.; Kim, D. H. Material-Based Approaches for the Fabrication of Stretchable Electronics. *Adv. Mater.* **2020**, *32* (15), 1902743. <https://doi.org/10.1002/adma.201902743>.
- (5) Ashizawa, M.; Zheng, Y.; Tran, H.; Bao, Z. Intrinsically Stretchable Conjugated Polymer Semiconductors in Field Effect Transistors. *Prog. Polym. Sci.* **2020**, *100*, 101181. <https://doi.org/10.1016/j.progpolymsci.2019.101181>.
- (6) Zheng, Y.; Zhang, S.; Tok, J. B. H.; Bao, Z. Molecular Design of Stretchable Polymer Semiconductors: Current Progress and Future Directions. *J. Am. Chem. Soc.* **2022**, *144* (11), 4699–4715. <https://doi.org/10.1021/jacs.2c00072>.
- (7) Lee, H.; Jiang, Z.; Yokota, T.; Fukuda, K.; Park, S.; Someya, T. Stretchable Organic Optoelectronic Devices: Design of Materials, Structures, and Applications. *Mater. Sci. Eng. R Reports* **2021**, *146* (April), 100631. <https://doi.org/10.1016/j.mser.2021.100631>.
- (8) Kim, J. H.; Lee, I.; Kim, T. S.; Rolston, N.; Watson, B. L.; Dauskardt, R. H. Understanding Mechanical Behavior and Reliability of Organic Electronic Materials. *MRS Bull.* **2017**, *42* (2), 115–123. <https://doi.org/10.1557/mrs.2017.3>.
- (9) Root, S. E.; Savagatrup, S.; Printz, A. D.; Rodriguez, D.; Lipomi, D. J. Mechanical Properties of Organic Semiconductors for Stretchable, Highly Flexible, and Mechanically Robust Electronics. *Chem. Rev.* **2017**, *117* (9), 6467–6499. <https://doi.org/10.1021/acs.chemrev.7b00003>.
- (10) Roth, B.; Savagatrup, S.; De Los Santos, N. V.; Hagemann, O.; Carlé, J. E.; Helgesen, M.; Livi, F.; Bundgaard, E.; Søndergaard, R. R.; Krebs, F. C.; Lipomi, D. J. Mechanical Properties of a Library of Low-Band-Gap Polymers. *Chem. Mater.* **2016**, *28* (7), 2363–2373. <https://doi.org/10.1021/acs.chemmater.6b00525>.
- (11) Rodriguez, D.; Kim, J. H.; Root, S. E.; Fei, Z.; Boufflet, P.; Heeney, M.; Kim, T. S.; Lipomi, D. J. Comparison of Methods for Determining the Mechanical Properties of Semiconducting Polymer Films for Stretchable Electronics. *ACS Appl. Mater. Interfaces* **2017**, *9* (10), 8855–8862. <https://doi.org/10.1021/acsami.6b16115>.
- (12) Yuan, Y.; Zhu, H.; Wang, X.; Zhang, G.; Qiu, L. Enhancing the Elasticity of Conjugated Polymers through Precise Control of the Spacing between the Backbone and Siloxane Side-Chains. *ACS Appl. Mater. Interfaces* **2023**, *15* (18), 22341–22350. <https://doi.org/10.1021/acsami.3c02841>.

- (13) Ren, H.; Tong, Y.; Ouyang, M.; Wang, J.; Zhang, L.; Fu, Y.; Tang, Q. Balancing the Trade-off between the Mechanical and Electrical Properties of Conjugated Polymer Blend Films for Organic Field-Effect Transistors. *J. Mater. Chem. C* **2022**, *10* (40), 14921–14928. <https://doi.org/10.1039/d2tc01771g>.
- (14) Wang, Z.; Wu, Y.; Zhou, Q.; Yang, L.; Yi, Z.; Yan, Y.; Liu, Y.; Zhao, Y. Aggregation Structure and Glass Transition of Intrinsically Stretchable Semiconducting Polymers. *Matter* **2023**, *6* (10), 3434–3448. <https://doi.org/10.1016/j.matt.2023.05.042>.
- (15) Stafford, C. M.; Harrison, C.; Beers, K. L.; Karim, A.; Amis, E. J.; Vanlandingham, M. R.; Kim, H. C.; Volksen, W.; Miller, R. D.; Simonyi, E. E. A Buckling-Based Metrology for Measuring the Elastic Moduli of Polymeric Thin Films. *Nat. Mater.* **2004**, *3* (8), 545–550. <https://doi.org/10.1038/nmat1175>.
- (16) Zhang, S.; Galuska, L. A.; Gu, X. Water-Assisted Mechanical Testing of Polymeric Thin-Films. *J. Polym. Sci.* **2022**, *60* (7), 1108. <https://doi.org/10.1002/pol.20210281>.
- (17) Kim, J. H.; Nizami, A.; Hwangbo, Y.; Jang, B.; Lee, H. J.; Woo, C. S.; Hyun, S.; Kim, T. S. Tensile Testing of Ultra-Thin Films on Water Surface. *Nat. Commun.* **2013**, *4*, 1–6. <https://doi.org/10.1038/ncomms3520>.
- (18) Bay, R. K.; Crosby, A. J. Uniaxial Extension of Ultrathin Freestanding Polymer Films. *ACS Macro Lett.* **2019**, *8* (9), 1080–1085. <https://doi.org/10.1021/acsmacrolett.9b00408>.
- (19) Liu, Y.; Chen, Y. C.; Hutchens, S.; Lawrence, J.; Emrick, T.; Crosby, A. J. Directly Measuring the Complete Stress-Strain Response of Ultrathin Polymer Films. *Macromolecules* **2015**, *48* (18), 6534–6540. <https://doi.org/10.1021/acs.macromol.5b01473>.
- (20) Zhang, S.; Ocheje, M. U.; Luo, S.; Ehlenberg, D.; Appleby, B.; Weller, D.; Zhou, D.; Rondeau-Gagné, S.; Gu, X. Probing the Viscoelastic Property of Pseudo Free-Standing Conjugated Polymeric Thin Films. *Macromol. Rapid Commun.* **2018**, *39* (14), 1800092. <https://doi.org/10.1002/marc.201800092>.
- (21) Peña-Alcántara, A.; Nikzad, S.; Michalek, L.; Prine, N.; Wang, Y.; Gong, H.; Ponte, E.; Schneider, S.; Wu, Y.; Root, S. E.; He, M.; Tok, J. B. H.; Gu, X.; Bao, Z. Effect of Molecular Weight on the Morphology of a Polymer Semiconductor–Thermoplastic Elastomer Blend. *Adv. Electron. Mater.* **2023**, 2201055. <https://doi.org/10.1002/aelm.202201055>.
- (22) Liu, D.; Lei, Y.; Ji, X.; Wu, Y.; Lin, Y.; Wang, Y.; Zhang, S.; Zheng, Y.; Chen, Y.; Lai, J. C.; Zhong, D.; Cheng, H. W.; Chiong, J. A.; Gu, X.; Gam, S.; Yun, Y.; Tok, J. B. H.; Bao, Z. Tuning the Mechanical and Electric Properties of Conjugated Polymer Semiconductors: Side-Chain Design Based on Asymmetric Benzodithiophene Building Blocks. *Adv. Funct. Mater.* **2022**. <https://doi.org/10.1002/adfm.202203527>.
- (23) Li, N.; Li, Y.; Cheng, Z.; Liu, Y.; Dai, Y.; Kang, S.; Li, S.; Shan, N.; Wai, S.; Ziaja, A.; Wang, Y.; Strzalka, J.; Liu, W.; Zhang, C.; Gu, X.; Hubbell, J. A.; Tian, B.; Wang, S. Bioadhesive Polymer Semiconductors and Transistors for Intimate Biointerfaces. *Science (80-.)*. **2023**, *381* (6658), 686–693. <https://doi.org/10.1126/science.adg8758>.

- (24) Sommerville, P. J. W.; Balzer, A. H.; Lecroy, G.; Guio, L.; Wang, Y.; Onorato, J. W.; Kukhta, N. A.; Gu, X.; Salleo, A.; Stingelin, N.; Luscombe, C. K. Influence of Side Chain Interdigitation on Strain and Charge Mobility of Planar Indacenodithiophene Copolymers. *ACS Polym. Au* **2022**. <https://doi.org/10.1021/acspolymersau.2c00034>.
- (25) Galuska, L. A.; Muckley, E. S.; Cao, Z.; Ehlenberg, D. F.; Qian, Z.; Zhang, S.; Rondeau-Gagné, S.; Phan, M. D.; Ankner, J. F.; Ivanov, I. N.; Gu, X. SMART Transfer Method to Directly Compare the Mechanical Response of Water-Supported and Free-Standing Ultrathin Polymeric Films. *Nat. Commun.* **2021**, *12* (1), 1–11. <https://doi.org/10.1038/s41467-021-22473-w>.
- (26) Ocheje, M. U.; Selivanova, M.; Zhang, S.; Van Nguyen, T. H.; Charron, B. P.; Chuang, C. H.; Cheng, Y. H.; Billet, B.; Noori, S.; Chiu, Y. C.; Gu, X.; Rondeau-Gagné, S. Influence of Amide-Containing Side Chains on the Mechanical Properties of Diketopyrrolopyrrole-Based Polymers. *Polym. Chem.* **2018**, *9* (46), 5531–5542. <https://doi.org/10.1039/c8py01207e>.
- (27) Wang, Y.; Zhang, S.; Freychet, G.; Li, Z.; Chen, K. L.; Liu, C. T.; Cao, Z.; Chiu, Y. C.; Xia, W.; Gu, X. Highly Deformable Rigid Glassy Conjugated Polymeric Thin Films. *Adv. Funct. Mater.* **2023**, *2306576*, 1–11. <https://doi.org/10.1002/adfm.202306576>.
- (28) Zheng, Y.; Yu, Z.; Zhang, S.; Kong, X.; Michaels, W.; Wang, W.; Chen, G.; Liu, D.; Lai, J. C.; Prine, N.; Zhang, W.; Nikzad, S.; Cooper, C. B.; Zhong, D.; Mun, J.; Zhang, Z.; Kang, J.; Tok, J. B. H.; McCulloch, I.; Qin, J.; Gu, X.; Bao, Z. A Molecular Design Approach towards Elastic and Multifunctional Polymer Electronics. *Nat. Commun.* **2021**, *12* (1), 1–11. <https://doi.org/10.1038/s41467-021-25719-9>.
- (29) Song, R.; Schrickx, H.; Balar, N.; Siddika, S.; Sheikh, N.; O’connor, B. T. Unveiling the Stress-Strain Behavior of Conjugated Polymer Thin Films for Stretchable Device Applications. *Macromolecules* **2020**, *53* (6), 1988–1997. <https://doi.org/10.1021/acs.macromol.9b02573>.
- (30) Oh, J. Y.; Rondeau-Gagné, S.; Chiu, Y. C.; Chortos, A.; Lissel, F.; Wang, G. J. N.; Schroeder, B. C.; Kurosawa, T.; Lopez, J.; Katsumata, T.; Xu, J.; Zhu, C.; Gu, X.; Bae, W. G.; Kim, Y.; Jin, L.; Chung, J. W.; Tok, J. B. H.; Bao, Z. Intrinsically Stretchable and Healable Semiconducting Polymer for Organic Transistors. *Nature* **2016**, *539* (7629), 411–415. <https://doi.org/10.1038/nature20102>.
- (31) Chung, S.; Kim, S. H.; Ok, E.; Kim, B. J.; Kang, B.; Cho, K. Structural Insights into Conjugated Polymers for Stretchable Organic Transistors. *Chem. Mater.* **2023**. <https://doi.org/10.1021/acs.chemmater.3c02394>.
- (32) Noriega, R.; Rivnay, J.; Vandewal, K.; Koch, F. P. V.; Stingelin, N.; Smith, P.; Toney, M. F.; Salleo, A. A General Relationship between Disorder, Aggregation and Charge Transport in Conjugated Polymers. *Nat. Mater.* **2013**, *12* (11), 1038–1044. <https://doi.org/10.1038/nmat3722>.
- (33) Zhang, S.; Alesadi, A.; Mason, G. T.; Chen, K. L.; Freychet, G.; Galuska, L.; Cheng, Y. H.; St. Onge, P. B. J.; Ocheje, M. U.; Ma, G.; Qian, Z.; Dhakal, S.; Ahmad, Z.; Wang, C.; Chiu, Y. C.; Rondeau-Gagné, S.; Xia, W.; Gu, X. Molecular Origin of Strain-Induced Chain Alignment in PDPP-Based Semiconducting

- Polymeric Thin Films. *Adv. Funct. Mater.* **2021**, *31*, 2100161. <https://doi.org/10.1002/adfm.202100161>.
- (34) Freychet, G.; Huang, Y.; Tan, W. L.; Gilhooly-Finn, P. A.; Nielsen, C. B.; Siringhaus, H.; McNeill, C. R. Drastic Enhancement of X-Ray Scattering Contrast between Amorphous and Crystalline Phases of Poly(3-Hexylthiophene) at the Sulfur K-Edge. *ACS Mater. Lett.* **2022**, 764–769. <https://doi.org/10.1021/acsmaterialslett.2c00049>.
- (35) Freychet, G.; Gann, E.; Zhernenkov, M.; McNeill, C. R. Anisotropic Resonant X-Ray Diffraction of a Conjugated Polymer at the Sulfur K-Edge. *J. Phys. Chem. Lett.* **2021**, *12* (15), 3762–3766. <https://doi.org/10.1021/acs.jpcclett.1c00532>.
- (36) Freychet, G.; Gann, E.; Thomsen, L.; Jiao, X.; McNeill, C. R. Resonant Tender X-Ray Diffraction for Disclosing the Molecular Packing of Paracrystalline Conjugated Polymer Films. *J. Am. Chem. Soc.* **2021**, *143* (3), 1409–1415. <https://doi.org/10.1021/jacs.0c10721>.
- (37) Wang, Y.; Chen, K. L.; Prine, N.; Rondeau-Gagné, S.; Chiu, Y. C.; Gu, X. Stretchable and Self-Healable Semiconductive Composites Based on Hydrogen Bonding Cross-Linked Elastomeric Matrix. *Adv. Funct. Mater.* **2023**, *2303031*, 1–10. <https://doi.org/10.1002/adfm.202303031>.
- (38) Wang, Y.; Chen, K.-L.; Awada, A.; Prine, N.; Cao, Z.; Zhu, C.; Chiu, Y.-C.; Rondeau-Gagné, S.; Gu, X. Leveraging Non-Covalent Interactions to Control the Morphology and Electrical and Mechanical Properties of Stretchable Semiconducting Composites. *Chem. Mater.* **2023**. <https://doi.org/10.1021/acs.chemmater.3c02131>.
- (39) Wang, G. J. N.; Gasperini, A.; Bao, Z. Stretchable Polymer Semiconductors for Plastic Electronics. *Adv. Electron. Mater.* **2018**, *4* (2), 1700429. <https://doi.org/10.1002/aelm.201700429>.
- (40) Weng, Y.; Yu, Z.; Wu, T.; Liang, L.; Liu, S. Recent Progress in Stretchable Organic Field-Effect Transistors: Key Materials, Fabrication and Applications. *New J. Chem.* **2023**, *47* (11), 5086–5109. <https://doi.org/10.1039/d2nj06190b>.
- (41) Xue, X.; Li, C.; Shanguan, Z.; Gao, C.; Chenchai, K.; Liao, J.; Zhang, X.; Zhang, G.; Zhang, D. Intrinsically Stretchable and Healable Polymer Semiconductors. *Adv. Sci.* **2023**, *2305800*, 1–20. <https://doi.org/10.1002/advs.202305800>.
- (42) Trung, T. Q.; Lee, N. E. Recent Progress on Stretchable Electronic Devices with Intrinsically Stretchable Components. *Adv. Mater.* **2017**, *29* (3), 201603167. <https://doi.org/10.1002/adma.201603167>.
- (43) Ocheje, M. U.; Charron, B. P.; Nyayachavadi, A.; Rondeau-Gagné, S. Stretchable Electronics: Recent Progress in the Preparation of Stretchable and Self-Healing Semiconducting Conjugated Polymers. *Flex. Print. Electron.* **2017**, *2* (4). <https://doi.org/10.1088/2058-8585/aa9c9b>.
- (44) Kline, R. J.; McGehee, M. D.; Kadnikova, E. N.; Liu, J.; Fréchet, J. M. J.; Toney, M. F. Dependence of Regioregular Poly(3-Hexylthiophene) Film Morphology and Field-Effect Mobility on Molecular Weight. *Macromolecules* **2005**, *38* (8), 3312–3319. <https://doi.org/10.1021/ma047415f>.
- (45) Likhtman, A. E.; Ponnurugan, M. Microscopic Definition of Polymer Entanglements. *Macromolecules* **2014**, *47*, 1470–1481.

- (46) Koch, F. P. V.; Rivnay, J.; Foster, S.; Müller, C.; Downing, J. M.; Buchaca-Domingo, E.; Westacott, P.; Yu, L.; Yuan, M.; Baklar, M.; Fei, Z.; Luscombe, C.; McLachlan, M. A.; Heeney, M.; Rumbles, G.; Silva, C.; Salleo, A.; Nelson, J.; Smith, P.; Stingelin, N. The Impact of Molecular Weight on Microstructure and Charge Transport in Semicrystalline Polymer Semiconductors-Poly(3-Hexylthiophene), a Model Study. *Prog. Polym. Sci.* **2013**, *38* (12), 1978–1989. <https://doi.org/10.1016/j.progpolymsci.2013.07.009>.
- (47) Galuska, L. A.; McNutt, W. W.; Qian, Z.; Zhang, S.; Weller, D. W.; Dhakal, S.; King, E. R.; Morgan, S. E.; Azoulay, J. D.; Mei, J.; Gu, X. Impact of Backbone Rigidity on the Thermomechanical Properties of Semiconducting Polymers with Conjugation Break Spacers. *Macromolecules* **2020**, *53* (14), 6032–6042. <https://doi.org/10.1021/acs.macromol.0c00889>.
- (48) Huang, G.; Wu, N.; Wang, X.; Zhang, G.; Qiu, L. Role of Molecular Weight in the Mechanical Properties and Charge Transport of Conjugated Polymers Containing Siloxane Side Chains. *Macromol. Rapid Commun.* **2022**, *43* (17), 1–10. <https://doi.org/10.1002/marc.202200149>.
- (49) Pei, D.; Wang, Z.; Peng, Z.; Zhang, J.; Deng, Y.; Han, Y.; Ye, L.; Geng, Y. Impact of Molecular Weight on the Mechanical and Electrical Properties of a High-Mobility Diketopyrrolopyrrole-Based Conjugated Polymer. *Macromolecules* **2020**, *53* (11), 4490–4500. <https://doi.org/10.1021/acs.macromol.0c00209>.
- (50) Choi, J.; Kim, W.; Kim, D.; Kim, S.; Chae, J.; Choi, S. Q.; Kim, F. S.; Kim, T. S.; Kim, B. J. Importance of Critical Molecular Weight of Semicrystalline N-Type Polymers for Mechanically Robust, Efficient Electroactive Thin Films. *Chem. Mater.* **2019**, *31* (9), 3163–3173. <https://doi.org/10.1021/acs.chemmater.8b05114>.
- (51) Zhao, B.; Pei, D.; Jiang, Y.; Wang, Z.; An, C.; Deng, Y.; Ma, Z.; Han, Y.; Geng, Y. Simultaneous Enhancement of Stretchability, Strength, and Mobility in Ultrahigh-Molecular-Weight Poly(Indacenodithiophene- Co-Benzothiadiazole). *Macromolecules* **2021**, *54* (21), 9896–9905. <https://doi.org/10.1021/acs.macromol.1c01513>.
- (52) Kim, J. S.; Kim, J. H.; Lee, W.; Yu, H.; Kim, H. J.; Song, I.; Shin, M.; Oh, J. H.; Jeong, U.; Kim, T. S.; Kim, B. J. Tuning Mechanical and Optoelectrical Properties of Poly(3-Hexylthiophene) through Systematic Regioregularity Control. *Macromolecules* **2015**, *48* (13), 4339–4346. <https://doi.org/10.1021/acs.macromol.5b00524>.
- (53) Cho, Y.; Park, J.; Jeong, S.; Park, H.; Kim, H. W.; Oh, J. H.; Yang, C. Stretchable N-Type High-Performance Polymers Based on Asymmetric Thierylvinyl-1,1-Dicyanomethylene-3-Indanone for Plastic Electronics. *Chem. Mater.* **2022**, *34* (4), 1554–1566. <https://doi.org/10.1021/acs.chemmater.1c03208>.
- (54) Matsuda, M.; Sato, K. ichiro; Terayama, K.; Ochiai, Y.; Enomoto, K.; Higashihara, T. Synthesis of Electron Deficient Semiconducting Polymers for Intrinsically Stretchable N-Type Semiconducting Materials. *Polym. J.* **2023**, *55* (4), 365–373. <https://doi.org/10.1038/s41428-022-00729-6>.
- (55) Zheng, Y.; Wang, G. J. N.; Kang, J.; Nikolka, M.; Wu, H. C.; Tran, H.; Zhang, S.; Yan, H.; Chen, H.; Yuen, P. Y.; Mun, J.; Dauskardt, R. H.; McCulloch, I.; Tok, J. B. H.; Gu, X.; Bao, Z. An Intrinsically Stretchable High-Performance Polymer

- Semiconductor with Low Crystallinity. *Adv. Funct. Mater.* **2019**, *29* (46), 1–12. <https://doi.org/10.1002/adfm.201905340>.
- (56) Mun, J.; Wang, G. J. N.; Oh, J. Y.; Katsumata, T.; Lee, F. L.; Kang, J.; Wu, H. C.; Lissel, F.; Rondeau-Gagné, S.; Tok, J. B. H.; Bao, Z. Effect of Nonconjugated Spacers on Mechanical Properties of Semiconducting Polymers for Stretchable Transistors. *Adv. Funct. Mater.* **2018**, *28* (43), 1804222. <https://doi.org/10.1002/adfm.201804222>.
- (57) Zhang, S.; Ocheje, M. U.; Huang, L.; Galuska, L.; Cao, Z.; Luo, S.; Cheng, Y. H.; Ehlenberg, D.; Goodman, R. B.; Zhou, D.; Liu, Y.; Chiu, Y. C.; Azoulay, J. D.; Rondeau-Gagné, S.; Gu, X. The Critical Role of Electron-Donating Thiophene Groups on the Mechanical and Thermal Properties of Donor–Acceptor Semiconducting Polymers. *Adv. Electron. Mater.* **2019**, *5* (5), 1800899. <https://doi.org/10.1002/aelm.201800899>.
- (58) Lipomi, D. J.; Chong, H.; Vosgueritchian, M.; Mei, J.; Bao, Z. Toward Mechanically Robust and Intrinsically Stretchable Organic Solar Cells: Evolution of Photovoltaic Properties with Tensile Strain. *Sol. Energy Mater. Sol. Cells* **2012**, *107*, 355–365. <https://doi.org/10.1016/j.solmat.2012.07.013>.
- (59) Wu, H. C.; Benight, S. J.; Chortos, A.; Lee, W. Y.; Mei, J.; To, J. W. F.; Lu, C.; He, M.; Tok, J. B. H.; Chen, W. C.; Bao, Z. A Rapid and Facile Soft Contact Lamination Method: Evaluation of Polymer Semiconductors for Stretchable Transistors. *Chem. Mater.* **2014**, *26* (15), 4544–4551. <https://doi.org/10.1021/cm502271j>.
- (60) Wu, N.; Huang, G.; Huang, H.; Wang, Y.; Gu, X.; Wang, X.; Qiu, L. Achieving High Performance Stretchable Conjugated Polymers via Donor Structure Engineering. *Macromol. Rapid Commun.* **2023**, *2300169*, 1–10. <https://doi.org/10.1002/marc.202300169>.
- (61) Lu, C.; Lee, W. Y.; Gu, X.; Xu, J.; Chou, H. H.; Yan, H.; Chiu, Y. C.; He, M.; Matthews, J. R.; Niu, W.; Tok, J. B. H.; Toney, M. F.; Chen, W. C.; Bao, Z. Effects of Molecular Structure and Packing Order on the Stretchability of Semicrystalline Conjugated Poly(Tetrathienoacene-Diketopyrrolopyrrole) Polymers. *Adv. Electron. Mater.* **2017**, *3* (2), 1–13. <https://doi.org/10.1002/aelm.201600311>.
- (62) Zhao, Y.; Zhao, X.; Zang, Y.; Di, C. A.; Diao, Y.; Mei, J. Conjugation-Break Spacers in Semiconducting Polymers: Impact on Polymer Processability and Charge Transport Properties. *Macromolecules* **2015**, *48* (7), 2048–2053. <https://doi.org/10.1021/acs.macromol.5b00194>.
- (63) Schroeder, B. C.; Chiu, Y. C.; Gu, X.; Zhou, Y.; Xu, J.; Lopez, J.; Lu, C.; Toney, M. F.; Bao, Z. Non-Conjugated Flexible Linkers in Semiconducting Polymers: A Pathway to Improved Processability without Compromising Device Performance. *Adv. Electron. Mater.* **2016**, *2* (7), 1–10. <https://doi.org/10.1002/aelm.201600104>.
- (64) Zhao, X.; Zhao, Y.; Ge, Q.; Butrouna, K.; Diao, Y.; Graham, K. R.; Mei, J. Complementary Semiconducting Polymer Blends: The Influence of Conjugation-Break Spacer Length in Matrix Polymers. *Macromolecules* **2016**, *49* (7), 2601–2608. <https://doi.org/10.1021/acs.macromol.6b00050>.
- (65) Zhao, Y.; Zhao, X.; Roders, M.; Qu, G.; Diao, Y.; Ayzner, A. L.; Mei, J.

- Complementary Semiconducting Polymer Blends for Efficient Charge Transport. *Chem. Mater.* **2015**, *27* (20), 7164–7170. <https://doi.org/10.1021/acs.chemmater.5b03349>.
- (66) Savagatrup, S.; Zhao, X.; Chan, E.; Mei, J.; Lipomi, D. J. Effect of Broken Conjugation on the Stretchability of Semiconducting Polymers. *Macromol. Rapid Commun.* **2016**, *37* (19), 1623–1628. <https://doi.org/10.1002/marc.201600377>.
- (67) Zhao, Y.; Gumyusenge, A.; He, J.; Qu, G.; McNutt, W. W.; Long, Y.; Zhang, H.; Huang, L.; Diao, Y.; Mei, J. Continuous Melt-Drawing of Highly Aligned Flexible and Stretchable Semiconducting Microfibers for Organic Electronics. *Adv. Funct. Mater.* **2018**, *28* (4). <https://doi.org/10.1002/adfm.201705584>.
- (68) Lin, Y. C.; Matsuda, M.; Sato, K. I.; Chen, C. K.; Yang, W. C.; Chueh, C. C.; Higashihara, T.; Chen, W. C. Intrinsically Stretchable Naphthalenediimide-Bithiophene Conjugated Statistical Terpolymers Using Branched Conjugation Break Spacers for Field-Effect Transistors. *Polym. Chem.* **2021**, *12* (42), 6167–6178. <https://doi.org/10.1039/d1py01154e>.
- (69) Chang, T.-W.; Weng, Y.-C.; Tsai, Y.-T.; Jiang, Y.; Matsuhisa, N.; Shih, C.-C. Chain-Kinked Design: Improving Stretchability of Polymer Semiconductors through Nonlinear Conjugated Linkers. *ACS Appl. Mater. Interfaces* **2023**, *15* (44), 51507–51517. <https://doi.org/10.1021/acsami.3c10033>.
- (70) Wang, X.; Xu, C.; Xu, N.; Jiang, L.; Wang, Y.; Ni, F.; Zhang, G.; Gu, X.; Qiu, L. Design, Synthesis, and Characterization of Semiconducting Polymers Incorporating a Ring-like Ureidopyrimidinone (UPy) Quadruple Hydrogen Bonding Structure. *Macromolecules* **2023**, *56* (14), 5369–5380. <https://doi.org/10.1021/acs.macromol.3c00443>.
- (71) Kim, A.; Ahn, Y.; Li, W.; Park, S. H.; Cho, M. J.; Choi, D. H.; Yang, H. Stretchable Semiconducting Polymers with Hydrogen-Bonding-Capable Conjugation Breakers: Synthesis and Application in Organic Thin-Film Transistors. *ACS Appl. Mater. Interfaces* **2023**. <https://doi.org/10.1021/acsami.3c12057>.
- (72) Yu, X.; Li, C.; Gao, C.; Zhang, X.; Zhang, G.; Zhang, D. Incorporation of Hydrogen-bonding Units into Polymeric Semiconductors toward Boosting Charge Mobility, Intrinsic Stretchability, and Self-healing Ability. *SmartMat* **2021**, *2* (3), 347–366. <https://doi.org/10.1002/smm2.1062>.
- (73) Ma, J.; Liu, Z.; Yao, J.; Wang, Z.; Zhang, G.; Zhang, X.; Zhang, D. Improving Ambipolar Semiconducting Properties of Thiazole-Flanked Diketopyrrolopyrrole-Based Terpolymers by Incorporating Urea Groups in the Side-Chains. *Macromolecules* **2018**, *51* (15), 6003–6010. <https://doi.org/10.1021/acs.macromol.8b01020>.
- (74) Yang, Y.; Liu, Z.; Chen, L.; Yao, J.; Lin, G.; Zhang, X.; Zhang, G.; Zhang, D. Conjugated Semiconducting Polymer with Thymine Groups in the Side Chains: Charge Mobility Enhancement and Application for Selective Field-Effect Transistor Sensors toward CO and H₂S. *Chem. Mater.* **2019**, *31* (5), 1800–1807. <https://doi.org/10.1021/acs.chemmater.9b00106>.
- (75) Yao, J.; Yu, C.; Liu, Z.; Luo, H.; Yang, Y.; Zhang, G.; Zhang, D. Significant Improvement of Semiconducting Performance of the Diketopyrrolopyrrole-

- Quaterthiophene Conjugated Polymer through Side-Chain Engineering via Hydrogen-Bonding. *J. Am. Chem. Soc.* **2016**, *138* (1), 173–185. <https://doi.org/10.1021/jacs.5b09737>.
- (76) Zhang, H.; Liu, K.; Wu, K. Y.; Chen, Y. M.; Deng, R.; Li, X.; Jin, H.; Li, S.; Chuang, S. S. C.; Wang, C. L.; Zhu, Y. Hydrogen-Bonding-Mediated Solid-State Self-Assembled Isoepindolidiones (IsoEpi) Crystal for Organic Field-Effect Transistor. *J. Phys. Chem. C* **2018**, *122* (11), 5888–5895. <https://doi.org/10.1021/acs.jpcc.7b11992>.
- (77) Ocheje, M. U.; Charron, B. P.; Cheng, Y. H.; Chuang, C. H.; Soldera, A.; Chiu, Y. C.; Rondeau-Gagné, S. Amide-Containing Alkyl Chains in Conjugated Polymers: Effect on Self-Assembly and Electronic Properties. *Macromolecules* **2018**, *51* (4), 1336–1344. <https://doi.org/10.1021/acs.macromol.7b02393>.
- (78) Wang, G. J. N.; Shaw, L.; Xu, J.; Kurosawa, T.; Schroeder, B. C.; Oh, J. Y.; Benight, S. J.; Bao, Z. Inducing Elasticity through Oligo-Siloxane Crosslinks for Intrinsically Stretchable Semiconducting Polymers. *Adv. Funct. Mater.* **2016**, *26* (40), 7254–7262. <https://doi.org/10.1002/adfm.201602603>.
- (79) Kim, S. H.; Chung, S.; Kim, M.; Yoo, D.; Ok, E.; Kim, S.; Song, K. C.; Song, Y. J.; Kang, B.; Cho, K. Designing a Length-Modulated Azide Photocrosslinker to Improve the Stretchability of Semiconducting Polymers. *Adv. Funct. Mater.* **2023**. <https://doi.org/10.1002/adfm.202212127>.
- (80) Zheng, Y.; Ashizawa, M.; Zhang, S.; Kang, J.; Nikzad, S.; Yu, Z.; Ochiai, Y.; Wu, H. C.; Tran, H.; Mun, J.; Zheng, Y. Q.; Tok, J. B. H.; Gu, X.; Bao, Z. Tuning the Mechanical Properties of a Polymer Semiconductor by Modulating Hydrogen Bonding Interactions. *Chem. Mater.* **2020**, *32* (13), 5700–5714. <https://doi.org/10.1021/acs.chemmater.0c01437>.
- (81) Kwon, Y.; Park, H.; Oh, J. H. Nature-Inspired Semiconducting Polymers with Peptide Conjugation Breakers for Intrinsically Stretchable and Self-Healable Transistors. *Chem. Mater.* **2023**. <https://doi.org/10.1021/acs.chemmater.3c02498>.
- (82) Matsuda, M.; Lin, C.-Y.; Sung, C.-Y.; Lin, Y.-C.; Chen, W.-C.; Higashihara, T. Unraveling the Effect of Stereoisomerism on Mobility–Stretchability Properties of n-Type Semiconducting Polymers with Biobased Epimers as Conjugation Break Spacers. *ACS Appl. Mater. Interfaces* **2023**, *15* (44), 51492–51506. <https://doi.org/10.1021/acsami.3c09951>.
- (83) Kulatunga, P.; Comí, M.; Gomes, T. C.; Seifi, M.; Majidzadeh, R.; Al-Hashimi, M.; Rondeau-Gagné, S. Tailoring the Mechanical Properties of Benzothiadiazole-Based Semiconducting Polymers through Chalcogen Atom Substitution. *J. Mater. Chem. C* **2023**, *11* (42), 14661–14670. <https://doi.org/10.1039/d3tc02386a>.
- (84) Yu, X.; Chen, L.; Li, C.; Gao, C.; Xue, X.; Zhang, X.; Zhang, G.; Zhang, D. Intrinsically Stretchable Polymer Semiconductors with Good Ductility and High Charge Mobility through Reducing the Central Symmetry of the Conjugated Backbone Units. *Adv. Mater.* **2023**, *35* (17), 1–10. <https://doi.org/10.1002/adma.202209896>.
- (85) Mei, J.; Bao, Z. Side Chain Engineering in Solution-Processable Conjugated Polymers. *Chem. Mater.* **2014**, *26* (1), 604–615. <https://doi.org/10.1021/cm4020805>.

- (86) Chueh, P. H.; Chang, C. Y.; Lin, Y. C.; Chen, W. C.; Chueh, C. C. Stretchable Diketopyrrolopyrrole-Based Conjugated Polymers with Asymmetric Sidechain Designs for Field-Effect Transistor Applications. *J. Taiwan Inst. Chem. Eng.* **2022**, *140* (September), 104566. <https://doi.org/10.1016/j.jtice.2022.104566>.
- (87) Chiang, Y. C.; Wu, H. C.; Wen, H. F.; Hung, C. C.; Hong, C. W.; Kuo, C. C.; Higashihara, T.; Chen, W. C. Tailoring Carbosilane Side Chains toward Intrinsically Stretchable Semiconducting Polymers. *Macromolecules* **2019**, *52* (11), 4393–4404. <https://doi.org/10.1021/acs.macromol.9b00589>.
- (88) Ding, Y.; Zhu, Y.; Wang, X.; Wang, Y.; Zhang, S.; Zhang, G.; Gu, X.; Qiu, L. Side Chain Engineering: Achieving Stretch-Induced Molecular Orientation and Enhanced Mobility in Polymer Semiconductors. *Chem. Mater.* **2022**, *34* (6), 2696–2707. <https://doi.org/10.1021/acs.chemmater.1c04085>.
- (89) Sugiyama, F.; Kleinschmidt, A. T.; Kayser, L. V.; Rodriguez, D.; Finn, M.; Alkhadra, M. A.; Wan, J. M. H.; Ramírez, J.; Chiang, A. S. C.; Root, S. E.; Savagatrup, S.; Lipomi, D. J. Effects of Flexibility and Branching of Side Chains on the Mechanical Properties of Low-Bandgap Conjugated Polymers. *Polym. Chem.* **2018**, *9* (33), 4354–4363. <https://doi.org/10.1039/c8py00820e>.
- (90) Yen, H.-C.; Lin, Y.-C.; Chen, W.-C. Modulation of the Hydrophilicity on Asymmetric Side Chains of Isoindigo-Based Polymers for Improving Carrier Mobility–Stretchability Properties. *Macromolecules* **2021**, *54*, 1665–1676. <https://doi.org/10.1021/acs.macromol.0c02322>.
- (91) Wu, H. C.; Hung, C. C.; Hong, C. W.; Sun, H. S.; Wang, J. T.; Yamashita, G.; Higashihara, T.; Chen, W. C. Isoindigo-Based Semiconducting Polymers Using Carbosilane Side Chains for High Performance Stretchable Field-Effect Transistors. *Macromolecules* **2016**, *49* (22), 8540–8548. <https://doi.org/10.1021/acs.macromol.6b02145>.
- (92) Liu, D.; Mun, J.; Chen, G.; Schuster, N. J.; Wang, W.; Zheng, Y.; Nikzad, S.; Lai, J. C.; Wu, Y.; Zhong, D.; Lin, Y.; Lei, Y.; Chen, Y.; Gam, S.; Chung, J. W.; Yun, Y.; Tok, J. B. H.; Bao, Z. A Design Strategy for Intrinsically Stretchable High-Performance Polymer Semiconductors: Incorporating Conjugated Rigid Fused-Rings with Bulky Side Groups. *J. Am. Chem. Soc.* **2021**, *143* (30), 11679–11689. <https://doi.org/10.1021/jacs.1c04984>.
- (93) Huang, Y. W.; Lin, Y. C.; Yen, H. C.; Chen, C. K.; Lee, W. Y.; Chen, W. C.; Chueh, C. C. High Mobility Preservation of near Amorphous Conjugated Polymers in the Stretched States Enabled by Biaxially-Extended Conjugated Side-Chain Design. *Chem. Mater.* **2020**, *32* (17), 7370–7382. <https://doi.org/10.1021/acs.chemmater.0c02258>.
- (94) Gasperini, A.; Wang, G. J. N.; Molina-Lopez, F.; Wu, H. C.; Lopez, J.; Xu, J.; Luo, S.; Zhou, D.; Xue, G.; Tok, J. B. H.; Bao, Z. Characterization of Hydrogen Bonding Formation and Breaking in Semiconducting Polymers under Mechanical Strain. *Macromolecules* **2019**, *52* (6), 2476–2486. <https://doi.org/10.1021/acs.macromol.9b00145>.
- (95) Lee, M. Y.; Dharmapurikar, S.; Lee, S. J.; Cho, Y.; Yang, C.; Oh, J. H. Regular H-Bonding-Containing Polymers with Stretchability up to 100% External Strain for Self-Healable Plastic Transistors. *Chem. Mater.* **2020**, *32* (5), 1914–1924.

- <https://doi.org/10.1021/acs.chemmater.9b04574>.
- (96) Zhao, B.; Pei, D.; Shi, Y.; Zhang, X.; Zhang, B.; Deng, Y.; Han, Y.; Geng, Y. Side-Chain-Functionalized Poly(Indacenodithiophene-Alt-Benzothiadizole)s as Stretchable High-Mobility Semiconductors with Improved Elasticity. *Macromolecules* **2023**. <https://doi.org/10.1021/acs.macromol.3c01888>.
- (97) Higashihara, T.; Fukuta, S.; Ochiai, Y.; Sekine, T.; Chino, K.; Koganezawa, T.; Osaka, I. Synthesis and Deformable Hierarchical Nanostructure of Intrinsically Stretchable ABA Triblock Copolymer Composed of Poly(3-Hexylthiophene) and Polyisobutylene Segments. *ACS Appl. Polym. Mater.* **2019**, *1* (3), 315–320. <https://doi.org/10.1021/acsapm.8b00087>.
- (98) Müller, C.; Goffri, S.; Breiby, D. W.; Andreasen, J. W.; Chanzy, H. D.; Janssen, R. A. J.; Nielsen, M. M.; Radano, C. P.; Siringhaus, H.; Smith, P.; Stingelin-Stutzmann, N. Tough, Semiconducting Polyethylene-Poly(3-Hexylthiophene) Diblock Copolymers. *Adv. Funct. Mater.* **2007**, *17* (15), 2674–2679. <https://doi.org/10.1002/adfm.200601248>.
- (99) Peng, R.; Pang, B.; Hu, D.; Chen, M.; Zhang, G.; Wang, X.; Lu, H.; Cho, K.; Qiu, L. An ABA Triblock Copolymer Strategy for Intrinsically Stretchable Semiconductors. *J. Mater. Chem. C* **2015**, *3* (15), 3599–3606. <https://doi.org/10.1039/c4tc02476a>.
- (100) Ji, D.; Yoon, S. Y.; Jeon, S.; Go, J. Y.; Byeon, G.; Choi, J. O.; Min, J.; Kim, Y.; Hwang, D. H.; Cho, K.; Lim, B.; Noh, Y. Y. Tuning of the Stretchability and Charge Transport of Bis-Diketopyrrolopyrrole and Carbazole-Based Thermoplastic Soft Semiconductors by Modulating Soft Segment Contents. *Adv. Mater. Interfaces* **2023**, *10* (19). <https://doi.org/10.1002/admi.202202186>.
- (101) Pei, D.; An, C.; Zhao, B.; Ge, M.; Wang, Z.; Dong, W.; Wang, C.; Deng, Y.; Song, D.; Ma, Z.; Han, Y.; Geng, Y. Polyurethane-Based Stretchable Semiconductor Nanofilms with High Intrinsic Recovery Similar to Conventional Elastomers. *ACS Appl. Mater. Interfaces* **2022**. <https://doi.org/10.1021/acsami.2c07445>.
- (102) Yamamoto, S.; Matsuda, M.; Lin, C. Y.; Enomoto, K.; Lin, Y. C.; Chen, W. C.; Higashihara, T. Intrinsically Stretchable Block Copolymer Composed of Polyisobutene and Naphthalenediimide-Bithiophene-Based π -Conjugated Polymer Segments for Field-Effect Transistors. *ACS Appl. Polym. Mater.* **2022**, *4* (12), 8942–8951. <https://doi.org/10.1021/acsapm.2c01336>.
- (103) Sato, K.; Hemmi, Y.; Kato, A.; Matsui, H.; Fuchise, K.; Higashihara, T. Precise Synthesis of α,ω -Chain-End-Functionalized Poly(Dimethylsiloxane) with Bromoaryl Groups for Incorporation in Naphthalene-Diimide-Based N-Type Semiconducting Polymers. *Polymer (Guildf)*. **2022**, *252*, 124934. <https://doi.org/10.1016/j.polymer.2022.124934>.
- (104) Sugiyama, F.; Kleinschmidt, A. T.; Kayser, L. V.; Alkhadra, M. A.; Wan, J. M. H.; Chiang, A. S. C.; Rodriguez, D.; Root, S. E.; Savagatrup, S.; Lipomi, D. J. Stretchable and Degradable Semiconducting Block Copolymers. *Macromolecules* **2018**, *51* (15), 5944–5949. <https://doi.org/10.1021/acs.macromol.8b00846>.
- (105) Chiang, Y. C.; Kobayashi, S.; Isono, T.; Shih, C. C.; Shingu, T.; Hung, C. C.; Hsieh, H. C.; Tung, S. H.; Satoh, T.; Chen, W. C. Effect of a Conjugated/Elastic Block Sequence on the Morphology and Electronic Properties of Polythiophene

- Based Stretchable Block Copolymers. *Polym. Chem.* **2019**, *10* (40), 5452–5464. <https://doi.org/10.1039/c9py01216h>.
- (106) An, C.; Dong, W.; Pei, D.; Qin, X.; Wang, Z.; Zhao, B.; Bu, L.; Chen, H.; Han, Y.; Chi, C.; Geng, Y. Elastic Semiconductor Blends with High Strain Cycling Durability Using an Oligothiophene-Based Multiblock Polyurethane Matrix. *Macromolecules* **2023**, *56* (14), 5314–5325. <https://doi.org/10.1021/acs.macromol.3c00703>.
- (107) Wu, W. N.; Tu, T. H.; Pai, C. H.; Cheng, K. H.; Tung, S. H.; Chan, Y. T.; Liu, C. L. Metallo-Supramolecular Rod-Coil Block Copolymer Thin Films for Stretchable Organic Field Effect Transistor Application. *Macromolecules* **2022**, *55* (23), 10670–10681. <https://doi.org/10.1021/acs.macromol.2c00957>.
- (108) Wang, P.; Yang, J.; Zhang, Y.; Hu, W.; Dong, H. Near-Amorphous Conjugated Polymers: An Emerging Class of Semiconductors for Flexible Electronics. *ACS Materials Letters*. 2022, pp 1112–1123. <https://doi.org/10.1021/acsmaterialslett.2c00138>.
- (109) Zhao, Y.; Zhao, X.; Roders, M.; Gumyusenge, A.; Ayzner, A. L.; Mei, J. Melt-Processing of Complementary Semiconducting Polymer Blends for High Performance Organic Transistors. *Adv. Mater.* **2017**, *29* (6), 1605056. <https://doi.org/10.1002/adma.201605056>.
- (110) Xu, J.; Wang, S.; Wang, G. J. N.; Zhu, C.; Luo, S.; Jin, L.; Gu, X.; Chen, S.; Feig, V. R.; To, J. W. F.; Rondeau-Gagné, S.; Park, J.; Schroeder, B. C.; Lu, C.; Oh, J. Y.; Wang, Y.; Kim, Y. H.; Yan, H.; Sinclair, R.; Zhou, D.; Xue, G.; Murmann, B.; Linder, C.; Cai, W.; Tok, J. B. H.; Chung, J. W.; Bao, Z. Highly Stretchable Polymer Semiconductor Films through the Nanoconfinement Effect. *Science* (80-.). **2017**, *355* (6320), 59–64. <https://doi.org/10.1126/science.aah4496>.
- (111) Zhang, G.; Lee, S.; Gutiérrez-Meza, E.; Buckley, C.; McBride, M.; Valverde-Chávez, D. A.; Kwon, Y. H.; Savikhin, V.; Xiong, H.; Dunn, T. J.; Toney, M. F.; Yuan, Z.; Silva, C.; Reichmanis, E. Robust and Stretchable Polymer Semiconducting Networks: From Film Microstructure to Macroscopic Device Performance. *Chem. Mater.* **2019**, *31* (17), 6530–6539. <https://doi.org/10.1021/acs.chemmater.8b05224>.
- (112) Song, E.; Kang, B.; Choi, H. H.; Sin, D. H.; Lee, H.; Lee, W. H.; Cho, K. Stretchable and Transparent Organic Semiconducting Thin Film with Conjugated Polymer Nanowires Embedded in an Elastomeric Matrix. *Adv. Electron. Mater.* **2016**, *2*, 1500250. <https://doi.org/10.1002/aelm.201500250>.
- (113) Zhang, G.; McBride, M.; Persson, N.; Lee, S.; Dunn, T. J.; Toney, M. F.; Yuan, Z.; Kwon, Y. H.; Chu, P. H.; Risteen, B.; Reichmanis, E. Versatile Interpenetrating Polymer Network Approach to Robust Stretchable Electronic Devices. *Chem. Mater.* **2017**, *29* (18), 7645–7652. <https://doi.org/10.1021/acs.chemmater.7b03019>.
- (114) Choi, D.; Kim, H.; Persson, N.; Chu, P. H.; Chang, M.; Kang, J. H.; Graham, S.; Reichmanis, E. Elastomer-Polymer Semiconductor Blends for High-Performance Stretchable Charge Transport Networks. *Chem. Mater.* **2016**, *28* (4), 1196–1204. <https://doi.org/10.1021/acs.chemmater.5b04804>.
- (115) Nikzad, S.; Wu, H. C.; Kim, J.; Mahoney, C. M.; Matthews, J. R.; Niu, W.; Li, Y.; Wang, H.; Chen, W. C.; Toney, M. F.; He, M.; Bao, Z. Inducing Molecular

- Aggregation of Polymer Semiconductors in a Secondary Insulating Polymer Matrix to Enhance Charge Transport. *Chem. Mater.* **2020**, *32* (2), 897–905. <https://doi.org/10.1021/acs.chemmater.9b05228>.
- (116) Jeong, Y. J.; Jung, J.; Suh, E. H.; Yun, D. J.; Oh, J. G.; Jang, J. Self-Healable and Stretchable Organic Thermoelectric Materials: Electrically Percolated Polymer Nanowires Embedded in Thermoplastic Elastomer Matrix. *Adv. Funct. Mater.* **2020**, *30* (9). <https://doi.org/10.1002/adfm.201905809>.
- (117) Zhang, S.; Cheng, Y.; Galuska, L.; Roy, A.; Lorenz, M.; Chen, B.; Luo, S.; Li, Y.; Hung, C.; Qian, Z.; St. Onge, P. B. J.; Mason, G. T.; Cowen, L.; Zhou, D.; Nazarenko, S. I.; Storey, R. F.; Schroeder, B. C.; Rondeau-Gagné, S.; Chiu, Y.; Gu, X. Tacky Elastomers to Enable Tear-Resistant and Autonomous Self-Healing Semiconductor Composites. *Adv. Funct. Mater.* **2020**, *30* (27), 2000663. <https://doi.org/10.1002/adfm.202000663>.
- (118) Scott, J. I.; Xue, X.; Wang, M.; Kline, R. J.; Hoffman, B. C.; Dougherty, D.; Zhou, C.; Bazan, G.; O'Connor, B. T. Significantly Increasing the Ductility of High Performance Polymer Semiconductors through Polymer Blending. *ACS Appl. Mater. Interfaces* **2016**, *8* (22), 14037–14045. <https://doi.org/10.1021/acsami.6b01852>.
- (119) Janasz, L.; Borkowski, M.; Blom, P. W. M.; Marszalek, T.; Pisula, W. Organic Semiconductor/Insulator Blends for Elastic Field-Effect Transistors and Sensors. *Adv. Funct. Mater.* **2022**, *32* (7), 2105456. <https://doi.org/10.1002/adfm.202105456>.
- (120) Liu, D.; Ding, Z.; Wu, Y.; Liu, S. F.; Han, Y.; Zhao, K. In Situ Study of Molecular Aggregation in Conjugated Polymer/Elastomer Blends toward Stretchable Electronics. *Macromolecules* **2022**, *55* (1), 297–308. <https://doi.org/10.1021/acs.macromol.1c01537>.
- (121) Chiang, Y. C.; Shih, C. C.; Tung, S. H.; Chen, W. C. Blends of Polythiophene Nanowire/Fluorine Rubber with Multiscale Phase Separation Suitable for Stretchable Semiconductors. *Polymer (Guildf)*. **2018**, *155* (May), 146–151. <https://doi.org/10.1016/j.polymer.2018.09.044>.
- (122) Kulatunga, P.; Yousefi, N.; Rondeau-Gagné, S. Polyethylene and Semiconducting Polymer Blends for the Fabrication of Organic Field-Effect Transistors: Balancing Charge Transport and Stretchability. *Chemosensors* **2022**, *10* (6), 201. <https://doi.org/10.3390/chemosensors10060201>.
- (123) Shin, M.; Oh, J. Y.; Byun, K. E.; Lee, Y. J.; Kim, B.; Baik, H. K.; Park, J. J.; Jeong, U. Polythiophene Nanofibril Bundles Surface-Embedded in Elastomer: A Route to a Highly Stretchable Active Channel Layer. *Adv. Mater.* **2015**, *27* (7), 1255–1261. <https://doi.org/10.1002/adma.201404602>.
- (124) Riera-Galindo, S.; Leonardi, F.; Pfattner, R.; Mas-Torrent, M. Organic Semiconductor/Polymer Blend Films for Organic Field-Effect Transistors. *Adv. Mater. Technol.* **2019**, *4* (9), 1900104. <https://doi.org/10.1002/admt.201900104>.
- (125) Tran, H.; Feig, V. R.; Liu, K.; Wu, H. C.; Chen, R.; Xu, J.; Deisseroth, K.; Bao, Z. Stretchable and Fully Degradable Semiconductors for Transient Electronics. *ACS Cent. Sci.* **2019**, *5* (11), 1884–1891. <https://doi.org/10.1021/acscentsci.9b00850>.
- (126) Xu, J.; Wu, H. C.; Zhu, C.; Ehrlich, A.; Shaw, L.; Nikolka, M.; Wang, S.; Molina-

- Lopez, F.; Gu, X.; Luo, S.; Zhou, D.; Kim, Y. H.; Wang, G. J. N.; Gu, K.; Feig, V. R.; Chen, S.; Kim, Y.; Katsumata, T.; Zheng, Y. Q.; Yan, H.; Chung, J. W.; Lopez, J.; Murmann, B.; Bao, Z. Multi-Scale Ordering in Highly Stretchable Polymer Semiconducting Films. *Nat. Mater.* **2019**, *18* (6), 594–601. <https://doi.org/10.1038/s41563-019-0340-5>.
- (127) Qin, R.; Wu, Y.; Ding, Z.; Zhang, R.; Yu, J.; Huang, W.; Liu, D.; Lu, G.; Liu, S.; Zhao, K.; Han, Y. Highly Stretchable Conjugated Polymer/Elastomer Blend Films with Sandwich Structure. *Macromol. Rapid Commun.* **2023**, *2300240*, 1–10. <https://doi.org/10.1002/marc.202300240>.
- (128) Patrício, P. S. O.; Calado, H. D. R.; De Oliveira, F. A. C.; Righi, A.; Neves, B. R. A.; Silva, G. G.; Cury, L. A. Correlation between Thermal, Optical and Morphological Properties of Heterogeneous Blends of Poly(3-Hexylthiophene) and Thermoplastic Polyurethane. *J. Phys. Condens. Matter* **2006**, *18* (32), 7529–7542. <https://doi.org/10.1088/0953-8984/18/32/002>.
- (129) Zhang, T.; Zhang, L.; Wang, S.; Li, J.; Zuo, J.; Chen, R.; Yu, X.; Peng, J.; Zhang, Q.; Han, Y. Enhancing the Enrichment of Conjugated Polymer at Surfaces of Its Elastomer Blend Film via Increasing Molecular Weight to Induce Desired Nanofibril Network for Highly Stretchable Polymer Film. *Polymer (Guildf)*. **2023**, *278* (May), 125986. <https://doi.org/10.1016/j.polymer.2023.125986>.
- (130) Khang, D.-Y.; Jiang, H.; Huang, Y.; Rogers, J. A. A Stretchable Form of Single-Crystal. *Science (80-.)*. **2006**, *311* (January), 208–212.
- (131) Kim, D. H.; Ahn, J. H.; Won, M. C.; Kim, H. S.; Kim, T. H.; Song, J.; Huang, Y. Y.; Liu, Z.; Lu, C.; Rogers, J. A. Stretchable and Foldable Silicon Integrated Circuits. *Science (80-.)*. **2008**, *320* (5875), 507–511. <https://doi.org/10.1126/science.1154367>.
- (132) Kaltenbrunner, M.; White, M. S.; Głowacki, E. D.; Sekitani, T.; Someya, T.; Sariciftci, N. S.; Bauer, S. Ultrathin and Lightweight Organic Solar Cells with High Flexibility. *Nat. Commun.* **2012**, *3*. <https://doi.org/10.1038/ncomms1772>.
- (133) Son, D.; Lee, J.; Qiao, S.; Ghaffari, R.; Kim, J.; Lee, J. E.; Song, C.; Kim, S. J.; Lee, D. J.; Jun, S. W.; Yang, S.; Park, M.; Shin, J.; Do, K.; Lee, M.; Kang, K.; Hwang, C. S.; Lu, N.; Hyeon, T.; Kim, D. H. Multifunctional Wearable Devices for Diagnosis and Therapy of Movement Disorders. *Nat. Nanotechnol.* **2014**, *9* (5), 397–404. <https://doi.org/10.1038/nnano.2014.38>.
- (134) Jung, S. W.; Choi, Z. J. S.; Koo, J. B.; Park, C. W.; Na, B. S.; Oh, J. Y.; Lee, S. S.; Chu, H. Y. Stretchable Organic Thin-Film Transistors Fabricated on Elastomer Substrates Using Polyimide Stiff-Island Structures. *ECS Solid State Lett.* **2014**, *4* (1), P1–P3. <https://doi.org/10.1149/2.0011501ssl>.
- (135) Wang, Z.; Zhang, L.; Duan, S.; Jiang, H.; Shen, J.; Li, C. Kirigami-Patterned Highly Stretchable Conductors from Flexible Carbon Nanotube-Embedded Polymer Films. *J. Mater. Chem. C* **2017**, *5* (34), 8714–8722. <https://doi.org/10.1039/c7tc01727h>.
- (136) Huang, X.; Liu, Y.; Cheng, H.; Shin, W. J.; Fan, J. A.; Liu, Z.; Lu, C. J.; Kong, G. W.; Chen, K.; Patnaik, D.; Lee, S. H.; Hage-Ali, S.; Huang, Y.; Rogers, J. A. Materials and Designs for Wireless Epidermal Sensors of Hydration and Strain. *Adv. Funct. Mater.* **2014**, *24* (25), 3846–3854.

- <https://doi.org/10.1002/adfm.201303886>.
- (137) Song, J.; Huang, Y.; Xiao, J.; Wang, S.; Hwang, K. C.; Ko, H. C.; Kim, D. H.; Stoykovich, M. P.; Rogers, J. A. Mechanics of Noncoplanar Mesh Design for Stretchable Electronic Circuits. *J. Appl. Phys.* **2009**, *105* (12).
<https://doi.org/10.1063/1.3148245>.
- (138) Shin, M.; Song, J. H.; Lim, G. H.; Lim, B.; Park, J. J.; Jeong, U. Highly Stretchable Polymer Transistors Consisting Entirely of Stretchable Device Components. *Adv. Mater.* **2014**, *26* (22), 3706–3711.
<https://doi.org/10.1002/adma.201400009>.
- (139) Ma, R.; Chou, S. Y.; Xie, Y.; Pei, Q. Morphological/Nanostructural Control toward Intrinsically Stretchable Organic Electronics. *Chem. Soc. Rev.* **2019**, *48* (6), 1741–1786. <https://doi.org/10.1039/c8cs00834e>.
- (140) Choi, S.; Han, S. I.; Kim, D.; Hyeon, T.; Kim, D. H. High-Performance Stretchable Conductive Nanocomposites: Materials, Processes, and Device Applications. *Chem. Soc. Rev.* **2019**, *48* (6), 1566–1595.
<https://doi.org/10.1039/c8cs00706c>.
- (141) Graz, I. M.; Cotton, D. P. J.; Robinson, A.; Lacour, S. P. Silicone Substrate with in Situ Strain Relief for Stretchable Thin-Film Transistors. *Appl. Phys. Lett.* **2011**, *98* (12). <https://doi.org/10.1063/1.3570661>.
- (142) Wu, H.; Kustra, S.; Gates, E. M.; Bettinger, C. J. Topographic Substrates as Strain Relief Features in Stretchable Organic Thin Film Transistors. *Org. Electron.* **2013**, *14* (6), 1636–1642. <https://doi.org/10.1016/j.orgel.2013.02.037>.
- (143) Choudhary, K.; Chen, A. X.; Pitch, G. M.; Runser, R.; Urbina, A.; Dunn, T. J.; Kodur, M.; Kleinschmidt, A. T.; Wang, B. G.; Bunch, J. A.; Fenning, D. P.; Ayzner, A. L.; Lipomi, D. J. Comparison of the Mechanical Properties of a Conjugated Polymer Deposited Using Spin Coating, Interfacial Spreading, Solution Shearing, and Spray Coating. *ACS Appl. Mater. Interfaces* **2021**, *13* (43), 51436–51446. <https://doi.org/10.1021/acsami.1c13043>.
- (144) Gao, W.; Qiao, J.; Hu, J.; Guan, Y.; Li, Q. Recent Advances in Intrinsically Stretchable Electronic Materials and Devices. *Responsive Mater.* **2024**, No. September 2023. <https://doi.org/10.1002/rpm.20230022>.
- (145) Yang, J. C.; Mun, J.; Kwon, S. Y.; Park, S.; Bao, Z.; Park, S. Electronic Skin: Recent Progress and Future Prospects for Skin-Attachable Devices for Health Monitoring, Robotics, and Prosthetics. *Adv. Mater.* **2019**, *31* (48), 1–50.
<https://doi.org/10.1002/adma.201904765>.
- (146) Zhu, C.; Bao, Z. Skin-Inspired Electronics for Emerging Display Technology. *Dig. Tech. Pap. - SID Int. Symp.* **2021**, *52* (1), 1052–1055.
<https://doi.org/10.1002/sdtp.14872>.
- (147) Someya, T.; Bauer, S.; Kaltenbrunner, M. Imperceptible Organic Electronics. *MRS Bull.* **2017**, *42* (2), 124–130. <https://doi.org/10.1557/mrs.2017.1>.
- (148) Wang, S.; Oh, J. Y.; Xu, J.; Tran, H.; Bao, Z. Skin-Inspired Electronics: An Emerging Paradigm. *Acc. Chem. Res.* **2018**, *51* (5), 1033–1045.
<https://doi.org/10.1021/acs.accounts.8b00015>.
- (149) Roy, S.; Deo, K. A.; Lee, H. P.; Soukar, J.; Namkoong, M.; Tian, L.; Jaiswal, A.; Gaharwar, A. K. 3D Printed Electronic Skin for Strain, Pressure and Temperature

- Sensing. *Adv. Funct. Mater.* **2024**, 2313575, 1–13.
<https://doi.org/10.1002/adfm.202313575>.
- (150) Liu, K.; Ouyang, B.; Guo, X.; Guo, Y.; Liu, Y. Advances in Flexible Organic Field-Effect Transistors and Their Applications for Flexible Electronics. *npj Flex. Electron.* **2022**, 6 (1). <https://doi.org/10.1038/s41528-022-00133-3>.
- (151) Dai, Y.; Hu, H.; Wang, M.; Xu, J.; Wang, S. Stretchable Transistors and Functional Circuits for Human-Integrated Electronics. *Nat. Electron.* **2021**, 4 (1), 17–29. <https://doi.org/10.1038/s41928-020-00513-5>.
- (152) Park, H.; Kim, D. C. Structural and Material-Based Approaches for the Fabrication of Stretchable Light-Emitting Diodes. *Micromachines* **2023**, 15 (1), 66. <https://doi.org/10.3390/mi15010066>.
- (153) Li, S.; Zhao, H.; Shepherd, R. F. Flexible and Stretchable Sensors for Fluidic Elastomer Actuated Soft Robots. *MRS Bull.* **2017**, 42 (2), 138–142. <https://doi.org/10.1557/mrs.2017.4>.
- (154) Liang, J.; Tong, K.; Sun, H.; Pei, Q. Intrinsically Stretchable Field-Effect Transistors. *MRS Bull.* **2017**, 42 (2), 131–137. <https://doi.org/10.1557/mrs.2016.326>.
- (155) Song, J.; Liu, H.; Zhao, Z.; Lin, P.; Yan, F. Flexible Organic Transistors for Biosensing: Devices and Applications. *Adv. Mater.* **2023**, 2300034, 1–49. <https://doi.org/10.1002/adma.202300034>.
- (156) Khau, B. V.; Scholz, A. D.; Reichmanis, E. Advances and Opportunities in Development of Deformable Organic Electrochemical Transistors. *J. Mater. Chem. C* **2020**, 8 (43), 15067–15078. <https://doi.org/10.1039/d0tc03118f>.
- (157) St. Onge, P. B. J.; Ocheje, M. U.; Selivanova, M.; Rondeau-Gagné, S. Recent Advances in Mechanically Robust and Stretchable Bulk Heterojunction Polymer Solar Cells. *Chem. Rec.* **2019**, 19 (6), 1008–1027. <https://doi.org/10.1002/tcr.201800163>.
- (158) Fukuda, K.; Yu, K.; Someya, T. The Future of Flexible Organic Solar Cells. *Adv. Energy Mater.* **2020**, 10 (25), 1–10. <https://doi.org/10.1002/aenm.202000765>.
- (159) Park, J. S.; Kim, G. U.; Lee, S.; Lee, J. W.; Li, S.; Lee, J. Y.; Kim, B. J. Material Design and Device Fabrication Strategies for Stretchable Organic Solar Cells. *Adv. Mater.* **2022**, 34 (31), 1–37. <https://doi.org/10.1002/adma.202201623>.
- (160) Wan, Q.; Seo, S.; Lee, S. W.; Lee, J.; Jeon, H.; Kim, T. S.; Kim, B. J.; Thompson, B. C. High-Performance Intrinsically Stretchable Polymer Solar Cell with Record Efficiency and Stretchability Enabled by Thymine-Functionalized Terpolymer. *J. Am. Chem. Soc.* **2023**, 145 (22), 11914–11920. <https://doi.org/10.1021/jacs.3c02764>.
- (161) Noh, J.; Kim, G. U.; Han, S.; Oh, S. J.; Jeon, Y.; Jeong, D.; Kim, S. W.; Kim, T. S.; Kim, B. J.; Lee, J. Y. Intrinsically Stretchable Organic Solar Cells with Efficiencies of over 11%. *ACS Energy Lett.* **2021**, 6, 2512–2518. <https://doi.org/10.1021/acseenergylett.1c00829>.
- (162) White, M. S.; Kaltenbrunner, M.; Głowacki, E. D.; Gutnichenko, K.; Kettlgruber, G.; Graz, I.; Aazou, S.; Ulbricht, C.; Egbe, D. A. M.; Miron, M. C.; Major, Z.; Scharber, M. C.; Sekitani, T.; Someya, T.; Bauer, S.; Sariciftci, N. S. Ultrathin, Highly Flexible and Stretchable PLEDs. *Nat. Photonics* **2013**, 7 (10), 811–816.

- <https://doi.org/10.1038/nphoton.2013.188>.
- (163) Liu, W.; Zhang, C.; Alessandri, R.; Diroll, B. T.; Li, Y.; Liang, H.; Fan, X.; Wang, K.; Cho, H.; Liu, Y.; Dai, Y.; Su, Q.; Li, N.; Li, S.; Wai, S.; Li, Q.; Shao, S.; Wang, L.; Xu, J.; Zhang, X.; Talapin, D. V.; de Pablo, J. J.; Wang, S. High-Efficiency Stretchable Light-Emitting Polymers from Thermally Activated Delayed Fluorescence. *Nat. Mater.* **2023**, *22* (6), 737–745. <https://doi.org/10.1038/s41563-023-01529-w>.
- (164) Kim, D. H.; Lu, N.; Ma, R.; Kim, Y. S.; Kim, R. H.; Wang, S.; Wu, J.; Won, S. M.; Tao, H.; Islam, A.; Yu, K. J.; Kim, T. II; Chowdhury, R.; Ying, M.; Xu, L.; Li, M.; Chung, H. J.; Keum, H.; McCormick, M.; Liu, P.; Zhang, Y. W.; Omenetto, F. G.; Huang, Y.; Coleman, T.; Rogers, J. A. Epidermal Electronics. *Science* (80-.). **2011**, *333* (6044), 838–843. <https://doi.org/10.1126/science.1206157>.
- (165) Lipomi, D. J.; Bao, Z. Stretchable and Ultraflexible Organic Electronics. *MRS Bull.* **2017**, *42* (2), 93–97. <https://doi.org/10.1557/mrs.2016.325>.
- (166) Ma, Z.; Li, H.; Jing, X.; Liu, Y.; Mi, H. Y. Recent Advancements in Self-Healing Composite Elastomers for Flexible Strain Sensors: Materials, Healing Systems, and Features. *Sensors Actuators, A Phys.* **2021**, *329*, 112800. <https://doi.org/10.1016/j.sna.2021.112800>.
- (167) Latif, S.; Amin, S.; Haroon, S. S.; Sajjad, I. A. Self-Healing Materials for Electronic Applications: An Overview. *Mater. Res. Express* **2019**, *6* (6). <https://doi.org/10.1088/2053-1591/ab0f4c>.
- (168) Yue, H.; Wang, Z.; Zhen, Y. Recent Advances of Self-Healing Electronic Materials Applied in Organic Field-Effect Transistors. *ACS Omega* **2022**, *7* (22), 18197–18205. <https://doi.org/10.1021/acsomega.2c00580>.
- (169) Mashkoo, F.; Lee, S. J.; Yi, H.; Noh, S. M.; Jeong, C. Self-Healing Materials for Electronics Applications. *Int. J. Mol. Sci.* **2022**, *23* (2), 1–40. <https://doi.org/10.3390/ijms23020622>.
- (170) Müllen, K.; Pisula, W. Donor-Acceptor Polymers. *J. Am. Chem. Soc.* **2015**, *137* (30), 9503–9505. <https://doi.org/10.1021/jacs.5b07015>.
- (171) Himmelberger, S.; Salleo, A. Engineering Semiconducting Polymers for Efficient Charge Transport. *MRS Commun.* **2015**, *5* (3), 383–395. <https://doi.org/10.1557/mrc.2015.44>.
- (172) Nielsen, C. B.; Turbiez, M.; McCulloch, I. Recent Advances in the Development of Semiconducting DPP-Containing Polymers for Transistor Applications. *Adv. Mater.* **2013**, *25* (13), 1859–1880. <https://doi.org/10.1002/adma.201201795>.
- (173) Tsao, H. N.; Müllen, K. Improving Polymer Transistor Performance via Morphology Control. *Chem. Soc. Rev.* **2010**, *39* (7), 2372–2386. <https://doi.org/10.1039/b918151m>.
- (174) Sirringhaus, H.; Bird, M.; Richards, T.; Zhao, N. Charge Transport Physics of Conjugated Polymer Field-Effect Transistors. *Adv. Mater.* **2010**, *22* (34), 3893–3898. <https://doi.org/10.1002/adma.200902857>.
- (175) Kang, J.; Tok, J. B. H.; Bao, Z. Self-Healing Soft Electronics. *Nat. Electron.* **2019**, *2* (4), 144–150. <https://doi.org/10.1038/s41928-019-0235-0>.
- (176) Ditte, K.; Perez, J.; Chae, S.; Hamsch, M.; Al-Hussein, M.; Komber, H.; Formanek, P.; Mannsfeld, S. C. B.; Fery, A.; Kiriy, A.; Lissel, F. Ultrasoft and

- High-Mobility Block Copolymers for Skin-Compatible Electronics. *Adv. Mater.* **2021**, *33* (4), 2005416. <https://doi.org/10.1002/adma.202005416>.
- (177) Hsu, L. C.; Kobayashi, S.; Isono, T.; Chiang, Y. C.; Ree, B. J.; Satoh, T.; Chen, W. C. Highly Stretchable Semiconducting Polymers for Field-Effect Transistors through Branched Soft-Hard-Soft Type Triblock Copolymers. *Macromolecules* **2020**, *53* (17), 7496–7510. <https://doi.org/10.1021/acs.macromol.0c00381>.
- (178) Printz, A. D.; Lipomi, D. J. Competition between Deformability and Charge Transport in Semiconducting Polymers for Flexible and Stretchable Electronics. *Appl. Phys. Rev.* **2016**, *3* (2). <https://doi.org/10.1063/1.4947428>.
- (179) Li, C. H.; Wang, C.; Keplinger, C.; Zuo, J. L.; Jin, L.; Sun, Y.; Zheng, P.; Cao, Y.; Lissel, F.; Linder, C.; You, X. Z.; Bao, Z. A Highly Stretchable Autonomous Self-Healing Elastomer. *Nat. Chem.* **2016**, *8* (6), 618–624. <https://doi.org/10.1038/nchem.2492>.
- (180) Yu, R.; Yang, Y.; He, J.; Li, M.; Guo, B. Novel Supramolecular Self-Healing Silk Fibroin-Based Hydrogel via Host–Guest Interaction as Wound Dressing to Enhance Wound Healing. *Chem. Eng. J.* **2021**, *417* (November 2020), 128278. <https://doi.org/10.1016/j.cej.2020.128278>.
- (181) Xu, J. H.; Ding, C. Di; Chen, P.; Tan, L. H.; Chen, C. B.; Fu, J. J. Intrinsic Self-Healing Polymers for Advanced Lithium-Based Batteries: Advances and Strategies. *Appl. Phys. Rev.* **2020**, *7* (3). <https://doi.org/10.1063/5.0008206>.
- (182) Oh, J. Y.; Son, D.; Katsumata, T.; Lee, Y.; Kim, Y.; Lopez, J.; Wu, H. C.; Kang, J.; Park, J.; Gu, X.; Mun, J.; Wang, N. G. J.; Yin, Y.; Cai, W.; Yun, Y.; Tok, J. B. H.; Bao, Z. Stretchable Self-Healable Semiconducting Polymer Film for Active-Matrix Strain-Sensing Array. *Sci. Adv.* **2019**, *5* (11). <https://doi.org/10.1126/sciadv.aav3097>.
- (183) Bag, M.; Banerjee, S.; Faust, R.; Venkataraman, D. Self-Healing Polymer Sealant for Encapsulating Flexible Solar Cells. *Sol. Energy Mater. Sol. Cells* **2016**, *145*, 418–422. <https://doi.org/10.1016/j.solmat.2015.11.004>.
- (184) Tillet, G.; Boutevin, B.; Ameduri, B. Chemical Reactions of Polymer Crosslinking and Post-Crosslinking at Room and Medium Temperature. *Prog. Polym. Sci.* **2011**, *36* (2), 191–217. <https://doi.org/10.1016/j.progpolymsci.2010.08.003>.
- (185) Wojtecki, R. J.; Meador, M. A.; Rowan, S. J. Using the Dynamic Bond to Access Macroscopically Responsive Structurally Dynamic Polymers. *Nat. Mater.* **2011**, *10* (1), 14–27. <https://doi.org/10.1038/nmat2891>.
- (186) Mavila, S.; Eivgi, O.; Berkovich, I.; Lemcoff, N. G. Intramolecular Cross-Linking Methodologies for the Synthesis of Polymer Nanoparticles. *Chem. Rev.* **2016**, *116* (3), 878–961. <https://doi.org/10.1021/acs.chemrev.5b00290>.
- (187) Nair, K. P.; Breedveld, V.; Weck, M. Complementary Hydrogen-Bonded Thermoreversible Polymer Networks with Tunable Properties. *Macromolecules* **2008**, *41* (10), 3429–3438. <https://doi.org/10.1021/ma800279w>.
- (188) Osada, Y.; Gong, J.-P. Soft and Wet Materials: Polymer Gels. *Adv. Mater.* **1998**, *10* (11), 827–837. [https://doi.org/10.1002/\(sici\)1521-4095\(199808\)10:11<827::aid-adma827>3.3.co;2-c](https://doi.org/10.1002/(sici)1521-4095(199808)10:11<827::aid-adma827>3.3.co;2-c).
- (189) Rieth, L. R.; Eaton, R. F.; Coates, G. W. Polymerization of Ureidopyrimidinone-Functionalized Olefins by Using Late-Transition Metal Ziegler-Natta Catalysts:

- Synthesis of Thermoplastic Elastomeric Polyolefins. *Angew. Chemie - Int. Ed.* **2001**, *40* (11), 2153–2156. [https://doi.org/10.1002/1521-3773\(20010601\)40:11<2153::AID-ANIE2153>3.0.CO;2-W](https://doi.org/10.1002/1521-3773(20010601)40:11<2153::AID-ANIE2153>3.0.CO;2-W).
- (190) Song, P.; Wang, H. High-Performance Polymeric Materials through Hydrogen-Bond Cross-Linking. *Adv. Mater.* **2020**, *32* (18), 1901244. <https://doi.org/10.1002/adma.201901244>.
- (191) Feldman, K. E.; Kade, M. J.; Meijer, E. W.; Hawker, C. J.; Kramer, E. J. Phase Behavior of Complementary Multiply Hydrogen Bonded End-Functional Polymer Blends. *Macromolecules* **2010**, *43* (11), 5121–5127. <https://doi.org/10.1021/ma1003776>.
- (192) Stuparu, M. C.; Khan, A.; Hawker, C. J. Phase Separation of Supramolecular and Dynamic Block Copolymers. *Polym. Chem.* **2012**, *3* (11), 3033–3044. <https://doi.org/10.1039/c2py20368e>.
- (193) Neal, J. A.; Mozhdehi, D.; Guan, Z. Enhancing Mechanical Performance of a Covalent Self-Healing Material by Sacrificial Noncovalent Bonds. *J. Am. Chem. Soc.* **2015**, *137* (14), 4846–4850. <https://doi.org/10.1021/jacs.5b01601>.
- (194) Yan, X.; Liu, Z.; Zhang, Q.; Lopez, J.; Wang, H.; Wu, H. C.; Niu, S.; Yan, H.; Wang, S.; Lei, T.; Li, J.; Qi, D.; Huang, P.; Huang, J.; Zhang, Y.; Wang, Y.; Li, G.; Tok, J. B. H.; Chen, X.; Bao, Z. Quadruple H-Bonding Cross-Linked Supramolecular Polymeric Materials as Substrates for Stretchable, Antitearing, and Self-Healable Thin Film Electrodes. *J. Am. Chem. Soc.* **2018**, *140* (15), 5280–5289. <https://doi.org/10.1021/jacs.8b01682>.
- (195) Choi, H. H.; Cho, K.; Frisbie, C. D.; Sirringhaus, H.; Podzorov, V. Critical Assessment of Charge Mobility Extraction in FETs. *Nat. Mater.* **2017**, *17* (1), 2–7. <https://doi.org/10.1038/nmat5035>.
- (196) Ouyang, L.; Musumeci, C.; Jafari, M. J.; Ederth, T.; Inganäs, O. Imaging the Phase Separation between PEDOT and Polyelectrolytes during Processing of Highly Conductive PEDOT:PSS Films. *ACS Appl. Mater. Interfaces* **2015**, *7* (35), 19764–19773. <https://doi.org/10.1021/acsami.5b05439>.
- (197) Lee, I.; Kim, G. W.; Yang, M.; Kim, T. S. Simultaneously Enhancing the Cohesion and Electrical Conductivity of PEDOT:PSS Conductive Polymer Films Using DMSO Additives. *ACS Appl. Mater. Interfaces* **2016**, *8* (1), 302–310. <https://doi.org/10.1021/acsami.5b08753>.
- (198) Angunawela, I.; Nahid, M. M.; Ghasemi, M.; Amassian, A.; Ade, H.; Gadisa, A. The Critical Role of Materials' Interaction in Realizing Organic Field-Effect Transistors Via High-Dilution Blending with Insulating Polymers. *ACS Appl. Mater. Interfaces* **2020**, *12* (23), 26239–26249. <https://doi.org/10.1021/acsami.0c04208>.
- (199) Campbell, C. G.; Storey, R. F. Functional Polyisobutylenes via Electrophilic Cleavage/Alkylation. *J. Polym. Sci. Part A Polym. Chem.* **2017**, *55* (12), 1991–1997. <https://doi.org/10.1002/pola.28570>.
- (200) Rao, Y. L.; Chortos, A.; Pfattner, R.; Lissel, F.; Chiu, Y. C.; Feig, V.; Xu, J.; Kurosawa, T.; Gu, X.; Wang, C.; He, M.; Chung, J. W.; Bao, Z. Stretchable Self-Healing Polymeric Dielectrics Cross-Linked through Metal-Ligand Coordination. *J. Am. Chem. Soc.* **2016**, *138* (18), 6020–6027.

- <https://doi.org/10.1021/jacs.6b02428>.
- (201) Sekitani, T.; Zschieschang, U.; Klauk, H.; Someya, T. Flexible Organic Transistors and Circuits with Extreme Bending Stability. *Nat. Mater.* **2010**, *9* (12), 1015–1022. <https://doi.org/10.1038/nmat2896>.
- (202) Yu, K.; Park, B.; Kim, G.; Kim, C. H.; Park, S.; Kim, J.; Jung, S.; Jeong, S.; Kwon, S.; Kang, H.; Kim, J.; Yoon, M. H.; Lee, K. Optically Transparent Semiconducting Polymer Nanonetwork for Flexible and Transparent Electronics. *Proc. Natl. Acad. Sci. U. S. A.* **2016**, *113* (50), 14261–14266. <https://doi.org/10.1073/pnas.1606947113>.
- (203) Wang, S.; Fabiano, S.; Himmelberger, S.; Puzinas, S.; Crispin, X.; Salleo, A.; Berggren, M. Experimental Evidence That Short-Range Intermolecular Aggregation Is Sufficient for Efficient Charge Transport in Conjugated Polymers. *Proc. Natl. Acad. Sci. U. S. A.* **2015**, *112* (34), 10599–10604. <https://doi.org/10.1073/pnas.1501381112>.
- (204) Bhaumik, S.; Ntetsikas, K.; Hadjichristidis, N. Noncovalent Supramolecular Diblock Copolymers: Synthesis and Microphase Separation. *Macromolecules* **2020**, *53* (15), 6682–6689. <https://doi.org/10.1021/acs.macromol.9b02326>.
- (205) Chen, S.; Binder, W. H. Dynamic Ordering and Phase Segregation in Hydrogen-Bonded Polymers. *Acc. Chem. Res.* **2016**, *49* (7), 1409–1420. <https://doi.org/10.1021/acs.accounts.6b00174>.
- (206) Rao, J.; Păunescu, E.; Mirmohades, M.; Gadwal, I.; Khaydarov, A.; Hawker, C. J.; Bang, J.; Khan, A. Supramolecular Mimics of Phase Separating Covalent Diblock Copolymers. *Polym. Chem.* **2012**, *3* (8), 2050–2056. <https://doi.org/10.1039/c2py20125a>.
- (207) Lin, Y. H.; Darling, S. B.; Nikiforov, M. P.; Strzalka, J.; Verduzco, R. Supramolecular Conjugated Block Copolymers. *Macromolecules* **2012**, *45* (16), 6571–6579. <https://doi.org/10.1021/ma300829u>.
- (208) Chen, Y.; Kushner, A. M.; Williams, G. A.; Guan, Z. Multiphase Design of Autonomic Self-Healing Thermoplastic Elastomers. *Nat. Chem.* **2012**, *4* (6), 467–472. <https://doi.org/10.1038/nchem.1314>.
- (209) Galuska, L. A.; Ocheje, M. U.; Ahmad, Z. C.; Rondeau-Gagné, S.; Gu, X. Elucidating the Role of Hydrogen Bonds for Improved Mechanical Properties in a High-Performance Semiconducting Polymer. *Chem. Mater.* **2022**, *34* (5), 2259–2267. <https://doi.org/10.1021/acs.chemmater.1c04055>.
- (210) Son, D.; Kang, J.; Vardoulis, O.; Kim, Y.; Matsuhisa, N.; Oh, J. Y.; To, J. W.; Mun, J.; Katsumata, T.; Liu, Y.; McGuire, A. F.; Krason, M.; Molina-Lopez, F.; Ham, J.; Kraft, U.; Lee, Y.; Yun, Y.; Tok, J. B. H.; Bao, Z. An Integrated Self-Healable Electronic Skin System Fabricated via Dynamic Reconstruction of a Nanostructured Conducting Network. *Nat. Nanotechnol.* **2018**, *13* (11), 1057–1065. <https://doi.org/10.1038/s41565-018-0244-6>.
- (211) Schwartz, G.; Tee, B. C. K.; Mei, J.; Appleton, A. L.; Kim, D. H.; Wang, H.; Bao, Z. Flexible Polymer Transistors with High Pressure Sensitivity for Application in Electronic Skin and Health Monitoring. *Nat. Commun.* **2013**, *4* (May). <https://doi.org/10.1038/ncomms2832>.
- (212) Jiang, Y.; Zhang, Z.; Wang, Y. X.; Li, D.; Coen, C. T.; Hwaun, E.; Chen, G.; Wu,

- H. C.; Zhong, D.; Niu, S.; Wang, W.; Saberi, A.; Lai, J. C.; Wu, Y.; Wang, Y.; Trotsyuk, A. A.; Loh, K. Y.; Shih, C. C.; Xu, W.; Liang, K.; Zhang, K.; Bai, Y.; Gurusankar, G.; Hu, W.; Jia, W.; Cheng, Z.; Dauskardt, R. H.; Gurtner, G. C.; Tok, J. B. H.; Deisseroth, K.; Soltesz, I.; Bao, Z. Topological Supramolecular Network Enabled High-Conductivity, Stretchable Organic Bioelectronics. *Science* (80-.). **2022**, *375* (6587), 1411–1417. <https://doi.org/10.1126/science.abj7564>.
- (213) Larson, C.; Peele, B.; Li, S.; Robinson, S.; Totaro, M.; Beccai, L.; Mazzolai, B.; Shepherd, R. Highly Stretchable Electroluminescent Skin for Optical Signaling and Tactile Sensing. *Science* (80-.). **2016**, *351* (6277), 1071–1074. <https://doi.org/10.1126/science.aac5082>.
- (214) Chen, A. X.; Kleinschmidt, A. T.; Choudhary, K.; Lipomi, D. J. Beyond Stretchability: Strength, Toughness, and Elastic Range in Semiconducting Polymers. *Chem. Mater.* **2020**, *32* (18), 7582–7601. <https://doi.org/10.1021/acs.chemmater.0c03019>.
- (215) Wu, F.; Liu, Y.; Zhang, J.; Duan, S.; Ji, D.; Yang, H. Recent Advances in High-Mobility and High-Stretchability Organic Field-Effect Transistors: From Materials, Devices to Applications. *Small Methods* **2021**, *5* (12), 1–25. <https://doi.org/10.1002/smt.202100676>.
- (216) Pawlak, A.; Galeski, A. Plastic Deformation of Crystalline Polymers: The Role of Cavitation and Crystal Plasticity. *Macromolecules* **2005**, *38* (23), 9688–9697. <https://doi.org/10.1021/ma050842o>.
- (217) Zhang, S.; Koizumi, M.; Cao, Z.; Mao, K. S.; Qian, Z.; Galuska, L. A.; Jin, L.; Gu, X. Directly Probing the Fracture Behavior of Ultrathin Polymeric Films. *ACS Polym. Au* **2021**, *1* (1), 16–29. <https://doi.org/10.1021/acspolymersau.1c00005>.
- (218) Pandolfi, R. J.; Allan, D. B.; Arenholz, E.; Barroso-Luque, L.; Campbell, S. I.; Caswell, T. A.; Blair, A.; De Carlo, F.; Fackler, S.; Fournier, A. P.; Freychet, G.; Fukuto, M.; Gürsoy, D.; Jiang, Z.; Krishnan, H.; Kumar, D.; Kline, R. J.; Li, R.; Liman, C.; Marchesini, S.; Mehta, A.; N'Diaye, A. T.; Parkinson, D. Y.; Parks, H.; Pellouchoud, L. A.; Perciano, T.; Ren, F.; Sahoo, S.; Strzalka, J.; Sunday, D.; Tassone, C. J.; Ushizima, D.; Venkatakrisnan, S.; Yager, K. G.; Zwart, P.; Sethian, J. A.; Hexemer, A. Xi-Cam: A Versatile Interface for Data Visualization and Analysis. *J. Synchrotron Radiat.* **2018**, *25* (4), 1261–1270. <https://doi.org/10.1107/S1600577518005787>.
- (219) Sarapas, J. M.; Martin, T. B.; Chremos, A.; Douglas, J. F.; Beers, K. L. Bottlebrush Polymers in the Melt and Polyelectrolytes in Solution Share Common Structural Features. *Proc. Natl. Acad. Sci. U. S. A.* **2020**, *117* (10), 5168–5175. <https://doi.org/10.1073/pnas.1916362117>.
- (220) Cao, Z.; Li, Z.; Zhang, S.; Galuska, L.; Li, T.; Do, C.; Xia, W.; Hong, K.; Gu, X. Decoupling Poly(3-Alkylthiophenes)' Backbone and Side-Chain Conformation by Selective Deuteration and Neutron Scattering. *Macromolecules* **2020**, *53* (24), 11142–11152. <https://doi.org/10.1021/acs.macromol.0c02086>.
- (221) Zhao, H.; Shanahan, J. J.; Samson, S.; Li, Z.; Ma, G.; Prine, N.; Galuska, L.; Wang, Y.; Xia, W.; You, W.; Gu, X. Manipulating Conjugated Polymer Backbone Dynamics through Controlled Thermal Cleavage of Alkyl Side Chains. *Macromol. Rapid Commun.* **2022**, 2200533. <https://doi.org/10.1002/marc.202200533>.

- (222) Plimpton, S. Fast Parallel Algorithms for Short-Range Molecular Dynamics. *Journal of computational physics*. 1995, pp 1–19. <https://doi.org/10.1039/c7sm02429k>.
- (223) Humphrey, W.; Dalke, A.; Schulten, K. VMD: Visual Molecular Dynamics. *J. Mol. Graph.* **1996**, *14* (October 1995), 33–38.
- (224) Toepperwein, G. N.; Riggelman, R. A.; De Pablo, J. J. Dynamics and Deformation Response of Rod-Containing Nanocomposites. *Macromolecules* **2012**, *45* (1), 543–554. <https://doi.org/10.1021/ma2017277>.
- (225) Balar, N.; Rech, J. J.; Henry, R.; Ye, L.; Ade, H.; You, W.; O'Connor, B. T. The Importance of Entanglements in Optimizing the Mechanical and Electrical Performance of All-Polymer Solar Cells. *Chem. Mater.* **2019**, *31* (14), 5124–5132. <https://doi.org/10.1021/acs.chemmater.9b01011>.
- (226) Arasaratnam, P.; Sivakumaran, K. S.; Tait, M. J. True Stress-True Strain Models for Structural Steel Elements. *ISRN Civ. Eng.* **2011**, *2011*, 1–11. <https://doi.org/10.5402/2011/656401>.
- (227) Chen, S.-A. A.; Ni, J.-M. M. Structure/Properties of Conjugated Conductive Polymers. 1. Neutral Poly(3-Alkylthiophene)S. *Macromolecules* **1992**, *25* (23), 6081–6089. <https://doi.org/10.1021/ma00049a001>.
- (228) Alkhadra, M. A.; Root, S. E.; Hilby, K. M.; Rodriguez, D.; Sugiyama, F.; Lipomi, D. J. Quantifying the Fracture Behavior of Brittle and Ductile Thin Films of Semiconducting Polymers. *Chem. Mater.* **2017**, *29* (23), 10139–10149. <https://doi.org/10.1021/acs.chemmater.7b03922>.
- (229) Butler, M. F.; Donald, A. M.; Ryan, A. J. Time Resolved Simultaneous Small- and Wide-Angle X-Ray Scattering during Polyethylene Deformation - II. Cold Drawing of Linear Polyethylene. *Polymer (Guildf)*. **1998**, *39* (1), 39–52. [https://doi.org/10.1016/S0032-3861\(97\)00226-7](https://doi.org/10.1016/S0032-3861(97)00226-7).
- (230) O'Connor, B.; Kline, R. J.; Conrad, B. R.; Richter, L. J.; Gundlach, D.; Toney, M. F.; DeLongchamp, D. M. Anisotropic Structure and Charge Transport in Highly Strain-Aligned Regioregular Poly(3-Hexylthiophene). *Adv. Funct. Mater.* **2011**, *21* (19), 3697–3705. <https://doi.org/10.1002/adfm.201100904>.
- (231) O'Connor, B. T.; Reid, O. G.; Zhang, X.; Kline, R. J.; Richter, L. J.; Gundlach, D. J.; DeLongchamp, D. M.; Toney, M. F.; Kopidakis, N.; Rumbles, G. Morphological Origin of Charge Transport Anisotropy in Aligned Polythiophene Thin Films. *Adv. Funct. Mater.* **2014**, *24* (22), 3422–3431. <https://doi.org/10.1002/adfm.201303351>.
- (232) Huang, W. Y.; Lee, C. C.; Wang, S. G.; Han, Y. K.; Chang, M. Y. Side Chain Effects of Poly(3-Alkylthiophene) on the Morphology and Performance of Polymer Solar Cells. *J. Electrochem. Soc.* **2010**, *157* (9), B1336. <https://doi.org/10.1149/1.3461139>.
- (233) Shafiee, A.; Salleh, M. M.; Yahaya, M. Determination of HOMO and LUMO of [6,6]-Phenyl C61-Butyric Acid 3-Ethylthiophene Ester and Poly (3-Octyl-Thiophene-2, 5-Diyl) through Voltametry Characterization. *Sains Malaysiana* **2011**, *40* (2), 173–176.
- (234) Lei, T.; Cao, Y.; Fan, Y.; Liu, C.; Yuan, S.; Pei, J. High-Performance Air-Stable Organic Field-Effect Transistors: Isoindigo-Based Conjugated Polymers. **2011**, 6099–6101.

- (235) Salleo, A.; Kline, R. J.; DeLongchamp, D. M.; Chabinyc, M. L. Microstructural Characterization and Charge Transport in Thin Films of Conjugated Polymers. *Adv. Mater.* **2010**, *22* (34), 3812–3838. <https://doi.org/10.1002/adma.200903712>.
- (236) Gurau, M. C.; DeLongchamp, D. M.; Vogel, B. M.; Lin, E. K.; Fischer, D. A.; Sambasivan, S.; Richter, L. J. Measuring Molecular Order in Poly(3-Alkylthiophene) Thin Films with Polarizing Spectroscopies. *Langmuir* **2007**, *23* (2), 834–842. <https://doi.org/10.1021/la0618972>.
- (237) Li, Z.; Liao, Y.; Zhang, Y.; Zhang, Y.; Xia, W. Microstructure and Dynamics of Nanocellulose Films: Insights into the Deformational Behavior. *Extrem. Mech. Lett.* **2022**, *50*, 101519. <https://doi.org/10.1016/j.eml.2021.101519>.
- (238) Ding, Z.; Liu, D.; Zhao, K.; Han, Y. Optimizing Morphology to Trade Off Charge Transport and Mechanical Properties of Stretchable Conjugated Polymer Films. *Macromolecules* **2021**, *54* (9), 3907–3926. <https://doi.org/10.1021/acs.macromol.1c00268>.
- (239) Zheng, Z.; Yim, K. H.; Saifullah, M. S. M.; Welland, M. E.; Friend, R. H.; Kim, J. S.; Huck, W. T. S. Uniaxial Alignment of Liquid-Crystalline Conjugated Polymers by Nanoconfinement. *Nano Lett.* **2007**, *7* (4), 987–992. <https://doi.org/10.1021/nl070022k>.
- (240) Campbell, C. G.; Ummadisetty, S.; Storey, R. F. Decoupling and Functionalization of Coupled Polyisobutylene via Alkoxybenzene Quenching. *Macromolecules* **2016**, *49* (20), 7642–7652. <https://doi.org/10.1021/acs.macromol.6b01754>.